

The *Far Ultraviolet Spectroscopic Explorer* Survey of O VI Absorption in the Disk of the Milky Way

David V. Bowen¹, Edward B. Jenkins¹, Todd M. Tripp^{1,2}, Kenneth R. Sembach³, Blair D. Savage⁴, H. Warren Moos⁵, William R. Oegerle⁶, Scott D. Friedman³, Cecile Gry⁷, Jeffrey W. Kruk⁵, Edward Murphy⁸, Ravi Sankrit⁹, J. Michael Shull¹⁰, George Sonneborn⁶, Donald G. York¹¹

¹ Princeton University Observatory, Peyton Hall, Ivy Lane, Princeton, NJ 08544

² Dept. of Astronomy, University of Massachusetts, Amherst, MA 01003

³ Space Telescope Science Institute, 3700 San Martin Dr., Baltimore, MD 21218

⁴ Dept. of Astronomy, University of Wisconsin, 475 N. Charter Street, Madison, WI 53706

⁵ Dept. of Physics and Astronomy, Johns Hopkins University, Baltimore, MD 21218

⁶ Astrophysics Science Division, Code 660, NASA/Goddard Space Flight Center, Greenbelt, MD 20771

⁷ Laboratoire d'Astrophysique de Marseille, 13376 Marseille, France

⁸ Dept. of Astronomy, University of Virginia, Box 400325, Charlottesville, VA 22904-4325

⁹ Space Science Laboratory, University of California, Berkeley, Berkeley, CA 94270-7450

¹⁰ Dept. of Astrophysical and Planetary Sciences, University of Colorado, Boulder, CO 80309-0389

¹¹ Dept. of Astronomy and Astrophysics, University of Chicago, Enrico Fermi Institute, 5640 South Ellis Avenue, Chicago, IL 60637.

Received: 11-July-2007; Accepted: 19-October-2007

ABSTRACT

To probe the distribution and physical characteristics of interstellar gas at temperatures $T \approx 3 \times 10^5$ K in the disk of the Milky Way, we have used the *Far Ultraviolet Spectroscopic Explorer* (*FUSE*) to observe absorption lines of O VI $\lambda 1032$ toward 148 early-type stars situated at distances > 1 kpc. After subtracting off a mild excess of O VI arising from the Local Bubble, combining our new results with earlier surveys of O VI, and eliminating stars that show conspicuous localized X-ray emission, we find an average O VI mid-plane density $n_0 = 1.3 \times 10^{-8} \text{ cm}^{-3}$. The density decreases away from the plane of the Galaxy in a way that is consistent with an exponential scale height of 3.2 kpc at negative latitudes or 4.6 kpc at positive latitudes. Average volume densities of O VI along different sight lines exhibit a dispersion of about 0.26 dex, irrespective of the distances to the target stars. This indicates that O VI does not arise in randomly situated clouds of a fixed size and density, but instead is distributed in regions that have a very broad range of column densities, with the more strongly absorbing clouds having a lower space density. Line widths and centroid velocities are much larger than those expected from differential Galactic rotation, but they are nevertheless correlated with distance and $N(\text{O VI})$, which reinforces our picture of a diverse population of hot plasma regions that are ubiquitous over the entire Galactic disk. The velocity extremes of the O VI profiles show a loose correlation with those of very strong lines of less ionized species, supporting a picture of a turbulent, multiphase medium churned by shock-heated gas from multiple supernova explosions.

Subject headings: Galaxy:disk — ISM: clouds — ISM:kinematics and dynamics — ISM:structure — ultraviolet:ISM

1. INTRODUCTION

Very hot plasmas are recognized as important constituents in a broad range of astrophysical contexts, ranging from the solar and stellar transition layers and coronae up to the largest arrangements of matter in the universe that form web-like structures that bridge groups and clusters of galaxies. In all cases, the processes responsible for heating the gas give important insights on evolutionary and dynamical phenomena in the systems under study. On the largest scales, there is a recognition that hot gas in the intracluster media and even the intergalactic media at low redshifts probably dominate the baryonic content of the universe (e.g. Cen & Ostriker 1999; Tripp et al. 2000; Danforth & Shull 2005; Bregman 2007). In this paper, we focus on the presence of hot gas within the interstellar medium (ISM) of the Milky Way, a system intermediate in size between the extremes just mentioned. This is a topic that has been studied over the last 3 decades, and shortly (§1.2) we will look back upon some of the key developments in this field to help define the motivations for our present study.

1.1. Basic Principles of Detecting Hot Gas

Atoms within plasmas at temperatures $T > 10^5$ K have many of their outer electrons stripped by collisions. As a consequence, there is an upward shift in the energy of their resonance transitions, pushing important spectroscopic information into the ultraviolet and X-ray bands. It is for this reason that progress in understanding the distribution and properties of hot gases in space have had to await the development of space-borne instruments that could observe radiation at energies above those in the visible band.¹ Of all the transitions from highly ionized atoms at wavelengths longward of the Lyman limit, the $\lambda\lambda 1032, 1037$ doublet of O VI is the most suitable for study. The advantages of observing O VI are threefold: (1) the ionization potential of O⁺⁴ is high enough (114 eV) to insure that there is no appreciable contamination by cooler material photoionized by starlight,² as is the case with other partly stripped, Li-like atoms such as

Si IV and C IV (Cowie et al. 1981b), (2) the transitions are strong [$\log f\lambda = 2.138$ for the 1032 Å transition (Morton 2003)], and (3) the cosmic abundance of oxygen is high. One mildly negative factor is that the peak abundance of the five-times ionized form of oxygen (22% at $T = 3 \times 10^5$ K under collisional ionization equilibrium conditions) is lower than representative fractions that can be reached by other ionization stages just below or above that of O VI (Shapiro & Moore 1976a; Shull & van Steenberg 1982; Sutherland & Dopita 1993). Also, the temperature range over which O VI is the dominant species is smaller than that of many other ions, such as O VII λ 21.6 seen in the X-ray band.

The easiest way to observe the O VI transitions is to record them in absorption in the spectrum of a UV-bright source. In the disk of the Galaxy, the most suitable stars are those hotter than spectral type B3 that have large projected rotation velocities $v \sin i$. Difficulties with poorly behaved stellar continua sometimes arise to create ambiguities in the absorption strengths; this issue is one that we address later in §2.6 for our current study. For probing the Galactic halo, AGNs and quasars make excellent background sources.

Energetic collisions in a hot gas not only ionize the atoms, but they also excite them to electronic states at energies well above the ground state. As a consequence, the atoms emit radiation in their strong resonance lines. O VI can be seen in emission (see, e.g., Table 1 of Dixon et al. 2006; Otte & Dixon 2006) although the flux levels are very faint ($\sim 1 - 4 \times 10^{-18}$ ergs cm⁻² s⁻¹ arcsec⁻²) and require long integration times to achieve a satisfactory detection. A principal difference between the absorption and emission measurements is that the former is proportional to the line integral of the electron density, while the latter senses the square of the electron density [but with some sensitivity to temperature beyond just the variation from the ion fraction curve (Shull & Slavin 1994)]. This difference can be exploited to measure the filling factor of the gas, $\langle n_e \rangle^2 / \langle n_e^2 \rangle$. One drawback in measuring the O VI emission is that self absorption and resonant scattering can complicate the interpretation if the optical depths are of order or greater than unity (Shelton et al. 2001). Also, the emission can be attenuated by the absorption caused by dust in the foreground.

Line emission from atoms other than O VI also radiate from hot gases. As a rule, the characteristic energy bands where the emissions are strongest and most plentiful increase toward higher energies as the tem-

¹Forbidden transitions in the visible from highly ionized atoms are generally too weak to observe (Graney & Sarazin 1990), except as seen in emission for exceptionally bright sources such as supernova remnants (Woodgate et al. 1974, 1975; Teske 1990; Sauvageot & Decourchelle 1995; Sauvageot et al. 1999; Szentgyorgyi et al. 2000).

²Except for small contributions from very hot, He-poor white dwarfs (Dupree & Raymond 1983).

perature rises. For gas at temperatures of 282,000 K where O VI has its maximum ion fraction in collisional equilibrium, the characteristic energy of the strongest emission-line features is below 300 eV (Kato 1976). Unfortunately, there are a number of drawbacks that limit our ability to make good use of the X-ray background measurements as we interpret the O VI absorption data. First, at energies below 300 eV the absorption by foreground neutral hydrogen and helium is strong (Morrison & McCammon 1983). Second, it is often difficult to know how much emission arises from beyond the target used for the O VI measurement. Third, over recent years there has been an increasing awareness that the soft X-ray background is contaminated by emission from charge exchange between heavy solar wind ions and the local interstellar gas (Cravens 2000; Cravens et al. 2001), a process identical to that which produces X-ray emission from comets (Kharchenko & Dalgarno 2000; Krasnopolsky et al. 2002; Kharchenko et al. 2003). This contamination may be as much as half of the observed diffuse background level (Lallement 2004). Finally, with the exception of the lowest energy X-ray measurements, such as those that operate below the 111 eV absorption cutoff of a beryllium filter (Bloch et al. 1986), the observations have much stronger responses to gases that are too hot ($T \gtrsim 2 \times 10^6$ K) to yield much O VI. All but the second reason listed above may help to explain why Savage et al. (2003) found a poor correlation between soft X-ray emission and the strength of O VI absorption toward extragalactic targets at high Galactic latitudes.

1.2. Early Developments

Prior to the advent of space astronomy, an ingenious insight on the probable existence of a large volume of space that contains hot gases was provided by Spitzer (1956), who noted that cold clouds found in the Galactic halo had to have some means of confinement. He speculated that such clouds were stabilized by the external thermal pressure of a hot Galactic corona. It was not until some 18 years later that firm evidence on the pervasiveness of this type of material within the Galactic disk was demonstrated by direct observations of absorption by the O VI doublet at 1032 and 1038 Å in the spectra of 32 stars (Jenkins & Meloy 1974; York 1974), accompanied by a recognition by Williamson et al. (1974) that the diffuse soft X-ray emission observed by instruments on sounding rockets (Bowyer et al. 1968; Bunner et al. 1971; Davidsen et al. 1972;

Yentis et al. 1972) probably came from the same type of material.

Following the initial discoveries, Jenkins (1978a) (hereafter J78) conducted a survey of O VI absorption which increased the accumulation of cases to 72 Milky Way stars. From this body of data, he offered some conclusions on the nature of the hot gas and how it is distributed in space (Jenkins 1978b,c). In particular, the statistical fluctuations of absorption strengths and velocities from one sight line to the next indicated that approximately 6 hot gas regions, each with a column density $N(\text{O VI}) \approx 10^{13} \text{ cm}^{-2}$, are distributed across a representative distance of 1 kpc. Later, inspired by evidence from the soft X-ray surveys that the Sun is surrounded by a volume of hot gas out to a distance of around 100 pc (Sanders et al. 1977; McCammon & Sanders 1990; Snowden et al. 1990, 1998), a structure now called the Local Bubble (hereafter, ‘LB’), Shelton & Cox (1994) conceived of a slightly more elaborate model that accounted for a possible constant foreground contribution of O VI, with $N(\text{O VI})$ averaging about $1.6 \times 10^{13} \text{ cm}^{-2}$, which reduced the apparent fluctuations of a much more patchy distribution at greater distances. Their re-interpretation of the O VI data suggested that outside the Local Bubble the Galactic disk is populated by regions that have column densities in the range $2 - 7 \times 10^{13} \text{ cm}^{-2}$ with separations 450 – 1300 pc. With the advent of the *Far Ultraviolet Spectroscopic Explorer* (FUSE), Oegerle et al. (2005) looked at weak O VI lines towards nearby white dwarfs (WDs), and determined the average volume density to be $2.4 \times 10^{-8} \text{ cm}^{-3}$. They concluded that the local O VI contribution is much less than that estimated by Shelton & Cox (1994) unless it is confined to a thin shell at the edge of the LB, i.e., just beyond the white dwarfs. A much larger survey of nearby WDs was conducted by Savage & Lehner (2006), who measured the average O VI density to be $3.6 \times 10^{-8} \text{ cm}^{-3}$.

A challenge that was presented to the early O VI investigators was a proposal by Castor et al. (1975) that all of the O VI arose from bubbles that were created by stellar mass-loss winds from the target stars. Jenkins (1978c) addressed this issue and concluded that some O VI could arise from the bubbles, but that most of the hot gas was truly interstellar in nature. We return to this topic once again in this paper (§3.4).

After the end of the *Copernicus* era, there was a long period where only the transitions of N V, Si IV and C IV could be seen in absorption using the *International Ultraviolet Explorer* (IUE) and the *Hubble*

Space Telescope (HST). Because these species can be created at lower energies (ionization potentials of the next lower stages are only 33, 48 and 77 eV, respectively), there was a persistent concern that photoionized gases could be responsible for these species, especially in low density environments. Even so, important conclusions emerged about the distributions of highly ionized material in the Galactic halo (Savage & Massa 1987; Sembach et al. 1991; Sembach & Savage 1992), the Magellanic Clouds (de Boer & Savage 1980; Fitzpatrick & Savage 1985), and within the Galactic disk (Cowie et al. 1981b; Walborn et al. 1984; Edgar & Savage 1992; Spitzer & Fitzpatrick 1992; Sembach 1993, 1994; Tripp et al. 1993; Savage et al. 1994; Sembach et al. 1994; Huang et al. 1995), often using distant UV sources fainter than the sensitivity limit of *Copernicus*. Further studies of O VI, however, were confined to results that were more limited in scope (Ferguson et al. 1995; Hurwitz et al. 1995; Dixon et al. 1996; Hurwitz & Bowyer 1996; Widmann et al. 1998; Sembach et al. 1999) because they came from short-lived missions, such as the *Hopkins Ultraviolet Telescope (HUT)* (Davidsen 1993) and the *Orbiting Retrievable Far and Extreme Ultraviolet Spectrograph (ORFEUS-SPAS)* (Hurwitz et al. 1998). With the availability of *FUSE*, we can now return to large-scale surveys of O VI absorption. Already, interstellar O VI has been studied in the Galactic halo (Oegerle et al. 2000; Richter et al. 2001; Howk et al. 2002a; Fox et al. 2004; Savage et al. 2003; Sembach et al. 2003; Wakker et al. 2003), Large Magellanic Cloud (Howk et al. 2002b), Small Magellanic Cloud (Hoopes et al. 2002), and the Local Bubble (Oegerle et al. 2005; Savage & Lehner 2006). Likewise, intergalactic O VI has been found for absorption systems at redshifts that are too low for coverage with *HST* (Oegerle et al. 2000; Sembach et al. 2001; Tripp et al. 2001; Savage et al. 2002; Jenkins et al. 2003; Prochaska et al. 2004; Richter et al. 2004; Sembach et al. 2004; Danforth & Shull 2005). With the current paper, we cover yet another important realm, the Galactic disk.

Through the years, theoretical investigations kept pace with the observations, starting with initial assessments by Shapiro & Field (1976) on the nature of a possible Galactic fountain, and an early proposal by Cox & Smith (1974) on the origin of a pervasive network (“tunnels”) of hot gas that is kept alive by the channeling of shock waves (from supernovae) within it. This picture was investigated in more detail by Smith (1977). McKee & Ostriker (1977) presented a

seminal treatise on the different phases of the medium, accounting for mass and energy balance between a hot interstellar medium created by supernovae and the more conventional phases at lower temperatures. This theory was a very important advance over an earlier model for ISM phases developed by Field et al. (1969) that overlooked the hot phase and its secondary effects. Some noteworthy consequences that might arise from the hot gas production include mechanical energy transport to the embedded cool clouds (Cox 1979) and a feedback mechanism that may regulate star formation in disk galaxies (Cox 1981). Enhanced accumulations of O VI-bearing gas will undoubtedly arise from hot gas at the edges of, and within, the interiors of supernova remnants, which is discussed in the models presented by Chevalier (1974), Cowie et al. (1981a), Slavin & Cox (1992), Edgar & Cox (1993), Smith & Cox (2001), and Shelton (2006).

More recently, exciting realizations of how the ISM may be configured from supernova explosions have been conducted by de Avillez (2000), de Avillez & Breitschwerdt (2004) and de Avillez & Breitschwerdt (2005a) using hydrodynamic and magnetohydrodynamic simulations. Their models predict global equilibrium in the disk-halo circulation when the explosions in the ISM are traced over several hundred Myr, and demonstrate how effective turbulent diffusion can be in mixing hot and cold gas. de Avillez & Breitschwerdt (2005b) predict specifically the expected O VI column densities along random lines of sight over distances of up to 1 kpc, and find good agreement with the *FUSE* WD and *Copernicus* data. Their models predict a clumpy turbulent ISM in which O VI vortices and filaments are intercepted every ~ 100 pc, each with $N(\text{O VI}) \simeq 1 - 2 \times 10^{12} \text{ cm}^{-2}$.

1.3. Current Topics

A persistently debated unknown quantity is the volume filling factor of the hot gas in the Galactic disk (Ferrière 1995). Equally important is the topology of the gas: is it confined to isolated, compact bubbles or does it comprise a matrix of multiply connected regions within which the rest of the ISM is confined? For observers, it is easy to measure the average amount of O VI in the Galactic disk, and with reasonable assumptions we may relate this quantity to the total amount of gas in the temperature regime $10^5 - 10^6$ K. However, a much more difficult task is to understand the structure of the gas along the viewing direction, i.e., information that is lost by the projection of everything along

the sight line, which is compounded by the restriction that not all directions in the sky can be sensed. Jenkins (1978b) placed an approximate upper limit of 20% for the filling factor from the apparent lack of an anticorrelation between the amount of O VI and denser (mostly neutral) hydrogen, as revealed by the color excesses of the target stars (however, this argument can equally well be used to say the filling factor is greater than 80%). Models that propose that the hot gas has a very large filling factor [e.g. that of McKee & Ostriker (1977)] must be restrained by observations by Heiles (1980) that indicate that the neutral, warm medium (gas that emits 21-cm radiation but has a high spin temperature and thus negligible absorption) has its own significant filling factor. One feature of the McKee & Ostriker model is that it assumes that supernovae occur at random locations and time. Actually, supernovae are highly correlated (McCray & Snow 1979; Heiles 1990), and this should influence theories on the pervasiveness of O VI-bearing material, leading to fewer, but larger volumes whose interiors hold the hot gas. The existence of such large, coherent structures seems to be validated by observations of enormous shells of gas seen in 21-cm line emission (Heiles 1979, 1984; McClure-Griffiths et al. 2002).

The kinematics of O VI and its relationship with other forms of gas, those that are highly ionized and those that are not, can provide important clues on the nature of the hot gas on a more microscopic level. One of the first conclusions to emerge from the velocity profiles of the O VI features is that they were broader than those produced by less ionized species, such as Si II and Si III (York 1974), indicating that the O VI was not simply a more ionized counterpart of the lower excitation gas. The absorptions exhibited by York were of very good quality, which enabled him to place upper limits to the Doppler motions that corresponded to a range $T = 4 \times 10^5$ to 2×10^6 for different cases. The most striking conclusion from the survey by Jenkins (1978b) was that the scatter of velocity centroids, amounting to only 26 km s^{-1} , is far below the shock speeds needed to create the post-shock temperatures that can strip 5 electrons from the oxygen atoms, i.e., at least $130\text{--}160 \text{ km s}^{-1}$. (Raymond 1979; Shull & McKee 1979) A similarly small dispersion of 21 km s^{-1} was reported recently by Savage et al. (2003) for sight lines through the Galactic halo. The assertion that O VI does not have extraordinarily large velocities must be viewed with caution however. We can not rule out the presence of some additional O VI that is

moving very rapidly, for if the absorption profiles of such high velocity material were very broad and shallow, they would be very difficult to detect against the undulating stellar continua.

Simply put, O VI is not created in zones that immediately follow the shocks that heated the gas to high temperatures. Instead, the low velocities indicate that what we see arises either from some interaction with the normal, low-ionization material or, alternatively, perhaps ions whose velocities are regulated by magnetic fields in the disk (Roger & Landecker 1988) that might have been compressed and amplified by the motions of expanding supernova remnants (Spitzer 1990). For the former possibility, we may consider two alternatives. One is that the O VI originates in transition layers where heat flows by conduction across interfaces established between regions that hold very hot ($T > 10^6 \text{ K}$) gas and denser, cooler material (Cowie & McKee 1977; McKee & Cowie 1977; Begelman & McKee 1990; Bertoldi & McKee 1990; McKee & Begelman 1990). Material is transported between the regions: at early times cool gas evaporates into the hot region, whereas later, after radiative cooling becomes important, hot gas condenses onto the cool gas (Borkowski et al. 1990). If there is a substantial difference in velocity between the cool and hot material, an additional means of transporting heat and matter operates: instabilities in the transition zone create turbulence which acts as a source of mechanical mixing of the cool and hot phases (Begelman & Fabian 1990; Slavin et al. 1993).

Observational support for links between O VI-bearing gas and the cooler material was provided by Cowie et al. (1979), who noted correlations in velocity between O VI and the ions Si III and N II. Additional support was provided by the good velocity correspondence between O VI and C II absorption along short path lengths through the local ISM (Savage & Lehner 2006). One way to gain insights on the relative importance of the different processes discussed above, as well as to see if the gas is simply radiatively cooling (Edgar & Chevalier 1986) instead of being cooled by contact with low temperature material, is to test whether or not various other highly ionized atoms (N V, Si IV and C IV) agree with theoretical predictions for the different regimes (Spitzer 1996; Fox et al. 2003).

In addition to the possibilities listed above, we must be watchful for another physical condition, that, under certain circumstances, may apply to the regions that

are responsible for O VI absorption. In a discussion of hot gas within the Local Bubble, Breitschwerdt & Schmutzler (1994) considered the possibility that an explosion in a dense region followed by expansion in a lower density medium would lead to adiabatic cooling of the hot gas. The lag in recombination as the gas cools would be even more severe than for a radiatively cooling gas. They envision the possibility that we are surrounded by gas at $T \sim 50,000\text{K}$ that still has an appreciable concentration of ions that normally appear in equilibrium at much higher temperatures. It is important to note that we cannot depend on identifying this gas on the basis that the lines have a velocity dispersion characteristic of the Doppler broadening at the lower temperatures, since the expansion process itself creates a broadening that replaces the thermal broadening.

In the discussion presented up to now, we have considered a number of contemporary problems in the study of gases responsible for O VI absorption in the disk of the Galaxy. More comprehensive discussions are provided by review papers written by Cox & Reynolds (1987), Savage (1987), Jenkins (1987), and Spitzer (1990).

1.4. Outline of This Paper—A Summary

The capability of *FUSE* to record spectra of stars much fainter than the magnitude limit of *Copernicus* ($V \leq 7.5$), allows us to probe regions well beyond the original O VI survey of J78. In this paper, we present a new *FUSE* sample of disk stars which has about twice as many stars as the older survey. These two considerations allow us to overcome some shortcomings of the earlier work and address such issues as the possible presence of very large scale structures containing either more or less than the usual amount of O VI, and whether or not the apparent decrease of O VI at moderate distances from the Galactic plane agrees with an exponential scale height of $\sim 2.3\text{kpc}$ as determined from sources well outside the Galaxy (Savage et al. 2003). Also, with the larger column densities that arise from the greater lengths of the sight lines, we should be less sensitive to distortions of the results arising from *i*) the presence of bubbles around the target stars and *ii*) an over-representation of the region surrounding the Sun that arises from the constraint that all sight lines must emanate from a single point.

This paper focuses on three principal topics. First, we describe in detail the data collection and reduction

of the *FUSE* spectra, and the analysis of the O VI absorption line profiles. Second, we present a re-evaluation of the distances to the targeted stars, which is an important parameter for understanding how O VI is distributed in the Galactic disk. Third, we discuss the global properties of O VI absorption in the disk, which, of course, is the main science goal of this survey.

As far as the first of these topics is concerned, the data reduction of *FUSE* spectra is not unlike that of any other data taken with modern photon-counting devices. We were concerned, however, that we should be able to precisely calibrate the wavelength scale of the spectra, since *FUSE* does not take calibration spectra contemporaneously with an object. This led us to compare the data from many of our sight lines with high quality, high resolution *HST* data, from which we found that the standard *FUSE* wavelength scale for the pipeline calibration (CalFUSE 2.0.5) required a correction of 10 km s^{-1} . This analysis is introduced in §2.4 and described in detail in Appendix A.

In analyzing the O VI lines, we faced two main obstacles. First, J78 realized that any O VI $\lambda 1032$ line is contaminated to some degree by the HD 6–0 R(0) line at 1031.9 \AA . Before measuring the physical parameters of an O VI line, the contribution from this HD line must be removed. Fortunately, in the *FUSE* data, there exist other HD lines that are free of the dense H₂ ‘forest’ and which can be used to model the contaminating HD line. We found that removing the model using Voigt profile line-fitting techniques was highly successful and actually presented few problems for the subsequent analysis of the O VI $\lambda 1032$ line. Details are given in §2.5 and 2.7; §3.3 also discusses a consistency check on the efficacy of the HD removal using multi-epoch data.

A more problematic obstacle in analyzing the O VI lines arose in determining the shape of a star’s continuum. With the data reduced, we quickly discovered that the gradient of the continuum was probably varying on scales less than the width of an O VI line. The most extreme variations were prevalent among the O9–B1 type stars. It became clear that we needed to track three possible continuum fits: the adopted best fit, and two possible variations above and below this fit — ‘upper’ and ‘lower’ continuum fits, as we will refer to them throughout this paper. Although measuring continuum errors in absorption-line studies is far from unusual, in many cases, the interstellar lines under study are quite narrow, and continuum errors are largely ir-

relevant. For our *FUSE* data, however, we found that continuum errors actually dominated the O VI column density errors, and not the usual Poisson counting statistical errors. We discuss how we chose our continua in §2.6. With the spectra normalized, we were able to derive column densities, Doppler parameters and line velocities using both Voigt profile fitting (§2.8.1) and the Apparent Optical Depth (AOD) method (§2.8.2), both of which gave very similar results, as expected. For the subsequent analysis, we assumed that the absorbing gas had no small-scale velocity structures hidden within the broad profile that might invalidate either analysis method (§2.9). We favored the results from the Voigt profile fitting procedure, but used AOD measurements when no line was clearly present and an upper limit to the O VI column density was required (§2.8.2 and Appendix D). The spectra themselves are presented in §E.

The second principal goal of this paper is to re-evaluate the distances to the stars used in our survey. There are several databases now available (the *Hipparcos*, *Tycho*, and 2MASS catalogs) which provide a more reliable estimate of a distance than was possible a decade ago. We introduce the problem first in §3.2, where we show the distribution of stars in the Galactic plane. We expound a full discussion in Appendix B, since the methods used to derive distances are technical and outside the main scope of our discussion on O VI in the Galactic disk. A reader disinterested in the mechanisms of deriving stellar distances can certainly skip this Appendix, and instead simply note that the most egregious error in determining a distance arises from the difficulty in determining the absolute magnitude of a star, M_V . This is not because of a problem in knowing M_V for the particular spectral type or luminosity class of a star, but because of the problems inherent in defining the type and class correctly in the first place. The error in M_V is not only a function of the type and class, but depends on the quality of the stellar spectra used to define these parameters, and on the skill and experience of the observer making the measurements. Despite the significant improvements in measuring various stellar parameters with modern techniques, we believe that errors in stellar distances range from 10–30%, and that even larger deviations are possible. A full explanation is given in Appendix B.3.

The final topic of this paper is, of course, the global properties of O VI absorption in the disk of the Milky Way. Our motivation for the study has already been

introduced in the previous sections, but we note the following. With the huge amounts of data available from satellites that cover many different regions of the electromagnetic spectrum, it is now possible to compare the results from absorption-line surveys with results from other types of studies. In this paper, we concentrate on X-ray emission data taken with the *Röntgen Satellite (ROSAT)*. Although X-ray emitting gas is nominally at a higher temperature than we would expect for O VI absorbing gas, one can imagine a natural confluence of hot gas in structures that might be detected in both O VI absorption and X-ray emission. In §3.4 and 3.5, we describe the types of X-ray emission in *ROSAT* maps seen towards our *FUSE* stars. In many cases, these maps indicate regions of hot gas along the line of sight from bubbles of gas around stellar associations or supernova remnants. These observations lead us to classify the morphology of X-ray emitting patches (or absence thereof) around or near our target stars.

Using these classifications, we show in §3.7.3 that the average line of sight density $N(\text{O VI})/d$ is somewhat higher for sight lines which pass through X-ray enhanced regions, leading us to conclude that a small fraction of $N(\text{O VI})$ towards some stars does indeed arise in circumstellar material or wind-blown bubbles. This information is important, because by selecting sight lines with no clear X-ray emission, and by correcting O VI column densities for absorption by the Local Bubble using recently published data, we can derive a less biased value of the mid-plane density of O VI, n_0 . We discuss this value at some length in §3.7, concluding with our best determination of n_0 and its likely errors in §3.8.3. In calculating these values, we quantify the significance in the difference in $N(\text{O VI})$ towards stars in the north and south Galactic hemispheres originally found by Savage et al. (2003) (§3.8.1). The difference has no effect on the value of n_0 we derive, but does produce two different values of the scale height of the O VI gas layer in the plane of the Milky Way.

In §3.9 we show that $N(\text{O VI})$ is directly correlated with the distance to a star in the plane of the disk. This correlation can most easily be understood as the effect of longer sight lines passing through more absorbing clouds. This shows that O VI absorption cannot arise primarily from the circumstellar environment of the observed stars, but must be a truly interstellar phenomenon. The data also reveal a discontinuity in $N(\text{O VI})$ with distance beyond a few hundred pc, in

that column densities appear to be too high for a given distance. As we show, however, this arises from excess contributions to the measured $N(\text{O VI})$ from the Local Bubble.

However, the data also suggest that the hot O VI-absorbing ISM is neither a smoothly distributed homogeneous gas layer, nor a population of randomly distributed clouds with similar properties. First, there is no acceptable fit to the decrease in O VI density with height above the plane of the Galaxy unless an additional ‘error’ is introduced, a term which represents an intrinsic ‘clumpiness’ in the interstellar medium (§3.8.2). Second, this clumpiness does not decrease with distance, as would be expected if a sight line simply passed through more a greater number of generic clouds (§3.9). To explain this, we propose a picture of the O VI absorbing ISM that contains a mixture of cloud sizes, with small, randomly distributed small clouds and sparsely distributed large clouds. We also note an alternative explanation, that we may be seeing the clustering of many small clouds.

There are other lines of evidence that suggest that the O VI absorbing ‘clouds’ are actually one component in a complex, evolving, turbulent ISM. The velocities of the bulk of the O VI absorption do not follow the general pattern of differential co-rotation in the disk of the Galaxy (§3.11). Moreover, if we compare the extremes of the O VI absorption line profiles with the extremes of other lower ionization species (O I, C II, C III and Si III) we find that they match each other quite closely (§3.12). This apparent ‘coupling’ of at least some of the components in the absorption line profiles (at least those with the highest peculiar velocities along a sight line) suggests that the structures giving rise to absorption from hot gas are multi-ionized.

A natural explanation for all these phenomena has been discussed above. The numerical simulations of de Avillez & Breitschwerdt (2005b, and references therein) vividly realize how the ISM may look when driven by supernovae explosions. Their two dimensional density maps (for example) in the plane of the Galaxy show how hot gas arises in bubbles around supernovae, which is then sheared through turbulent diffusion, destroying the bubble and stretching the hot absorbing gas into filaments and vortices that dissipate with time. In §3.14 we confirm the relationship between $N(\text{O VI})$ and Doppler parameter found by other authors, and determine that the O VI lines are too wide to arise from differential Galactic rotation alone.

Clearly, the velocity fields that govern the O VI components along a sight line are much larger than can be reproduced by the simple motions of the Galactic disk, and of course, expanding supernova shells naturally explain these large velocities. When considering an ensemble of such regions along long sight lines, it seems plausible that the correlation of b with $N(\text{O VI})$ could arise from the existence of exceptionally large internal motions inside large clouds, or that smaller clouds within clusters are moving more rapidly than the gases within individual clouds.

de Avillez & Breitschwerdt (2005b) found good apparent agreement between their models and the *FUSE* WD data and the results from *Copernicus* over a path length of ~ 1 kpc. Our results are also likely to be consistent with these models, although a detailed comparison is beyond the scope of this paper. The data presented herein should provide sufficient information to test these, and any other detailed simulations, over larger scales.

2. *FUSE* OBSERVATIONS, DATA REDUCTION, AND ANALYSIS

2.1. Sample Selection

The core of our sample of sight lines comprises stars observed under the auspices of the *FUSE* PI Team-time programs P102 and P122. Stars for these programs were originally selected based on a variety of criteria: they were more than 1 kpc distant, in order to probe regions of the Galaxy beyond those studied by *Copernicus*; they had low values of reddening [$E(B-V) < 0.3$] to minimize contamination by H_2 lines; they lay within ± 10 degrees of the Galactic plane to confine the study to the Milky Way disk; they had spectral types of O9 or earlier, or O9 to B2 if their projected rotational velocities ($v \sin i$) were known to be $> 100 \text{ km s}^{-1}$; they had luminosity classes of III to I for O9 spectral types (or earlier), or class V if $v \sin i$ was high; their spectra were not known to show emission line characteristics; and there existed ancillary data of the star from previous UV satellites such as *IUE* or *ORFEUS-SPAS*, or from ground-based optical observations.

In addition to the stars selected for the PI Team-time programs, we added data from the *FUSE Multi-mission Archive at the Space Telescope Science Institute* (MAST). To investigate a range of ISM environments, we took data from PI Team programs P116 and P216 (“Molecular Hydrogen in Translucent Clouds”),

P117 (“Hot Stars”), and P101 (“The Properties of Hot Gas in the Milky Way and Magellanic Clouds”). In all cases, we selected only sight lines within $|b| < 10^\circ$ of the Galactic plane, again, in order to focus primarily on absorbing gas in the disk of the Milky Way. We only included data that had signal-to-noise (S/N) ratios at least as high as those obtained for stars in the core program and we rejected stars that had highly irregular continua (see §2.6).

We also searched the *FUSE* MAST archive to find stars from Guest Investigator (GI) programs that might also provide suitable targets. We adopted criteria very similar to those used for selecting targets for the P102 and P122 programs; we did, however, exclude regions inside the Vela supernova remnant region, at Galactic longitudes $260^\circ \leq l \leq 270^\circ$, and the Carina Nebula, $280^\circ \leq l \leq 300^\circ$. We also avoided any *FUSE* programs whose science goals were obviously oriented towards studying O VI absorption along especially selected sight lines³. We eventually collected all suitable data available prior to April 2003. Our sample comprises 148 stars in total, whose parameters are listed in Table 1. To introduce this table, we note the following: column 1 is a unique identifier (“unique ID”) assigned solely to help cross-reference stars in different figures and tables in this paper. Column 2 gives the name of the star, while column 3, labelled ‘Prog ID’ is the combination of *FUSE* program ID (the first three numerals) and a number assigned within that program (the last two numerals) for a particular star. Columns 4 and 5 list Galactic coordinates l and b ; for many of the tables in this paper, the sight lines are sorted by Galactic longitude, in order to map any variations in the physical characteristics of the O VI absorption along the plane of the Milky Way. Table 2 lists all the stars sorted by HD number instead, and includes the unique ID number (as well as l and b) which can be cross-referenced with entries in Table 1 and any other tables or figures. The remaining entries for Table 1 are discussed in later sections below.

2.2. *FUSE* Observations

Of the 148 stars in our sample, 111 were observed as part of PI-Team programs P102 and P122. A journal

³As we shall see, our Team-time programs P102 and P122 did include stars toward both the Vela and Carina regions, and those data are presented in this paper; however, by the time we searched the *FUSE* MAST archive it had become clear that the absorption towards these regions is far more complex than that seen in the rest of the Galactic disk (see §3.7.2) and requires a separate analysis.

of observations is given in Table 2, which includes the observation date and exposure time. For some stars, more than one day passed between return visits to a star, in which case we list the second (or third) date of the exposure in column 6. There are also examples where a PI Team program star was reobserved by a Guest Observer (‘GO’; the first letter of these programs run from ‘A’ to ‘D’ for Cycles 1–4); these are also listed after the PI-Team program entry. In a few cases, some stars were observed with very large time intervals between satellite visits. These data are useful for determining how strongly our results are influenced by possible time variations in the underlying stellar spectra. This in turn gives us an indication of how accurately we are able to normalize a star’s continuum around an O VI absorption line. We discuss this topic more fully in §3.3.

For each star, the data obtained usually consisted of several individual spectra (hereafter “sub-exposures”) which needed to be co-added. The exposure time T_{exp} in column 7 represents the total time actually spent on-target after the co-addition of useable sub-exposures; so, if individual sub-exposures were discarded (due, e.g. to loss of signal in a channel) the sub-exposure exposure time was not included in column 7. In total, just over 754 ksec was expended on programs P102 and P122. All stars were observed through the $30'' \times 30''$ LWRS aperture, except HD 175754, HD 041161 and HD 069106, which were observed with the $4'' \times 20''$ MDRS aperture.

Details of the *FUSE* satellite and instrumentation are given by Moos et al. (2000) and Sahnou et al. (2000). The wavelength regions of interest for detecting O VI are covered by four separate mirror/grating and detector combinations, namely the LiF1A/2B and the SiC1A/2B channels. However, we made measurements mainly using only LiF1A data, because that channel provides the highest effective area, the astigmatism correction point was designed to be at 1030 Å in the LiF channels, and the LiF1A data were initially the best calibrated. There are two exceptions: the HD 041161 and HD 060196 spectra came from the SiC1A and LiF2B channels, respectively, as no LiF1A data were available.

2.3. Sub-Exposure Corrections and Co-Addition

The raw data for all the stars in our survey were reduced using version 2.0.5 of CalFUSE, which was the most advanced version available during the data

reduction. Since the stars observed in this study are bright, the S/N ratios of individual sub-exposures were usually high enough for shifts between sub-exposures (caused by thermal motions in the spectrograph) to be seen. To determine possible shifts, we used the sub-exposure with the highest S/N ratio near the O VI $\lambda 1032$ line as the template spectrum against which other sub-exposures were compared. An initial shift of a sub-exposure was determined by cross-correlating a 10 \AA region of the data (centered at 1032 \AA) with the template. A more refined shift was then made visually, in order to determine a shift to within $\simeq \pm 0.5$ pixels ($\simeq 1 \text{ km s}^{-1}$). Both flux and error arrays were shifted using sinc interpolation if a shift of more than ± 0.5 pixels was measured. Ideally, we would like to have moved spectra only by integer numbers of pixels to properly preserve the noise characteristics of a spectrum. However, shifts of less than a pixel were clearly evident in data with good S/N, so fractional shifts were required. (As we will discuss later, continuum uncertainties dominate the errors in our data analysis, so noise errors are only of secondary interest.)

With individual sub-exposures mapped to the wavelength scale of the sub-exposure with the highest S/N, the wavelength and flux arrays of all the data were rebinned by a factor of 3, in order to increase the signal-to-noise of the spectra but still properly sample the data. The error arrays were rebinned by the same amount and reduced by a factor of $\sqrt{3}$. The initial dispersion of the data (from the CalFUSE calibration) was $\simeq 0.0067 \text{ \AA pix}^{-1}$,⁴ but the resolution of the LiF1A channel is between 15 and 20 km s^{-1} (0.052 – 0.069 \AA at 1030 \AA) FWHM. After rebinning, the final dispersion of the data was $0.020 \text{ \AA pix}^{-1}$, close to that required for optimally sampling the data. Individual sub-exposures were then co-added, with the flux weighted by the inverse of the variance formed from error arrays which were usually smoothed by 7 pixels.

2.4. Wavelength-scale Accuracy and Zero-Point Correction

An important quantity to measure in the *FUSE* spectra is the velocity of the detected O VI $\lambda 1032$ lines, the precision of which depends in large part on

⁴Note that this dispersion was less than the dispersion of $0.013 \text{ \AA pix}^{-1}$ used by later versions (> 3.0) of CalFUSE. This new number samples approximately one-quarter of a *FUSE* spectral resolution element (Dixon et al. 2007).

the accuracy of the wavelength calibration. Unfortunately, *FUSE* has no on-board facilities to provide such calibration in situ. Instead, CalFUSE assigns a wavelength scale to the data, accounting for distortions in the dispersion and spatial directions, and correcting for instrumental distortions.

Even with these corrections, errors arise in the zero-point of the wavelength calibrations, because, e.g., the source is not centered in the aperture, or, for channels other than LiF1, from misalignment of the primary mirrors. The LiF1 channel has the most stable wavelength calibration, since for the observations in this paper, the Fine Error Sensor used light from this channel to acquire an object. However, since we found small offsets between sub-exposures taken during the observations of a single star, we expected to find small errors in the absolute wavelength scale. (Indeed, although we used the sub-exposure with the highest S/N as a template against which to shift all the other sub-exposures, there was no reason to believe that the zero-point for this spectrum would be any more reliable than that of any other exposure.)

Fortunately, CalFUSE adequately corrects for extreme non-linearities when mapping pixels to wavelength, particularly over the region of interest around the O VI $\lambda 1032$ line. The measured velocities of the two molecular hydrogen (H_2) lines which flank the O VI $\lambda 1032$ line always agreed with each other (to within a 1σ dispersion of $\simeq 2$ – 3 km s^{-1}), which validates this assumption. We therefore needed only to find and apply a zero-point offset to the spectrum to correct the wavelength scale.

To derive a zero-point for a subset of the *FUSE* stars, we compared the velocities of H_2 lines near the O VI $\lambda 1032$ line, with that of a Cl I $\lambda 1347$ line in Archival *HST* data of the same stars, where the wavelength calibration is more precise than that for *FUSE*. In all, we were able to correct 55 spectra out of the total 148 spectra using this method. A comparison between the CalFUSE wavelength scale and the corrected value showed that for the remaining spectra, a shift of 10 km s^{-1} would correct the zero-point to within $\pm 5 \text{ km s}^{-1}$ of the true value. Full details of this analysis are given in Appendix A.

2.5. The O VI Wavelength Region and Contaminating Lines

An important step in the processing of the *FUSE* data was to normalize the spectrum of each star. Be-

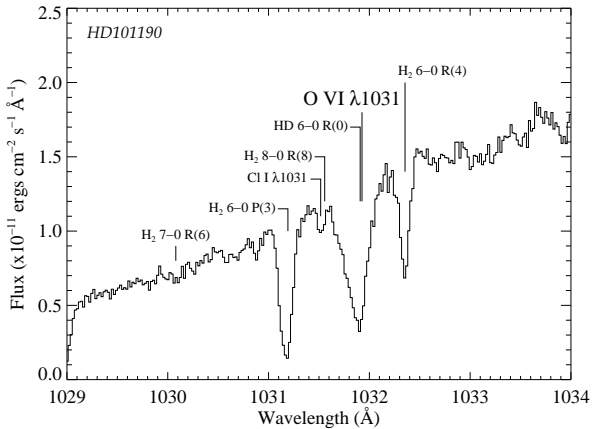


Figure 1: The spectrum of HD 101190, showing wavelengths of possible contaminating absorption lines around and within the O VI $\lambda 1032$ line.

fore describing this process, however, it is helpful to first discuss the identification of contaminating lines in the wavelength region around the O VI $\lambda 1032$ absorption line itself. As we show in §2.6, understanding the expected strengths of these lines was important for correctly determining the true shape of the continuum.

The positions of possible contaminating lines are shown in Figure 1, where we plot the the unnormalized spectrum of HD 101190 over the wavelength range 1029–1034 Å. The wavelengths of the lines shown in the figure are given in Table 3. This table also lists other lines that were used in our study (often at wavelengths far from the O VI wavelength region discussed in this section) and which will be introduced in later sections of this paper.

The most serious contaminant is the Lyman HD 6–0 R(0) line at 1031.909 Å, which is coincident in wavelength with the O VI $\lambda 1031.927$ line if the velocity differences are only moderate. For strong O VI lines, the contamination is largely negligible, but for weaker O VI lines, the contribution of the HD line can be significant. We discuss in §2.7 how we removed the contribution from this HD line.

Cl I $\lambda 1031$ is expected to arise at 1031.507 Å. This line was often seen in the *FUSE* spectra, always narrow and weak. We attempted to use the Cl I $\lambda 1004.678$ line to estimate the Cl I column density and thereby model the line at 1031 Å, since the 1004 Å line is

relatively free of other contaminating lines. Our attempts were unsuccessful, for two principal reasons. First, defining the rapidly changing continuum around both the 1031 and 1004 Å lines proved quite difficult, a problem that made the depths of these intrinsically weak lines highly uncertain. Second, even in the few (rare) cases where the continua were well behaved, we could not fit both lines consistently with a single cloud model of column density and Doppler parameter, leading us to suspect that problems may exist with published oscillator strengths. Recent work by Sonnen-trucker et al. (2006) confirms these suspicions, at least for the 1004 Å line.

Hence, in our analysis of the O VI $\lambda 1032$ line, we note where Cl I $\lambda 1031$ is expected, but no attempt has been made to model it. Fortunately, the position of the Cl I line is usually sufficiently blueward of the O VI feature that its contamination is unimportant. There are sight lines where the O VI feature can become blended with the Cl I line; however, as we discuss more fully in §2.8.1, the fitting of Voigt profiles to the O VI line is unaffected by the presence of Cl I, and the contribution to the computed O VI column density is negligible.

Close to the Cl I line is the H₂ 8–0 R(8) line at 1031.557 Å. To predict if we should see this line, we looked at the 7–0, 6–0, and 4–0 R(8) lines at 1042.745, 1054.520 and 1079.932 Å, respectively. These lines are relatively free of contamination by other interstellar species, and have similar oscillator strengths (see Table 3) compared to the 8–0 line, thereby providing suitable comparisons. We found absorption from these three R(8) transitions only along the line of sight to HDE 303308, which lies in the Carina Nebula. For those data we modelled the H₂ column density for the 8–0 line from the other three transitions and removed the profile from the spectrum. Weak R(8) lines may also be present in the spectrum of HD 187282, but there is significant blending with other H₂ features. Fortunately, the velocity of the 8–0 line is well enough removed from the O VI that it poses no threat of contamination to the O VI absorption.

As shown in Figure 1, O VI $\lambda 1032$ is flanked by the two strong H₂ lines at 1031.192 and 1032.354 Å, the 6–0 P(3) and 6–0 R(4) Lyman lines. These often blend with the O VI feature, but can be modeled and removed quite accurately, as we discuss in the following section.

2.6. Continuum Fitting

Even with a complete inventory of the lines expected near the O VI $\lambda 1032$ line, normalization of the stellar spectra proved challenging. We adopted the method of fitting continua as described by Sembach & Savage (1992), whereby continuum levels are defined by least-square fits of Legendre polynomials to intensities either side of a line. Unfortunately, for many stars, we found that the stellar continuum varied in shape over widths comparable to that of the O VI features.

No interstellar absorption lines are expected between the H₂ 7–0 R(6) line at 1030.08 Å and the first of the H₂ lines flanking the O VI feature, the 6–0 P(3) line at 1031.192 Å. This gap of 1.1 Å should provide ~ 50 (rebinned) pixels from which the blue side of the continuum can be well defined. Except for O VI with high negative velocities, there was indeed a small amount of continuum available between the P(3) feature and the O VI line in our spectra, again helping to tie down the continuum fit on the blue side of the O VI feature. There was, however, often contamination from the Cl I $\lambda 1031$ line, potentially leading us to underestimate where the flux should lie between the P(3) line and the O VI. Fortunately, the Cl I line was always weak and narrow, and its effect on causing continuum misplacement was small.

As we shall see, the O VI $\lambda 1032$ lines themselves are wide, and there was often good reason to believe that the continuum was changing shape at 1032 Å in many of our spectra. Further, at the red edge of the O VI line, absorption from the second flanking H₂ feature — the 6–0 R(4) line — is expected to set in. In many cases, we found that the O VI and the R(4) line were clearly beginning to blend together. By the time the continuum had recovered redward of the H₂ absorption, it was often a very different flux than that predicted simply by extrapolating from the (well fitted) continuum blueward of the P(3) line.

We attempted to find some consistency checks for the continua that we adopted. As a first step, we compared the P(3) and R(4) lines with their profiles from modeling other H₂ lines in the *FUSE* spectrum. For the R(4) line, we used the 5–0 and 4–0 R(4) lines at 1044.542 and 1057.376 Å, respectively. These lines are relatively free of contaminating features, and have similar oscillator strengths to the 6–0 lines. For the P(3) line, we used only the 4–0 P(3) line at 1056.472 Å. In both cases, we fitted Voigt profiles

(convolved with the instrumental line spread function — see §2.8.1) to the data to derive column densities and Doppler parameters for the R(4) and P(3) transitions, calculated the expected profiles for the 6–0 P(3) and R(4) lines, and compared those with the observed lines.⁵

In Appendix E we show all the spectra in our survey (see Fig. 24; a full description of this Figure is given in Appendix E). The top panel (the first of three) for each star shows the adopted continuum, along with the $\pm 1\sigma$ error ‘envelopes’ which express the positive and negative deviations possible in the polynomial coefficients used to define the continuum. (We will refer to these as the ‘upper’ and ‘lower’ continuum fits throughout this paper.) The middle panel shows the *predicted* profile fits to the H₂ lines, blended with O VI line fits (§2.8.1), for the normalized spectra. Given the inherent uncertainties in producing the H₂ models from the other H₂ lines in the *FUSE* spectra, these fits appear to predict the observed features quite well. We notice a tendency for the theoretical profiles of the flanking R(4) and P(3) lines to be slightly stronger than the data in many cases. This probably arises from an incomplete knowledge of the *FUSE* Line Spread Function (LSF) at the wavelengths used for the H₂ models as well as the lines near O VI, since the LSF is largely uncharacterized for the spectrograph and is known to change with wavelength. We should say, however, that these models did not provide particularly rigorous constraints on the continuum fits. Since the H₂ lines were always quite strong, even fairly large continuum deviations around the lines produced very small differences in the depths of the line profiles.

The most difficult continua to fit occurred when the O VI absorption arose in a region where the stellar flux is reaching some local maximum. For example, the top panel of Figure 2 shows the flux of HD 178487, which has one of the most difficult continua to characterize of all the stars in our sample. The solid line in the figure shows a plausible fit, but it is clear that the dotted lines could also represent the true underlying continuum. As we describe below, we can calculate column densities from the data normalized by our adopted fit (second panel of Figure 2) but we can also re-calculate the val-

⁵In fact, the range of oscillator strengths for all the R(4) lines available in the *FUSE* channels are too small to allow a unique determination of the R(4) H₂ column densities, given the *FUSE* resolution. We base our use of the 6–0 line on the fact that we can correctly recreate the equivalent width of the line given the equivalent width of the other R(4) lines.

ues assuming that the upper or lower fits are correct (third and fourth panels). For HD 178487, the O VI lines are strong, and even a continuum as uncertain as the one indicated in the figure introduces errors of only $\simeq \pm 0.1$ dex in the total O VI column density. Fortunately, for all the stars with these type of continua, the O VI $\lambda 1032$ line was indeed strong, and we were able to characterize the likely range of column densities through the errors adopted for the continuum fits.

A far more common problem in fitting continua can be seen for one particular star, HD 094493, in Figure 3. There are two possible continuum fits: one which continues upward from an extrapolation of the fit blueward of the H₂ P(3) line, before having to turnover beyond the R(4) (labelled ‘Fit-2’ in the Figure); and one which quickly drops downwards to meet the small amount of continuum flux left between the O VI line and the H₂ feature (‘Fit-1’).

The difference depends on whether Fit-1 is the correct continuum, despite the unsettling sudden deviation around the O VI $\lambda 1032$ line, or if the stellar flux is instead depressed by a high velocity extension to the main O VI absorption. The second panel of Figure 3 shows the data normalized by Fit-1, and the resulting O VI absorption and H₂ R(4) are easily reproduced with a single component fit. If Fit-2 is adopted instead, then a single component fit is no longer satisfactory. The third panel of Figure 3 shows the data normalized by Fit-2, with a single component fit to the O VI line (along with the predicted line profile for the H₂ R(4) line). There is clearly excess absorption between the O VI and H₂ line. The blue side of the H₂ line is also poorly matched. To account for this absorption, a second component is required at higher velocity. Such a fit is shown in the bottom panel of Figure 3.

This type of problem occurs for 26 stars in our sample. Perhaps significantly, the difficulties are confined to stars of a particular stellar type. Of the 26 problem stars, 21 (81 %) are of type O9 to B1 (inclusive). (In contrast, for the remaining stars, only 52% are of type O9 to B1.) In many cases, it seems that O VI absorption arises in the blue wing of a narrow O VI emission line feature which predominates in these types of stars. There is no evidence of excess high (positive) velocity O VI absorption in the majority of earlier spectral types. Nor are these problem stars confined to a particular region of the sky, where, e.g. Galactic rotation (or some other coherent kinematical process) might be expected to produce additional O VI absorption. We also note that when we compare the expected profile of the

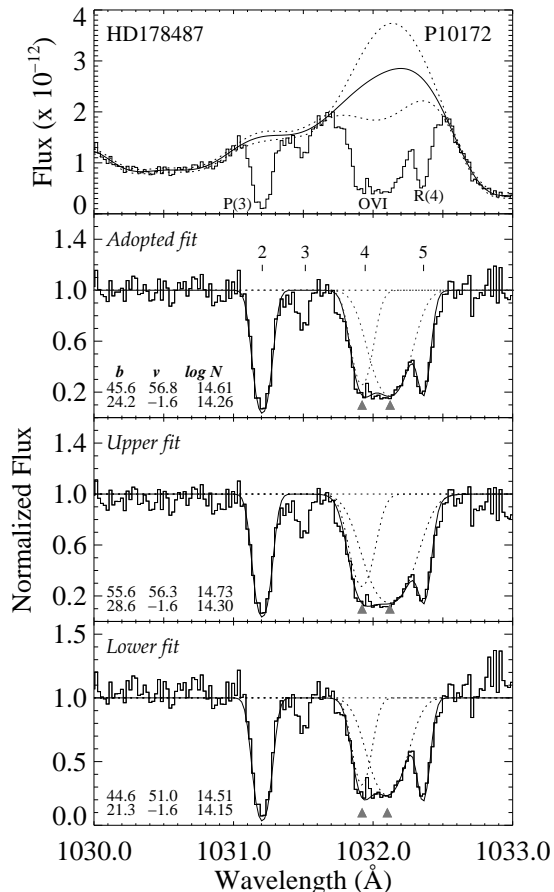


Figure 2: An example of the worst case for fitting a continuum to a star when the O VI and H₂ 6–0 R(4) lines are strong and placed in a wavelength region where the continuum reaches a local maximum. The solid curve in the top panel shows the adopted fit to the observed flux, while the dotted curves mark two extremes arising from the $\pm 1\sigma$ errors on the Legendre polynomial coefficients. All three are plausible fits to the data. The second panel shows the profile fits for the O VI and the molecular lines, given the adopted fit. Two components are needed to fit the O VI profile in this example, and the centroid of each is shown with a gray triangle. The lower panels show the fits for the upper and lower continua. However, because the absorption is strong, the errors in the total O VI column density are only 0.1 dex. (See Appendix E for full details of how this plot is marked.)

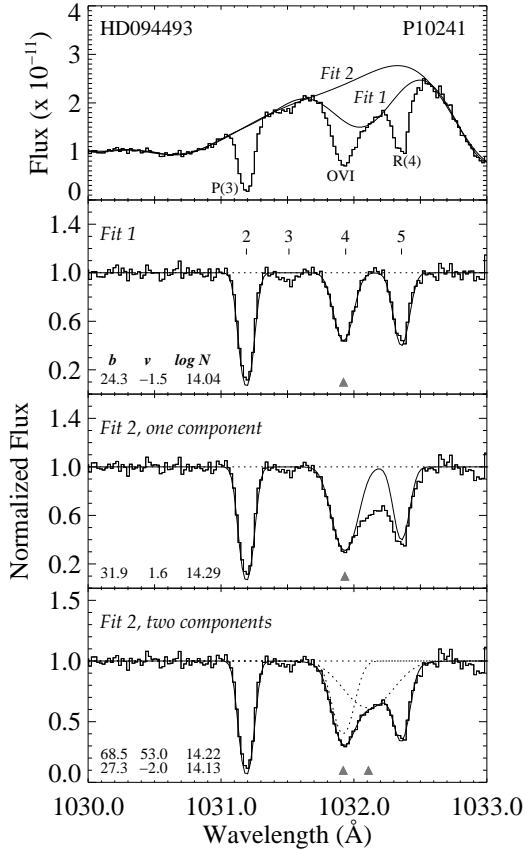


Figure 3: A small subset of stars in our survey have continua whose shape can be fit with one of two possible choices. Here we show one such star, HD 094493. In the top panel, Fit-2 is based on a simple extrapolation of the continuum from the blue side of the spectrum, while Fit-1 assumes that the flux between the O VI and R(4) line is real continuum. Adopting Fit-1 means that the O VI line is easily fit with a single component (panel 2; the centroid of the component is indicated by a gray triangle). Using Fit-2 results in additional O VI which cannot be fit with a single component (panel 3) but requires a second, broad, higher-velocity component (panel 4; the centroids of both components are indicated with gray triangles). Many of the stars in our sample have this ambiguous continuum shape, but for reasons discussed in §2.6, we adopt continua with shapes similar to those of ‘Fit-1’ above. (See Appendix E for full details of how this plot is marked.)

R(4) line with the data normalized by Fit-1 type continua (marked as line ‘5’ in the second panel of Figure 3), we find that the predicted profile agrees well with the data every time.

For these reasons, we adopt continuum levels of the type shown by Fit-1 for the 26 problem stars. Can we rule out the possibility that we are excluding real additional, high velocity O VI components? If such components exist, then the absorbing clouds must have a rather unique set of properties: they must always be of lower column density than the lower velocity component; they must always be about twice as broad; and they must always be $\sim 50 \text{ km s}^{-1}$ redward of the lower velocity component. Such a fixed set of characteristics from sight lines scattered across the plane of the Milky Way seems contrived, and we believe that continua fits similar to Fit-2 in Figure 3 are simply incorrect. In many cases, the difficult continua are likely to be the result of irregularly shaped P-Cygni profiles which arise from the winds around the stars themselves.

Table 4 details the results of our measurements of O VI lines towards all the stars in our survey except those for which we could not detect O VI absorption (see §2.8.2 for a discussion of these stars, which are listed in Table 5). Of particular relevance to the problem of continuum fitting is the information given in column 15 (labelled ‘Cont’), a flag that simply warns of possible problems in the continuum fits. For the stars discussed above, where we could have higher continua and a second, broad, positive velocity O VI component, we assign a value of ‘2’ for the continuum flag. There are also a few examples where the continuum could actually be drawn in such a way that additional O VI components might exist both redward *and* blueward of the O VI line. These are assigned a value of ‘1’. We consider it unlikely that these stars really have continua so very different from those we chose for them, but given the complex nature of stellar continua, we cannot rule out the possibility. In both cases, it is important to note that values for the continuum flag greater than zero are only assigned if a different observer could have adopted a continuum different from the one we adopted, by an amount which would *not* be covered by the continuum error envelopes introduced above.

2.7. Removal of the HD 6–0 R(0) Line

As indicated in §2.5, Figure 1, and Table 3, O VI absorption occurs at nearly the same wavelength as the

HD 6–0 R(0) line at 1031.909 Å. The line is a serious contaminant for weaker O VI lines, and must be removed before the properties of an O VI line can be measured.

To remove the HD line, we first constructed a profile of the 6–0 absorption line based on a fit (see §2.8.1) to another HD line, the 7–0 R(0) feature at 1021.453 Å. This line has a similar oscillator strength to the 6–0 line (see Table 3), and is usually well isolated from other interstellar features. The resulting profile created for the 6–0 line should therefore be, at the very least, an accurate reflection of the amount of equivalent width needed to be removed from the O VI profile.

We also checked to see if our fits to the 7–0 line were consistent with the 4–0 HD line at 1054.286 Å, which also has an f -value close to that of the 6–0 line and is relatively free of contaminating interstellar lines. We often found that although the equivalent width of the 4–0 line (as predicted from the 7–0 line) had roughly the correct equivalent width, the profile of the 4–0 feature sometimes departed from a single component Voigt profile. We did not therefore use the 4–0 line to constrain the HD model.

Having derived a plausible model for the HD absorption, we created a synthetic HD 6–0 line profile and removed it from the O VI absorption. The results of this removal can be seen in the top panels of Figure 24, where the difference in the flux before and after the subtraction is shown as a gray shaded region. Towards several stars (e.g. HD 210839, HD 005005A, HD 012323, etc.) there is no apparent O VI absorption after the subtraction of the HD line. Significantly, for these cases, our HD subtraction never leads to the production of extra flux *above* the predicted continuum (i.e., an ‘emission’ feature), at least beyond that expected from Poisson fluctuations. It seems likely therefore that our HD models are sufficiently accurate to properly remove the HD line.

2.8. Measurement of O VI Absorption Lines

To measure the column density of the O VI absorbing clouds, we would, ideally, like to use both members of the O VI doublet. Both lines were recorded for most of the stars observed with *Copernicus*, since the H₂ absorption along the sight lines was usually weak. For the *FUSE* stars, however, H₂ absorption was always too strong for us to use the 1037.6 Å line. An example is shown in Figure 4, which shows the region

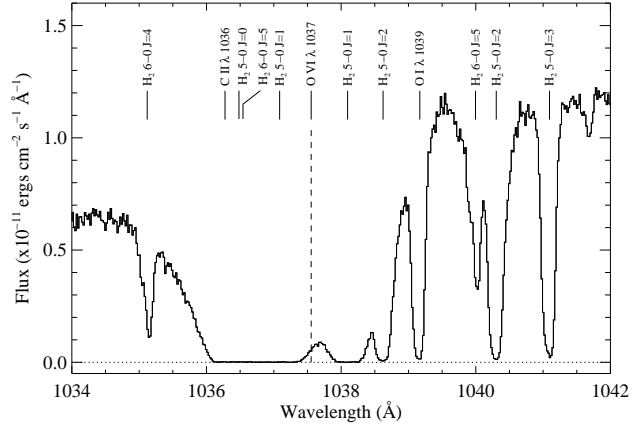


Figure 4: Example of a stellar spectrum around the expected position of the O VI $\lambda 1037$ line. The star is HD 67659, and shows the typical strengths of the H₂ features which make it impossible to measure the 1037 line.

around 1037 Å for the spectrum of HD 167659. These data are quite typical for the stars in our survey .

The O VI $\lambda 1037$ could sometimes be seen in the wing of the 5–0 R(1) line when the H₂ column density was low. In principle, it is possible to fit $J = 1$ lines in other parts of a spectrum, then calculate and remove the H₂ line profiles around 1037 Å and thereby recover the O VI $\lambda 1037$ line. We performed such an exercise for several sight lines where the H₂ column density was low, and the H₂ lines weak. The results were disappointing. Although reasonable fits could be made for the set of H₂ lines at, e.g. 1078 Å and 1063 Å, it was difficult to reproduce the H₂ complex at 1037 Å with sufficient accuracy (particularly without knowing the continuum a priori) to recover the O VI $\lambda 1037$ line with anywhere near the precision needed to make the resulting absorption line reliable enough to validate our measurements of the 1032 Å line. Indeed, lines of sight with a low H₂ column density along the sight line tended to be at relatively short distances; the O VI was itself relatively weak in these cases, making an accurate determination of the 1037 Å line even more difficult.

Consequently, all the analysis of O VI in this paper uses the O VI $\lambda 1032$ line alone. In the following sections we summarize the two methods used to an-

alyze the O VI $\lambda 1032$ lines toward our sample stars: the fitting of theoretical (Voigt) line profiles, and the Apparent Optical Depth (AOD) method.

2.8.1. Column Densities: Profile Fitting

As described above, a significant impediment to measuring O VI column densities towards some stars arose when the line was blended with contaminating Cl I $\lambda 1031$ and H₂ lines. The most straightforward way to circumvent this problem was to fit theoretical Voigt profiles to the regions of an O VI line which were clearly not blended with a contaminant.

This method has been used by researchers for many years. Details of our specific line-fitting procedures are given in Bowen et al. (1995). For the *FUSE* spectra, we generated (one or more) theoretical Voigt line profiles from an initial guess of the Doppler parameter b , line velocity v , and column density N . These were convolved with the instrumental LSF. A definitive LSF is not available for the *FUSE* channels, so we adopted a Gaussian of width 20 km s⁻¹ FWHM. Fortunately, the widths of most O VI lines are wider than this, so as long as the shape and width of the true LSF is close to the adopted value, the errors introduced are negligible.

For example, using an LSF with a width of 20 km s⁻¹ for the data of HD 134411 (#131), we find that the line has a Doppler parameter of 20.0 km s⁻¹ and column density 3.63×10^{13} cm⁻². This line is representative of lines with the smallest Doppler parameters in our survey (see §3.13) and would be most affected by changes in the LSF. In fact, if we had instead used an LSF of width 15 km s⁻¹, we would have measured a Doppler parameter of 21.5 km s⁻¹—an increase of 7% — and a column density of 3.59×10^{13} cm⁻²—a decrease of 1%. For O VI lines which are wider than that seen towards HD 134411, the relative changes in column density and Doppler parameter are even smaller.

Our fitting procedure allowed the O VI N , b and v to vary until a minimum was reached in the χ^2 fit between profile and data using the POWELL minimization routine (Press et al. 1992). Data points lying within the wavelength region predicted for the Cl I line were excluded from the fit. The O VI profile was often blended with the *predicted* profiles of the two flanking H₂ lines — predicted in the sense that N and b of the H₂ lines were fixed at the values derived from fitting the relevant lines in other parts of the spectrum (see §2.6), although v was allowed to vary for the H₂ lines in or-

der to take into account any small non-linearities in the wavelength scale of the data.

For each star, we first tried to fit only a single O VI component to the absorption. Additional components were added only if single components were clearly inadequate. It is important to note that this does *not* presuppose that absorption arises from a single cloud. Assuming such a model is likely to be erroneous, given the possible explanations for the origin of O VI absorption discussed in §1 and the results discussed later in this paper. However, in most cases the O VI line profiles appeared quite simple and shaped like a single component.

Line fits were made three times for each star, and the results are given in Table 4: once for the data normalized by the best continuum fit (giving column densities N and Doppler parameters b — columns 10 and 5, respectively), and twice more for the upper (N_u , b_u — columns 11 and 6, respectively) and lower (N_l , b_l — column 9 and 4, respectively) error envelopes discussed in §2.6. For all sight lines, changes in v for each of the three continua fits are negligible (< 0.1 km s⁻¹ in most cases). This procedure quantifies how the fit to the O VI changes from errors in the continuum, but does not address errors arising from Poisson statistics. To estimate these values, we performed a Monte-Carlo simulation (Bowen et al. 1995); for each sight line, we used the best fit values N , b and v to generate a theoretical line profile and added the amount of Poisson noise given by the *FUSE* error arrays (wherein each pixel is assigned a deviation σ_i). This new ‘synthetic’ spectrum was then refitted, and new values of N , b and v produced. This procedure was repeated 300 times, resulting in 300 different values of N , b and v . In most cases, the distributions of these values were Gaussian in shape and the values of σ for each were taken to represent the errors from noise, $\sigma(N)$, $\sigma(b)$ and $\sigma(v)$. The values for the first of these two quantities are given in Table 4 (columns 12 and 7, respectively). We do not list values of $\sigma(v)$ since, along nearly all sight lines, they are only ~ 1 km s⁻¹, less than the error in the wavelength scale.

In principle, these Monte-Carlo runs should have been repeated twice more for each star using the best-fit profiles derived from fits to the data normalized by the upper and lower continuum errors (i.e. [N_l , b_l] and [N_u , b_u]). In practice, however, since the values of σ_i at each pixel were the same, and the three profiles for each continuum fit were quite similar for most stars, the differences in $\sigma(N)$, $\sigma(b)$ and $\sigma(v)$ were negligible.

For the O VI lines, which are much wider than the LSF, $\sigma(b)$ and $\sigma(N)$ are uncorrelated, and can be treated independently. The total errors in the Doppler parameters, $\sigma(b)_T$ are given by two values $[b_u - b, b - b_l]$ added in quadrature to $\sigma(b)$. These values are given in column 8 of Table 4. In a few cases, the positive and negative values of $\sigma(b)_T$ in column 8 appear quite asymmetric. This usually occurred if the upper and lower continuum fits for a star were very different in shape from each other. The final errors in N , $\sigma(N)_T$, are formed in the same way, since the two sources of error in N are independent of each other, with $[N_u - N, N - N_l]$ added in quadrature to $\sigma(N)$. Column 13 of Table 4 shows these errors in the form $N[+\sigma(N)_T, -\sigma(N)_T]$.

Towards some stars, more than a single component was needed to fit the O VI line. For convenience, column 13 of Table 4 lists the sum of the column densities, N_{TOTAL} , along with their errors. In the case of a multicomponent fit, the final errors in N_{TOTAL} are formed in a similar way to those of single component fits. Since the continuum errors affect all components in the same way, the error in N_{TOTAL} from the continuum fit is $[(\sum_i N_{i,u} - \sum_i N_i), (\sum_i N_i - \sum_i N_{i,l})]$, where i is the component number. For the noise error, the column densities for all the components are added for each Monte-Carlo run, and σ is calculated from the distribution of 300 values of $\sum_i (N_i)$. Again, the continuum error and noise error are added in quadrature to give the errors listed in column 13 of Table 4.

Some stars from our survey are not listed in Table 4. They have no appreciable O VI absorption that can be fitted with a theoretical line profile. The limits to their column densities are tabulated in Table 5 and discussed below.

2.8.2. Column Densities: Apparent Optical Depth (AOD) and Upper Limits

Clearly, the Voigt profile fitting method described above is only applicable when an absorption line is clearly detected. In some of our spectra, there was good evidence that an O VI line was not detected. In order to rigorously define either the presence of very weak O VI lines, or meaningful upper limits, we used the AOD method of analysis, which yields a straightforward formal measurement of $N(\text{O VI})$ and its associated error. A desire to accurately characterize marginal detections, or the lack of any detections, with a well-posed quantitative calculation, was the motiva-

tion for carrying out AOD measurements.

The AOD method is described in detail by e.g. Savage & Sembach (1991) and Jenkins (1996). To summarize: the optical depth, τ_i , at a given pixel i (usually in velocity space, where the width of a pixel is δv) is given by $\tau_i = -\ln F_i$ where F_i is the normalized flux. If σ_i is the error in the normalized data at the i 'th pixel, then the corresponding error in τ is $\sigma_\tau = \sigma_i/F_i$ provided that $\sigma_i \ll F_i$. The AOD column density associated with this single pixel, N_i , in units of cm^{-2} , is then given by

$$N_i = \frac{m_e c}{\pi e^2} \frac{\tau_i}{f \lambda_0} \delta v = 3.768 \times 10^{14} \frac{\tau_i}{f \lambda_0} \delta v \quad (1)$$

where f is the oscillator strength of the absorption line, λ_0 the rest wavelength of the line in \AA , δv is the pixel velocity width in km s^{-1} , and the other symbols have their usual meaning. Similarly, in the absence of continuum errors, the error at the i 'th pixel, $\sigma(N_i)$, is simply

$$\sigma(N_i) = 3.768 \times 10^{14} \frac{\sigma(\tau_i)}{f \lambda_0} \delta v \quad (2)$$

The final column density and its variance, integrated over the whole line (n pixels) are then

$$N = \sum_i^n N_i; \quad [\sigma(N)]^2 = \sum_i^n [\sigma(N_i)]^2 \quad (3)$$

For the *FUSE* data, σ_i was taken from the error arrays supplied by CalFUSE, which measures fluctuations from Poisson counting statistics, and includes a contribution from the (modeled) background subtraction. The error arrays do not take into account fixed-pattern noise (FPN) since no stable flat-field is available. Fortunately, much of the FPN in the one dimensional spectra is averaged out when individual sub-exposures are co-added (§2.3), provided that some drift was found in the spectra along the dispersion direction between sub-exposures. Our re-sampling of the data by a factor of three also ensured that the FPN was smeared out while preserving the shape and strength of an absorption line, at least when the FPN features were narrow.

As we discussed, the O VI profiles towards our sample stars were often contaminated by Cl I or H₂ lines. Our approach to reconstructing the $N(v)$ profiles

without these interfering lines was to fit theoretical Voigt profiles to the contaminants and remove them. In most cases, there was sufficient information (i.e., a large enough number of pixels) to define the shape of a line quite precisely. For this procedure, we do not need to know the true column density or width of a line to obtain a good fit; we need only assume that the LSF is a Gaussian. If this assumption is correct, we need only fit the profile and remove it to recover the true O VI $N(v)$ profile.

With the contaminating lines removed, we measured the AOD column density as follows. For each sight line, we measured N using the number of pixels that corresponds to a velocity interval of $-120 < \Delta v < +120 \text{ km s}^{-1}$. A measurement was also made of a column density limit over the same velocity range, defined as

$$[\sigma(N)_T]^2 = \left(\frac{N_u - N_l}{2} \right)^2 + \sigma(N)^2. \quad (4)$$

If the measured value of N was greater than $\sigma(N)_T$, we considered the line to be detected (see below). Although Δv was the same for all stars, in some cases the $N(v)$ profile clearly extended beyond this range, so Δv was increased accordingly to produce the correct value of N . We again measured N three times, once for the data normalized by the best continuum fit, and twice more for the upper and lower error envelopes to give N , N_u and N_l .

In principle, we could list these AOD column densities when O VI was detected in Table 4. However, these quantities turned out to have very similar values to those measured using the line profile fitting procedure described in §2.8.1. We noted, however, a slight systematic difference in $N(\text{O VI})$, in that column densities measured with the AOD method were slightly over-estimated at the lowest column densities. This effect, caused by the difference in the behavior of τ for positive and negative fluxes, is well understood, and discussed, e.g., by Fox et al. (2005). For this reason, we do not list the AOD values in Table 4. The AOD values are given, however, in the bottom panel of the figures which show the *FUSE* spectra, as described in Appendix E.

In some cases, the values of $N(\text{O VI})$ measured from the AOD method can be far less than the errors, and sometimes even negative values can arise. For these, one has some freedom in how the numbers should be treated, depending on the problem at hand.

For example, in a study that combines results from many sight lines, it is perhaps best to combine the formal numbers and their errors in some optimum way to arrive at some improved global value. In this case, noise uncertainties in the individual cases are allowed to cancel one another, which allows one to achieve an answer that is more meaningful than a large collection of upper limits. However, it may be more useful instead to give a more precise statistical interpretation of the outcome for an individual sight line, such as stating to a given confidence level an upper limit for $N(\text{O VI})$. For the latter, we propose that one could make use of a limit calculation for nonsignificant measures in the presence of Gaussian noise defined by Marshall (1992). Full details of this procedure are given in Appendix D.

As mentioned above, in deciding whether only an upper limit exists for an O VI line, we adopted the following procedure. If the measured value of N was less than $\sigma(N)_T$, we considered O VI undetected, and instead listed the star with the measurements of $N(\text{O VI})$ in Table 5. Obviously, adopting a 1σ cutoff between detection and non-detection may seem somewhat arbitrary. Another way we could have decided whether data yielded only an upper limit might have been to argue that a limit should be adopted when no Voigt profile could be fit to the data. In fact, these two procedures are equivalent. There exists only one sight line where we could have tried to fit a profile, but where the measured value of N was less than $\sigma(N)_T$. [That star was HD 052463 (unique ID 70), and the depression at the expected position of O VI has a reality that indeed appears ambiguous.]

Hence Table 5 contains *all* the pertinent information available for the O VI column densities towards the stars (except, perhaps, for HD 052463). Columns 3–5 give the measured values of $N(\text{O VI})$ and the values measured using the upper and lower continuum fits, N_u and N_l . Column 6 lists the error from the noise, $\sigma(N)$, while $\sigma(N)_T$ is the quadratic sum of all the errors, as defined in equation 4. Column 8 gives the 2σ limit as defined by Marshall (1992) and discussed in detail in Appendix D. Ultimately, whether one uses the AOD measurement of $N(\text{O VI})$ or N_{limit} depends on the situation, and we discuss these issues later in the paper.

2.9. Misleading Effects from Unrecognized Saturation?

A final consideration centers on the question of whether or not the column densities we measure for the *FUSE* stars might be underestimated due to saturation effects that are not evident in the apparent optical depths. Since the O VI $\lambda 1037$ line is unobservable (§2.8), it cannot be used to check for line saturation. If the lines are resolved, then the Voigt profile fitting (when a suitable LSF is convolved with the theoretical profile) accounts for any possible saturation. The more problematic situation occurs when the line is actually composed of many components, some of which are unresolved but blended (and perhaps hidden by broader, resolved components). Profiles that have a mixture of clouds with high and low optical depths instead appear as if they are composed of only a few clouds with moderate optical depths after being smeared by the instrumental LSF. [For more details, see Jenkins (1986).]

There are several observations that suggest that narrow unresolved O VI lines do not exist. O VI lines can arise from clouds that are either photoionized or collisionally ionized. If the absorbing gas is in collisional ionization equilibrium, the thermal width of the line is given by $b^2 = 2kT/m_{\text{O}}$, (where m_{O} is the atomic mass of oxygen) which for oxygen gives $T = 969b^2$ or, equivalently, $b = 0.0321T^{1/2}$. The ionization fraction of O VI peaks at $\log T_{\text{max}} = 5.45$, which would give $b = 16.6 \text{ km s}^{-1}$, and decreases sharply⁶ as the temperature falls, declining to a fraction 10^{-3} of the total oxygen at $\log T = 5.2$ (e.g., Shapiro & Moore 1976b; Sutherland & Dopita 1993; Nahar & Pradhan 2003). This lower value equates to a Doppler parameter of 13 km s^{-1} . Clearly, the Doppler parameters corresponding to either the peak temperature or this lower value are of the same magnitude as the *FUSE* LSF at 1030 \AA .

It remains possible that O VI arises in collisionally ionized gas that is not in equilibrium (due to rapid cooling, for example), or in photoionized gas. In these instances, the line may be narrower. We consider the existence of such narrow O VI components unlikely, for the following reasons: *i*) in high resolution ($\simeq 3 \text{ km s}^{-1}$ FWHM) *Interstellar Medium Absorption Profile Spectrograph* (IMAPS) data, there is no evidence for narrow multiple sub-components in O VI

profiles (Jenkins et al. 1998); *ii*) along path lengths through the entire Galactic halo, where $N(\text{O VI})$ ranges from $\simeq 1 - 4 \times 10^{14} \text{ cm}^{-2}$, comparisons of the AOD profiles for *both* the O VI $\lambda 1032$ and the $\lambda 1037$ lines show that unresolved saturation effects are relatively small (Wakker et al. 2003; Savage et al. 2003); *iii*) no narrow components have been found in High Velocity Clouds, where the high velocity of the absorbing gas might make such features distinct from (broader) absorption by the Galactic halo (Sembach et al. 2003; Collins et al. 2005); *iv*) similarly, in cases where an O VI component has a high enough velocity to be separated from the bulk of the absorption, such as Carina and Vela, no very narrow components are seen. Although the environment in which these clouds exist (circumstellar or SNR outflows) are likely different from the rest of the ISM, none have widths $b < 20 \text{ km s}^{-1}$; *v*) the widths of the O VI lines seen towards stars within only 100 pc of the sun — although hard to measure due to the weakness of the lines — are rarely $< 20 \text{ km s}^{-1}$ (Oegerle et al. 2005; Savage & Lehner 2006). We also detect few lines with $b \leq 20 \text{ km s}^{-1}$ in the *FUSE* sample (see §3.13). So, even when the number of absorbing clouds along a sight line is a minimum, no particularly narrow lines are seen. For these reasons, we conclude that although the number of clouds intercepted in the disk may be large, no significant column density errors arise from narrow (perhaps saturated) O VI components.

It is interesting to note that in a recent study of *extragalactic* O VI absorbers, Tripp et al. (2007) found evidence that approximately one-third of the extragalactic O VI lines in low-redshift QSO spectra arise in relatively cool gas with $\log T < 5$. However, those O VI lines are frequently located in truly intergalactic regions that have much lower densities and larger sizes than the gas clouds in the Milky Way disk. The cool, photoionized clouds found in the IGM cannot exist in the higher density, shorter-path regions that we are probing in the Galactic plane.

2.10. The Final *FUSE* Sample

All the spectra belonging to the *FUSE* survey described in this paper are presented in Appendix E and Figure 24. A detailed explanation of the material shown for each sight line is also given.

Although observed as part of programs P102 and P122, several stars were excluded from the final dataset. For completeness, these are listed in Table 6

⁶For temperatures T which are different from T_{max} , $b = 16.6(T/T_{\text{max}})^{1/2} \text{ km s}^{-1}$.

and plotted in Figure 5. Most of these sight lines were excluded because we could not choose reliable continua. HD093204 (P10235) was rejected because no reliable fit to the HD line could be obtained.

3. INTERPRETATION

3.1. Inclusion of Other Data Sets

The sight lines in our *FUSE* survey were selected to cover distances beyond ~ 1 kpc in order to study the distribution of O VI absorbing gas over a significant fraction of the Galactic disk. However, there are several other sets of O VI absorption line data that probe gas over different scales, from a few tens of parsecs in the local bubble ('LB'), to halo gas in the outer regions of the Milky Way. As we will show, we need to include these in our analysis to fully understand the nature of the O VI absorption. In this section, we briefly discuss each of the datasets used and note any modifications we made to the published data in order to avoid systematic differences between quantities used for the *FUSE* sample and those used by other authors.

3.1.1. White Dwarf Sight Lines

Few O- and B-type stars can be found within a few tens of parsecs of the Sun. The nearest OB associations lie in the Sco-Cen association, and are 118–145 pc away (de Zeeuw et al. 1999). Investigations with *FUSE* therefore used nearby white dwarf stars (WDs) to study O VI absorption over very short path lengths. The first *FUSE* survey to study LB O VI absorption was completed by Oegerle et al. (2005). This was superseded by the larger survey of Savage & Lehner (2006, hereafter SL06), whose data we use in this paper. We adopt most of the values given in Tables 1 and 3 of SL06, who claim that distances to the WDs are known to ± 20 –30%. In our analysis we therefore use a distance range defined by $\pm 25\%$ of the distance. O VI column densities and Doppler parameters are taken from measurements made using line profile fitting procedures similar to our own. SL06 define O VI to be absent when the equivalent width $W_\lambda < 2\sigma(W_\lambda)$, as measured over an interval ≈ 100 km s $^{-1}$ (see column 11 of their Table 1). This is somewhat different than the method we adopted in §2.8.2, but since SL06 do not measure $N(v)$ in these cases we simply use column density upper limits derived from the $2\sigma(W_\lambda)$ limits. We do not include a WD sight line if SL06 suggest that detected O VI may be photospheric in origin.

3.1.2. Copernicus Sight Lines

The *Copernicus* satellite was able to obtain O VI measurements towards some of the nearest (brightest) stars lying a few hundred parsecs away, most of which are too bright to be re-observed with *FUSE*, unfortunately. The data were originally presented in Jenkins & Meloy (1974), York (1974), and Jenkins (1978a) (J78). In this paper, we have re-derived many of the stellar parameters for the *Copernicus* stars using the same procedures used for the *FUSE* sample stars, so that the two samples can be properly combined. The changes made are discussed more fully in Appendix C.1. Two stars observed by *Copernicus* (HDs 041161 and 186994) were re-observed with *FUSE*; these latter data supersede the *Copernicus* results and the information for the stars can be found in Table 1 (unique IDs 52 and 27, respectively).

O VI column densities for the *Copernicus* sight lines are taken directly from Table 1 of J78. That table also lists a value $\Delta^2 = \langle (v - \langle v \rangle)^2 \rangle$ for the O VI $\lambda 1032$ line, which is the second moment of the line profile after the second moment of the *Copernicus* LSF has been removed. We convert this to a Doppler parameter in the usual way, $b = \sqrt{2}\Delta$. No errors were given for the derived column densities due to the difficulties in fitting the stellar continua over the short wavelength regions scanned by *Copernicus*. We have, however, made some simple estimates of the likely errors in $N(\text{O VI})$; these can also be found in Appendix C.1.

3.1.3. Sight Lines to the Vela SNR

Our sample contains three stars which lie behind the Vela supernova remnant (SNR), HD 074920 (unique ID #77), HD 074711 (#78) and HD 075309 (#79). These are discussed below in §3.5 and §3.7.2. We added to these the stars discussed by Jenkins et al. (1976) and Slavin et al. (2004). Distances to these stars were recalculated according to the prescription laid out in Appendix B.

3.1.4. Distant Halo Stars and Extragalactic Sight Lines

For some of the analysis presented later, it is useful to compare the O VI absorption seen in the Galactic disk with that observed by *FUSE* over very long path lengths towards distant halo stars and extragalactic sight lines. Zsargó et al. (2003, hereafter Z03) observed a small sample of stars in the Galactic halo. Three of these were retrieved by us from

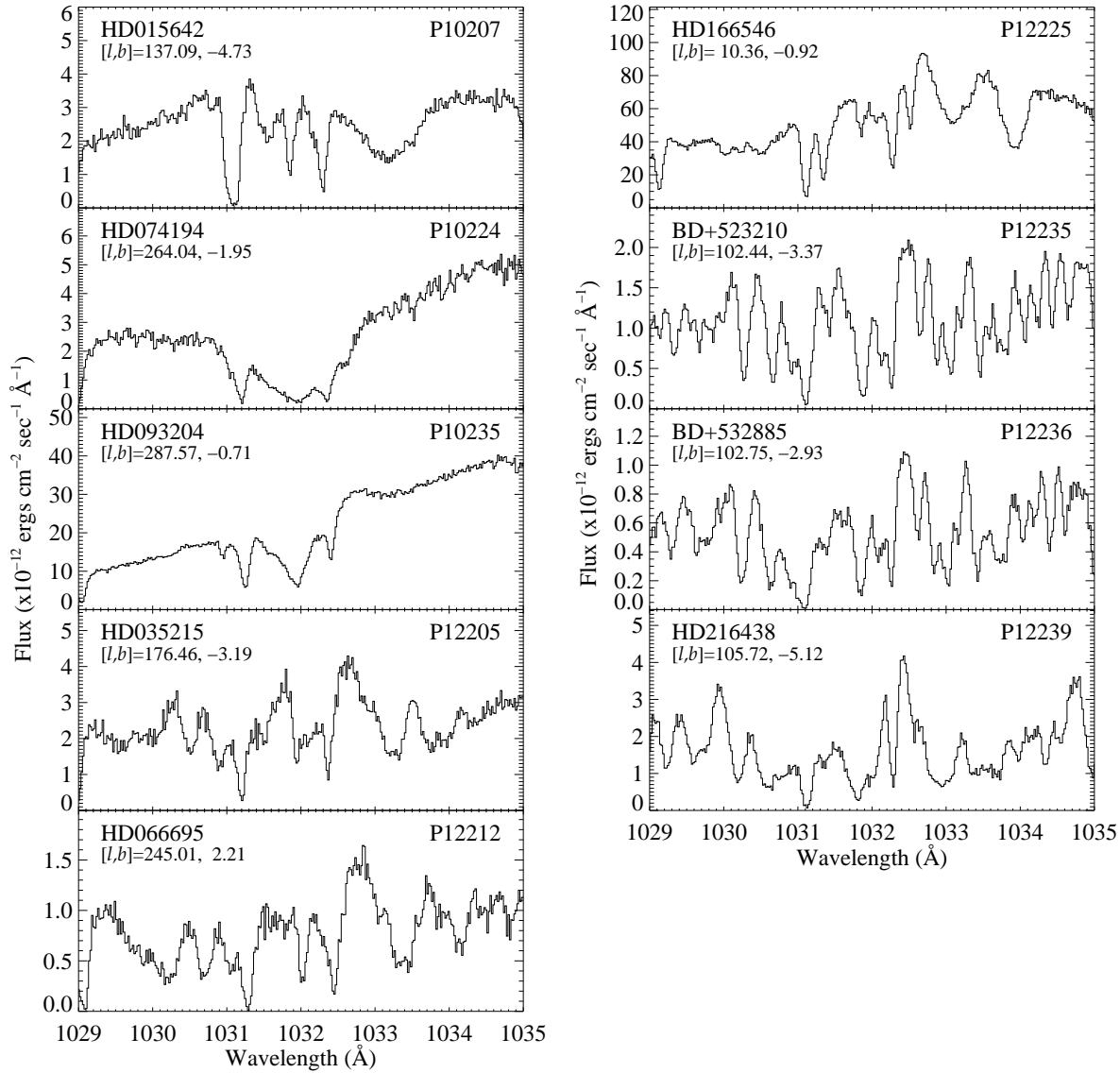


Figure 5: Spectra from programs P102 and P122 for which a reliable normalized O VI $\lambda 1032$ profile could not be analyzed.

the *FUSE* MAST archive (HD 088115, HD 148422, and HDE 225757) before Z03's results were available, because they lie at latitudes $|b| < 10^\circ$. The O VI towards these sight lines is strong, and we would expect errors in HD subtraction and continuum placement to be largely insignificant (particularly since Z03 rejected stars with difficult continua). In fact, we find that $\log N(\text{O VI})$ from our measurements agree well

with Z03's analysis. The difference in $\log N(\text{O VI})$ is ≤ 0.08 dex for all three stars, and identical within the 1σ errors.

For the rest of the stars in Z03, we have used the O VI column densities, Doppler parameters, and absorption line velocities given in their Tables 4 & 5. We have, however, re-derived some of the distances to the

stars using the same procedures used for all the other stars described in this paper. Details are given in Appendix C.2.

Finally, we have included the extragalactic sight lines observed with *FUSE* by Savage et al. (2003) and Wakker et al. (2003). We only use data that have S/N ratios > 9 per 20 km s^{-1} bin [i.e., those with codes 'Q=3' or '4' in Table 2A of Savage et al. (2003)]. The distances to these objects can be regarded as infinite for the purpose of studying Galactic O VI, and no new distances need to be computed except for one halo star: PG 0832+675, for which we use $d = 8.1 \text{ kpc}$.

3.2. Distribution of Stars in the Galactic Plane

An important parameter in the study of the O VI distribution in the Galaxy is the distance to any particular background star in our sample. Unfortunately, for stars beyond a few hundred parsecs from the Sun, the only way to measure stellar distances is through the use of “spectroscopic parallaxes”, which convert the observed magnitude of a star to its distance assuming that the spectral type and luminosity class of a star are known, along with a calibration of the true absolute magnitude of a star of that particular type and class. Knowledge of the interstellar extinction along a given sightline, $E(B - V)$, is also required. Although distances for many of our stars have been calculated before with this procedure, in this paper we have re-derived stellar distances using more modern databases. Since the details are complicated and not directly relevant to the analysis of interstellar O VI absorption, we document our procedures at the end of this paper, in Appendix B.

The distribution of our *FUSE* survey sight lines in the plane of the Galactic disk is shown in Figure 6. To illustrate the regions of the Galaxy in which the stars lie, we have plotted in gray the distribution of the electron density in the Milky Way, as modeled by Cordes & Lazio (2002), using their NE2001 program⁷. Overplotted are the spiral arm models from the meta-analysis of Vallée (2002). Vallée et al. used a value of 7.2 kpc for the distance of the Sun to the center of the Galaxy; for consistency with the rest of the analysis in this paper, we have changed this distance to 8.5 kpc , and altered the pitch angle of the arms to 11.3° . The structures shown are *only meant to be illustrative* of where in the Galactic plane the stars lie. For

⁷<http://astrosun2.astro.cornell.edu/~cordes/NE2001>. See also Cordes (2004) for a summary of NE2001.

more precise details about the likely structure of gas in the Milky Way, see Levine et al. (2006) and references therein.

In Figure 7 we show the distribution of stars in the plane of the Galaxy superimposed on a map of the diffuse X-ray emission constructed from the *ROSAT All Sky Survey* (RASS). This map includes all the *FUSE* stars shown in Figure 6, as well as stars from the other datasets discussed above. The map is a composite of data from three *ROSAT* bands, the R1 ($0.11 - 0.28 \text{ keV}$) and R2 ($0.14 - 0.28 \text{ keV}$) bands, and the sum of the R4–R6 ($0.44 - 1.56 \text{ keV}$) bands. In the figure, the R1, R2 and R4–R6 bands are assigned the colors red, green and blue, respectively. The precise interpretation of the emissivity at different energies is somewhat complicated, and is discussed in detail by Snowden et al. (1997). However, in §3.4 and §3.5 below, we use the X-ray data to examine in more detail the circumstellar environments around the stars observed for this paper.

3.3. Variability of O VI Absorption Lines Determined from Multi-epoch Data

O VI absorption from the Galactic ISM is superimposed on stellar continua which may show broad O VI P-Cygni profiles from stellar winds. Although the widths of these profiles can span several thousand km s^{-1} , their shapes are often highly irregular — a fact which likely leads to the problems we encountered in §2.6 in fitting many difficult continua. Moreover, the shapes of these wind profiles are known to vary on many different timescales, and can show ‘discrete absorption components’ (DACs) which vary in velocity as well as width and strength (York 1977; Snow et al. 1980; Massa et al. 2000; Lehner et al. 2003). In principle, O VI $\lambda 1037$ DACs from outflowing gas at velocities $\sim -1650 \text{ km s}^{-1}$ could become blended with the interstellar O VI $\lambda 1032$ absorption studied in this paper. A DAC which contaminated the interstellar O VI line at one epoch might only be shown to exist by temporal variations in its properties, as recorded in multi-epoch data.

To understand whether these complicated continua variations might adversely affect accurate measurements of interstellar O VI absorption, Lehner et al. (2001) studied a small sample of stars which had been observed repeatedly over time intervals of either a few days or several months. Lehner et al. concluded that, at least on these timescales, stellar wind variably had

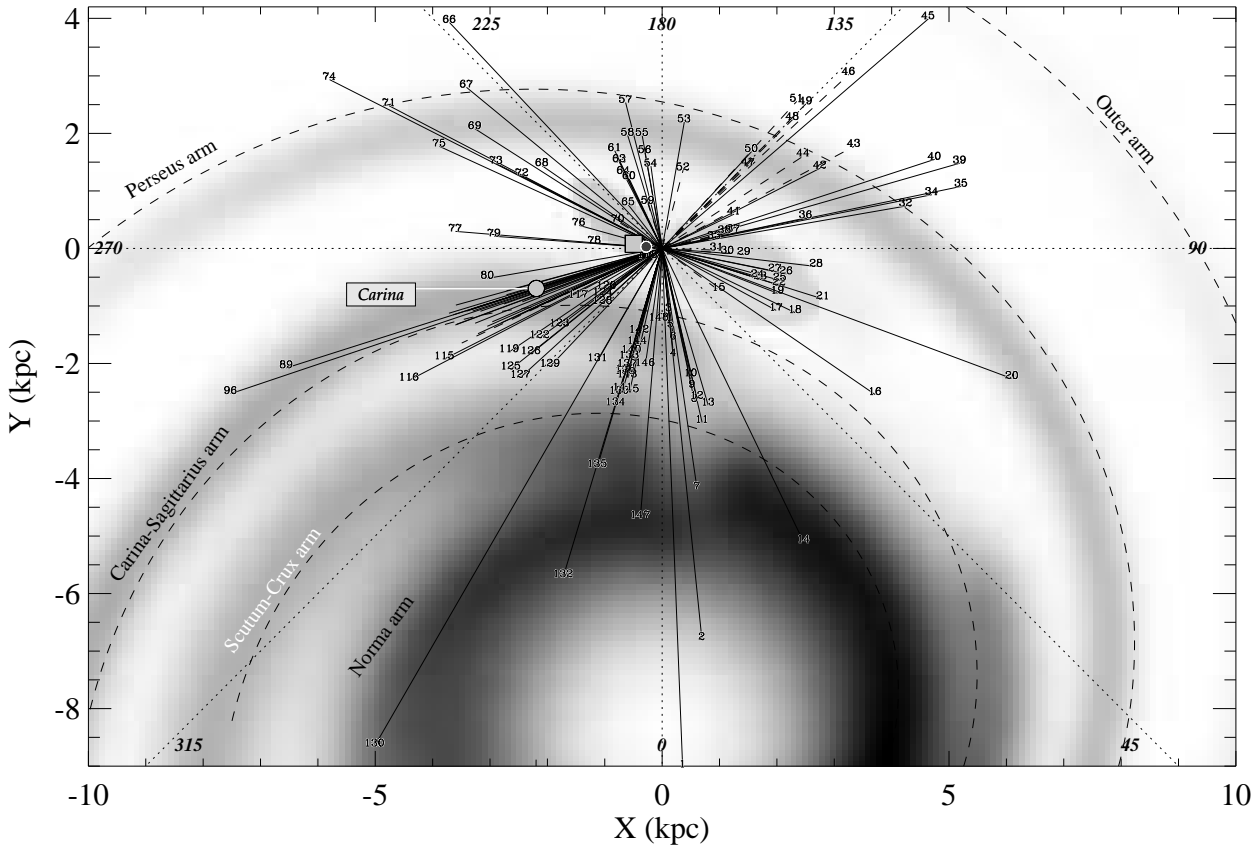


Figure 6: Distribution of sight lines in our *FUSE* survey, looking down into the Galactic plane. For illustrative purposes, the grayscale regions reproduce the electron density distribution modeled by Cordes (2004), while the dashed lines show the positions of the spiral arms from models by Vallée (2002). [The electron densities shown are the sum of components measured for the inner thin disk, the spiral arms, and the local ISM; the grayscale for the spiral arms represent electron densities of $\approx 0.01 - 0.1 \text{ cm}^{-3}$ —see Cordes (2004) for more details.] There is insufficient room to label all the stars observed towards Carina ($l = 287.7$, $d = 2.5$ kpc), so we indicate the region in the Sagittarius arm where the majority of the observed stars lie with a light-gray circle. The gray box close to the Sun represents the Gum nebula; the small dark-gray circle next to it shows the position of the Vela supernova remnant ($l = 263.9$, $d = 0.25$ kpc). The number for each star refers to the unique ID number given in Table 2. Sight lines for which only upper limits to the O VI column density are found are shown as straight dashed lines.

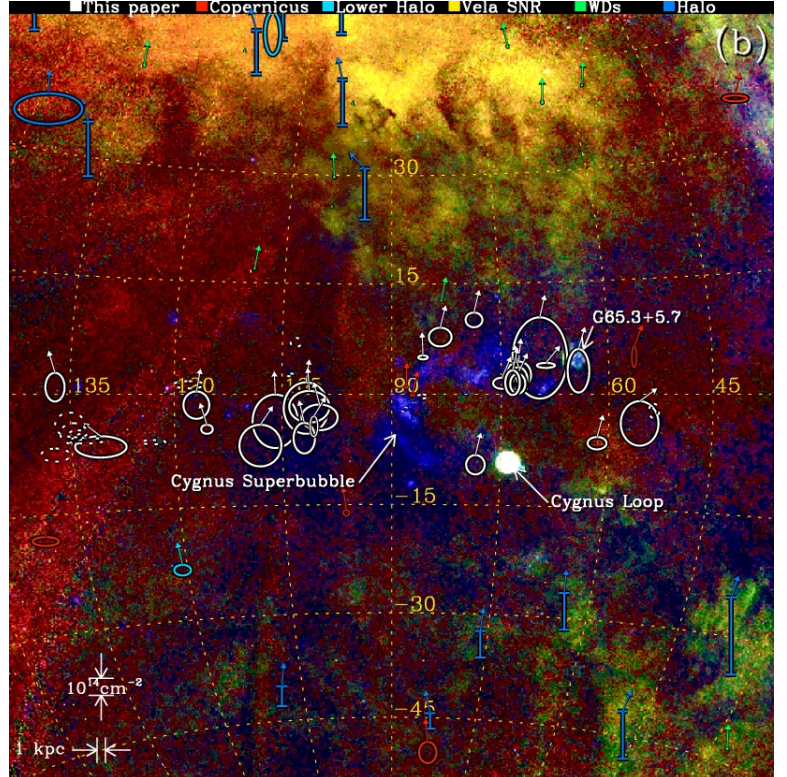
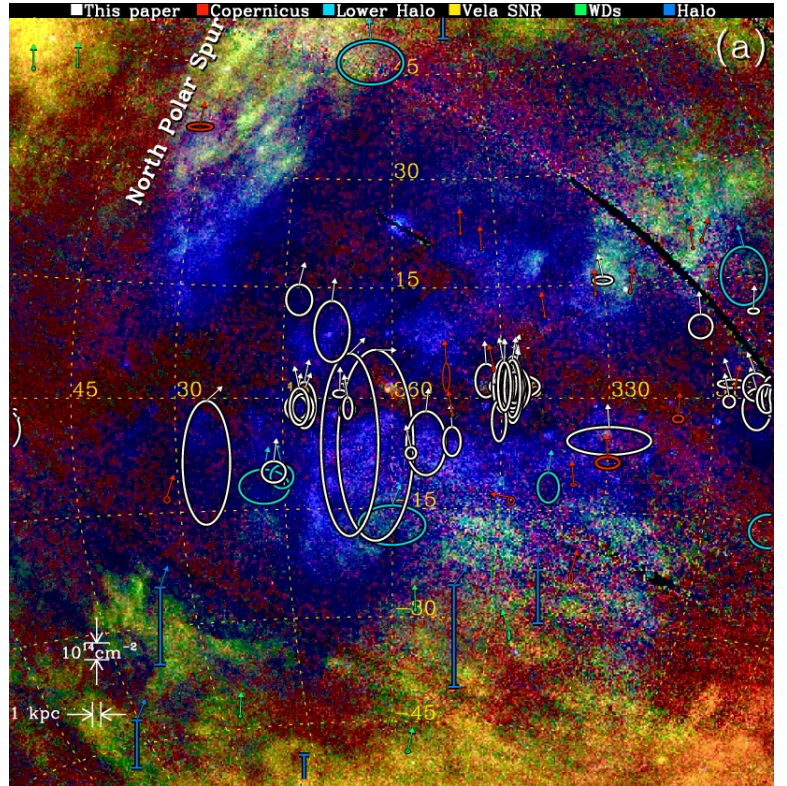
little influence on the measurement of O VI column densities.

We can perform a similar experiment for our *FUSE* sample of stars, over slightly larger timescales. Given the assumptions we made in §2.6 for fitting the continua of stars, a comparison of O VI column densities measured along the same sight line at different epochs—particularly when the continuum is a different shape at those epochs—is a useful indicator of the reliability of our data analysis. We can also search for contamination from DACs, if only along a few specific sight lines.

Six stars in our *FUSE* sample were observed at

times more than a few months apart and for which spectra with good S/N ratios were obtained at all epochs; these are listed in Table 7. The four spectra with the highest S/N are shown in Figure 8. As the left-hand panels of Figure 8 show, the continua changed to some degree for most of the stars. To search for variability in the O VI line, we compare the normalized data at each epoch in the right-hand panels of Figure 8. By accident, several of the stars in this small sample had low O VI column densities compared to the sample as a whole. To avoid detecting differences in absorption line profiles arising from difficulties in subtracting the HD R(0) line, we show only the O VI

Figure 7: O VI results superposed on a depiction of the diffuse X-ray emission recorded by the *ROSAT* All Sky Survey (RASS) over the longitude range *a*) $\ell = 310^\circ$ to 50° , *b*) $\ell = 40^\circ$ to 140° , *c*) $\ell = 130^\circ$ to 230° , and *d*) $\ell = 220^\circ$ to 320° . Ellipses are centered on the positions of target probes; their vertical axes are proportional to $N(\text{O VI})$ (totaled over all velocity components), and their horizontal axes signify the distance to the targets, both of which can be gauged by the scales in the lower left corner of the figure. A circle corresponds to an average sight-line density of $1.62 \times 10^{-8} \text{ cm}^{-3}$ [i.e., $N(\text{O VI}) = 5 \times 10^{13} \text{ cm}^{-2}$ over a distance of 1 kpc], which is a representative average for the whole survey. It follows that tall, skinny ellipses indicate more O VI than usual for a particular distance, while the converse is true for short, fat ellipses. O VI absorption towards stars at distances $< 100 \text{ pc}$ are not plotted since the size of their ellipses in both the horizontal and vertical direction would be too small to be seen using these scaling rules. The direction of a small arrow on the top of each ellipse signifies the average velocity of all of O VI absorption, with an angular deflection to the left (negative velocities) or right (positive velocities) whose magnitude in degrees corresponds to the radial LSR velocity in km s^{-1} . Cases with only upper limits are shown as dotted ellipses, where the $N(\text{O VI})$ upper limit defines the height of the ellipse in the same manner as described above. White ellipses mark stars in the *FUSE* survey reported in this paper, red ellipses denote *Copernicus* measurements (Jenkins & Meloy 1974; York 1974; Jenkins 1978a) and light blue ellipses identify targets in a *FUSE* survey of stars in the Galactic halo (Zsargó et al. 2003). Yellow ellipses show the data from Jenkins et al. (1976) and Slavin et al. (2004) for the Vela supernova remnant. Green arrows represent O VI absorption towards nearby WDs from the data of Savage & Lehner (2006). Vertical dark blue bars at high Galactic latitude show the results from the *FUSE* survey of extragalactic objects by Savage et al. (2003) and Wakker et al. (2003), and have no width because they lie outside the Galaxy. Colors in the X-ray sky are keyed to the *ROSAT* R1 (0.11–0.28 keV) band (red), R2 (0.14–0.28 keV) band (green), and the sum of the R4–R6 (0.44–1.56 keV) bands (blue), with scale factors that yielded a good differentiation of colors across different regions. The RASS results were obtained from an ftp download site <http://www.xray.mpe.mpg.de/rosat/survey/sxrb/12/fits.html> maintained by the Max-Planck-Institut für Extraterrestrische Physik.



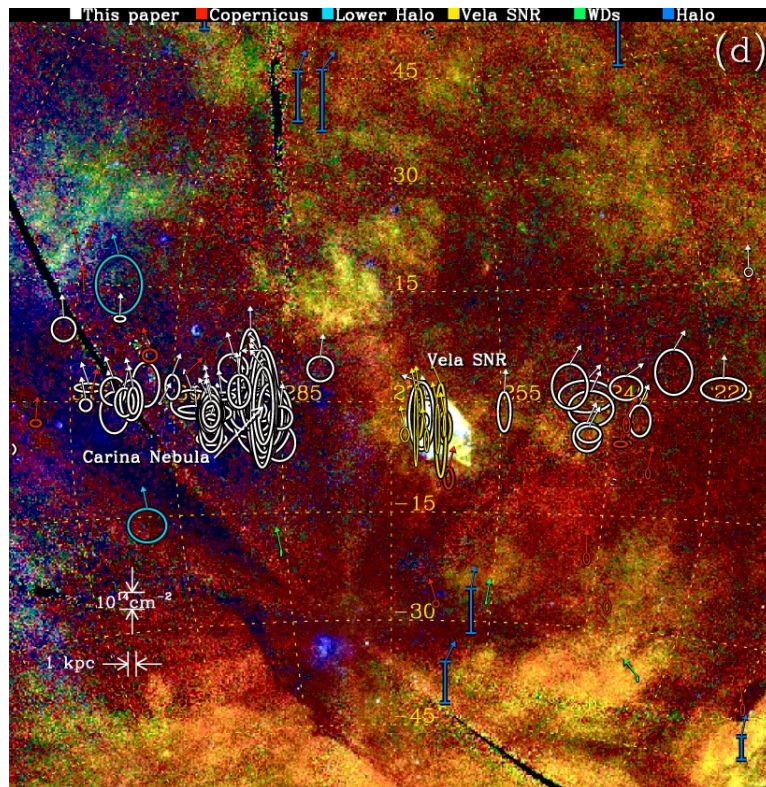
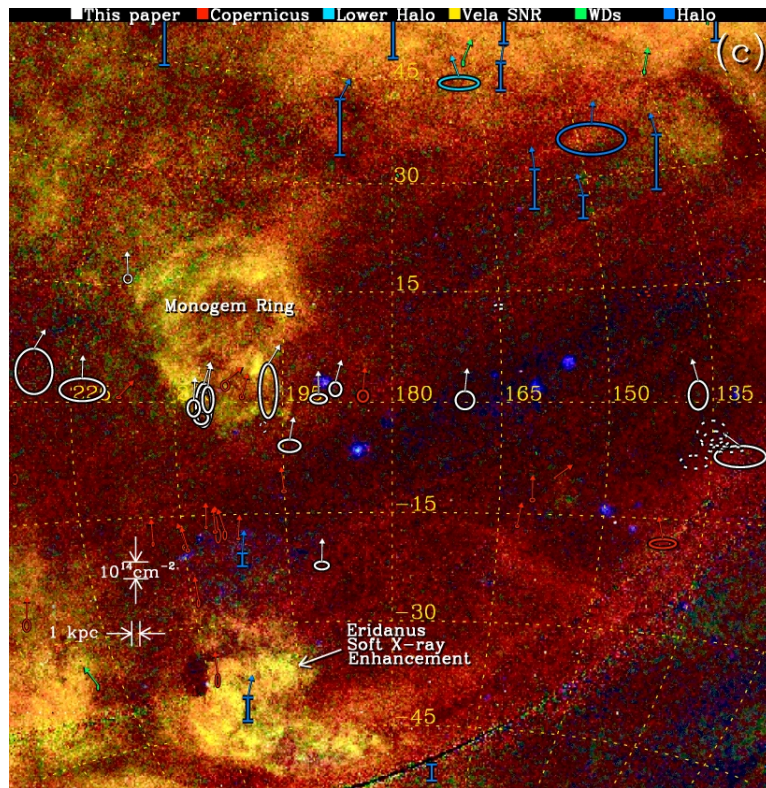


Figure 7: continued

profile before the removal of the HD line. (To see the strength of O VI after the HD removal, see Fig. 24.)

Figure 8 shows that there is little evidence for any variation in the O VI(+HD) absorption. Any differences seen can be attributed to problems in fitting the continuum. The absorption towards HD 103779 is a particularly interesting example: the continuum is very hard to fit at both observed epochs, yet the absorption at 1032 Å is remarkably similar in observations made four years apart. Note that the line towards HD 000108 is entirely HD absorption (again, see Fig. 24, ID #43).

Although we find no evidence for variations in absorption over differences of 3–4 years, the spectra do allow us to test how robust our measurements of $N(\text{O VI})$ really are. Although the O VI line in Figure 8 is blended with HD absorption, we can proceed with the analysis described in the previous sections by removing the HD line and measuring the resulting $N(\text{O VI})$. The results are given in the last column of Table 7. Despite having to contend with difficult continua (e.g. HD 103779), and removing HD lines that are a significant fraction of the O VI column density [because $N(\text{O VI})$ is relatively weak], the column densities measured for each epoch agree to within their errors. (The upper limits for the spectra of HD 000108 observed a year apart are obviously more a reflection of the S/N of the data, which were similar due to the similar exposure times. For both spectra, however, the HD could be modeled and removed to show that no O VI was obviously present.) This implies that our measurements of $N(\text{O VI})$ are quite insensitive to temporal variations, continuum changes, and HD removal.

3.4. Accounting for Circumstellar Bubbles

The target stars and their association members produce strong stellar winds (Garmany et al. 1981; Lamers 1981; Garmany & Conti 1984) which inject substantial amounts of energy into their surrounding gaseous media (Abbott 1982; McKee 1986). From an initial theoretical investigation of the probable consequences of such wind-driven shells, Castor et al. (1975) proposed that nearly all of the low-velocity O VI features seen in the spectra of early-type stars recorded by *Copernicus* and reported by Jenkins & Meloy (1974) probably arose from a thin conduction zone situated between an interior region of hot, shocked wind material at $T \sim 10^6$ K and the surrounding medium, rather than from the general interstellar medium. In a more refined investigation of

these circumstellar structures, Weaver et al. (1977) predicted that a typical bubble interface could produce $N(\text{O VI}) \approx 2 \times 10^{13} \text{ cm}^{-2}$. While this amount of O VI is small compared to the typical column densities registered in our *FUSE* survey, we must recognize that our inventory of truly interstellar O VI could be elevated by the contributions from circumstellar bubbles.

Many factors can influence the structure of a bubble, such as the star’s age, its wind energy, its motion through the medium, and the density of the surrounding gas. These elements, together with the added effects from neighboring stars, make it difficult to make trustworthy predictions about the O VI contributions for specific cases. Nevertheless, we know that the internal hot gas within a bubble should emit soft X-rays. Thus, stars with well established bubbles should be detectable in the RASS, although target regions for which there is strong foreground absorption by neutral hydrogen may show up in only the highest energy bands. While we do not expect a simple one-to-one correspondence between the X-ray emitting properties of a bubble and its ability to contribute O VI absorption, we can still try to establish an empirical relation between the two and thus gain some insight on the probable effects from bubbles in general.

Figure 9 shows selected RASS image fields⁸ that include groups of stars in our survey. These examples illustrate the fact that some stars are surrounded by clearly defined X-ray emitting zones, while others are not. Sometimes there are several stars that reside within a common envelope that is bright in X-rays.

Ultimately, we need to determine the approximate magnitude of the bubble contributions to the O VI column densities that we measured, so that we can arrive at a clearer understanding of how much O VI is distributed in the general regions of the Galactic disk. However the distinction between “bubble” and “non-bubble” O VI-bearing gas is somewhat arbitrary, since there is probably a continuum of bubble properties that extend from well formed, identifiable bubbles with distinct boundaries to highly disrupted structures that begin to blend into the general medium. Despite this limitation, we felt it was important to make a distinction between stars that had visible bubbles, ac-

⁸The *ROSAT* images were obtained from the *ROSAT Data Browser* at the web site <http://www.xray.mpe.mpg.de/cgi-bin/rosat/data-browser>, using the default settings except for the full-scale limits being set to Band 1 = 5, Band 2 = 6, Band 3 = 4 counts $\text{deg}^{-2} \text{ s}^{-1}$ for Figs. 9a-d and f, while Band 1 = 5, Band 2 = 12, Band 3 = 8 was implemented for Fig. 9e.

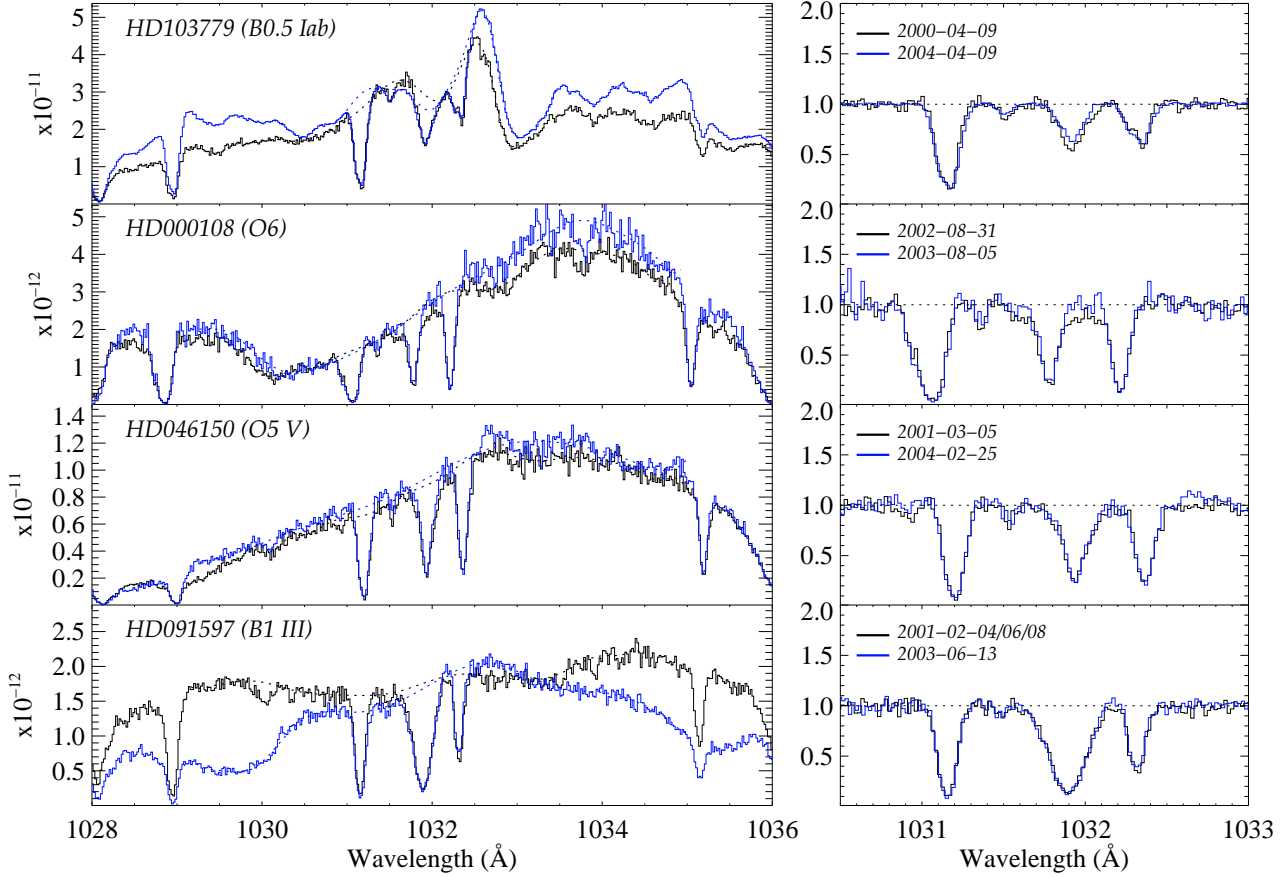


Figure 8: Four stars (of six) for which multi-epoch data are available. Black/blue spectra represent the earlier/later epoch data. The left hand panel shows the variation in absolute flux at two different epochs, along with the continua used to normalize the data. Fluxes are in the usual units of $\text{ergs cm}^{-2} \text{s}^{-1} \text{\AA}^{-1}$. The right-hand panel shows the normalized flux *before* subtraction of the HD 6–0 R(0) line, while the dates of the two epochs used are given in the top left of each panel. Small shifts ($\leq 0.06 \text{\AA}$) in the wavelength scale have been added where necessary to align the features.

cording to some specific criterion, and those that did not. To accomplish this, we assigned each target to one of three categories according to appearances in the RASS fields, based on the concepts of having no evidence of surrounding emission, having an intermediate or doubtful level of emission, or having a clear, surrounding bubble. For convenience, we assign the symbol R to represent a category. We then have:

- $R = 0$: the target is in an X-ray-dark portion of the sky, well free of any emission;

- $R = 1$: the target is in or near a general diffuse enhancement of X-ray emission or is on the edge of a bright spot;
- $R = 2$: the target is clearly situated in projection in a bright X-ray spot that appears to have been created by the star and/or its association neighbors

(An additional category will be assigned in §3.5.)

The immediate surroundings of virtually all early-

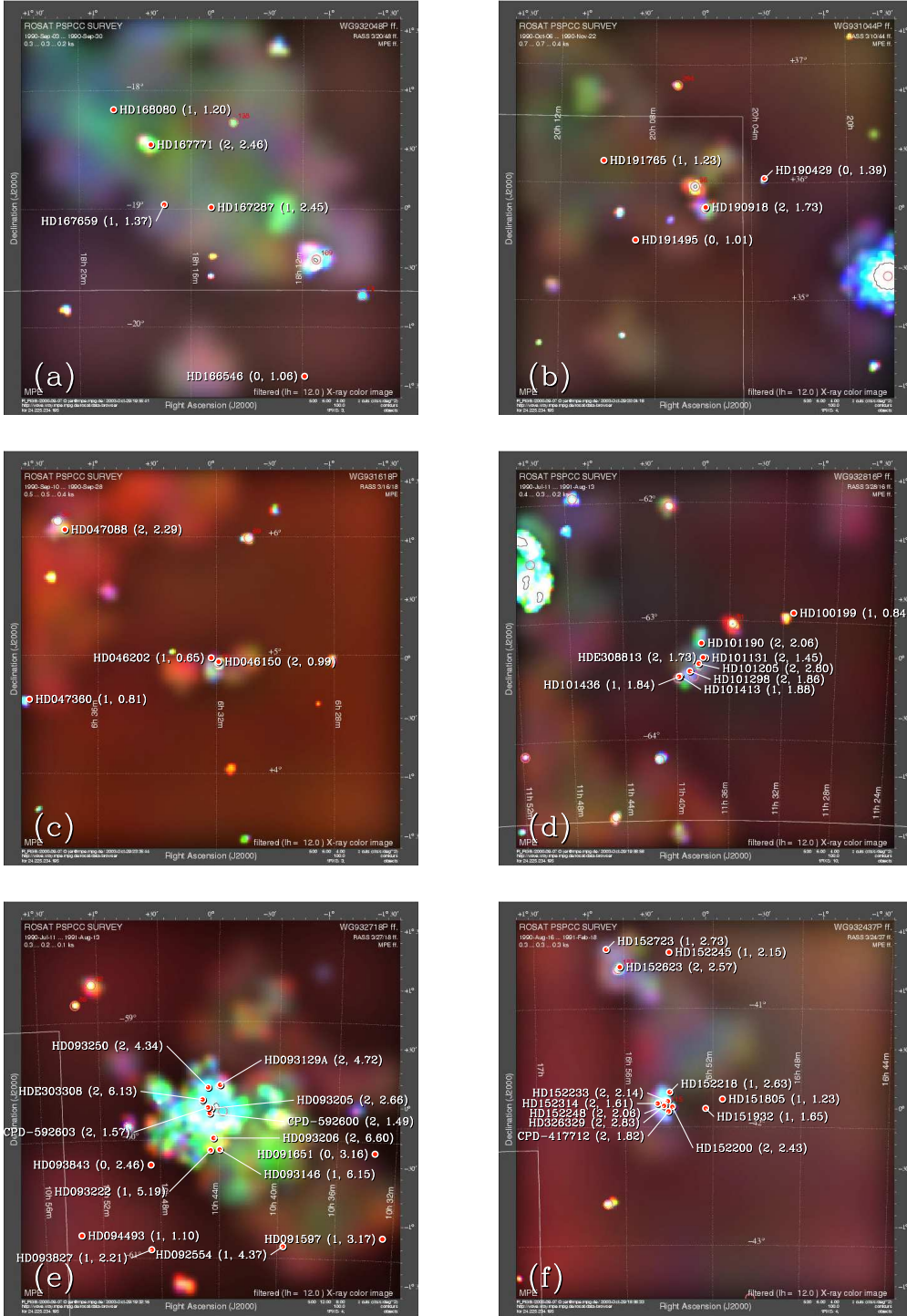


Figure 9: X-ray emission observed in the *ROSAT* All Sky Survey (RASS) within fields centered on close groups of stars selected as targets for the O VI survey. Intensities for the low, middle and high energy bands are depicted with varying brightness levels of red, green and blue, respectively. The positions of O VI survey targets are identified; following each star's name are parentheses that contain our designation of *ROSAT* category followed by the value for $N(\text{O VI})/10^{14} \text{ cm}^{-2}$.

type stars exhibit some X-ray emission arising from shocked stellar winds (Hillier et al. 1993; Berghoefer & Schmitt 1994; Cassinelli et al. 1994; Berghoefer et al. 1996, 1997). Absorption features from O VI should arise from such material, but the large wind speeds allow these contributions to be separated from the interstellar features (Lehner et al. 2001, 2003). For this reason, we refrained from classifying stars as $R = 2$ if the emission was not clearly extended in the sky beyond the smearing by *ROSAT* point-spread function. As an aid to determining whether or not the emission was extended, we examined entries in the *ROSAT* bright and faint source catalogs (Voges et al. 1999). Sources coincident with the star positions that were not clearly extended (extent likelihood ≤ 1) were considered to arise from fast winds, which we considered grounds for rejecting the assignment of $R = 2$.

3.5. Accounting for Supernova Remnants

In addition to bubbles around the target stars, extraordinary enhancements of O VI can in principle arise if any of the lines of sight penetrate a supernova remnant. This is clearly the case for 3 of our stars, HDs 074920, 074711 and 075309, which lie in the direction of the conspicuous Vela SNR [see Fig. 7*d*]. The near edge of this remnant is at a distance of only about 250 pc (Cha et al. 1999), a value that is consistent with the slightly greater distance (~ 280 pc) to the nebula’s center as determined from the distance to the Vela pulsar (Ögelman et al. 1989; Caraveo et al. 2001; Dodson et al. 2003) and X-ray observations of the nebula (Bocchino et al. 1999). Thus, there is no question that the remnant is in front of these stars with distances ranging from 1.1 to 2.7 kpc.

It is important to identify less obvious cases where sight lines may penetrate SNRs. A comparison of our target locations with those in a compilation of identified remnants (Green 2001) reveals a number of coincidences, which are listed in Table 8. Once again, in order to exclude special cases from our general assay of O VI, we have added one more category to the ones defined in §3.4 above:

- $R = 3$: stars are situated inside the boundary of a supernova remnant and are not clearly in the foreground.

To be conservative, when the relative distances are in doubt, we assign a Category 3. Unlike the situation for the Vela SNR, the distances to the remnants

presented in Table 8 may have large errors. For this reason, we sometimes experienced difficulties in determining with much confidence whether or not the targets are behind the SNRs. Two stars that fall into this category are HD 168080 and HD 047417. For HD 124314, we could find no distance estimate for the remnant in the literature. For other stars, such as HD 185418 and HD 199579, the differences in distance between the stars and the remnants are so large that we can be more certain that they are indeed in the foreground. Without the knowledge that HD 185418 was by chance situated in front of G53.6 -2.2 (with angular dimensions of only $33 \times 28'$), we would have assigned a rating of $R = 2$ for this star (i.e., by mistaking the X-ray emission as coming from a bubble surrounding the star) instead of our adopted $R = 0$. Although one might have said the same for HD 199579, we have retained the $R = 2$ assignment because there is a bright X-ray spot centered at the position the star that appears to be on top of the more extended emission from the SNR. While it may seem that HD 134411 lies far behind its remnant, we must recognize that the distance estimate for this SNR is probably much less accurate than the others, since it is based on the empirical (z -adjusted) surface-brightness—distance ($\Sigma - D$) relation for estimating remnant distances (Milne 1979).

A very young remnant G266.2 -1.2 has a diameter of 2° and is located in projection inside the boundary of the much larger Vela SNR (Aschenbach 1998; Iyudin et al. 1998). Redman et al. (2002) suggest that a nearby nebula RCW 37 (the Pencil Nebula) is created by a collision between a collimated flow of gas ejected from G266.2 -1.2 and a boundary of the Vela SNR. If this interpretation is correct, the distance of G266.2 -1.2 should be nearly the same as that of the Vela SNR. If not, we can still rely on an upper limit of 0.5 kpc based on the present-day strength of gamma ray emission from ^{44}Ti (Aschenbach et al. 1999). The two stars listed in Table 8 have total column densities (in units of 10^{14} cm^{-2}) of 1.96 (HD 074920) and 3.37 (HD 075309), along with 3.0 for HD 075821 (Jenkins et al. 1976), which is also inside G266.2 -1.2 . By comparison, stars that are still inside the main Vela remnant but outside G266.2 -1.2 include HD 074711 in our survey along with HDs 074455, 072108 and 074753 in the study by Jenkins et al. (1976). These stars have $N(\text{O VI})/10^{14} \text{ cm}^{-2} = 0.7, 4.5, 1.3,$ and $0.8,$ respectively. It is thus not clear that the smaller remnant contributes much extra O VI. Perhaps most of the gas inside this young remnant is too hot to show O VI; its

X-ray spectrum indicates that gases exist at a temperature in excess of 3×10^7 K (Aschenbach et al. 1999).

There are a number of targets in the vicinity of the Cygnus Superbubble, a horseshoe-shaped X-ray emitting region with a diameter of about 13° (Cash et al. 1980) (see Fig. 7*b*). Recent investigations indicate that this may not be a single structure, but rather a superposition of unrelated shell and bubble-like objects at different distances (Bochkarev & Sitnik 1985; Uyaniker et al. 2001). We therefore refrain from assigning $R = 3$ to stars that appear near the edge of this emission.

The stars HDs 045314, 047417, 047088, and 047360 overlap with the Monogem Ring (Plucinsky et al. 1996), but Figure 9*c*) shows that HD 046202 and HD 046150 are just outside the edge of this remnant (visible in the top left corner). The yellow color of the Monogem Ring depicted in Figure 7*c*) indicates the presence of a strong low-energy X-ray flux that has not been appreciably absorbed by foreground neutral hydrogen [i.e., compare with the blue color of the Cygnus Superbubble in Fig. 7*b*], and indeed Plucinsky et al. (1996) estimate that only 5×10^{19} cm⁻² of neutral hydrogen is in front of the nebula. Our stars in this vicinity all have $N(\text{H I}) > 10^{21}$ cm⁻² (Diplas & Savage 1994), so they are clearly at greater distances. As with the stars behind the Vela SNR, these stars show more O VI than expected for their distances.

Stars in the general vicinity of $\ell = 240^\circ$ are behind a large superbubble GSH 238+00+09 identified by Heiles (1998), who estimated 0.8 kpc for a distance to this structure. Figure 7*d*) shows no appreciable departures from the general average $N(\text{O VI})$ per unit distance for the stars behind this superbubble, although all of the O VI velocities are consistently positive. Perhaps this velocity pattern arises from O VI in the back edge of an expanding bubble.

3.6. ROSAT Categories For Other Datasets

For completeness, we also assigned *ROSAT* categories to the stars observed with *Copernicus*, and those observed by Zsargó et al. (2003), using the same system we used for the *FUSE* stars described above. These values are given in Tables 12 and 13 in Appendix C.1 and C.2.

ROSAT categories were also derived for the WDs of SL06. The majority of these stars were assigned to $R = 1$ or $R = 2$ categories — there were very few WDs with no detectable ($R = 0$) X-ray emission, largely due

to their small distances. The WDs give us an interesting opportunity to look for a correlation between X-ray flux and $N(\text{O VI})$. Since WDs are very close by, interstellar O VI absorption is likely to be much less important than it is over longer path lengths, and circumstellar O VI absorption might in principle be the dominant source of O VI absorption. Using WDs also provides the advantage of using sources with uniform properties. Although not shown here, we searched for a correlation between X-ray flux and $N(\text{O VI})$, but found none. The circumstellar environment of a WD may, of course, be different from that of a stellar association, but for the WDs, the detected O VI absorption is unrelated to the WD X-ray flux.

3.7. Average O VI Line of Sight Volume Density

3.7.1. Sample Definitions and Basic Statistics

Savage et al. (2003) demonstrated that O VI absorbing gas can be traced several kpc above the plane of the Milky Way. In the Galactic halo, the volume density falls with height, but the derivation of the mid-plane density n_0 requires fitting an assumed model to the observed data (see next section, §3.8). The stars in our sample (excluding the halo stars of Z03) have a distance above the Galactic plane $z = d \sin b$ with a mean⁹ distributed around $z = 0$ and with 98% of the stars below $|z| = 1$ kpc. We would therefore expect a simple average of the densities $n = N(\text{O VI})/d$ to be close to the mid-plane density since the scale height is ~ 2.3 kpc according to Savage et al. (2003). (Again, we discuss this assumption in §3.8.) With the sight lines coded by the presence or absence of X-ray emission, it should also be possible to see if n is different for lines of sight with and without enhanced X-ray emission.

The first problem in determining n involves deciding how to treat sight lines when only upper limits are available for $N(\text{O VI})$. We initially employed various survival statistics, including the well known Kaplan-Meier (K-M) estimator, which calculates the true distribution function of randomly censored data and yields the distribution's mean and median (Feigelson & Nelson 1985; Isobe et al. 1986). Given measured values of, and upper limits to, $N(\text{O VI})/d$, we should in principal have been able to recover $\langle n \rangle$. However, as Isobe (1992) makes clear, the K-M technique only works when the upper limits are distributed randomly

⁹The precise mean is $\langle z \rangle = -44$ pc, with a dispersion $\sigma = 98$ pc.

with respect to the overall distribution (“Type 2 censoring”). Although the method worked well for SL06, who had upper limits with values comparable to the distribution of detected values of n towards WDs, all of our upper limits for n were clustered below the apparent mean of n .

Instead, we simply defined a sample for which the column densities were set at the upper limits given in Table 5 or as stated in the other surveys when no line was present. We discuss the possible errors introduced by defining the sample with these upper limits in the next section. Table 9 summarizes the statistical tests employed, and the results obtained. We calculated two statistics: (1) the average value of n derived from the ensemble of $\log(n)$ values¹⁰; and (2) the distance weighted average $\sum N(\text{O VI})/\sum d$. The data were further subdivided into two subsets: stars at distances > 2 kpc and those with distances between 0.2 and 2 kpc. These distance categories partition the data into two halves with approximately equal numbers (the median distance to the stars is 2040 pc). Of course, the two subsets contain data from different surveys in disproportionate numbers: the $d = 0.2-2$ kpc subset contains a mixture of *Copernicus* and *FUSE* data (45 and 43 sight lines, respectively) while the $d > 2$ kpc contains almost exclusively *FUSE* data (97 of 102 sight lines). Although the *Copernicus* sight lines are essential for mapping O VI absorption at distances less than ~ 1 kpc, the errors in $N(\text{O VI})$ (Appendix C.1) are very much larger than the *FUSE* $N(\text{O VI})$ errors. The distance-selected subsets have the advantage, however, of subdividing the data according to whether or not the sight lines are strongly influenced by O VI from the Local Bubble. Finally, within each of these categories, the samples were subdivided further into subsets according to their *ROSAT* classifications.

3.7.2. The O VI Volume Density n : (i) Differences for Near and Distant stars.

Examples of the distributions of n values are shown in Figure 10. In each case, the distribution of n for sight lines regardless of their *ROSAT* classification (“All- R ”) is given in gray, while $R = 0$ sight lines are shown as white histograms. All the histograms are normalized by the total number of stars used to create

the distribution. The top panels include stars at “far” distances $d > 2$ kpc; the bottom panels show stars at “near” distances of $0.2 < d < 2$ kpc. The mean of a distribution¹¹ is shown by an inverted triangle, and a Gaussian profile for the All- R distribution using this mean and the standard deviation given in Table 9 is shown with a dotted line. A cross marks the distance-weighted average $\log[\sum N(\text{O VI})/\sum d]$. As Figure 10 shows, the histograms are reasonably well approximated by log-normal distributions, enabling us to define means and standard deviations consistent with a theoretical normal distribution.

In parallel with these measurements, we constructed a synthetic dataset of absorption line profiles in order to better understand the distributions shown in Figure 10 and the values tabulated in Table 9. We were particularly interested in how well we might reproduce the observed distributions if we based a simulation on a single value of n , and hence whether the dispersion in the data might really be some artifact of the quality of our data. We therefore took a set of random distances, used a fixed value of n to derive $N(\text{O VI})$, created line profiles (adopting a fixed value of $b = 40 \text{ km s}^{-1}$), added a fixed amount of noise (similar to that obtained for the majority of the *FUSE* sight lines), and re-measured $N(\text{O VI})$ and the appropriate errors. We also adopted the same procedures for defining an upper limit to the column density as described in §2.8.2 when lines were barely detected, and included the upper limits to n determined from the upper limits to $N(\text{O VI})$. Finally, we calculated the ‘measured’ values of n and determined how close they were to the original value.

The simulation provided several interesting results. How well we could reproduce $\langle n \rangle$ (using the same methods described in the previous section and shown in Table 9) depended primarily on the S/N we adopted when adding noise to the theoretical profiles. With a high S/N, all lines were recovered and n was indistinguishable from the original value. With very low S/N data, many lines had measured column densities which were either negative, or were less than the upper limit determined from the noise. As a consequence, the mean value of n became larger than the original value (since an upper limit is larger than the true original value).

¹⁰This is a simple average, without weights that account for the different magnitudes of the errors. The analysis presented in §3.8.2 evaluates minima in χ^2 which automatically recognizes differences in the size of the errors.

¹¹ $\bar{x} = \Sigma(\log n_i)/N$, where N is the total number of i points used. The standard deviation entries in Table 9 are then the usual $\sigma^2 = \Sigma(\log n_i - \bar{x})^2/N$; they are not the uncertainties of the listed averages.

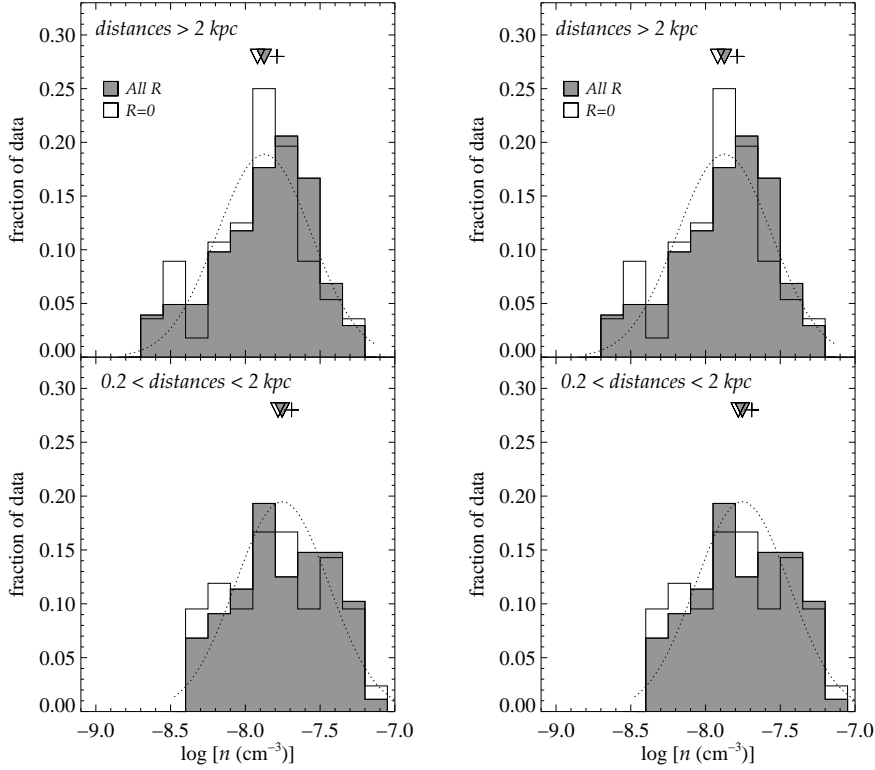


Figure 10: **Left:** Distribution of O VI line of sight volume densities, $\log n = \log[N(\text{O VI})/d]$, divided into two sets, one for stars beyond 2 kpc (upper panel), the other for stars in the interval $0.2 < d < 2$ kpc (lower panel). The gray histogram shows the distribution of stars regardless of *ROSAT* class, while the white histogram shows only $R=0$ sight lines. The dotted line shows a Gaussian with a mean and standard deviation for the All- R samples given in Table 9, while the inverted triangles show the means of each distribution. A cross marks the distance weighted average of $N(\text{O VI})$. (More details are given in Table 9.) Note: distant high-latitude halo stars, extragalactic sight lines, and sight lines towards the Vela SNR and Carina Nebula are not included. Each histogram is normalized by the total number of objects making up the histogram. **Right:** The same distributions, only with the Local Bubble (LB) column density [$N_{\text{LB}}(\text{O VI}) = 1.11 \times 10^{13} \text{ cm}^{-2}$] removed for each sight line, and distances reduced by the radius of the LB, which we take to be 100 pc.

Translating these findings to our *FUSE* and *Copernicus* data sets is not so straightforward, since the real data have differing S/N s (more precisely, the spectra all have different $N(\text{O VI})$ upper limits). However, our simulations show that while the error in the true mean of n depends on the S/N of the data, it is equivalently dependent on the relative number of lines which are lost (lower S/N means more n upper limits). Hence it is possible to simply count the number of non-detections (upper limits) we find in our data and use the results of the simulations as a guide to the likely over-estimation of $\langle n \rangle$.

In the near sample ($0.2 < d < 2.0$ kpc) 14% of our sight lines show no O VI absorption lines and have upper limits for $N(\text{O VI})$. For the far sample ($d > 2$ kpc) only 7% have upper limits. In our simulation, we find that these percentages of non-detections cause an over-estimate of $\sim 12\%$ and $\sim 6\%$ for the near and far samples, respectively. Hence, *if* the underlying O VI column density can be represented by a constant value, then the numbers shown in Table 9 are likely to be over-estimated by only a small amount after including column density upper limits.

Another result from the simulation was that the

largest values of n (in cm^{-3}) recovered arose from the weakest $N(\text{O VI})$ lines, and hence towards the closest stars. This was because weaker lines were more easily lost in the noise, and were more likely to give *erroneously* large values of n , just because of noise fluctuations¹² Given this possibility, we considered whether large values of n measured in our data were actually real, and not just a consequence of selecting lower quality data. In fact, values of $\log(n) > -7.5$ are found at all distances and column densities and so are real over-densities in the global distribution of O VI absorption. Moreover, seven sight lines have $\log(n) > -7.0$, all of which arise towards the Vela SNR. We also noticed that most of the sight lines towards the Carina Nebula also had large values of n .

Sight lines through the Carina Nebula (NGC 3372, $[l,b] = [287.7, -0.8]$), of course, are not typical probes of the Galactic ISM. The nebula is a giant H II region (1–2 degrees in radius in optical emission) powered by more than a dozen star clusters, and although most of the gas has been blown away by the clusters, low- and intermediate-mass star formation remains at the peripheries (Smith et al. 2003). The distance to Carina is somewhat ambiguous, but appears to be in the range 2.5–3 kpc (Feinstein 1995; Walborn 1995). Most of the stellar distances we derive to stars towards Carina (Appendix B and Table 1) are consistent with this distance, as expected. The extent of the nebular in X-ray emission can be seen in Figure 9e, which also shows the positions of the stars observed by *FUSE*.

It has been known for a long time that the spectra of Carina stars show complex, multicomponent absorption line profiles, with individual components distributed over several hundred km s^{-1} at both positive and negative velocities (Walborn & Hesser 1975, 1982). Absorption from ions in both high and low ionization states is seen (Walborn et al. 1984, 2002a, 2007, and references therein). Most of the stars in our *FUSE* sample in this region are of very early spectral type and have reasonably well determined continua, which makes the detection of interstellar O VI straightforward. They generally show clear evidence for absorption at large negative velocities away from the bulk of the absorption at $v \sim 0$, high velocity features which are not seen along other sight lines through the ISM

¹²These inherently weaker lines were also more likely to give erroneously *small* or negative values of n as well; however, since weak lines deemed below the noise were set to upper limits, the distribution of $\log n$ values discussed above does not include these small- $\log(n)$ outliers.

(except towards the Vela SNR — see below). In some cases, a component can be clearly resolved from the main complex; in other cases, the additional negative velocity gas produces a discernable asymmetry to the $v \sim 0$ complex. It seems reasonable to link this additional absorption to gas directly associated with the nebula. Detecting high positive velocity gas in absorption is somewhat harder, since the H_2 6–0 R(4) line lies at a wavelength that corresponds to any O VI absorption offset from rest by $+121 \text{ km s}^{-1}$, potentially masking any high positive velocity components. Nevertheless, it is clear that there is no preponderance of very strong O VI absorption lines at $\approx 100 \text{ km s}^{-1}$, since the profiles of the 6–0 R(4) lines are always close to the shape predicted by fitting other H_2 lines in different regions of the spectra (see §2.6). Only towards HD 093146 (#92) is there good evidence for excess O VI absorption at positive velocities.

As noted in §3.5, the Vela SNR ($[l,b] = [263.9, -3.3]$) is much closer than Carina, at a distance of only $250 \pm 30 \text{ pc}$ (Cha et al. 1999). Sight lines which pass through Vela again show complicated multicomponent absorption line complexes (see, e.g. Slavin et al. 2004, and references therein). An initial study of O VI absorption was made using four stars situated behind Vela (Slavin et al. 2004); our *FUSE* sample includes an additional three stars which lie behind the SNR: HD 074920, HD 075309, and HD 074711 (#77–79). The first two of these show evidence for multicomponent absorption. HD 075309 in particular appears unusual, with very weak O VI absorption at $v_{\odot} = 33 \text{ km s}^{-1}$, and much stronger absorption at -74 km s^{-1} . Again, the kinematic structure of the O VI absorption seen towards HD 074920 and HD 075309 seems quite atypical of that seen in the rest of the Galactic ISM.

A full analysis of the conditions within the Carina Nebula and Vela SNR inferred from absorption line data is beyond the scope of this paper. Nevertheless, the sight lines towards these regions present us with a dilemma. Although they present a particularly interesting opportunity to study phenomena local to active star formation and destruction, they also present particularly extreme examples of O VI absorption and probably do not represent the more general distribution of O VI absorbing gas in the ISM. For this reason, we excluded Carina and Vela sight lines from all the measurements presented in Table 9.

We make one final note concerning the possible effect that the non-detections of O VI might have on

the values of $\langle n \rangle$ given in Table 9. For the distance-weighted statistic $\Sigma N(\text{O VI})/\Sigma d$ (column 4 of Table 9), it is also possible to set all upper limits to zero and see whether $\langle n \rangle$ is very different than that calculated using the upper limit values¹³. When calculated this way, we find that $\langle n \rangle$ is only 7% and 14% smaller for the near and far (“All- R ” — see below) sample, respectively.

Shelton & Cox (1994) first showed that the LB has a higher average density than the rest of the Galactic disk. (We see this effect in Fig. 15 in §3.14.) To better reflect the value of $\langle n \rangle$ in the ISM beyond the LB, we recalculated all the statistics after subtracting a column density representative of that from the LB, for which we used a recent value of the LB volume density of O VI found by SL06, $n_{\text{LB}} = 3.6 \times 10^{-8} \text{ cm}^{-3}$. For a bubble with a radius of 100 pc, this corresponds to a column density $N_{\text{LB}}(\text{O VI}) = 1.11 \times 10^{13} \text{ cm}^{-2}$. We also subtracted 100 pc from all stellar distances. Values of $\langle n \rangle$ corrected in this way are given in Table 9; these are labelled as “-LB” measurements, compared to the values for which no LB contribution is removed, “+LB”.

The corrected distributions of $\log(n)$ are shown in the right-hand stack-plot of Figure 10 and tabulated in Table 9. For the distant $d > 2$ kpc stars, it is unsurprising that there is little difference (0.05 dex) between the +LB and -LB means. For the nearer ($0.2 < d < 2.0$ kpc) stars, the difference is far more pronounced (0.13–0.18 dex), as would be expected. Moreover, the near and far +LB samples (for the same *ROSAT* classes) also show large differences (0.09–0.14 dex); yet with the contribution from the LB removed, the means between the near and far samples are nearly identical. We conclude that *after* correction for the Local Bubble, the average line of sight density of O VI is the same for all distances beyond 200 pc. Note that in the bottom-right panel, the width of the near, -LB sample is much wider than in the other three panels. This is because of the increase in the relative errors in $N(\text{O VI})$ — and hence $\log(n)$ — that arise after subtracting $N_{\text{LB}}(\text{O VI})$. This can also be seen in the standard deviations listed in column 3 of Table 9, which are much larger for the near, -LB sample.

¹³ Obviously, $\log[N(\text{O VI})/d]$ cannot be calculated if $N(\text{O VI})$ is set to zero, which is why we could not calculate $\langle n \rangle$ from a distribution using such a sample of column densities.

3.7.3. The O VI Volume Density n : (ii) Differences for Different *ROSAT* Classes.

We repeated the statistical tests described above, for stars separated by *ROSAT* class. The results can be seen in Table 9, where average densities are broken into categories defined by samples of sight lines which include “All- R ”, or which have $R = 0$ or $R > 0$. Table 9 shows that within each of the four near/far, +LB/-LB classes, the differences in the means between the $R = 0$ and the $R > 0$ sub-samples are between 0.05 and 0.1 dex. Are such differences significant?

To test if these differences are real, we used two well established tests on the +LB sample of stars. We first considered the results from a Student’s t -test, which tests the null hypothesis that the means of two populations are equal. For the $d > 2$ kpc stars, we found a t -statistic of $t = -1.6$, and a probability that we might incorrectly reject the hypothesis that the means are equal of only $P = 0.11$. For the $0.2 < d < 2$ kpc stars, we found $t = -0.8$, and $P = 0.44$. We would conclude from these numbers that there is a small difference in n between $R = 0$ and $R > 0$ sight lines beyond 2 kpc, but that no significant difference can be found nearer than 2 kpc.

Student’s t -test is a parametric test whose accuracy relies on the fact that the two populations being tested are normally distributed. To avoid problems in comparing two distributions when the underlying distributions are not known, we used the standard non-parametric Kolmogorov-Smirnov (K-S) test. For the distant stars, the K-S D parameter was measured to be $D = 0.3$, with $P = 0.014$, while for the nearer stars, we found $D = 0.13$ and $P = 0.84$. These numbers confirmed the conclusion that the $R = 0$ and $R > 0$ have different distributions of $\log(n)$ for distant stars, but very similar means for the nearby stars. The numbers from the K-S tests and from the Student’s t -test changed little if we used the -LB instead of the +LB sample.

Figure 11 shows the distribution of $\log(n)$ values for the two +LB *ROSAT* classes with the two distance subsets combined, i.e., for all stars beyond 200 pc. For the $R = 0$ and the $R > 0$ samples, the means and standard deviations are $\langle \log(n) \rangle = -7.85 \pm 0.32$ and -7.77 ± 0.31 , respectively. A t -test shows that the likelihood of a difference between the two sub-classes has increased by combining the near and far samples: $t = -1.9$, $P = 0.07$. A K-S test gives $D = 0.20$, $P = 0.03$. As we mentioned above, these tests were

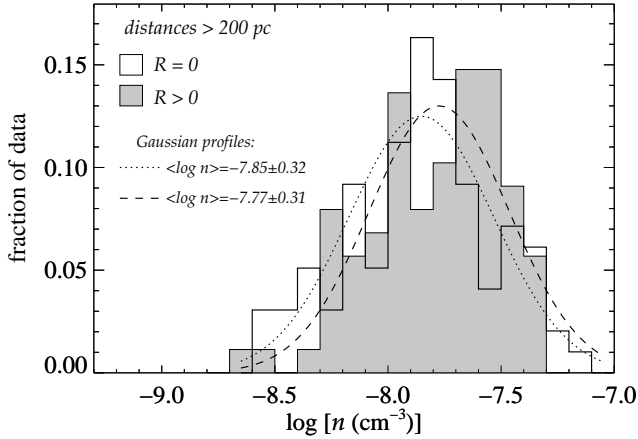


Figure 11: Distribution of O VI line of sight volume densities for all stars in the Galactic disk (thereby excluding halo stars) beyond 200 pc, divided into $R = 0$ (white histogram) and $R > 0$ (gray histogram) subsets for the +LB samples. Each histogram is normalized by the total number of objects making up the histogram. Gaussian profiles for the $R = 0$ (dotted line) and $R > 0$ (dashed line) samples are drawn with means and standard deviations given in §3.7.3.

performed with Vela and Carina sight lines excluded. If we include those sight lines, most of which have $R > 0$, the two distributions become very different ($t = -3.6$, $P = 3 \times 10^{-4}$; $D = 0.26$, $P = 1 \times 10^{-3}$) because the lines of sight clearly intercept regions with higher densities. Again, these values change little if we use the -LB instead of the +LB sample.

We discussed the likely origins for higher (on average) values of n towards $R > 0$ sight lines in §3.4 and §3.5. Bubbles visible in X-rays and the volumes within SNRs probably contain some gas in the temperature range that favors the production of O VI, and although the effect is small, sight lines towards these structures show elevated O VI column densities.

We note a few interesting exceptions, however. HDs 199579 and 110432 have $R = 2$, and yet they both show virtually no O VI absorption at our level of sensitivity. A more spectacular example of this effect is γ Cas observed by J78. The upper limit of $N(\text{O VI}) < 10^{12} \text{ cm}^{-2}$ is considerably below the *FUSE* detection limit, and yet this star is centered on an extended source that is $19''$ in diameter, according to the *ROSAT Bright Source Catalog* (Voges et al. 1999).

However γ Cas is only at a distance of 0.2 kpc, which means that the detected X-rays are emitted within 0.02 pc of the star. This dimension is far smaller than a classical, well developed bubble. Thus, the emission could arise from the more extended parts of the hypersonic wind from the star, rather than an established interface region. It is also likely that if this star was ten times further away, at the typical *FUSE* sample distances, the X-ray emission would probably be undetected.

The reason for being able to see the differences between the $R = 0$ and the $R > 0$ sight lines to distant stars and not nearby ones is likely due to selection effects. X-ray fluxes fall with distance as $1/d^2$, and neutral gas absorbs X-rays, so for the more distant stars we probably only see the very largest, brightest interstellar bubbles which have the largest enhancements of $N(\text{O VI})$. Nearby stars are less likely to be members of dense star-forming regions, and their X-ray fluxes are probably easier to detect; so, for these, we assign a $R > 0$ category even if the circumstellar bubbles are not particularly bright and there is little enhancement in $N(\text{O VI})$ from the bubble.

Finally, we note one other experiment we performed with the data. We attempted to subtract a column density that might be representative of circumstellar O VI absorption, $N_{\text{circ}}(\text{O VI})$. Our aim was to find a value of $N_{\text{circ}}(\text{O VI})$ which could be subtracted from the $R = 2$ sample, leaving a sample with a mean which was the same as the $R = 0$ sample. Unfortunately, we were unable to find a plausible value of $N_{\text{circ}}(\text{O VI})$; the distribution of n for the $d > 2$ kpc sample was largely unaffected by subtracting a small $N_{\text{circ}}(\text{O VI})$ from each sight line, but it greatly changed the $0.2 < d < 2$ kpc sample, sending the majority of the n values to values less than zero. This probably reflects the selection effect mentioned above: the value of $N_{\text{circ}}(\text{O VI})$ towards the more distant stars is probably higher than $N_{\text{circ}}(\text{O VI})$ towards nearby stars, because our $R > 0$ categories include very large, very X-ray-luminous bubbles at large distances, and smaller, less luminous (but still detectable by *ROSAT*) bubbles at smaller distances.

3.7.4. Bias Toward Stars with Small Reddening

In large part, our selection of targets is governed by the limitation that the stars must not be so faint at 1032 \AA that a prohibitively large amount of observing time is needed to obtain spectra with respectable

values for the S/N. One consequence of this is that more distant stars tend to have much lower than normal amounts of reddening per unit distance. For closer stars, this selection is not as strong. It is fair to ask whether or not this bias in the sampling of the Galactic disk volume distorts our conclusions on the general distribution and properties of the regions that hold O VI, and in particular, on the volume densities we have derived above. This could be an important consideration if O VI-bearing gas is strongly correlated or anticorrelated with the cold gas that causes reddening. For instance, surveys of the soft X-ray background radiation exhibit an anticorrelation, which probably arises from the effect that the X-ray emitting gas displaces the cold material (McCammon & Sanders 1990).

To examine the issue of whether or not we must acknowledge and attempt to correct for a bias in our survey, we must determine the likelihood that the character of the O VI, either its average volume density or velocity dispersion, is affected somehow by the reddening per unit distance. Figure 12 shows the distribution of all stars in our FUSE survey on a diagram of $E(B-V)$ vs. distance, with the points having a color coding that represents either the O VI volume density n (top panel) or the second moment of the absorption profile $\langle v^2 \rangle$ (bottom panel). The expected selection effect in our survey is clearly evident from the fact that there are no points in the upper right-hand portion of the diagrams. Nevertheless, from the distribution of colors shown in the plots, we gain the impression that internally within our collection of targets, there is no tendency for the results to be driven much by the reddening per unit distance. We can easily imagine that if the diagram were populated more evenly, i.e., without the exclusion of cases where color excesses increase roughly in proportion to distance, the outcome would not be appreciably different from what we have already found.

Looking at the problem more quantitatively, we find a median reddening per unit distance of $0.10 \text{ mag kpc}^{-1}$, represented by the dotted line in each panel of the figure¹⁴. For the half of our measurements that are above this value, the median value of n is $1.64 \times 10^{-8} \text{ cm}^{-3}$, while for the half of the sample below the median $E(B-V)/d$, the median value for

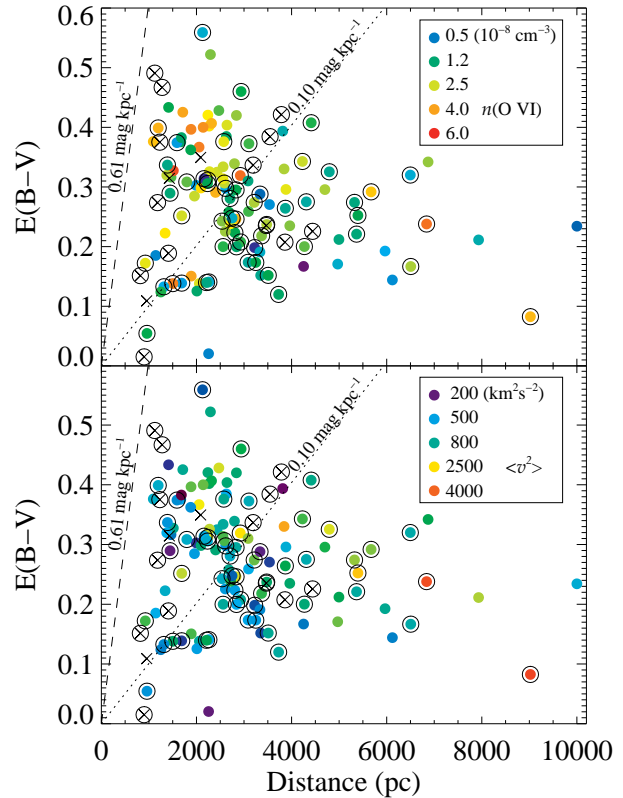


Figure 12: The distribution of targets with regard to their color excesses $E(B-V)$ and distances d , excluding targets towards the Carina Nebula or the Vela supernova remnant (which are atypical). In each panel, the dotted line indicates the median value of $E(B-V)/d = 0.10 \text{ mag kpc}^{-1}$ in our survey, and the dashed line represents the general average of $0.61 \text{ mag kpc}^{-1}$ in our part of the Galaxy. Points with circles around them are targets that have *ROSAT* classifications of $R = 0$, and the crosses represent cases where only upper limits for $N(\text{O VI})$ could be obtained. The colors in the top panel indicate $n(\text{O VI})$, while those in the bottom panel indicate the second moment of the absorption profile $\langle v^2 \rangle$.

n is $1.30 \times 10^{-8} \text{ cm}^{-3}$. This outcome is opposite to our expectation that regions with less reddening than usual might be more likely to hold more than the usual amount of O VI. However, an apparent correspondence between $E(B-V)/d$ and $N(\text{O VI})/d$ could arise purely from the fact that errors in a common denominator, i.e.,

¹⁴Our median reddening per unit distance is considerably lower than the general average of $0.61 \text{ mag kpc}^{-1}$ (Spitzer 1978; Fitzgerald 1968). Whether or not this is important depends on the volume occupation fractions of gases at different densities.

the distances, might make the quantities appear to be mildly correlated when, in fact, they are not. A K-S test on whether the two separate samples of n could arise from the same population indicate that there is an 8% probability that differences this large or larger could arise simply from chance, given that the two samples are drawn from the same population. (Such a test cannot be run for the velocity dispersions because they are indeterminate when O VI is not detected.)

Finally, we note that even if the selection of sight lines is biased against highly reddened sight lines, the clouds which cause the reddening are likely to occupy only a small volume compared to the volume that the O VI-absorbing gas occupies. If so, then the value of n we calculate along a line of sight will be unaffected by whatever the extinction happens to be.

3.8. O VI Mid-Plane Volume Density

The correlation between $N(\text{O VI})\sin|b|$ and the height z above the plane of the Galaxy has been determined before (Jenkins 1978b; Savage et al. 2003). However, the increased size of our sample of disk stars, and a well determined column density for the LB, makes it worthwhile revisiting the problem.

The O VI volume density as a function of z is usually defined such that $n = n_0 f(|z|)$. The column density for any individual sight line at a height $|z| = d \sin|b|$ above or below the Galactic plane is then

$$\begin{aligned} N(\text{O VI}) &= \int_0^d n(r) dr = \int_0^{|z_{\text{star}}|} n(|z|) \csc(|b|) d(|z|) \\ &= n_0 \csc(|b|) \int_0^{|z_{\text{star}}|} f(|z|) d(|z|), \end{aligned} \quad (5)$$

where r is the distance along a sight line. Conventionally, it has been assumed that the O VI volume density, n , falls off exponentially with height above the disk, so that $f(|z|) = e^{-|z|/h}$ which means that

$$n = n_0 e^{-|z|/h} \quad (6)$$

where h is the scale height of the O VI absorbing gas. Equations 5 and 6 then lead us to an expression for the column density projected on a line perpendicular to the Galactic plane,

$$N(\text{O VI}) \sin|b| = n_0 h (1 - e^{-|z|/h}) \quad (7)$$

Obviously, to measure n_0 and h , we can fit the function given in equation 7 to the data. The data we

include are those from our own *FUSE* survey, data from *Copernicus*, the WD sample of SL06, the halo stars observed by Z03, and the extragalactic sight lines measured by Savage et al. (2003) and Wakker et al. (2003). However, including the latter dataset forces us to consider an important problem uncovered by these authors, which we must discuss before we attempt to derive n_0 and h , namely the difference between sight lines in the northern and southern Galactic hemispheres. Further, we must also introduce the problem that, although the density of O VI does decrease in the way suggested by equation 7, the layer of O VI absorbing gas in the disk is not smoothly stratified, but instead is rather clumpy. We discuss these two problems below.

3.8.1. The North-South Divide

In their survey of extragalactic sight lines, Savage et al. (2003) reported an excess of 0.20–0.30 dex in the average value of $\log[N(\text{O VI})\sin b]$ for the north Galactic Polar region towards sight lines at $b > 45^\circ$ compared to lower latitude directions in the north and to the entire southern Galactic sky. To investigate the asymmetry in more detail, we examined whether the extragalactic O VI column densities measured at latitudes $b > 0$ — the ‘N’ or ‘North’ sample — were statistically different from those measured at $b < 0$ — the ‘S’ or ‘South’ sample. In all cases, column densities were reduced by a factor $\sin|b|$. We first considered the results from a Student’s t -test; for the N and S samples of $\log[N(\text{O VI})\sin b]$, we found a t -statistic of $t = 4.1$, and a probability that we might incorrectly reject the hypothesis that the means are equal of only $P = 1 \times 10^{-4}$. A K-S test yields $D = 0.42$, $P = 4 \times 10^{-4}$. Such results clearly bear out the assertion of Savage et al. that a significant difference between $N(\text{O VI})$ exists in the northern and southern Galactic hemispheres towards extragalactic sight lines.

As described in §3.1.4, we decided to use only the higher-quality data from Savage et al. (2003) and Wakker et al. (2003) ($Q > 2$) in our analysis. If we repeat these two tests for this sub-sample alone, the difference between the N & S samples is smaller, but still significant. Student’s t -test gives $t = 2.4$ and $P = 0.02$, while the K–S test gives $D = 0.39$ and $P = 0.05$.

Despite these variations, which occur in the Milky Way halo, we see no difference in our disk stars for similar N and S samples. For stars beyond 200 pc, there is no clear difference between the two samples

when measured by a t -test ($t = 0.5$, $P = 0.62$) or a K-S test ($D = 0.11$, $P = 0.62$). This conclusion holds whether or not a correction is made to the observed column densities for the Local Bubble.

For this reason, in fitting the theoretical relationship of $N(\text{O VI}) \sin |b|$ with $|z|$ given in equation 7 to the data, we use all our sight lines regardless of whether they lie in the northern or southern Galactic plane, except for the extragalactic sight lines: we derive n_0 and h twice, once each using the northern and southern extragalactic sight lines.

3.8.2. Clumpiness in the O VI Absorbing Gas and Errors Used for $N(\text{O VI}) \sin |b|$

To measure n_0 and h , we fitted the function given in equation 7 to the data by varying n_0 and h and minimizing the χ^2 statistic between the theoretical function and the data. The first obvious result we found was that although the data were clearly correlated in the way described by equation 7, the reduced χ^2_ν was much greater than the expected value of unity¹⁵.

At face value, we might say that large values of χ^2_ν arise either because the assumed errors in the data are inadequate or that the underlying model must be wrong. We discuss the second of these conclusions below. As far as the first conclusion is concerned, we have taken special care to derive realistic errors for the quantities measured. A similar problem was found by Savage et al. (1990) for the distribution of Al III in the Galactic plane. Their solution was to introduce an additional “error”, which takes into account the patchiness or clumpiness of the absorbing gas that is ignored by using equation 7. Although the density of O VI follows, primarily, an exponential decrease with height above the plane, the distribution is not smooth and planar, but is, at some level, clumpy. Adding an additional “error”, σ_{CL} , allows for deviations caused by this additional clumpiness when seeking an acceptable value of χ^2_ν . The σ_{CL} term is applied assuming that the quantity is independent of distance, an assumption which we demonstrate to be true in §3.9.

Given the introduction of σ_{CL} , we can combine the natural deviations attributed to this term with the experimental errors in determining $N(\text{O VI}) \sin |b|$. Ordinarily, this operation would be problematic because variations of the parameter of a fit would respond dif-

ferently to the two different kinds of errors. In our case, we are fortunate to have most of our measurements made at heights $|z| < h$. When this is true, the slope of the dependent variable x in the fitting function in relation to the data points y is fixed to unity. With this constraint, errors in x are equivalent to errors in y . For each data point, therefore, we describe a total error exclusively in terms of an error in just the y -direction equal to a value

$$\sigma_T^2 = \sigma_N^2 + \sigma_d^2 + \sigma_{\text{CL}}^2. \quad (8)$$

These individual errors are all relative errors: σ_N applies to the measurement error in the column density¹⁶, $\sigma[N(\text{O VI})]/N(\text{O VI})$; σ_d is the relative error in the distance, $\sigma(d)/d$; and σ_{CL} is the additional fractional error we derive by requiring χ^2_ν to be unity when minimizing the fit of $N(\text{O VI}) \sin |b|$ with $|z|$ to the data. The absolute error in each point is then simply

$$\sigma[N(\text{O VI}) \sin |b|] = N(\text{O VI}) \sin |b| \times \sigma_T. \quad (9)$$

It should be understood that σ_{CL} is introduced *not* simply to justify a model whose functional representation is wrong. In principle, we could propose some other trend of decreasing $N(\text{O VI})$ with distance from the Galactic plane, but we would still require the use of σ_{CL} to account for an intrinsic scatter in the observed O VI column densities that exceeds the measurement errors.

3.8.3. The Mid-Plane Density and Scale Height of O VI

A plot of $\log[N(\text{O VI}) \sin |b|]$ with $\log(|z|)$ is shown in the top panel of Figure 13, where we distinguish between $R = 0$ (black points) and $R > 0$ stars (gray points). In §3.7.2 we found evidence that the density of the ISM beyond a few hundred pc was better represented with the removal of a contribution from the LB. Hence, to derive n_0 and h , we used the $R = 0$ sample of stars, and subtracted a column density $N_{\text{LB}}(\text{O VI}) = 1.11 \times 10^{13} \text{ cm}^{-2}$ for the LB along each sight line. Accordingly, we also subtracted the LB radius — 100 pc — from all distances. Sight lines with only upper limits to $N(\text{O VI})$ have no σ_N errors, yet values are needed

¹⁵Here, we use the conventional definition of $\chi^2_\nu = \chi^2/\nu$, where ν is the number of data points used in the fit minus the number of variables used, in this case 2.

¹⁶As discussed in §2.8.1, the column density errors are asymmetric due to the different continuum errors. Here, for σ_N , we simply take the average of the two column density errors. As we will show, however, $\sigma_N \ll \sigma_d$, so the exact errors in the column densities have little effect on the derivation of n_0 and h .

for calculating χ^2 . For these points, we used the median σ_N (0.08 dex) for the sample with detected O VI.

The fit of $N(\text{O VI}) \sin |b|$ with $|z|$ must be made in log-log-space, for the following reasons. In a χ^2 fit, the errors in each point determine the weight that that point gives to the value of χ^2 . Unfortunately, the absolute error in the column density is proportional to $N(\text{O VI})^{17}$, and because (as we will show in § 3.9) $N(\text{O VI})$ is proportional to the distance to a star, the absolute error in the column density is also proportional to distance. Similarly, $\sigma(d)$ is more or less a fixed constant of $\approx 20-30\%$ of d (see Appendix B), so the absolute error in d also increases with d . The result is that the final absolute error is proportional to distance, so that more distant stars would have had lower weights in the χ^2 fit had we chosen the linear representation. If, instead, we fit $\log[N(\text{O VI}) \sin |b|]$ against $\log |z|$ (i.e., a fit in log-log-space), then the error is the same relative error as that given in equation 8, and is no longer proportional to the distance.

With the data divided into two samples containing separate northern and southern extragalactic sight lines (§3.8.1) we found the following:

$$\begin{aligned} \text{N: } n_0 &= 1.33 \times 10^{-8} \text{ cm}^{-3}, \\ &h = 4.6 \text{ kpc}, \sigma_{\text{CL}} = 0.25 \text{ dex} \\ \text{S: } n_0 &= 1.34 \times 10^{-8} \text{ cm}^{-3}, \\ &h = 3.2 \text{ kpc}, \sigma_{\text{CL}} = 0.28 \text{ dex} \end{aligned}$$

Unsurprisingly, the value of n_0 does not depend on whether the N or S samples are used, since n_0 depends primarily on the data below $|z| \simeq 1$ kpc. Conversely, the values of h do depend on which extragalactic sight lines are used. As described in §3.8.2, the values of σ_{CL} are set to give $\chi^2_{\nu} = 1$. We note that these values of $\log n_0 = -7.89$ are almost identical to the centers of the Gaussian fits made to the distribution of n values discussed in § 3.7.2 (column 5 of Table 9 for the $R = 0$, -LB sample).

The results from this fit are shown in the bottom panel of Figure 13 (where we only plot -LB, $R = 0$ data points). Note that we only show the original column density errors, and not the values of σ_T used for

minimizing χ^2 . In fact, the derived value of σ_{CL} dominates the errors, with $\sigma_N \ll \sigma_d < \sigma_{\text{CL}}$. For example, increasing the errors in the distances to the stars by as much as 1.5 times their assumed value has no effect on the values of n_0 and h ; it is the inherent clumpiness of the interstellar medium that dominates the dispersion in $N(\text{O VI}) \sin |b|$ seen in Figure 13.

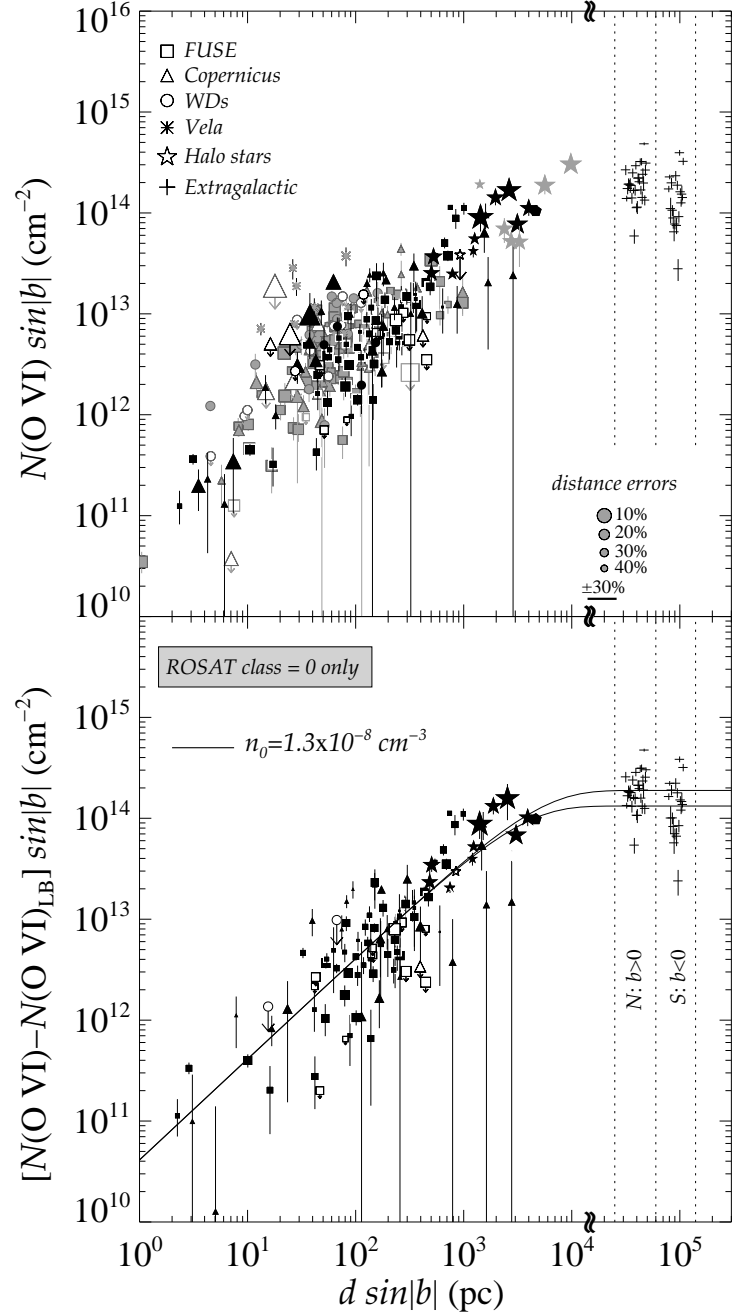
The new values of h given above differ from the single scale height calculated by Savage et al. (2003), $h = \langle \log[N(\text{O VI}) \sin |b|] \rangle / n_0 = 2.3$ kpc. Most of the difference in h for the southern hemisphere comes from the reduction in n_0 , for which Savage et al. used a preliminary value of $1.7 \times 10^{-8} \text{ cm}^{-3}$ (e.g. Jenkins 2002), a value which included all sight lines through the Galactic disk (including those toward Vela and Carina as well as the $R > 0$ sight lines) and for which no correction was made for the LB.

Savage et al. noted that $N(\text{O VI}) \sin |b|$ towards extragalactic objects was enhanced by ~ 0.25 dex in the high latitude directions $45^\circ < b < 90^\circ$ compared to lower latitudes in the north and compared to all southern hemisphere directions. Rather than reporting two scale heights as we have, they instead described the distribution of O VI in the halo with a single scale height combined with a high latitude northern hemisphere 0.25 dex enhancement. (Savage et al. considered a number of possible explanations for the origin of the enhancement.) With the smaller mid-plane density found in this paper, the single scale height used in Savage et al.'s model would increase from 2.3 to 2.9 kpc.

What are the likely errors in these values of n_0 and h ? It is straightforward to calculate χ^2 for values of n_0 and h away from those that gave the minimum χ^2 . Figure 14 shows contours of χ^2 for different values of n_0 and h , with each contour level drawn at a particular limiting value of $\chi^2 = \chi_L^2$. The value of χ_L^2 is calculated as $\chi_L^2 = \chi_{\text{min}}^2 + \chi_p^2(\alpha)$ (Lampton et al. 1976). Here, $\chi_p^2(\alpha)$ is the value of χ^2 which would be exceeded a fraction α of the time in a set of random trials, where the degrees of freedom is set to the number of free parameters p that we allow to vary (2 in our case). Given some contour χ_L^2 set by adopting a significance α , we would expect the true value of n_0 and h to lie within the χ_L^2 contour in a $1 - \alpha$ fraction of similar O VI surveys. In Figure 14 we adopt values of χ_L^2 for confidence levels $1 - \alpha$ of 0.38, 0.68, 0.95 and 0.997, which were chosen because they resemble the conventional interpretation of the 0.5, 1, 2 and 3 σ confidence levels that apply to a normal distribution. It should be understood,

¹⁷This is because strong lines are wider at the continuum, and have higher continuum errors. Since $\sigma(N)$ in the *FUSE* data is dominated by continuum errors, $\sigma(N)$ and N are roughly correlated, even though there is no correlation between distance and the quality of the data.

Figure 13: **Top:** Plot of O VI column density reduced by the sine of the Galactic latitude b , against the height of a star above (or below) the plane of the Milky Way, $|z| = d \sin|b|$. Point shapes, explained by the key in the top left corner, refer to datasets obtained by various authors, and include the measurements made in this paper (“FUSE”), those obtained by *Copernicus* (Jenkins 1978a), local WDs discussed by Savage & Lehner (2006), sight lines towards the Vela SNR (Slavin et al. 2004; Jenkins et al. 1976), those towards halo stars (Zsargó et al. 2003), and the extragalactic sight lines observed by Wakker et al. (2003) and Savage et al. (2003). Points colored black refer to stars which have *ROSAT* class $R = 0$, while gray points have $R > 0$ (see §3.4 and §3.5). The extragalactic sight lines are shown as crosses at an arbitrarily large distance; they have no *ROSAT* classification, and are separated into sight lines above (Northern, or ‘N’ sight lines, left group of crosses) and below (Southern, or ‘S’ sight lines, right group of crosses) the Galactic plane. Their distances are slightly offset from each other so that the errors in the column densities can be seen. Two-sigma upper limits are shown by downward-pointing arrows attached to open symbols. (The type of symbol again indicates which dataset the limits are taken from.) The size of a point indicates the relative uncertainty in the distance to the star: a key at the lower right indicates how the size is related to the uncertainty (large points represent smaller uncertainties so that they are more influential in guiding the eye). An absolute error of $\pm 30\%$ in any distance is shown below this key. **Bottom:** The same plot, only with a contribution from the Local Bubble subtracted from every sight line [$N_{\text{LB}}(\text{O VI}) = 1.11 \times 10^{13} \text{ cm}^{-2}$], and a distance of 100 pc removed from every sight line. Only $R = 0$ stars are plotted. The solid line shows the best fit to the data assuming that the O VI volume density n varies as $n = n_0 e^{(-|z|/h)}$ where n_0 is the mid-plane density and h is the scale height. Although the value of n_0 remains unchanged (because all stellar sight lines were used in fitting n to the data), the value of h is different depending on whether N or S extragalactic sight lines are used. The two curves show the fit for $h = 4.6 \text{ kpc}$ (N) and $h = 3.2 \text{ kpc}$ (S).



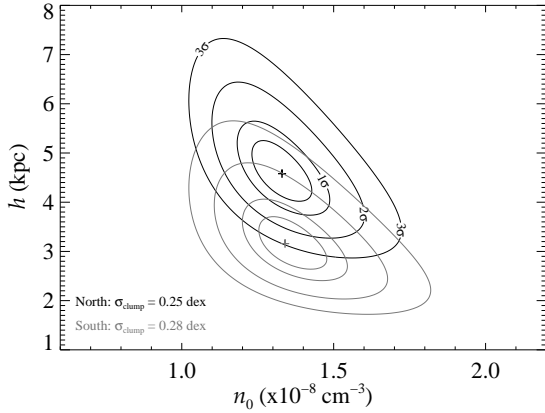


Figure 14: Contour plots of χ^2 about the minimum found for fitting $\log[N(\text{O VI})\sin|b|]$ against $\log|z|$. Contour levels are drawn at levels of χ^2 which correspond to a significance of $\alpha = 0.62, 0.32, 0.046$ and 0.0027 , or confidence levels $1 - \alpha = 0.38, 0.68, 0.95$ and 0.997 . Although the distribution function of χ^2 is not described by a normal distribution, we use the analogy to describe the contours as 0.5, 1, 2 and 3 sigma confidence levels.

of course, that the distribution function for χ^2 with a small number of free parameters is *not* normally distributed.

The values of σ_{CL} given above seem to suggest that the clumpiness of the O VI absorbing gas may be slightly different between the northern and southern hemispheres. Are these differences real? The problem for estimating the errors in σ_{CL} are somewhat different than deriving the confidence levels for n_0 and h discussed above. σ_{CL} is not a variable in the function used to measure χ^2 , so does not enter into the minimization of χ^2 . Changing σ_{CL} changes the numerical value of χ^2 when the minimum is found, but the values of n_0 and h do not change¹⁸. However, we can ask how much we can vary σ_{CL} before we get ‘unreasonable’ values of χ^2_{min} . Given the number of degrees of freedom (number of data points - 2) for our data, we know how χ^2_{min} *should* be distributed. We can therefore select the two values of χ^2 within which the χ^2_{min} outcomes are expected by chance 68% of the time (i.e.,

¹⁸This is not entirely true of course. With, for example, σ_{CL} set to zero, the values of σ_T — and hence the weights for the χ^2 fit — are different for each point, which leads to small differences in the minimum value of n_0 and h . These differences are very small, however.

a $\pm 1\sigma$ probability interval), and then consider the limiting values of σ_{CL} that make our evaluations of χ^2_{min} conform to these two χ^2 limits.

For the values of n_0 and h given above, we find that for values of χ^2 within $\pm 1\sigma$ of the expected value, we obtain $\sigma_{\text{CL}} = 0.25(+0.02, -0.03)$ dex for the northern sample, and $\sigma_{\text{CL}} = 0.28(+0.02, -0.03)$ dex for the southern sample. Since the two values of σ_{CL} are within $\pm 1\sigma$ of each other for the N and S sight lines, it seems that there is no significant difference in σ_{CL} in the northern or southern hemispheres. If we simply average these two values then, we have $\sigma_{\text{CL}} \simeq 0.26 \pm 0.02$ dex.

We conclude this section by noting that in the simulations of de Avillez & Breitschwerdt (2005b) this mid-plane density has a somewhat different meaning than the single value which equation 6 implies exists at $|z| = 0$. In their models, hot gas is generated by SN explosions throughout the plane of the Galaxy, and O VI arises in clumps, vortices and filaments which arise from the mixing of hot (interior) and cold (exterior) gas associated with the SNRs. Inside these clumps, the O VI volume density can vary by as much as 6 dex, although typical clouds have densities of $\log n \sim -9$ to -6 . Although there is, therefore, no ‘single value’ of $n(\text{O VI})$ in the disk of the Milky Way in these models, the regions are sufficiently small ($\sim 100 - 200$ pc) that over long path lengths, there is, obviously, an average value of n . de Avillez & Breitschwerdt (2005b) find that the average is constant over time, and has a value of $1.8 \times 10^{-8} \text{ cm}^{-3}$ (during a time period of 100 to 400 Myr and assuming solar metallicities). This number is surprisingly close to the values we list in Table 9 for $d < 2$ kpc stars when we make no distinction in *ROSAT* class and subtract no contribution from the LB, as is appropriate for comparison with the simulations.

3.9. Distribution of O VI Column Density with Effective Distance

Following Jenkins (1978b) we calculate a *reduced* distance to a star to take into account the decline in n with $|z|$ discussed above:

$$d_e = h(1 - e^{-|z|/h}) \csc|b| \quad (10)$$

In fact, these distances are nearly identical to the regular distances d for the stars studied herein—except for halo stars, whose long path lengths and high distances

above and below the plane of the Galaxy require correcting for the change in n with $|z|$.

The top panel of Figure 15 shows the correlation of $N(\text{O VI})$ and d_e , along with the expected value $N(\text{O VI}) = n_0 d_e$ using the value of n_0 found above in §3.8.3. We would expect this line to pass through the majority of the $R = 0$ points, and this is the case for distances beyond a few hundred pc. Below these distances, however, there is a clear departure from the linear relationship. This apparent discrepancy can be removed by plotting the column density for each point reduced by the LB contribution. This is shown in the bottom panel of Figure 15. The excess of points above the $n_0 d_e$ line below a few hundred pc now disappear below the y -axis limit shown in the figure.

The fact that $N(\text{O VI})$ and d_e are correlated has some important consequences. First, it means that the O VI absorbing gas is interstellar, and cannot be primarily circumstellar in origin. Second, if the O VI lines arise in discrete structures, and not in a uniform smooth plane of gas (see below), then the lines must be composed of many individual components which are so close in velocity to each other that they blend together to form a ‘single’ line with no apparent velocity structure. Third, because the correlation arises using sight lines in all four quadrants of the Milky Way (Fig. 6), then the physical structures of the ISM which give rise to O VI absorption must be ubiquitous over all the Galaxy.

Figure 16 shows how $n(\text{O VI})$ (with a contribution from the LB removed) for stars at distances $d > 1$ kpc varies with Galactic longitude. Ignoring sightlines towards the Vela SNR and the Carina Nebular, we find little difference in n in whichever direction we look, with one exception: of the 23 *FUSE* sight lines in the region $l = 80^\circ - 140^\circ$ and with $d > 1$ kpc, ten have only upper limits to $N(\text{O VI})$. This direction corresponds to the outer Perseus Arm (see Fig. 6). One could argue that there exists a genuine deficiency of O VI in the anti-center direction. However, more than half the sight lines have $n(\text{O VI})$ commensurate with the rest of the Galactic disk. We discuss below whether the scatter in n with Galactic longitude is significant.

Figure 15 shows that the dispersion of column densities around the best-fit line at a given distance is large. This in itself suggests that the O VI absorbing ISM is far from being a smoothly distributed intercloud medium — otherwise the points would more closely follow a $N(\text{O VI}) = n_0 d_e$ relationship. The figure also indicates that absorption does not simply arise

from randomly distributed uniform clouds. If absorption arose in an ensemble of generic clouds, each with a fixed column density N_0 , then the total column density measured by intercepting p clouds would be $p N_0$. For a random distribution of clouds the dispersion in the total column density should go as $\pm \sqrt{p} N_0$, and the fractional error in $N(\text{O VI})$ would fall as $1/\sqrt{p}$. Hence the dispersion in the observed column densities should decrease at larger distances, which is clearly not observed.

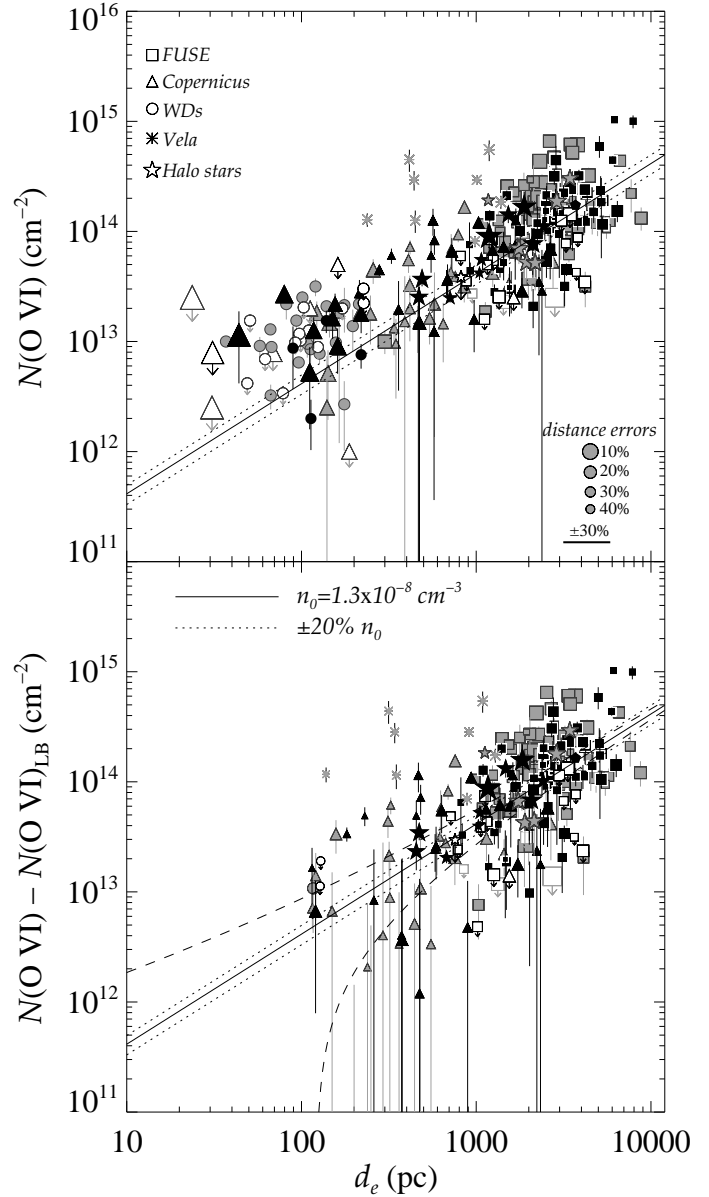
To demonstrate this, we plot dashed lines in the bottom panel of Figure 15 to show how the error in $N(\text{O VI})$ would decrease with distance, assuming $N_0 = 5 \times 10^{12} \text{ cm}^{-2}$, which is typically the smallest column density detected towards WDs. [Smaller values of N_0 produce no dispersion in $N(\text{O VI})$ at any distances, while larger values exceed the smallest column densities measured.] This suggests that the O VI absorbing regions have deviations over a wide range of N_0 (or scale sizes) compared to fluctuations caused by randomly situated clouds with a single value of N_0 .

It follows that the largest of these clouds have a low space density, so that they do not appreciably increase the overall average density n_0 , but instead reveal themselves by creating large relative deviations in $N(\text{O VI})$ for long sight lines. This is done in a manner that compensates for the expected $1/\sqrt{p}$ decrease. Alternatively, the maintenance of a constant level of relative deviations in average space density at large distances could arise from a large-scale clustering of small clouds.

Another way to measure the variation of clumpiness with distance is to repeat our fit of $N(\text{O VI}) \sin |b|$ against $|z|$ for sets of stars at different distances, and examine how the values of σ_{CL} change. We can, once again, divide our stars into two sets, those at distances between 0.2–2 kpc and those beyond 2 kpc; we assume that there is no difference between sight lines in the northern and southern Galactic hemispheres, and that we can therefore use all our stellar sight lines. If we use column densities with a contribution from the LB removed, and all *ROSAT* classes, we find that at distances $d > 2$ kpc, $\sigma_{\text{CL}} = 0.28(+0.03, -0.02)$ dex, while for $0.2 < d < 2$ kpc, $\sigma_{\text{CL}} = 0.29(+0.04, -0.03)$ dex. These results imply that σ_{CL} is indeed independent of distance.

Could these similarities simply arise from the fact that the volumes sampled by the more distant stars have greater separations than those toward the nearby targets? That is, could large-scale regional differences

Figure 15: **Top:** Plot of O VI column density against the *effective distance* d_e to a star, given by $d_e = h [1 - e^{-(d \sin |b|/h)}] \csc |b|$, where h is the scale height, b is the Galactic latitude, and $d \sin |b| = |z|$ is the height above (or below) the plane of the Milky Way. The values of h used are the same as those shown in Fig. 13, but since most of the stars are in the plane of the Galaxy, d_e and d are virtually indistinguishable, except for the halo stars. The size, shape and shading of the symbols used to plot the data are the same as those given in Fig. 13. The solid line shows the predicted value of the O VI column density if $N(\text{O VI}) = n_0 d_e$, using the value of n_0 shown in the bottom plot. (Note, this value of n_0 is the value derived for $R = 0$ sight lines, which in this plot are shown by black points. Hence the fit should pass through the body of these data.) A difference of $\pm 20\%$ in n_0 is shown by dotted lines. **Bottom:** The same plot, but with a contribution from the Local Bubble subtracted from every sight line [$N_{\text{LB}}(\text{O VI}) = 1.11 \times 10^{13} \text{ cm}^{-2}$]. The two dashed lines demonstrate how the dispersion in $n(\text{O VI})$ should change if $N(\text{O VI})$ simply increases by intercepting more clouds of a fixed column density (in this case $5 \times 10^{12} \text{ cm}^{-2}$; see §3.9).



in the Galaxy, which are not evident in the short sight lines, create variations that almost exactly compensate for the expected decrease in the dispersion in $\log n$ for a random distribution of uniform clouds? We can gain an insight on the possible importance of this effect by performing an analysis of variance (e.g. Wolf 1974). We divide all 56 cases for $R = 0$ and $d > 2$ kpc into

$k = 7$ Galactic longitude bins¹⁹ having indices i , with $m = 8$ samples (with indices j) per bin. We performed a Kruskal-Wallis H -test to see if the deviations of the results from one bin to the next are significant, and we found that they are to a 96% level of confidence

¹⁹The bin boundaries were set to the following longitudes (in degrees): 28, 73, 104, 210, 244, 292, and 314. The widths of the bins differ because of our requirement to have an equal number of samples in each bin. As before, we exclude sight lines to Carina and Vela.

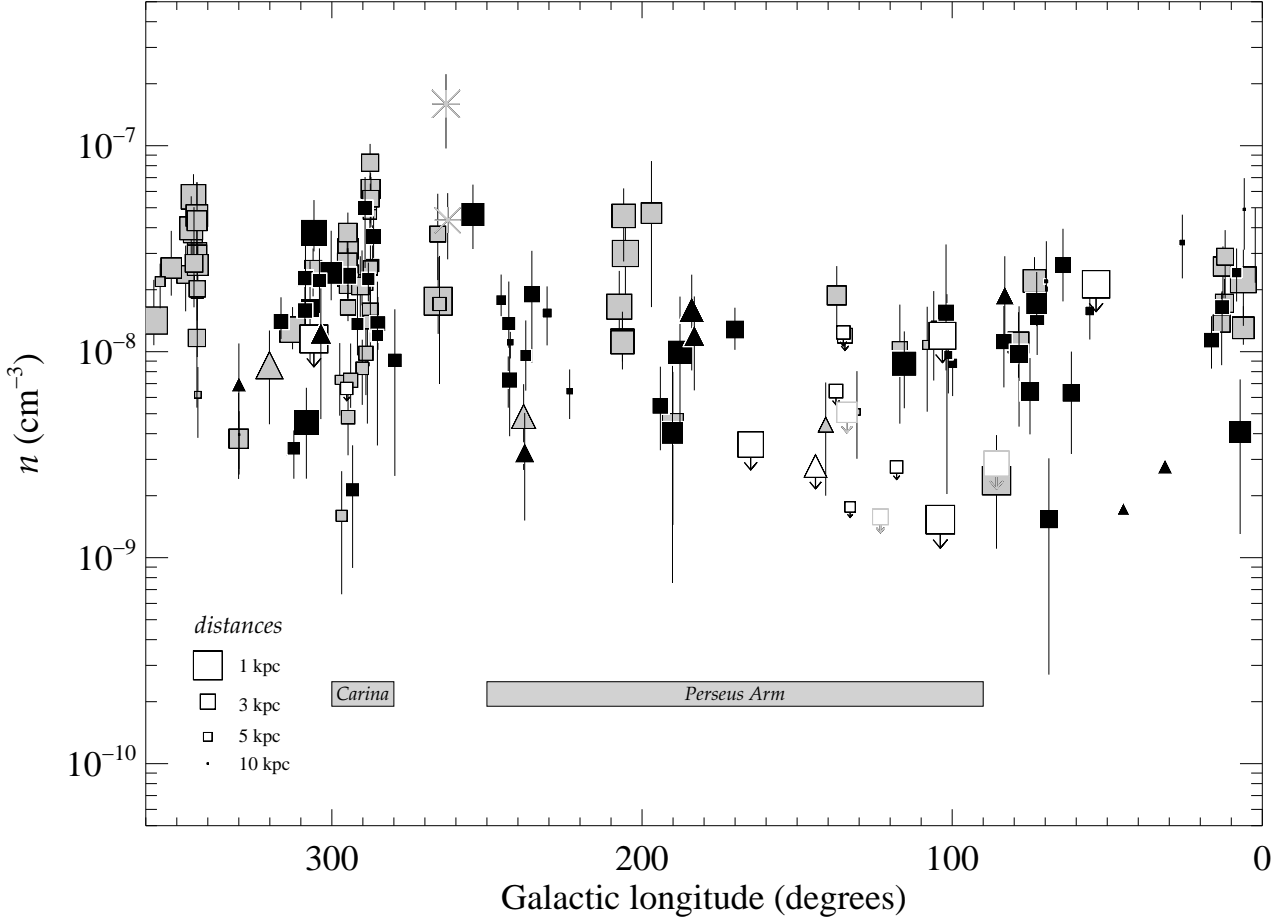


Figure 16: Average O VI volume density $n [= N(\text{O VI})/d]$ along sight lines as a function of Galactic longitude. Only stars more distant than 1 kpc are included. Sight lines toward the Vela SNR are indicated by star symbols. More distant stars are shown with smaller symbols, as indicated in the legend. Squares represent stars observed as part of our *FUSE* survey, while triangles represent stars observed with *Copernicus* (J78). Squares are colored black for $R = 0$ sight lines and gray for $R > 0$ sightlines. Upper limits to n are shown by open symbols with downward pointing arrows; again, symbols representing upper limits towards stars with $R = 0$ have black outlines, while those representing upper limits towards stars with $R > 0$ have gray outlines. The extent of the Perseus Arm in the outer Galaxy is indicated (see Fig. 6).

($H = 13.3$). Given that these deviations are probably real, we now must understand quantitatively what fraction of the overall sum of the squares of the deviations from the mean value of $\log n$

$$S_0 = \sum_{i=1}^k \sum_{j=1}^m (\log n_{i,j} - \langle \log n \rangle_{\text{tot}})^2 \quad (11)$$

arises from deviations from one longitude group to the

next,

$$S_1 = m \sum_{i=1}^k (\langle \log n \rangle_i - \langle \log n \rangle_{\text{tot}})^2 \quad (12)$$

as opposed to the cumulative effect of deviations within each group,

$$S_2 = \sum_{i=1}^k \sum_{j=1}^m (\log n_{i,j} - \langle \log n \rangle_i)^2 \quad (13)$$

where $\langle \log n \rangle_{\text{tot}}$ is the overall average $\log n$ and $\langle \log n \rangle_i$ is the average $\log n$ within each group i . It can be shown that, in general, $S_0 = S_1 + S_2$. For the samples defined above, we found the values,

$$S_0 = 5.22, S_1 = 1.30, \text{ and } S_2 = 3.92 \quad (14)$$

which shows us that only 25% of the variance of the entire sample arises from deviations from one longitude set to the next. We conclude that σ_{CL} is invariant with distance and that for the most part this effect arises from the basic texture of the volumes that hold O VI absorbing gas, while a smaller contribution arises from large scale regional variations in the Galactic plane.

Finally, we note that if the contribution from the LB is not removed, the values of σ_{CL} change slightly, but there is still no difference between nearby stars and the stars further away: $\sigma_{\text{CL}} = 0.25(+0.03, -0.02)$ dex for $d > 2$ kpc, and $\sigma_{\text{CL}} = 0.24(+0.03, -0.02)$ dex for $0.2 < d < 2$ kpc.

3.10. Variation of O VI volume density with Milky Way Spiral Arms

On the premise that most of the O VI is generated by blast waves from supernovae, we might expect to find evidence in our data that the number density of such events and the character of their development could be strongly influenced by whether their surrounding volumes are located within spiral arms or interarm regions. In order to explore this issue, we attempted to detect an arm vs. interarm contrast in the averages for the O VI volume density n . We defined spiral arms in terms of their electron densities n_e sensed by pulsar dispersion measures, which ultimately were assembled into the model created by Cordes & Lazio (2002) shown in Figure 6. Our test was a simple one: we attempted to find a correlation between sight-line values of $\langle n \rangle$ and $\langle n_e \rangle$, where the latter was expressed in terms of the model's dispersion measure along the sight line divided by its length. We performed this comparison for all stars that had a *ROSAT* class $R = 0$ and distance $d > 0.2$ kpc, again excluding Vela and Carina stars. The Pearson correlation coefficient between $\log \langle n \rangle$ and $\log \langle n_e \rangle$ was 0.08 for 98 sight lines, which means that no significant correlation could be found. (We recognize that errors in distance can induce a spurious correlation, but this is not an issue here since we are not claiming to see a correlation.) In short, we see no clear evidence that variations

in sight-line values of $\langle n \rangle$ are strongly influenced by the presence or lack of spiral arms.

3.11. Variation of O VI Velocity with Galactic Longitude

Another question to consider in our quest to understand how O VI is distributed in the Galaxy is to ask whether the velocities of the O VI absorption follow that predicted from differential Galactic rotation.

To construct the LSR velocities v that we would see along any particular line of sight, assuming the absorbing gas co-rotated with the Milky Way disk, we use the Galactic rotation curve obtained by Clemens (1985), with $R_0 = 8.5$ kpc and $\Theta = 220$ km s⁻¹. Since v is a function of the distance, we can calculate a minimum and maximum velocity where we might expect absorption. In Figure 17 we plot bars that show the allowed LSR velocities as a function of Galactic longitude for each target. The variation of permitted velocities with distance is not linear — velocities often approach a constant value for a given distance, for example, and can sometimes backtrack at large distances to the same velocities predicted at smaller distances. To show this, each bar has a gray-scale in which darker gray colors mark velocities where the velocity of the gas is changing only very slowly with distance, i.e., darkness $\propto 1/(dv/dr)$. [Note, each bar has grayscale coding scaled relative to the individual sight line, so a particular gray value for one sight line does not represent the same $1/(dv/dr)$ along another sight line.] Bars identical to these are also shown in the bottom panels of Figure 24, although the velocities shown there are heliocentric values.

On top of each of the predicted-velocity bars, we plot the velocity and width of the O VI absorption components measured towards a star either as a square, if the wavelength scale of the data was corrected using available STIS data, or a triangle, if the adopted +10 km s⁻¹ shift was applied (see §2.4 and Appendix A). If no shift was thought to be appropriate, we plot a circle. We also plot the velocity of the H₂ 6–0 R(4) line as a cross. Regardless what kind of velocity correction was made, the location of the H₂ velocity with respect to that of the O VI was always correct, since the two were adjusted in the same manner. All O VI and H₂ components are shown, and sight lines with no detectable O VI are still included (although obviously no O VI positions are marked).

The figure shows that there is a considerable lack of

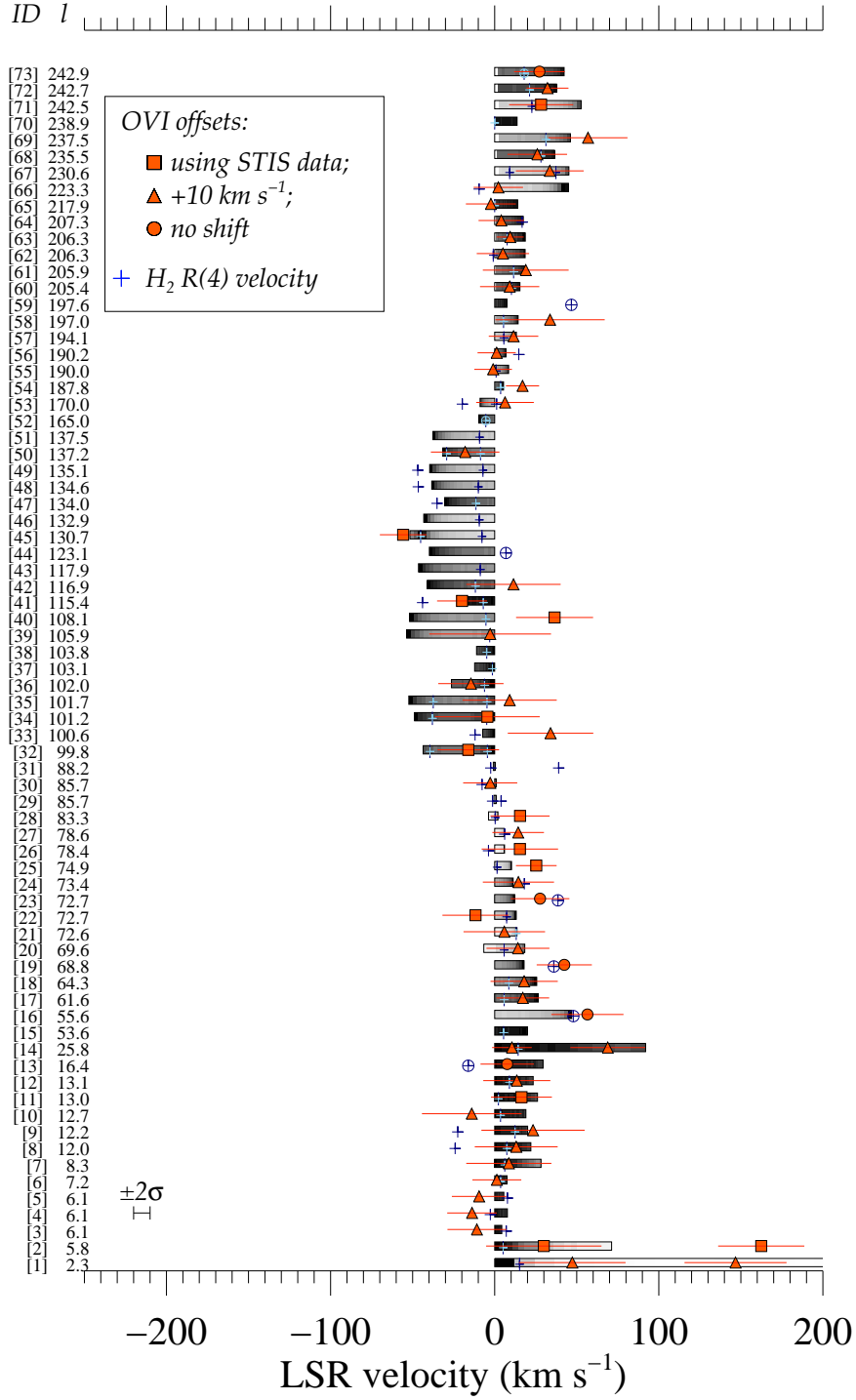


Figure 17: In this figure, permitted velocities for gas rotating in the plane of the Galactic disk are shown as gray bars, sorted by Galactic longitude. The measured velocities of O VI absorption lines are overplotted with red triangles, squares, or circles (depending on how the offsets for the *FUSE* wavelength zero-point were calibrated — see legend box); R(4) H₂ absorption lines are overplotted as blue crosses. (Blue crosses in circles indicate H₂ measured in spectra which had no shifts applied.) The IDs assigned to the stars (see Table 2) are given to the left of the Galactic longitude of each star, in square parentheses. To show the width of the O VI absorption, a red line extends a distance of $\pm b_i/2$ from the centroid velocity of each absorption component (where b_i is the Doppler parameter of component i).

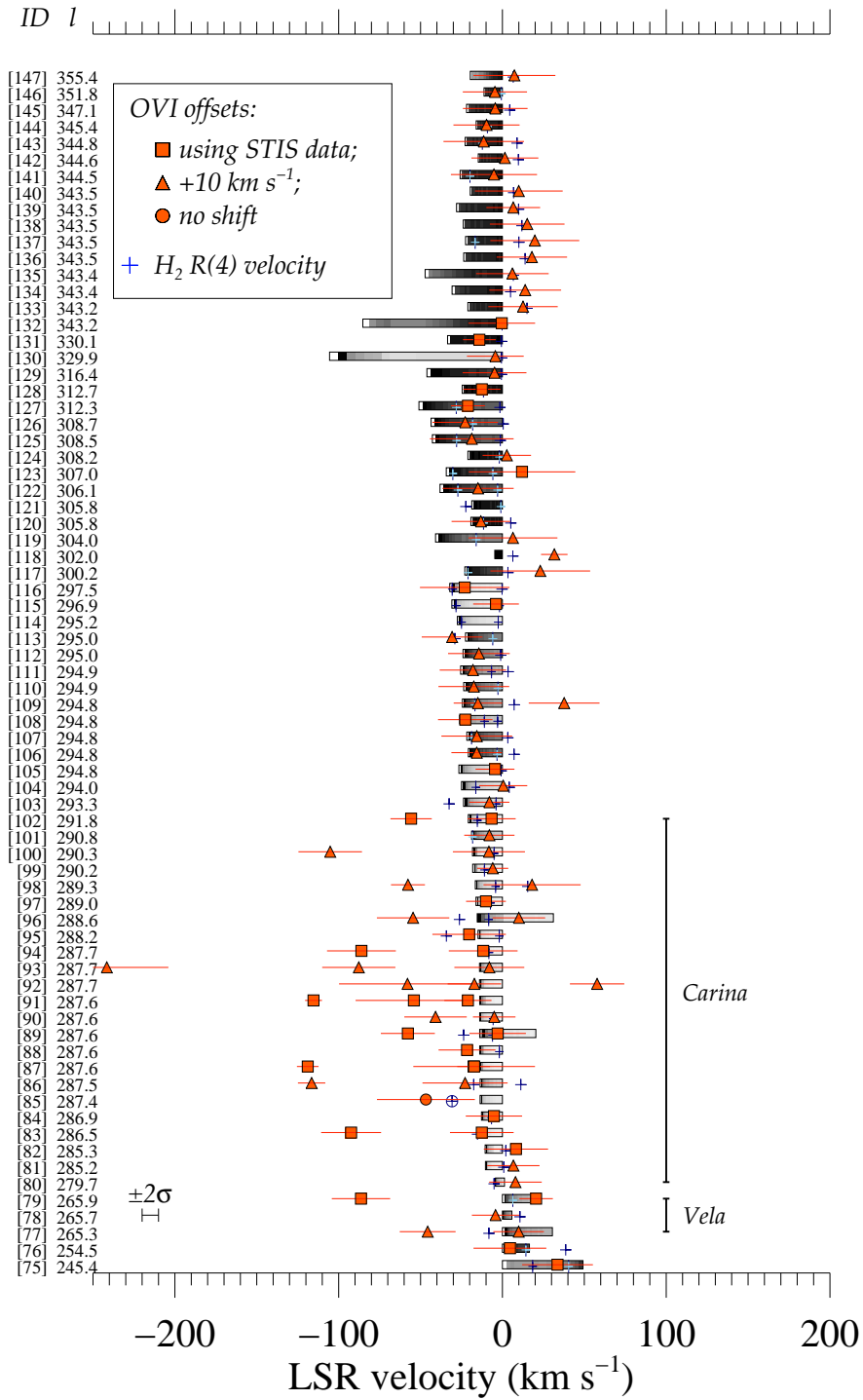


Figure 17: continued.

correlation between the velocities of O VI components and those predicted from differential Galactic rotation, even if one ignores regions where the gas is violently disturbed (i.e., Vela and Carina). The H₂ lines often agree better with that predicted from rotation, but they

too can be found outside the permitted range. At some longitudes (e.g. $l \sim 343^\circ$), there appears to be some coherence where all the O VI is at the same velocity. In most cases, however, this is simply because the stars are all at nearly the same longitude. For the 147 indi-

vidual O VI components plotted in Figure 17, 52 % have centroids outside the predicted range.

Of course, the O VI absorption velocities only show the centroid of the absorption (values listed in Table 4, but converted to LSR velocities) and its width. As can be seen in Figure 24, there is often some overlap between velocities allowed by Galactic rotation, and some part of an O VI profile. Again, of the 147 individual O VI components plotted in Figure 17, only 16% have Doppler widths which do not extend into the region predicted for differential Galactic rotation. If the O VI line is comprised of many components, then some O VI absorbing regions will be correlated with the general kinematics of the ISM. However, Figure 17 shows that *the bulk* of the O VI knows little about the rotation of the Galactic disk, or that a mechanism exists to generate large peculiar motions in clouds that do follow Galactic rotation.

3.12. Comparison of Low and High Ion Velocity Extremes

Figure 17 shows that the velocities of the O VI centroids often fall outside the kinematic limits defined by differential Galactic rotation. Also, a direct comparison of H₂ and O VI velocities show that the two correspond to each poorly. This implies that the bulk of the O VI absorption does not mimic the behavior of the cool neutral interstellar medium of the Milky Way which makes up the Galactic disk.

Measuring the centroids of the O VI absorption and comparing them with either the range of velocities predicted from differential Galactic rotation or the velocities of other interstellar features tells only part of the story, however. If one considers *the outer edges* of the O VI absorption line profiles and compares them to these velocities (see the bottom panels of Fig 24) the differences are even larger.

To see how the extremes of the O VI lines compare to the extremes of other lower ionization species, we have investigated the absorption line profiles of four other species: C III $\lambda 977$, O I $\lambda 1039$, Si III $\lambda 1206$ and C II $\lambda 1335$ lines. All these transitions have large f -values and produce extremely strong absorption lines with sharp edges. These features are so strongly saturated that we can expect even relatively low column density gas that is well removed from the core velocities to yield detectable absorption components. The first two of these four lines are recorded in our *FUSE* data, while the second two arise at longer wavelengths

and were taken from the STIS data for the stars listed in Table 10. Since STIS data were not available for all the stars in our *FUSE* sample, the number of Si III and C II lines studied is smaller than the number of C III and O I lines.

The C III $\lambda 977$ line lies in one of the SiC channels, and for our analysis we usually used the SiC2A channel. To ensure that the wavelength calibration of the SiC channel matched that of the LiF channel, we compared the H₂ line nearest in velocity to the C III line [the 11–0 P(3) line at 978.217 Å] with the 6–0 P(3) line next to the OVI absorption at 1031.192 Å. Matching these lines in velocity provided the correct *relative* wavelength scales. No relative correction was made for the O I $\lambda 1039$ since the line lies in the same channel as the O VI line, and we assumed that the wavelength scale was sufficiently accurate at both wavelengths. The *absolute* wavelength of the C III, O I, and O VI lines finally rested on how well the LiF channel zero-point was corrected using available STIS data or assuming a 10 km s⁻¹ shift (§2.4). The Si III $\lambda 1206$ and C II $\lambda 1335$ lines in the STIS data were assumed to have negligible wavelength scale errors.

To calculate the velocity extremes of all these species, v_e , we first converted normalized absorption line profiles to AOD $N(v)$ column density profiles. For O VI, we used the $N(v)$ profiles for which the H₂ lines had been removed (§2.8.2). We then fitted a high-order polynomial to the wings of each $N(v)$ profile and measured the velocity extreme *at a given* $N(v)$. The values of $N(v)$ used for the O VI, O I, C II, C III and Si III lines were: 2×10^{11} , 5×10^{12} , 1×10^{12} , 4×10^{11} , and 1×10^{11} cm⁻² (km s⁻¹)⁻¹, respectively. (We comment on these values below.) In the few cases where individual absorption components could be seen resolved from the main body of the absorption, we used the outer edge of that component if it had $N(v)$ values that crossed the adopted $N(v)$ limits.

The results are shown in Figure 18. The error bars arise from re-measuring v_e for profiles normalized by upper and lower continua error envelopes (see §2.6). The figure shows that there is a good correlation between the velocity extremes of all the species selected and those of the O VI absorption. In each panel, we show the Pearson correlation coefficients for the positive and negative edges considered separately. The figure demonstrates that there is some form of coupling between the hot medium and the warm or cool phases. This correlation was seen earlier by Cowie et al. (1979) from the *Copernicus* O VI survey, and was thought to

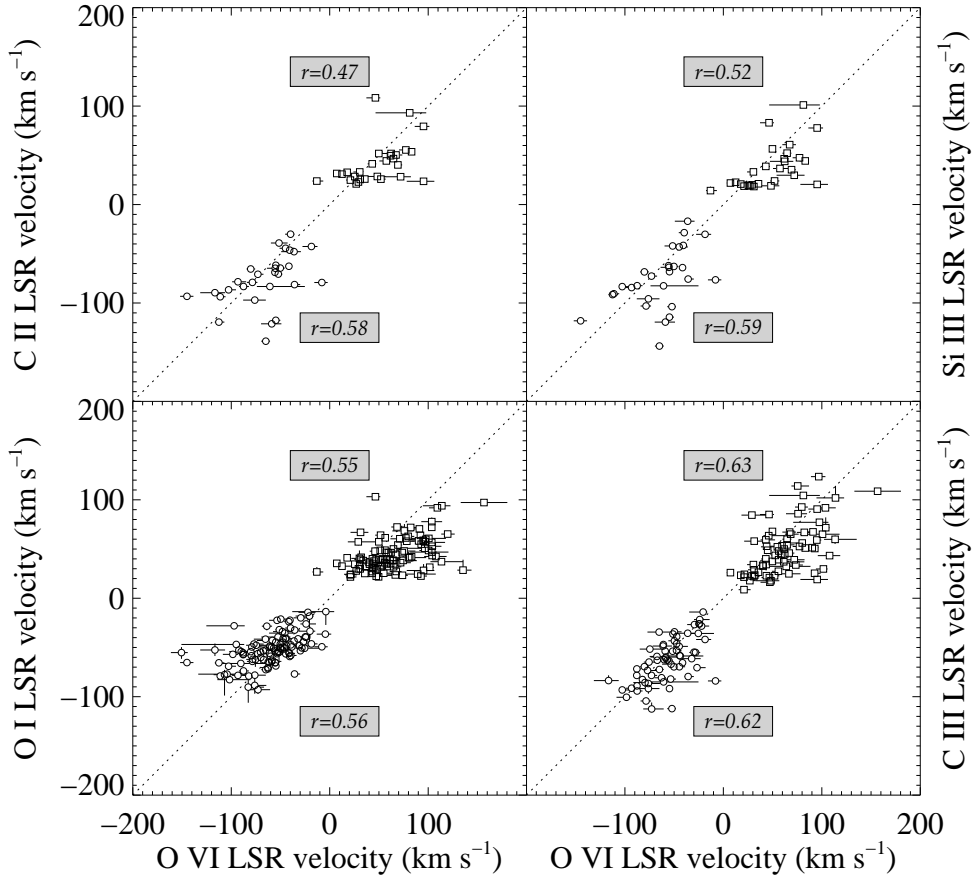


Figure 18: Velocity extremes for the profiles of the C II $\lambda 1335$, Si III $\lambda 1206$, C III $\lambda 977$ and O I $\lambda 1039$ lines plotted against the velocity extremes of the O VI $\lambda 1032$ lines. Circles represent negative edges, while squares represent positive edges of the absorption lines. For the positive and negative edges, the Pearson correlation coefficient r is shown at the top and bottom of each panel, respectively. The dotted line represents the line of equality for the velocities of any two ions.

arise from conduction/evaporation interfaces between the two phases. The interface origin for some of the O VI absorption has been confirmed over short paths through the local ISM by Savage & Lehner (2006).

This behavior is not unprecedented. Very strong lines from low-ionization species exhibit extraordinary dispersions of their velocity extremes, a phenomenon studied in detail by Cowie & York (1978a,b). One may imagine that very small fractions of the low-ionization material are stirred up by the same dynamical processes that produce the O VI absorbing material, such as the influences from supernova blast waves or mass-

loss flows from stars, as we have discussed previously. In this case, we would expect little correlation between the velocity of gas in these structures and the bulk motion of the cool ISM, as we discussed above in §3.11.

We note, however, that Figure 18 should be interpreted with some degree of caution. The exact value of v_e depends on the value of $N(v)$ at which v_e is evaluated, which in turn can be influenced by the resolution of the data. The Si III and C II lines in the STIS data have very sharp edges because of the high resolution at which they were measured. In these cases, the exact value of $N(v)$ adopted is less important, since the line

edges are well defined. For the O I and C III lines measured at lower resolution in the *FUSE* data, the edges are smeared by the instrumental LSF. Inspection of the profiles used in this study show that these effects are likely to be small; the values of $N(\nu)$ we adopted to measure ν_e were set so as to ensure that the majority of lines would have reliable measurements of ν_e as close to $N(\nu) = 0$ as possible, given the typical S/N of the *FUSE* and STIS data.

3.13. Minimum O VI Line Widths

The fraction of oxygen in the form of O VI peaks for collisionally ionized gas at temperatures of $\log T_{\max} = 5.45$ if the gas is in collisional ionization equilibrium, at which point 20% of the oxygen is in the form of O⁺⁵ ions. This temperature corresponds to a Doppler width of $b = 0.0321\sqrt{T} = 16.6 \text{ km s}^{-1}$. What is the minimum reliable Doppler parameter in our sample? There are several sight lines for which we have measured $b \lesssim 16 \text{ km s}^{-1}$. For these, however, either the O VI line is weak, and the removal of strong HD 6–0 R(0) absorption has made the line profile uncertain (HD 110432), or the line is actually a separate component blended with other stronger components (HD 093205, HDE 303308). The sight lines with the narrowest, reliable values of b are towards HD 046202, with $b = 16.4^{+4.3}_{-3.7} \text{ km s}^{-1}$ and HD 093250 with $b = 16.7 \pm 1.6 \text{ km s}^{-1}$. These are consistent with the smallest values of b found towards WDs (see, e.g. Fig. 10 of SL06). There are many more profiles with $b \geq 20 \text{ km s}^{-1}$, a number which provides a reliable lower limit for b . Thus, our smallest value of b is consistent with detecting single thermally broadened, collisionally ionized clouds. We cannot be sure however, that our narrowest absorption lines actually arise from single clouds, since their column densities (0.65 and $0.83 \times 10^{14} \text{ cm}^{-2}$) are much greater than the weak lines seen towards local WDs and nearby *Copernicus* stars. These sight lines may intercept several clouds whose relative motions along the line of sight are at a minimum. Alternatively, if sight lines intercept clouds of very different sizes (§3.9) the narrowest lines we detect may indeed represent absorption from single large clouds with moderate column densities.

3.14. Distribution of O VI Column Density with Doppler Parameter, and with Distance

A Gaussian profile well fits the distribution of Doppler parameters b found for the *FUSE* dataset.

The profile is centered at $\langle b \rangle = 37 \text{ km s}^{-1}$ and has a standard deviation of 11 km s^{-1} . However, the Doppler parameters are not entirely independent quantities. A correlation between $N(\text{O VI})$ and b was first discussed by Heckman et al. (2002), who studied the trend using extragalactic sight lines and data from early investigations of O VI in our Galaxy. Although our survey does not include O VI absorption systems from clouds outside of the Local Group of galaxies, our increased sample size of Galactic systems permits a closer examination of the correlation. Figure 19 shows that the correlation exists in the datasets adopted in this paper. To understand better the origin of the trend, we have again indicated which sight lines have *ROSAT* categories $R = 0$ or $R > 0$, and which have distances $d < 1 \text{ kpc}$ or $d > 1 \text{ kpc}$. The figure shows that there is no dependency on R ; it also shows that most low- $N(\text{O VI})$, low- b points are towards nearby stars.

We suggest that the N vs. b correlation has a simple interpretation: we recall from our findings on the lack of change in σ_{CL} with distance (§3.9) that stars that are further away intercept not only more O VI absorbing structures, but probably also larger, more sparsely distributed ones with higher values of O VI column densities. On theoretical grounds, it is plausible to imagine that these larger clouds have large internal motions because they have recently evolved from explosive events. The more numerous low- $N(\text{O VI})$ systems may represent pieces of much older regions that have been partitioned by incursions of the ambient, cooler medium, but have not yet had a chance to cool appreciably below the temperatures representative of O VI. These smaller regions may have had their internal velocities moderated because they have had a chance to couple dynamically to the surrounding quiescent gas phases. Alternatively, we can imagine that what we interpret to be large $N(\text{O VI})$ systems are actually clusters of small clouds, which have cloud-to-cloud velocity dispersions that are larger than that of the material inside individual clouds.

4. SUMMARY

1. We have used *FUSE* to observe early-type (mainly O2–B3) stars in the Galactic disk in order to characterize O VI $\lambda 1032$ absorption lines arising from interstellar gas in the plane of the Milky Way. A total of 120 stars was observed as part of *FUSE* PI team programs P102 and P122, of which nine were eventually rejected

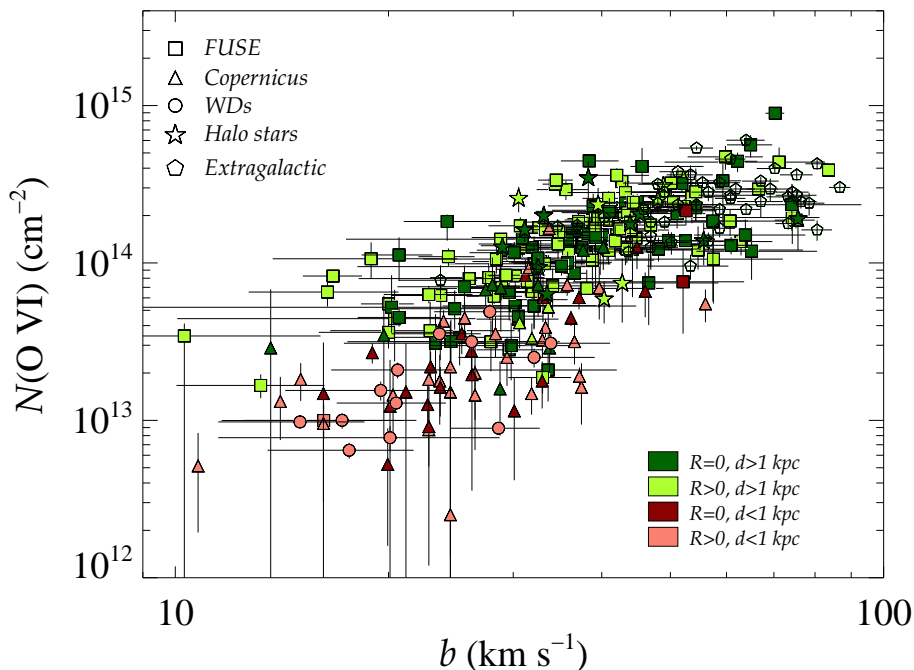


Figure 19: Doppler parameter b against O VI column density $N(\text{O VI})$. Reliable measurements exist for $b \geq 16 \text{ km s}^{-1}$; profiles of lines with b less than this are either weak and suffer from HD contamination, or are one of multiple component systems, and are strongly blended with other components. Errors in b are not available for the *Copernicus* or Zsargó et al. (2003) datasets. Extragalactic objects have no distance or *ROSAT* assignments, so are not colored.

from our survey; the remaining 111 stars constitute a total investment of 754 ksec of *FUSE* time. We supplemented these sight lines with archival data available April 2003 or earlier; our final sample consists of 148 stars, most of which are at Galactic latitudes $|b| < 10^\circ$ and distances of $> 1 \text{ kpc}$.

2. In order to derive accurate spectroscopic distances to the stars, we have used several modern databases to improve upon published distances (Appendix B). *Hipparcos* and *Tycho* catalogs have provided precise optical magnitudes, as well as identification of multiple systems and variable stars. 2MASS infrared magnitudes have enabled us to estimate the interstellar V -band extinction along a sight line, and the absolute magnitudes of stars — given a spectral type and luminosity class — have been constructed by collating available surveys from the literature. Despite these improvements, imprecise knowl-

edge of stellar types and classes continues to have the greatest uncertainty in deriving a spectroscopic distance, limiting the precision in a distance measurement to $\sim 10\text{--}30\%$.

3. Where appropriate, we have added the O VI measurements from several other O VI studies to our sample, in order to probe distances not covered by our *FUSE* stars. These include nearby ($\sim 20\text{--}100 \text{ pc}$) white dwarf stars (WDs) (Savage & Lehner 2006), intermediate distance ($\sim 100\text{--}1000 \text{ pc}$) stars observed by the *Copernicus* satellite (Jenkins 1978a), distant halo stars (Zsargó et al. 2003), and extragalactic sight lines (Savage et al. 2003; Wakker et al. 2003). For many of the stars (but not including the WDs), we have rederived distances using the same set of tools used to derive distances towards the *FUSE* sample of stars.
4. *ROSAT* X-ray maps show that many stars lie to-

wards regions of enhanced X-ray emission. This emission likely arises from hot bubbles blown out from the star or its stellar association. Other sight lines, however, are found at positions with very little X-ray emission, which we label as $R = 0$ sight lines. In contrast, lines of sight intercepting X-ray emitting regions have designations of $R > 0$ (§3.4 and §3.5). The average volume density towards stars in the Galactic disk, $n = N(\text{O VI})/d$, depends on whether we use $R = 0$ or $R > 0$ sight lines, and whether we subtract a contribution to the O VI column density from the Local Bubble (LB; §3.7.1). When we subtract a value of $N_{\text{LB}}(\text{O VI}) = 1.11 \times 10^{13} \text{ cm}^{-2}$ arising from the LB, we find little difference in n between stars with distances $0.2 < d < 2.0$ kpc and those with $d > 2$ kpc (§3.7.2); we also find that for stars $d > 2$ kpc, the $R > 0$ sight lines have slightly higher densities than $R = 0$ sight lines, even after excluding stars in the direction of the Vela SNR and Carina Nebula, which have the highest densities in our sample (§3.7.3). This is probably because the circumstellar environment of the star contributes a small excess to the O VI column density.

5. Our data well fit the relationship $N(\text{O VI})\sin|b| = n_0 h(1 - \exp^{-|z|/h})$, which naturally arises from assuming that the density n of O VI absorbing gas falls with height $|z|$ above the Galactic plane as $n = n_0 \exp^{-|z|/h}$. Here, n_0 is the mid-plane density and h is the characteristic scale height. We find $n_0 = 1.3 \times 10^{-8} \text{ cm}^{-3}$ [after subtracting a contribution to $N(\text{O VI})$ from the LB and using the $R = 0$ sight lines; §3.8.3], but that h depends on whether we use extragalactic lines of sight in the northern (N) or southern (S) Galactic hemispheres (as first noted by Savage et al. 2003, —see §3.8.1). We derive values of $h = [4.6, 3.2]$ kpc when using the [N,S] sample. We also find it necessary to include a clumpiness factor σ_{CL} to represent the fact that the dispersion in $\log[N(\text{O VI})\sin|b|]$ around the theoretical fit is much larger than can be accounted for by experimental errors alone (§3.8.2). Our best estimate is that $\sigma_{\text{CL}} \simeq 0.26 \pm 0.02$ dex.
6. $N(\text{O VI})$ and the distance to a star are correlated (§3.9). This shows that the processes which give rise to O VI absorption are ubiquitous over the entire Galactic disk, and certainly do not arise

primarily from circumstellar environments. The only inhomogeneity of the O VI volume density n can be found in a concentration of $N(\text{O VI})$ upper limits (10 out of 23 sight lines) towards $d > 1$ kpc *FUSE* sight lines in the region $l = 80^\circ - 140^\circ$, the outer Perseus arm of the Galaxy. There is no evidence that the volume density of O VI is influenced by the presence of Galactic spiral arms along the stellar sight lines.

7. Although O VI is distributed smoothly enough for $N(\text{O VI})$ to correlate with distance, the relative *dispersion* on either side of this correlation does not decrease with distance, as would be expected if more distant sight lines intercepted more clouds. Quantitatively, we find no difference in the dispersion (σ_{CL}) between nearby (0.2–2 kpc) and distant (> 2 kpc) stars. This indicates that in addition to a random placement of small clouds, there may also be sparsely distributed large clouds. Or, alternatively, some of the small clouds may simply be clustered over very large scales.
8. The velocity edges of the O VI lines and those of the strong transitions of C III $\lambda 977.02$, O I $\lambda 1039.23$, Si III $\lambda 1206$ and C II $\lambda 1335$, are all correlated. This suggests that, at least to first order, the processes that move the hot gas to high velocity also affect the velocities of other species (§3.12).
9. The smallest reliable O VI Doppler parameter we find in our sample is $b \simeq 16 - 17 \text{ km s}^{-1}$, which is consistent with that expected for a thermally broadened cloud at a temperature close to the peak in the ionization fraction curves, $\log T_{\text{max}} \simeq 5.45$ (§3.13). We also confirm earlier research which found that b and $N(\text{O VI})$ are correlated. We show, however, that the width of O VI lines cannot be accounted for by differential Galactic rotation; the lines are far wider than expected if absorption came from a smoothly distributed ISM corotating with the disk of the Milky Way (§3.14). The correlation suggests that the large clouds mentioned in Point 7 above have large internal motions, or, alternatively, that the small clouds within clusters are moving more rapidly than the gases within individual clouds.

This work is based on data obtained for the Guaranteed Time Team by the NASA-CNES-CSA FUSE mission operated by Johns Hopkins University. Financial support has been provided by NASA contract NAS5-32985. We have made extensive use of the SIMBAD database, operated at CDS, Strasbourg, France, and the VizieR catalog service (Ochsenbein et al. 2000), from which the *Hipparcos* catalogs (ESA 1997a) were downloaded. The *Two Micron All Sky Survey* (2MASS), is a joint project of the University of Massachusetts and the Infrared Processing and Analysis Center/California Institute of Technology, funded by the NASA and the NSF. Archive data were obtained from the *Multimission Archive at the Space Telescope Science Institute* (MAST). The Space Telescope Science Institute is operated by the Association of Universities for Research in Astronomy, Inc., under NASA contract NAS5-26555. Support for MAST for non-*HST* data is provided by the NASA Office of Space Science via grant NAG5-7584 and by other grants and contracts. *ROSAT* data came from the *ROSAT* Data Archive of the Max-Planck-Institut für extraterrestrische Physik (MPE) at Garching, Germany. The data used for this survey can be found on-line at www.astro.princeton.edu/~dvb/o6.

REFERENCES

- Abbott, D. C. 1982, *ApJ*, 263, 723
- Arnal, E. M., Cappa, C. E., Rizzo, J. R., & Cichowski, S. 1999, *AJ*, 118, 1798
- Aschenbach, B. 1998, *Nature*, 396, 141
- Aschenbach, B., Iyudin, A. F., & Schönfelder, V. 1999, *A&A*, 350, 997
- Bagnuolo, Jr., W. G., Gies, D. R., Hahula, M. E., Wiemker, R., & Wiggs, M. S. 1994, *ApJ*, 423, 446
- Banerjee, D. P. K., Rawat, S. D., & Janardhan, P. 2000, *A&AS*, 147, 229
- Barker, P. K. 1983, *PASP*, 95, 996
- Baume, G., Vázquez, R. A., & Feinstein, A. 1999, *A&AS*, 137, 233
- Begelman, M. C. & Fabian, A. C. 1990, *MNRAS*, 244, 26P
- Begelman, M. C. & McKee, C. F. 1990, *ApJ*, 358, 375
- Bellazzini, M., Ferraro, F. R., Sollima, A., Pancino, E., & Origlia, L. 2004, *A&A*, 424, 199
- Berghoefter, T. W. & Schmitt, J. H. M. M. 1994, *A&A*, 290, 435
- Berghoefter, T. W., Schmitt, J. H. M. M., & Cassinelli, J. P. 1996, *A&AS*, 118, 481
- Berghoefter, T. W., Schmitt, J. H. M. M., Danner, R., & Cassinelli, J. P. 1997, *A&A*, 322, 167
- Bertoldi, F. & McKee, C. F. 1990, *ApJ*, 354, 529
- Bloch, J. J., Jahoda, K., Juda, M., McCammon, D., Sanders, W. T., & Snowden, S. L. 1986, *ApJ*, 308, L59
- Bocchino, F., Maggio, A., & Sciortino, S. 1999, *A&A*, 342, 839
- Bochkarev, N. G. & Sitnik, T. G. 1985, *Ap&SS*, 108, 237
- Borkowski, K. J., Balbus, S. A., & Fristrom, C. C. 1990, *ApJ*, 355, 501
- Bowen, D. V., Blades, J. C., & Pettini, M. 1995, *ApJ*, 448, 634
- Bowyer, C. S., Field, G. B., & Mack, J. F. 1968, *Nature*, 217, 32
- Bregman, J. N. 2007, *ARA&A*, 45, 0, (astro-ph/0706.1787)
- Breitschwerdt, D. & Schmutzler, T. 1994, *Nature*, 371, 774
- Briot, D. & Robichon, N. 2000, in ASP Conf. Ser. 214: IAU Colloq. 175: The Be Phenomenon in Early-Type Stars, ed. M. A. Smith, H. F. Henrichs, & J. Fabregat, 117
- Briot, D., Robichon, N., & Hubert, A. M. 1997, in ESA SP-402: Hipparcos Venice Symposium '97, Vol. 402, 319-322
- Brown, A. G. A., Arenou, F., van Leeuwen, F., Lindgren, L., & Luri, X. 1997, in ESA SP-402: Hipparcos Venice Symposium '97, 63-68
- Bunner, A. N., Coleman, P. L., Kraushaar, W. L., & McCammon, D. 1971, *ApJ*, 167, L3
- Caraveo, P. A., De Luca, A., Mignani, R. P., & Biggiani, G. F. 2001, *ApJ*, 561, 930

- Cash, W., Charles, P., Bowyer, S., Walter, F., Garmire, G., & Riegler, G. 1980, *ApJ*, 238, L71
- Cassinelli, J. P., Cohen, D. H., MacFarlane, J. J., Sanders, W. T., & Welsh, B. Y. 1994, *ApJ*, 421, 705
- Castor, J., McCray, R., & Weaver, R. 1975, *ApJ*, 200, L107
- Cen, R. & Ostriker, J. P. 1999, *ApJ*, 514, 1
- Cha, A. N., Sembach, K. R., & Danks, A. C. 1999, *ApJ*, 515, L25
- Chauville, J., Zorec, J., Ballereau, D., Morrell, N., Cidale, L., & Garcia, A. 2001, *A&A*, 378, 861
- Chevalier, R. A. 1974, *ApJ*, 188, 501
- Clemens, D. P. 1985, *ApJ*, 295, 422
- Codina, S. J., de Freitas Pacheco, J. A., Lopes, D. F., & Gilra, D. 1984, *A&AS*, 57, 239
- Collins, J. A., Shull, J. M., & Giroux, M. L. 2005, *ApJ*, 623, 196
- Conti, P. S. & Vacca, W. D. 1990, *AJ*, 100, 431
- Cordes, J. M. 2004, in *Astronomical Society of the Pacific Conference Series*, Vol. 317, *Milky Way Surveys: The Structure and Evolution of our Galaxy*, ed. D. Clemens, R. Shah, & T. Brainerd, 211
- Cordes, J. M. & Lazio, T. J. W. 2002, *ArXiv Astrophysics e-prints*, astro-ph/0207156
- Cote, J. & van Kerkwijk, M. H. 1993, *A&A*, 274, 870
- Cowie, L. L., Jenkins, E. B., Songaila, A., & York, D. G. 1979, *ApJ*, 232, 467
- Cowie, L. L. & McKee, C. F. 1977, *ApJ*, 211, 135
- Cowie, L. L., McKee, C. F., & Ostriker, J. P. 1981a, *ApJ*, 247, 908
- Cowie, L. L., Taylor, W., & York, D. G. 1981b, *ApJ*, 248, 528
- Cowie, L. L. & York, D. G. 1978a, *ApJ*, 220, 129
- . 1978b, *ApJ*, 223, 876
- Cox, D. P. 1979, *ApJ*, 234, 863
- . 1981, *ApJ*, 245, 534
- Cox, D. P. & Reynolds, R. J. 1987, *ARA&A*, 25, 303
- Cox, D. P. & Smith, B. W. 1974, *ApJ*, 189, L105
- Cramer, N. 1997, in *ESA SP-402: Hipparcos Venice Symposium '97*, Vol. 402, 311–314
- Crampton, D., Bernard, D., Harris, B. L., & Thackeray, A. D. 1976, *MNRAS*, 176, 683
- Cravens, T. E. 2000, *ApJ*, 532, L153
- Cravens, T. E., Robertson, I. P., & Snowden, S. L. 2001, *J. Geophys. Res.*, 24883
- Danforth, C. W. & Shull, J. M. 2005, *ApJ*, 624, 555
- Davidson, A., Shulman, S., Fritz, G., Meekins, J. F., Henry, R. C., & Friedman, H. 1972, *ApJ*, 177, 629
- Davidson, A. F. 1993, *Science*, 259, 327
- de Avillez, M. A. 2000, *MNRAS*, 315, 479
- de Avillez, M. A. & Breitschwerdt, D. 2004, *A&A*, 425, 899
- . 2005a, *A&A*, 436, 585
- . 2005b, *ApJ*, 634, L65
- de Boer, K. S. & Savage, B. D. 1980, *ApJ*, 238, 86
- de Zeeuw, P. T., Hoogerwerf, R., de Bruijne, J. H. J., Brown, A. G. A., & Blaauw, A. 1999, *AJ*, 117, 354
- Diplas, A. & Savage, B. D. 1994, *ApJS*, 93, 211
- Dixon, W. V., et al 2007, *PASP*, 119, 527
- Dixon, W. V. D., Davidson, A. F., & Ferguson, H. C. 1996, *ApJ*, 465, 288
- Dixon, W. V. D., Sankrit, R., & Otte, B. 2006, *ApJ*, 647, 328
- Doazan, V., Franco, M., Sedmak, G., Stalio, R., & Rusconi, L. 1983, *A&A*, 128, 171
- Dodson, R., Legge, D., Reynolds, J. E., & McCulloch, P. M. 2003, *ApJ*, 596, 1137
- Dupree, A. K. & Raymond, J. C. 1983, *ApJ*, 275, L71
- Edgar, R. J. & Chevalier, R. A. 1986, *ApJ*, 310, L27
- Edgar, R. J. & Cox, D. P. 1993, *ApJ*, 413, 190
- Edgar, R. J. & Savage, B. D. 1992, *ApJ*, 396, 124

- ESA. 1997a, The Hipparcos and Tycho Catalogues, Tech. Rep. ESA SP-1200, European Space Agency
- . 1997b, The Hipparcos and Tycho Catalogues; Section 1.3: Photometric Data, Magnitudes, & Variability, Tech. Rep. ESA SP-1200, European Space Agency
- . 1997c, The Hipparcos and Tycho Catalogues; Section 2.2; Contents of the Tycho Catalogue, Tech. Rep. ESA SP-1200, European Space Agency
- . 1997d, The Hipparcos and Tycho Catalogues; Section 2.3: Double and Multiple Systems Annex (DMSA), Tech. Rep. ESA SP-1200, European Space Agency
- . 1997e, The Hipparcos and Tycho Catalogues; Section 2.4: Variability Annex, Tech. Rep. ESA SP-1200, European Space Agency
- Feigelson, E. D. & Nelson, P. I. 1985, ApJ, 293, 192
- Feinstein, A. 1995, in Revista Mexicana de Astronomia y Astrofisica Conference Series, ed. V. Niemela, N. Morrell, & A. Feinstein, Vol. 2, 57
- Feldman, P. D., Sahnou, D. J., Kruk, J. W., Murphy, E. M., & Moos, H. W. 2001, J. Geophys. Res., 106, 8119
- Ferguson, H. C., Dixon, W. V. D., Davidsen, A. F., & Dettmar, R. 1995, ApJ, 454, L23
- Ferrière, K. M. 1995, ApJ, 441, 281
- Field, G. B., Goldsmith, D. W., & Habing, H. J. 1969, ApJ, 155, L149
- Fitzgerald, M. P. 1968, AJ, 73, 983
- Fitzpatrick, E. L. & Savage, B. D. 1985, ApJ, 292, 122
- Fox, A. J., Savage, B. D., Sembach, K. R., Fabian, D., Richter, P., Meyer, D. M., Lauroesch, J., & Howk, J. C. 2003, ApJ, 582, 793
- Fox, A. J., Savage, B. D., & Wakker, B. P. 2005, AJ, 130, 2418
- Fox, A. J., Savage, B. D., Wakker, B. P., Richter, P., Sembach, K. R., & Tripp, T. M. 2004, ApJ, 602, 738
- Galazutdinov, G. A. & Krelowski, J. 2006, ApJ, 637, 342
- García, B. & Mermilliod, J. C. 2001, A&A, 368, 122
- Garmany, C. D. & Conti, P. S. 1984, ApJ, 284, 705
- Garmany, C. D., Olson, G. L., van Steenberg, M. E., & Conti, P. S. 1981, ApJ, 250, 660
- Garmany, C. D. & Stencel, R. E. 1992, A&AS, 94, 211
- Garrison, R. F. 1994, in ASP Conf. Ser. 60: The MK Process at 50 Years: A Powerful Tool for Astrophysical Insight, ed. C. J. Corbally, R. O. Gray, & R. F. Garrison, 3
- Garrison, R. F. & Beattie, B. 1996, Observer's Handbook, ed. R. Bishop (<http://www.astro.utoronto.ca/~garrison/oh.html>: The Royal Astronomical Society of Canada.)
- Garrison, R. F., Hiltner, W. A., & Schild, R. E. 1977, ApJS, 35, 111
- Garrison, R. F., Schild, R. E., & Hiltner, W. A. 1983, ApJS, 52, 1
- Gies, D. R., et al 1993, AJ, 106, 2072
- Graney, C. M. & Sarazin, C. L. 1990, ApJ, 364, 561
- Gratton, R. G., Bragaglia, A., Carretta, E., Clementini, G., Desidera, S., Grundahl, F., & Lucatello, S. 2003, A&A, 408, 529
- Green, D. A. 2001, A Catalogue of Galactic Supernova Remnants, Tech. rep., (Cambridge: Mullard Radio Astron. Obs.)
- Guetter, H. H. & Turner, D. G. 1997, AJ, 113, 2116
- Hanuschik, R. W., Hummel, W., Sutorius, E., Dietle, O., & Thimm, G. 1996, A&AS, 116, 309
- Harmanec, P. 1998, A&A, 335, 173
- Harmanec, P., et al 2002, A&A, 387, 580
- Harvin, J. A., Gies, D. R., Bagnuolo, Jr., W. G., Penny, L. R., & Thaller, M. L. 2002, ApJ, 565, 1216
- Heckman, T. M., Norman, C. A., Strickland, D. K., & Sembach, K. R. 2002, ApJ, 577, 691
- Heiles, C. 1979, ApJ, 229, 533
- . 1980, ApJ, 235, 833
- . 1984, ApJS, 55, 585

- . 1990, *ApJ*, 354, 483
- . 1998, *ApJ*, 498, 689
- Hillier, D. J., Kudritzki, R. P., Pauldrach, A. W., Baade, D., Cassinelli, J. P., Puls, J., & Schmitt, J. H. M. M. 1993, *A&A*, 276, 117
- Hiltner, W. A., Garrison, R. F., & Schild, R. E. 1969, *ApJ*, 157, 313
- Hiltner, W. A., Morgan, W. W., & Neff, J. S. 1965, *ApJ*, 141, 183
- Høg, E., et al 2000, *A&A*, 355, L27
- Hoopes, C. G., Sembach, K. R., Howk, J. C., Savage, B. D., & Fullerton, A. W. 2002, *ApJ*, 569, 233
- Houk, N. & Cowley, A. P. 1975, Michigan Catalogue of two-dimensional spectral types for the HD star (Ann Arbor: University of Michigan, Department of Astronomy, 1975)
- Howarth, I. D. & Prinja, R. K. 1989, *ApJS*, 69, 527
- Howk, J. C., Savage, B. D., Sembach, K. R., & Hoopes, C. G. 2002a, *ApJ*, 572, 264
- Howk, J. C., Sembach, K. R., Savage, B. D., Massa, D., Friedman, S. D., & Fullerton, A. W. 2002b, *ApJ*, 569, 214
- Huang, J., Songaila, A., Cowie, L. L., & Jenkins, E. B. 1995, *ApJ*, 450, 163
- Humphreys, R. M. 1978, *ApJS*, 38, 309
- Humphreys, R. M. & McElroy, D. B. 1984, *ApJ*, 284, 565
- Hurwitz, M. & Bowyer, S. 1996, *ApJ*, 465, 296
- Hurwitz, M., et al 1998, *ApJ*, 500, L1
- Hurwitz, M., Bowyer, S., Kudritzki, R.-P., & Lennon, D. J. 1995, *ApJ*, 450, 149
- Irvine, N. J. 1990, *PASP*, 102, 669
- Isobe, T. 1992, ASURV: A Software Package for Statistical Analysis of Astronomical Data Containing Nondetection, Tech. Rep. Rev 1.2, Dept. of Astronomy & Astrophysics, Penn State Univ.
- Isobe, T., Feigelson, E. D., & Nelson, P. I. 1986, *ApJ*, 306, 490
- Iyudin, A. F., et al 1998, *Nature*, 396, 142
- Jenkins, E. B. 1978a, *ApJ*, 219, 845 (J78)
- . 1978b, *ApJ*, 220, 107
- . 1978c, *Comments on Astrophysics*, 7, 121
- . 1986, *ApJ*, 304, 739
- . 1987, *Exploring the Universe with the IUE Satellite*, ed. K. Y. (Dordrecht, D. Reidel), 531–548
- . 1996, *ApJ*, 471, 292
- Jenkins, E. B. 2002, in *Astronomical Society of the Pacific Conference Series*, Vol. 253, *Chemical Enrichment of Intracluster and Intergalactic Medium*, ed. R. Fusco-Femiano & F. Matteucci, 365–+
- Jenkins, E. B., Bowen, D. V., Tripp, T. M., Sembach, K. R., Leighly, K. M., Halpern, J. P., & Lauroesch, J. T. 2003, *AJ*, 125, 2824
- Jenkins, E. B. & Meloy, D. A. 1974, *ApJ*, 193, L121
- Jenkins, E. B., Silk, J., & Wallerstein, G. 1976, *ApJS*, 32, 681
- Jenkins, E. B., Sofia, U. J., & Sonneborn, G. 1998, in *The Hot Universe*, *IAU Symposium* 188, 271
- Jenkins, E. B. & Tripp, T. M. 2001, *ApJS*, 137, 297
- Kato, T. 1976, *ApJS*, 30, 397
- Keenan, F. P., Brown, P. J. F., & Lennon, D. J. 1986, *A&A*, 155, 333
- Keenan, F. P., Shaw, C. R., Bates, B., Dufton, P. L., & Kemp, S. N. 1995, *MNRAS*, 272, 599
- Kharchenko, V. & Dalgarno, A. 2000, *J. Geophys. Res.*, 1854
- Kharchenko, V., Rigazio, M., Dalgarno, A., & Krasnopolsky, V. A. 2003, *ApJ*, 585, L73
- Kim Quijano, J. 2004, *STIS Instrument Handbook*, 7th edn., Space Telescope Science Institute
- Koubský, P., et al 2000, *A&A*, 356, 913
- Krasnopolsky, V. A., Christian, D. J., Kharchenko, V., Dalgarno, A., Wolk, S. J., Lisse, C. M., & Stern, S. A. 2002, *Icarus*, 160, 437
- Lallement, R. 2004, *A&A*, 422, 391

- Lamers, H. J. G. L. M. 1981, *ApJ*, 245, 593
- Lampton, M., Margon, B., & Bowyer, S. 1976, *ApJ*, 208, 177
- Lehner, N., Fullerton, A. W., Massa, D., Sembach, K. R., & Zsargó, J. 2003, *ApJ*, 589, 526
- Lehner, N., Fullerton, A. W., Sembach, K. R., Massa, D. L., & Jenkins, E. B. 2001, *ApJ*, 556, L103
- Lesh, J. R. 1979, in *IAU Colloq. 47: Spectral Classification of the Future*, p81
- Levine, E. S., Blitz, L., & Heiles, C. 2006, *Science*, 312, 1773
- Lipunova, N. A. & Putilina, E. V. 1985, *Informational Bulletin on Variable Stars*, 2766, 1
- Little, J. E., Dufton, P. L., Keenan, F. P., Hambly, N. C., Conlon, E. S., Brown, P. J. F., & Miller, L. 1995, *ApJ*, 447, 783
- Magee, H. R. M., Dufton, P. L., Keenan, F. P., Rolleston, W. R. J., Kilkenny, D., O'Donoghue, D., Koen, C., & Stobie, R. S. 2001, *MNRAS*, 324, 747
- Marshall, H. L. 1992, in *Statistical Challenges in Modern Astronomy*, ed. E. D. Feigelson & G. J. Babu (Springer-Verlag Berlin Heidelberg New York), 247
- Martins, D. H. & Fraquelli, D. A. 1987, *ApJS*, 65, 83
- Martins, F., Schaerer, D., & Hillier, D. J. 2005, *A&A*, 436, 1049
- Massa, D., et al 2000, *ApJ*, 538, L47
- Massey, P. & Johnson, J. 1993, *AJ*, 105, 980
- Mathys, G. 1988, *A&AS*, 76, 427
- McCammon, D. & Sanders, W. T. 1990, *ARA&A*, 28, 657
- McClure-Griffiths, N. M., Dickey, J. M., Gaensler, B. M., & Green, A. J. 2002, *ApJ*, 578, 176
- McCray, R. & Snow, T. P. 1979, *ARA&A*, 17, 213
- McKee, C. F. 1986, *Ap&SS*, 118, 383
- McKee, C. F. & Begelman, M. C. 1990, *ApJ*, 358, 392
- McKee, C. F. & Cowie, L. L. 1977, *ApJ*, 215, 213
- McKee, C. F. & Ostriker, J. P. 1977, *ApJ*, 218, 148
- Mennickent, R. E. 1991, *A&AS*, 88, 1
- Milne, D. K. 1979, *Australian Journal of Physics*, 32, 83
- Moitinho, A., Alves, J., Huéramo, N., & Lada, C. J. 2001, *ApJ*, 563, L73
- Moos, H. W., et al 2000, *ApJ*, 538, L1
- Morel, T., Marchenko, S. V., Pati, A. K., Kuppuswamy, K., Carini, M. T., Wood, E., & Zimmerman, R. 2004, *MNRAS*, 351, 552
- Morgan, W. W., Code, A. D., & Whitford, A. E. 1955, *ApJS*, 2, 41
- Morgan, W. W., Keenan, P. C., & Kellman, E. 1943, *An atlas of stellar spectra, with an outline of spectral classification* (Chicago, Ill., The University of Chicago press [1943])
- Morrell, N. & Levato, H. 1991, *ApJS*, 75, 965
- Morrison, R. & McCammon, D. 1983, *ApJ*, 270, 119
- Morton, D. C. 2003, *ApJS*, 149, 205
- Nahar, S. N. & Pradhan, A. K. 2003, *ApJS*, 149, 239
- Ochsenbein, F., Bauer, P., & Marcout, J. 2000, *A&AS*, 143, 23
- Oegerle, W. R., Jenkins, E. B., Shelton, R., Bowen, D. V., & Chayer, P. 2005, *ApJ*, 622, 377
- Oegerle, W. R., et al 2000, *ApJ*, 538, L23
- Ögelman, H., Koch-Miramond, L., & Aurière, M. 1989, *ApJ*, 342, L83
- Otte, B. & Dixon, W. V. D. 2006, *ApJ*, 647, 312
- Pinsonneault, M. H. & Stanek, K. Z. 2006, *ApJ*, 639, L67
- Plucinsky, P. P., Snowden, S. L., Aschenbach, B., Egger, R., Edgar, R. J., & McCammon, D. 1996, *ApJ*, 463, 224
- Pourbaix, D., et al 2004, *A&A*, 424, 727 (SB9)
- Press, W. H., Teukolsky, S. A., Vetterling, W. T., & Flannery, B. P. 1992, *Numerical recipes in C. The art of scientific computing*, 2nd edn. (Cambridge University Press), 412

- Prochaska, J. X., Chen, H.-W., Howk, J. C., Weiner, B. J., & Mulchaey, J. 2004, *ApJ*, 617, 718
- Rachford, B. L., et al 2001, *ApJ*, 555, 839
- Raymond, J. C. 1979, *ApJS*, 39, 1
- Redman, M. P., Meaburn, J., Bryce, M., Harman, D. J., & O'Brien, T. J. 2002, *MNRAS*, 336, 1093
- Reed, B. C. 1993, *PASP*, 105, 1465
- Richter, P., Savage, B. D., Tripp, T. M., & Sembach, K. R. 2004, *ApJS*, 153, 165
- Richter, P., Savage, B. D., Wakker, B. P., Sembach, K. R., & Kalberla, P. M. W. 2001, *ApJ*, 549, 281
- Roger, R. S. & Landecker, T. L., eds. 1988, *Overview of the Interstellar Medium: Supernova Related Issues*, ed. R. S. Roger & T. L. Landecker, *IAU Colloq. No. 101*, 73
- Rood, R. T., et al 1999, *ApJ*, 523, 752
- Ryans, R. S. I., Keenan, F. P., Rolleston, W. R. J., Sembach, K. R., & Davies, R. D. 1999, *MNRAS*, 304, 947
- Ryans, R. S. I., Keenan, F. P., Sembach, K. R., & Davies, R. D. 1997, *MNRAS*, 289, 986
- Sahnow, D. J., et al 2000, *ApJ*, 538, L7
- Samus, N. N., Durlevich, O. V., & et al. 2004, *Combined General Catalogue of Variable Stars*, Tech. rep., Institute of Astronomy of Russian Academy of Sciences and Sternberg State Astronomical Institute of the Moscow State University (GCVS)
- Sanders, W. T., Kraushaar, W. L., Nousek, J. A., & Fried, P. M. 1977, *ApJ*, 217, L87
- Sauvageot, J. L. & Decourchelle, A. 1995, *A&A*, 296, 201
- Sauvageot, J. L., Decourchelle, A., & Bohigas, J. 1999, *A&A*, 351, 669
- Savage, B. D. 1987, in *Interstellar Processes*, ed. D. J. Hollenbach & H. A. Thronson ((Dordrecht: Reidel)), 123–141
- Savage, B. D., Edgar, R. J., & Diplas, A. 1990, *ApJ*, 361, 107
- Savage, B. D. & Lehner, N. 2006, *ApJ*, 162, 134 (SL06)
- Savage, B. D. & Massa, D. 1987, *ApJ*, 314, 380
- Savage, B. D., Meade, M. R., & Sembach, K. R. 2001, *ApJS*, 136, 631
- Savage, B. D. & Sembach, K. R. 1991, *ApJ*, 379, 245
- Savage, B. D., Sembach, K. R., & Cardelli, J. A. 1994, *ApJ*, 420, 183
- Savage, B. D., Sembach, K. R., Tripp, T. M., & Richter, P. 2002, *ApJ*, 564, 631
- Savage, B. D., et al 2003, *ApJS*, 146, 125
- Schild, R. E., Hiltner, W. A., & Sanduleak, N. 1969, *ApJ*, 156, 609
- Schmidt-Kaler, T. 1982, *Landolt-Börnstein, New Series, Group, VI*, ed. K. Schaifers & H. H. Voigt, Vol. 2b (Berlin: Springer-Verlag), p1
- Sembach, K. R. 1993, *PASP*, 105, 983
- . 1994, *ApJ*, 434, 244
- Sembach, K. R., Howk, J. C., Savage, B. D., Shull, J. M., & Oegerle, W. R. 2001, *ApJ*, 561, 573
- Sembach, K. R. & Savage, B. D. 1992, *ApJS*, 83, 147
- Sembach, K. R., Savage, B. D., & Hurwitz, M. 1999, *ApJ*, 524, 98
- Sembach, K. R., Savage, B. D., & Jenkins, E. B. 1994, *ApJ*, 421, 585
- Sembach, K. R., Savage, B. D., & Massa, D. 1991, *ApJ*, 372, 81
- Sembach, K. R., Tripp, T. M., Savage, B. D., & Richter, P. 2004, *ApJS*, 155, 351
- Sembach, K. R., et al 2003, *ApJS*, 146, 165
- Shapiro, P. R. & Field, G. B. 1976, *ApJ*, 205, 762
- Shapiro, P. R. & Moore, R. T. 1976a, *ApJ*, 207, 460
- . 1976b, *ApJ*, 207, 460
- Shelton, R. L. 2006, *ApJ*, 638, 206
- Shelton, R. L. & Cox, D. P. 1994, *ApJ*, 434, 599
- Shelton, R. L., et al 2001, *ApJ*, 560, 730

- Shull, J. M. & McKee, C. F. 1979, *ApJ*, 227, 131
- Shull, J. M. & Slavin, J. D. 1994, *ApJ*, 427, 784
- Shull, J. M. & van Steenberg, M. 1982, *ApJS*, 48, 95
- Skrutskie, M. F., et al 2006, *AJ*, 131, 1163
- Slavin, J. D. & Cox, D. P. 1992, *ApJ*, 392, 131
- Slavin, J. D., Nichols, J. S., & Blair, W. P. 2004, *ApJ*, 606, 900
- Slavin, J. D., Shull, J. M., & Begelman, M. C. 1993, *ApJ*, 407, 83
- Smartt, S. J., Dufton, P. L., & Lennon, D. J. 1997, *A&A*, 326, 763
- Smith, B. W. 1977, *ApJ*, 211, 404
- Smith, N., Bally, J., & Morse, J. A. 2003, *ApJ*, 587, L105
- Smith, R. K. & Cox, D. P. 2001, *ApJS*, 134, 283
- Snow, Jr., T. P., Kunasz, P. B., & Wegner, G. A. 1980, *ApJ*, 238, 643
- Snowden, S. L., Cox, D. P., McCammon, D., & Sanders, W. T. 1990, *ApJ*, 354, 211
- Snowden, S. L., Egger, R., Finkbeiner, D. P., Freyberg, M. J., & Plucinsky, P. P. 1998, *ApJ*, 493, 715
- Snowden, S. L., et al 1997, *ApJ*, 485, 125
- Sonnentrucker, P., Friedman, S., & York, D. 2006, *ApJ*, 650, L115
- Spitzer, L. 1978, *Physical processes in the interstellar medium* (New York Wiley-Interscience, 1978. 333 p.), p155
- Spitzer, L. J. 1956, *ApJ*, 124, 20
- . 1990, *ARA&A*, 28, 71
- . 1996, *ApJ*, 458, L29
- Spitzer, L. J. & Fitzpatrick, E. L. 1992, *ApJ*, 391, L41
- Stetson, P. B. & Fitzgerald, M. P. 1985, *AJ*, 90, 1060
- Stickland, D. J., Lloyd, C., & Sweet, I. 1998, *The Observatory*, 118, 7
- Sutherland, R. S. & Dopita, M. A. 1993, *ApJS*, 88, 253
- Szentgyorgyi, A. H., Raymond, J. C., Hester, J. J., & Curiel, S. 2000, *ApJ*, 529, 279
- Tapia, M., Roth, M., Vázquez, R. A., & Feinstein, A. 2003, *MNRAS*, 339, 44
- Teske, R. G. 1990, *ApJ*, 365, 256
- Testa, V., Chieffi, A., Limongi, M., Andreuzzi, G., & Marconi, G. 2004, *A&A*, 421, 603
- Tripp, T. M., Giroux, M. L., Stocke, J. T., Tumlinson, J., & Oegerle, W. R. 2001, *ApJ*, 563, 724
- Tripp, T. M., Jenkins, E. B., Bowen, D. V., Prochaska, J. X., Aracil, B., & Ganguly, R. 2005, *ApJ*, 619, 714
- Tripp, T. M., Savage, B. D., & Jenkins, E. B. 2000, *ApJ*, 534, L1
- Tripp, T. M., Sembach, K. R., Bowen, D. V., Savage, B. D., Jenkins, E. B., Lehner, N., & Richter, P. 2007, *ArXiv e-prints*, 0706.1214
- Tripp, T. M., Sembach, K. R., & Savage, B. D. 1993, *ApJ*, 415, 652
- Turner, D. G. 1976, *ApJ*, 210, 65
- Tycner, C., et al 2005, *ApJ*, 624, 359
- Uyaniker, B., Fürst, E., Reich, W., Aschenbach, B., & Wielebinski, R. 2001, *A&A*, 371, 675
- Uytterhoeven, K., Willems, B., Lefever, K., Aerts, C., Telting, J. H., & Kolb, U. 2004, *A&A*, 427, 581
- Vacca, W. D., Garmany, C. D., & Shull, J. M. 1996, *ApJ*, 460, 914
- Valencic, L. A., Clayton, G. C., & Gordon, K. D. 2004, *ApJ*, 616, 912
- Vallée, J. P. 2002, *ApJ*, 566, 261
- van der Hucht, K. A. 2001, *New Astronomy Review*, 45, 135
- van Leeuwen, F., Evans, D. W., Grenon, M., Grossmann, V., Mignard, F., & Perryman, M. A. C. 1997, *A&A*, 323, L61
- van Leeuwen, F. & van Genderen, A. M. 1997, *A&A*, 327, 1070
- Voges, W., et al 1999, *A&A*, 349, 389

- Wakker, B. P., et al 2003, ApJS, 146, 1
- Walborn, N. R. 1971, ApJS, 23, 257
- . 1972, AJ, 77, 312
- . 1973, AJ, 78, 1067
- Walborn, N. R. 1995, in *Revista Mexicana de Astronomia y Astrofisica Conference Series*, ed. V. Niemela, N. Morrell, & A. Feinstein, Vol. 2, 51
- . 2002, AJ, 124, 507
- Walborn, N. R., Danks, A. C., Vieira, G., & Landsman, W. B. 2002a, ApJS, 140, 407
- Walborn, N. R., Heckathorn, J. N., & Hesser, J. E. 1984, ApJ, 276, 524
- Walborn, N. R. & Hesser, J. E. 1975, ApJ, 199, 535
- . 1982, ApJ, 252, 156
- Walborn, N. R., et al 2002b, AJ, 123, 2754
- Walborn, N. R., Smith, N., Howarth, I. D., Vieira Kober, G., Gull, T. R., & Morse, J. A. 2007, PASP, 119, 156
- Weaver, R., McCray, R., Castor, J., Shapiro, P., & Moore, R. 1977, ApJ, 218, 377
- Wegner, W. 1994, MNRAS, 270, 229
- . 2000, MNRAS, 319, 771
- Whittet, D. C. B. 1992, *Dust in the galactic environment* (Institute of Physics Publishing, p71)
- Widmann, H., et al 1998, A&A, 338, L1
- Williamson, F. O., Sanders, W. T., Kraushaar, W. L., McCammon, D., Borken, R., & Bunner, A. N. 1974, ApJ, 193, L133
- Wolf, F. L. 1974, *Elements of Probability and Statistics*, 2nd edn. (New York: McGraw Hill)
- Woodgate, B. E., Angel, J. R. P., & Kirshner, R. P. 1975, ApJ, 200, 715
- Woodgate, B. E., Stockman, H. S., Angel, J. R. P., & Kirshner, R. P. 1974, ApJ, 188, L79
- Yentis, D. J., Novick, R., & Vanden Bout, P. 1972, ApJ, 177, 375
- York, D. G. 1974, ApJ, 193, L127
- . 1977, ApJ, 213, 43
- Zsargó, J., Sembach, K. R., Howk, J. C., & Savage, B. D. 2003, ApJ, 586, 1019 (Z03)

This 2-column preprint was prepared with the AAS L^AT_EX macros v5.2.

TABLE 1
STELLAR PARAMETERS FOR *FUSE* TARGET STARS

ID (1)	Star (2)	Prog ID (3)	l (deg) (4)	b (deg) (5)	B (6)	V (7)	K (8)	Sp/L (9)	$E(B-V)$ (10)	$E(K-V)$ (11)	d (kpc) (12)	d_r (kpc) (13)	v_c (km s $^{-1}$) (14)	$[R]$ (15)	Sp/L ref (16)
1	HD167402	P10162	2.27	-6.39	8.97	9.09	...	B0.5Ib/B0III	0.08 ± 0.03	...	9.0	5.7, 12.2	8.6	0	1
2	HD168941	P10165	5.82	-6.31	9.36	9.37	...	O9.5II-III	0.24 ± 0.04	...	6.8	4.4, 9.6	9.3	0	2
3	HD164906	P10277	6.05	-1.33	7.54	7.40 ^f	...	B1Vpe	0.38 ± 0.03	...	1.1	0.7, 1.4	10.0	2	2
4	HD165052	P10278	6.12	-1.48	6.91	6.84	...	O6.5Vnf	0.36 ± 0.02	...	1.9 ^g	1.6, 2.3	10.0	2	2
5	HDE315021	P12224	6.12	-1.33	8.52	8.41	8.26	B2IVn	0.32 ± 0.07	-0.75 ± 0.07	1.4	0.9, 1.9	10.1	1	3
6	HD163892	P10276	7.15	0.62	7.57	7.48	7.11	O9IVn	0.37 ± 0.02	-1.16 ± 0.04	1.6	1.2, 2.1	10.5	0	2
7	HD158661	P12222	8.29	9.05	8.32	8.18	7.71	B0.5Ib	0.34 ± 0.02	-1.00 ± 0.04	4.2	3.2, 5.4	11.6	0	4
8	HD167287	P12226	11.99	-0.93	7.13	7.08	6.81	B1Ib	0.24 ± 0.02	-0.78 ± 0.04	2.7	1.8, 3.6	11.2	1	4
9	HD167659	P10280	12.20	-1.27	7.52	7.40	...	O7III	0.43 ± 0.02	...	2.5	2.1, 3.0	11.2	1	2
10	HD167771	P10281	12.70	-1.13	6.56	6.53	...	O7III:nf	0.33 ± 0.01	...	2.3 ^g	1.8, 2.6	11.3	2	2
11	HD157857	P10275	12.97	13.31	7.90	7.81	...	O6.5IIIf	0.37 ± 0.02	...	3.1	2.5, 3.5	12.7	0	2
12	HD168080	P12227	13.11	-1.27	7.66	7.61	7.26	B0.5II	0.26 ± 0.02	-0.88 ± 0.04	2.7	1.9, 3.6	11.3	3	4
13	HD175754	P10168	16.39	-9.91	6.92	7.02	...	O8III	0.20 ± 0.01	...	2.8	2.3, 3.5	10.6	0	2
14	HD178487	P10172	25.79	-8.56	8.78	8.69	8.34	B0.5Ib	0.29 ± 0.02	-0.88 ± 0.04	5.7	4.3, 7.2	12.1	0	5
15	HD185418	P11623	53.60	-2.17	7.65	7.52	7.11	B0.5V	0.38 ± 0.01	-1.10 ± 0.04	1.2 ^g	1.1, 1.7	14.7	0	4
16	HD187282	P11712	55.62	-3.79	10.54	10.46	...	WN44(h)+OB?	4.5 ^h	3.6, 5.4	14.4	0	6
17	HD191877	P10287	61.57	-6.45	6.22	6.27	6.37	B1Ib	0.14 ± 0.01	-0.41 ± 0.04	2.3	1.5, 3.0	13.9	0	2
18	HDE332407	P12228	64.28	3.11	8.78	8.63	8.05	B0.5III	0.38 ± 0.02	-1.25 ± 0.04	2.6	1.9, 3.7	15.0	0	2
19	HD187459	P10282	68.81	3.85	6.58	6.47	6.06	B0.5Ib	0.31 ± 0.01	-0.94 ± 0.04	2.2 ^g	1.6, 2.7	14.8	0	2
20	HDE25757	P10177	69.64	4.85	10.62	10.66	10.54	B1IIIn	0.17 ± 0.07	-0.77 ± 0.08	6.5	5.1, 10.1	14.9	0	7
21	HD190429	P10284	72.59	2.61	6.97	7.14 ^d	...	O4I	0.46 ± 0.03	...	2.9	2.1, 3.8	14.4	0	2
22	HD190918	P10285	72.65	2.06	6.20	6.82 ^d	...	WN4+O9.7Iab	2.1 ^h	1.7, 2.6	14.3	2	8
23	HD191495	P12229	72.74	1.41	8.47	8.42 ^g	8.27	B0V	0.31 ± 0.02	-0.91 ± 0.04	1.8	1.6, 2.4	14.2	0	4
24	HD191765	P11713	73.45	1.55	8.21	8.02 ^g	...	WN6	1.7 ^h	1.4, 2.1	14.2	1	2
25	HD192639	P11624	74.90	1.48	7.38	7.13	...	O7Ibf	0.56 ± 0.01	...	2.1	1.7, 2.6	14.1	0	9
26	HD201345	P12230	78.44	-9.54	7.61	7.75	8.24	O9V	0.14 ± 0.01	-0.29 ± 0.04	2.2	1.9, 2.9	12.2	0	2
27	HD186994	P21608	78.62	10.06	7.37	7.94	7.94	B0.2IV	0.13 ± 0.01	-0.28 ± 0.04	2.0	1.5, 2.7	14.5	1	10
28	HD192035	P10286	83.33	7.76	8.32	8.29 ^e	...	B0III-IVn	0.28 ± 0.01	...	2.7	1.7, 4.6	13.7	0	2
29	HD199579	P11625	85.70	-0.30	5.98	5.97	...	O6Vf	0.31 ± 0.01	...	1.4 ^g	1.3, 1.7	12.5	2	2
30	HD195965	P10288	85.71	5.00	6.91	6.98	7.25	B0V	0.19 ± 0.01	-0.49 ± 0.04	1.1	1.0, 1.5	13.1	1	2
31	HD202347	P10289	88.22	-2.08	7.38	7.49	7.88	B1.5V	0.11 ± 0.01	-0.23 ± 0.04	1.0	0.8, 1.5	12.0	1	10
32	HD210809	P12231	99.85	-3.13	7.58	7.57	7.44	O9Iab	0.28 ± 0.01	-0.86 ± 0.04	4.3	3.5, 5.5	9.8	0	2
33	HD212044	P12234	100.64	-4.35	7.26	7.32 ^e	...	B1Vnnp	0.17 ± 0.01	...	0.9	0.7, 1.5	9.5	0	2
34	BD+532820	P12232	101.24	-1.69	10.02	9.96	9.81	B0IVn	0.33 ± 0.05	-0.90 ± 0.06	4.8	3.6, 6.4	9.8	0	11
35	HDE235783	P12233	101.69	-1.87	8.82	8.74	8.29	B1Ib	0.27 ± 0.02	-0.96 ± 0.04	5.3	3.5, 7.0	9.6	0	2
36	HD207198	P12237	101.97	-5.93	9.62	9.58	9.69	B3III	0.20 ± 0.03	-0.36 ± 0.04	2.6	1.9, 5.1	9.0	0	4
37	HD210839	P11628	103.14	6.99	6.19	5.96	...	O9.5Ib-II	0.47 ± 0.01	...	1.3	0.9, 1.7	10.4	0	8
38	HD210839	P11631	103.83	2.61	5.32	5.15 ^e	...	O6Infp	0.49 ± 0.01	...	1.1	0.8, 1.5	9.8	0	2
39	HD216044	P12238	105.94	-3.64	8.55	8.52	8.49	B0II	0.25 ± 0.02	-0.62 ± 0.04	5.0 ^g	4.1, 6.4	8.6	0	4
40	HD218915	P10188	108.06	-6.89	7.19	7.22	...	O9.5Iab	0.21 ± 0.01	...	5.0 ^g	4.1, 6.4	7.7	2	2
41	HD224151	P12241	115.44	-4.64	6.18	6.04	5.43	B0.5II	0.34 ± 0.01	-1.14 ± 0.04	1.4 ^g	1.0, 1.9	6.3	0	2
42	HD224868	P12202	116.87	-1.44	7.39	7.30	6.96	B0Ib	0.31 ± 0.01	-0.93 ± 0.03	3.1	2.5, 3.8	6.4	1	12
43	HD000108	Z90101	117.93	1.25	7.49	7.38	...	O6pe	0.42 ± 0.01	...	3.8 ^g	2.1, 5.8	6.5	0	9

TABLE 1

ID	Star	Prog ID	l (deg)	b (deg)	B (6)	V (7)	K (8)	Sp/L (9)	$E(B-V)$ (10)	$E(K-V)$ (11)	d (kpc) (12)	d_r (kpc) (13)	v_c (km s ⁻¹) (14)	[R] (15)	Sp/L ref (16)
44	HD005005A	P10201	123.13	-6.24	8.68	8.63 ^d	...	O6.5Vf	2.9 ^b	2.8, 3.1	4.3	1	2
45	HD223252	P12201	130.70	-6.71	8.65	8.70	8.80	BIII	0.14 ± 0.02	-0.41 ± 0.04	6.1 ^a	4.0, 9.3	2.4	1	4
46	HD012323	P10202	132.91	-5.87	8.87	8.92	9.19	O9V	0.23 ± 0.02	-0.52 ± 0.04	4.4 ^a	3.9, 5.8	1.9	0	2
47	HD013268	P10203	133.96	-4.99	8.24	8.18	7.95	O8Vnn	0.35 ± 0.01	-1.07 ± 0.04	2.1	1.8, 2.7	1.7	1	2
48	HD013745	P10204	134.58	-4.96	7.99	7.90 ^f	7.46	O9.7IIIn	0.34 ± 0.01	-1.10 ± 0.04	3.2	2.2, 3.9	1.6	0	2
49	HD014434	P10205	135.08	-3.82	8.68	8.59 ^f	...	O5.5Vnfp	0.38 ± 0.02	...	3.5	3.1, 4.3	1.6	0	2
50	HD017520	B09702	137.22	0.88	9.05	8.82 ^d	...	O8Ve	0.52 ± 0.02	...	2.3	2.0, 2.9	1.6	1	8
51	HD015137	P10206	137.46	-7.58	7.87	7.88	...	O9.5II-IIIn	0.24 ± 0.01	...	3.5	2.2, 4.9	0.5	0	2
52	HD041161	P10210	164.97	12.89	6.66	6.76	7.04	O8Vn	0.19 ± 0.01	...	1.4	1.2, 1.8	-3.9	0	13
53	HD034656	P10113	170.04	0.27	6.80	6.80	...	O7III	0.31 ± 0.01	...	2.2	1.9, 2.7	-6.8	0	2
54	HD042087	P21603	187.75	1.77	6.05	5.90 ^d	...	B2.5Ibe	0.29 ± 0.01	...	1.4	0.8, 2.0	-10.3	0	4
55	HD042088	P10211	190.04	0.48	7.57	7.56	7.42	O6.5V	0.30 ± 0.01	-1.02 ± 0.04	2.0	1.7, 2.5	-10.9	1	2
56	HD030677	P10208	190.18	-22.22	6.79	6.85	...	B1II-IIIn	0.14 ± 0.01	...	1.7	1.1, 3.1	-12.8	0	2
57	HD039680	P10209	194.08	-5.88	7.96	7.66 ^f	...	O6.5Vnfp	0.30 ± 0.02	...	2.6	2.3, 3.2	-12.3	0	2
58	HD045314	P10213	196.96	1.52	6.74	6.65 ^f	...	O9pe	0.37 ± 0.01	...	2.1	0.8, 3.6	-11.9	3	2
59	HD042401	P10212	197.64	-3.33	7.70	7.76 ^f	...	B2V	0.15 ± 0.02	...	0.8	0.7, 1.3	-12.6	0	2
60	HD047417	P10216	205.35	0.35	6.91	6.95	7.03	B0IV	0.22 ± 0.01	-0.69 ± 0.04	1.3	1.0, 1.8	-13.2	3	2
61	HD047088	P15104	205.92	-0.40	7.53	7.59 ^f	7.82	B1IV	0.17 ± 0.02	-0.42 ± 0.04	1.6	1.1, 2.2	-13.4	3	14
62	HD046150	P10214	206.31	-2.07	6.85	6.78 ^f	...	O5Vf	0.38 ± 0.01	...	1.7	1.5, 2.0	-13.6	2	2
63	HD046202	P11610	206.31	-2.00	8.34	8.23 ^f	7.75	O9V	0.38 ± 0.03	-1.28 ± 0.05	1.7	1.5, 2.2	-13.6	1	13
64	HD047360	P10215	207.33	-0.79	8.34	8.26 ^f	...	B0.5V	0.32 ± 0.02	...	1.5	1.3, 2.0	-13.6	3	2
65	HD065079	P10222	217.87	15.93	7.64	7.80 ^f	...	B2Vne	0.05 ± 0.02	...	1.0	0.8, 1.5	-12.0	0	2
66	LS277	P12208	223.34	1.57	9.77	9.73	...	B1:	5.4 ^b	4.3, 6.5	-14.5	0	15
67	HD061347	P10220	230.60	3.79	8.53	8.39	7.88	O9Ib	0.41 ± 0.02	-1.24 ± 0.04	4.4	3.6, 5.4	-14.4	0	2
68	HD058510	P10219	235.52	-2.47	7.26	7.21 ^d	...	B1Ib-II	0.24 ± 0.02	...	2.5	1.3, 4.0	-15.2	0	2
69	HD062866	P12210	237.48	1.80	9.08	9.04	8.89	B0.5IIIIn	0.26 ± 0.02	...	3.9	2.9, 5.5	-14.7	0	15
70	HD052463	P10218	238.90	-10.52	8.13	8.30	...	B3V	0.02 ± 0.02	-0.82 ± 0.04	0.9	0.7, 1.4	-15.9	0	2
71	HD063005	P10221	242.47	-0.93	9.05	9.13	...	O6Vf	0.22 ± 0.02	...	5.4	4.7, 6.6	-14.9	0	2
72	HD060369	P10502	242.68	-4.30	8.13	8.16 ^d	...	O9IV	0.25 ± 0.01	...	2.7	2.1, 3.6	-15.2	0	16
73	HD060196	P12209	242.95	-4.65	8.99	9.03	9.02	B1III	0.17 ± 0.02	-0.65 ± 0.04	3.2	2.6, 5.0	-15.2	0	16
74	HD064568	P12211	243.14	0.71	9.42	9.41 ^f	...	O4Vf	0.32 ± 0.02	...	6.5	5.7, 7.7	-14.6	0	16
75	HD066788	P10118	245.43	2.05	9.35	9.43	9.69	O9V	0.20 ± 0.03	-0.53 ± 0.05	4.3	3.7, 5.6	-14.3	0	15
76	HD069106	P10223	254.52	-1.33	7.02	7.13	7.42	B0.5IVnn	0.14 ± 0.01	-0.40 ± 0.04	1.5	1.1, 2.0	-14.1	0	2
77	HD074920	P10226	265.29	-1.95	7.53	7.55	...	O8	0.28 ± 0.01	...	3.6	1.6, 6.1	-12.9	3	2
78	HD074711	P10225	265.74	-2.61	7.15	7.12	6.85	B1III	0.25 ± 0.01	-0.92 ± 0.03	1.2	0.9, 1.8	-12.9	3	2
79	HD075309	P10227	265.86	-1.90	7.83	7.84	7.80	B1IIf	0.18 ± 0.01	-0.55 ± 0.04	2.9	1.9, 4.5	-12.8	3	2
80	HD089137	P10228	279.70	4.45	7.92	7.99	8.14	O9.7IIIInp	0.17 ± 0.01	-0.59 ± 0.04	3.1	2.3, 4.4	-9.7	0	2
81	HD090087	P10229	285.16	-2.13	7.75	7.79	7.79	O9IIIIn	0.22 ± 0.01	-0.77 ± 0.04	2.8	2.2, 3.7	-9.4	0	17
82	HD088115	P10123	285.32	-5.53	8.26	8.31	8.44	B1.5IIIn	0.12 ± 0.02	-0.32 ± 0.05	3.7	2.3, 6.0	-9.8	0	2
83	HD091651	P10231	286.55	-1.72	8.83	8.87	8.83	O9Vcn	0.25 ± 0.02	-0.82 ± 0.04	2.8	2.5, 3.7	-9.1	0	2
84	HD091597	P10230	286.86	-2.37	9.70	9.61 ^f	...	B1IIIIne	0.30 ± 0.04	...	3.9	3.1, 6.0	-9.1	1	2
85	HD093129A	P11702	287.41	-0.57	7.36	7.16 ^f	...	O2If	2.8 ^b	2.2, 3.4	-8.8	2	8
86	HD093250	P10238	287.51	-0.54	7.51	7.38 ^f	...	O3Vf	0.44 ± 0.02	...	2.3	2.1, 2.7	-8.8	2	2

TABLE 1

ID	Star	Prog ID	l (deg)	b (deg)	B	V	K	Sp/L	$E(B-V)$	$E(K-V)$	d (kpc)	d_r (kpc)	v_c (km s ⁻¹)	[R]	Sp/L ref
(1)	(2)	(3)	(4)	(5)	(6)	(7)	(8)	(9)	(10)	(11)	(12)	(13)	(14)	(15)	(16)
87	HD093205	P10236	287.57	-0.71	7.75	7.73	...	O3Vf+	0.34 ± 0.03	...	3.3 ^a	3.0, 3.9	-8.8	2	2
88	CPD-592603	P12215	287.59	-0.69	8.96	8.82	...	O7Vf	0.43 ± 0.02	...	3.5 ^a	3.1, 4.4	-8.8	2	2
89	HD092554	P10232	287.60	-2.02	9.60	9.50	9.09	O9.5IIn	0.34 ± 0.04	-1.05 ± 0.05	6.9	5.0, 8.4	-8.9	1	2
90	CPD-592600	P12214	287.60	-0.74	8.84	8.65	...	O6Vf	0.49 ± 0.02	...	2.9	2.6, 3.6	-8.8	2	2
91	HDE303308	P12216	287.60	-0.61	8.14	8.12	...	O3Vf	0.33 ± 0.08	...	3.8	3.4, 4.5	-8.7	2	2
92	HD093146	P10233	287.67	-1.05	8.41	8.45	...	O6.5Vf	0.25 ± 0.10	...	3.5	3.1, 4.3	-8.8	1	2
93	HD093206	P10234	287.67	-0.94	6.44	6.36 ^d	...	O9.7Ib:n	0.33 ± 0.02	...	2.6 ^a	2.2, 3.2	-8.8	2	2
94	HD093222	P10237	287.74	-1.02	8.07	8.05	...	O7IIIf	0.32 ± 0.08	...	3.6	2.8, 4.2	-8.8	1	2
95	HD093843	P10240	288.24	-0.90	7.28	7.34	...	O5IIIf	0.24 ± 0.01	...	3.5	2.8, 4.0	-8.6	0	2
96	HD093827	P10239	288.56	-1.54	9.38	9.36	9.13	B1Ibn	0.21 ± 0.03	-0.74 ± 0.05	7.9	5.3, 10.4	-8.7	1	2
97	HD094493	P10241	289.02	-1.18	7.25	7.29 ⁸	7.24	B1Ib	0.15 ± 0.01	-0.55 ± 0.05	3.4	2.2, 4.4	-8.5	1	2
98	HD096917	P10244	289.29	3.06	7.15	7.11 ⁸	...	O8.5Ibf	0.32 ± 0.01	...	2.9	2.4, 3.6	-7.9	0	2
99	HD096670	P10242	290.20	0.40	7.53	7.43	7.03	O8Ibp	0.39 ± 0.02	-1.21 ± 0.04	3.8 ^a	3.1, 4.6	-8.1	1	2
100	HD096715	P10243	290.27	0.33	8.32	8.30	...	O4Vf	0.33 ± 0.02	...	3.8	3.4, 4.6	-8.1	1	2
101	HD097913	P12217	290.84	1.41	8.80	8.81	...	B0.5IVn	0.23 ± 0.02	-0.85 ± 0.04	2.6	1.9, 3.5	-7.8	1	16
102	HD09890	P10246	291.75	4.43	8.23	8.31	8.47	B0IIn	0.15 ± 0.01	-0.53 ± 0.04	3.5	2.6, 5.2	-7.2	0	2
103	HD100276	P10248	293.31	0.77	7.23	7.23	7.09	B0.5Ib	0.20 ± 0.01	-0.67 ± 0.04	3.2	2.4, 4.1	-7.3	0	2
104	HD100199	P12218	293.95	-1.48	8.17	8.21 ⁸	...	B0IIne	0.19 ± 0.02	...	3.3	2.5, 5.0	-7.4	1	16
105	HD09857	P10245	294.78	-4.94	7.60	7.53 ^d	...	B0.5Ib	0.27 ± 0.01	...	3.5	2.7, 4.5	-7.7	1	2
106	HD101131	P10249	294.78	-1.62	7.13	7.14	...	O6Vf	0.28 ± 0.01	...	2.0	1.7, 2.4	-7.3	2	2
107	HD101190	P10250	294.78	-1.49	7.33	7.33 ^d	...	O6Vf	0.30 ± 0.01	...	2.1	1.8, 2.6	-7.3	2	2
108	HDE308813	P12219	294.80	-1.61	9.30	9.32	9.17	O9.5V	0.26 ± 0.05	-0.92 ± 0.06	3.1	2.7, 4.1	-7.3	2	2
109	HD100213	P10247	294.81	-4.14	8.43	8.41	8.20	O8.5Vn	0.31 ± 0.02	-1.03 ± 0.04	2.6 ^a	2.3, 3.3	-7.6	0	2
110	HD101205	P10251	294.85	-1.65	7.10	7.10 ^d	...	O7IInf	0.29 ± 0.01	...	2.4	1.9, 2.8	-7.3	2	2
111	HD101298	P10252	294.94	-1.69	8.12	8.09	...	O6Vf	0.34 ± 0.02	...	2.8	2.4, 3.4	-7.2	2	2
112	HD101413	P10253	295.03	-1.71	8.37	8.34 ^d	...	O8V	0.32 ± 0.02	...	2.4	2.1, 3.1	-7.2	1	2
113	HD101436	P10254	295.04	-1.71	7.63	7.61 ^d	...	O6.5V	0.31 ± 0.01	...	2.2	1.9, 2.7	-7.2	1	2
114	HD102552	P10255	295.21	1.35	9.10	9.10	9.01	B1IIn	0.21 ± 0.02	-0.73 ± 0.04	3.9 ^a	3.0, 6.0	-6.8	0	2
115	HD103779	P10256	296.85	-1.02	7.18	7.22	7.23	B0.5Iab	0.17 ± 0.01	-0.52 ± 0.04	4.3	3.4, 5.6	-6.7	1	2
116	HD104705	P10257	297.46	-0.34	7.79	7.84 ⁸	...	B0Ib	0.17 ± 0.02	...	5.0	4.1, 6.1	-6.5	1	2
117	HD108639	A12013	300.22	1.95	7.87	7.83	7.62	B1III	0.25 ± 0.01	-0.85 ± 0.04	1.7	1.3, 2.6	-5.6	0	18
118	HD110432	P11614	301.96	-0.20	5.54	5.37 ^e	...	B0.5IIIe	0.3 ^{b,c}	0.2, 0.3	-5.4	2	19
119	HD112784	Z90150	304.00	2.26	8.29	8.27	8.18	O9.5III	0.27 ± 0.01	-0.85 ± 0.04	3.2	2.5, 4.4	-4.6	0	16
120	HD115071	P10259	305.77	0.15	8.23	8.07 ^e	...	B0.5V	0.40 ± 0.02	...	1.2	1.0, 1.7	-4.4	0	2
121	HD114441	P10258	305.80	7.40	8.17	8.11 ^e	...	B2IVpe	0.27 ± 0.01	...	1.2	0.8, 1.6	-3.5	0	2
122	HD115455	A12007	306.06	0.22	8.14	8.01	7.46	O7.5III	0.40 ± 0.01	-1.36 ± 0.04	2.6	2.1, 3.2	-4.3	1	13
123	HD116781	P10261	307.05	-0.06	7.80	7.72 ^d	...	B0IIne	0.31 ± 0.02	...	2.2	1.7, 3.3	-4.1	0	2
124	HD116538	P10260	308.23	10.68	7.83	7.91 ^e	...	B2IVn	0.13 ± 0.01	...	1.3	0.9, 1.8	-2.5	0	2
125	HD118969	P12221	308.52	-1.39	10.26	10.27 ^d	...	B1.5V	0.21 ± 0.03	...	2.9	2.3, 4.5	-3.9	0	20
126	HD118571	P12220	308.70	1.35	8.76	8.79	8.88	B0.5IVn	0.21 ± 0.01	-0.60 ± 0.05	2.9	2.1, 4.0	-3.5	0	16
127	HD122879	B07105	312.26	1.79	6.55	6.48 ⁸	...	B0Ia	0.29 ± 0.01	...	3.3	2.6, 3.7	-2.6	0	21
128	HD124314	P10262	312.67	-0.42	7.03	6.89 ^d	...	O6Vnf	0.43 ± 0.01	...	1.4	1.2, 1.7	-2.7	3	2
129	HD124979	P10263	316.41	9.08	8.58	8.58	...	O8Vf	0.30 ± 0.02	...	2.8	2.5, 3.6	-0.6	0	2

TABLE 1

ID	Star	Prog ID	l (deg)	b (deg)	B	V	K	Sp/L	$E(B-V)$	$E(K-V)$	d (kpc)	d_r (kpc)	v_e (km s $^{-1}$)	[R]	Sp/L ref
(1)	(2)	(3)	(4)	(5)	(6)	(7)	(8)	(9)	(10)	(11)	(12)	(13)	(14)	(15)	(16)
130	HD148422	P10150	329.92	-5.60	8.69	8.64	8.51	B1Ia	0.23 ± 0.02	-0.65 ± 0.04	10.0	7.4, 11.2	1.1	1	2
131	HD134411	P10265	330.07	15.53	9.36	9.55	...	B2Vn	0.02 ± 0.03	...	2.3	1.8, 3.5	3.6	3	2
132	HD151805	P10266	343.20	1.59	9.01	9.01 ^e	8.54	B1Ib	0.19 ± 0.05	-0.98 ± 0.06	6.0	4.0, 7.8	5.3	1	2
133	HD151932	P11708	343.23	1.43	6.72	6.49 ^g	...	WN7h	2.0 ^b	1.6, 2.4	5.3	1	2
134	CPD-417712	B02506	343.41	1.17	9.24	9.08	8.70	B0IV	0.42 ± 0.04	-1.14 ± 0.04	2.8	2.1, 3.8	5.3	2	22
135	HD152200	B02501	343.42	1.22	8.62	8.63	8.09	O9.5III	0.23 ± 0.07	-1.30 ± 0.09	4.0 ^a	3.0, 5.5	5.4	2	22
136	HD152248	P10268	343.47	1.18	6.23	6.12 ^d	...	O7Ib:np	0.42 ± 0.02	...	2.2 ^a	1.8, 2.7	5.4	2	2
137	HD326329	B02505	343.47	1.17	8.91	8.78	8.39	O9.5V	0.40 ± 0.04	-1.16 ± 0.05	2.1	1.9, 2.8	5.4	2	23
138	HD152233	P10267	343.48	1.22	6.64	6.54	...	O6III:fp	0.40 ± 0.02	...	2.3 ^a	1.8, 2.6	5.4	2	2
139	HD152314	P10269	343.52	1.14	7.87	7.75	...	O9.5III-IV	0.38 ± 0.02	...	2.6 ^a	1.7, 4.1	5.4	2	2
140	HD152218	P10154	343.53	1.28	7.76	7.64	7.10	O9.5IVn	0.40 ± 0.03	-1.31 ± 0.05	1.9 ^a	1.4, 2.5	5.4	1	2
141	HD152245	Z90160	344.45	2.02	8.44	8.38	...	B0III/O9.5V	0.31 ± 0.02	...	2.6	1.7, 4.6	5.7	1	16
142	HD152623	P10270	344.62	1.61	7.05	7.01 ^d	...	O7V:mf	0.33 ± 0.01	...	1.5	1.3, 1.9	5.7	2	2
143	HD152723	P10271	344.81	1.61	7.40	7.28 ^d	...	O6.5III:fp	0.41 ± 0.03	...	2.3	1.9, 2.6	5.7	1	2
144	HD156292	P10274	345.35	-3.08	7.70	7.53	6.87	O9.5III	0.43 ± 0.02	-1.42 ± 0.04	1.7	1.3, 2.4	5.3	1	2
145	HD153426	P10272	347.14	2.38	7.55	7.49	...	O9II-III	0.33 ± 0.02	...	2.6	1.7, 3.5	6.4	1	2
146	HD161807	P12223	351.78	-5.85	6.91	7.01	7.30	B0:III:n	0.14 ± 0.01	-0.40 ± 0.04	2.1	1.5, 3.1	6.4	1	24
147	HD163758	P10159	355.36	-6.10	7.32	7.33	...	O6.5Iaf	0.30 ± 0.01	...	4.7	3.9, 5.3	7.2	1	2
148	HD165955	P10279	357.41	-7.43	9.13	9.19	9.48	B3Vn	0.12 ± 0.03	-0.20 ± 0.05	1.3	1.0, 1.9	7.5	1	2

NOTE.—Explanation of columns: (1)—ID number corresponding to panel numbers shown in Fig. 24; (2)—star name; (3)—root of *FUSE* dataset; (4,5)—Galactic l and b ; (6,7)—Johnson B - and V -band magnitudes, converted from *Tyccho* B_T and V_T values; (8)—Johnson K -band magnitude, converted from 2Mass K -band magnitude. Value is not given if $E(K-V)$ was not derived for the sight line (see Appendix B.2); (9)—spectral type and luminosity class; (10)—optical color excess. Not given if distance to star taken from literature; (11)—IR color excess; (12) distance to star; (13)—range in possible distances, based on the uncertainties discussed in Appendix B.3; (14)—correction required to move heliocentric velocities observed along a sight line to LSR velocities ($v_{LSR} = v_e + v_{\odot}$); (15)—our *ROSAT* classification discussed in §3.4 and §3.5. Quantities which are taken from the *Hipparcos/Tyccho* catalogs were downloaded from table I/239 from the *VizieR* Service. (16)—reference to the Sp/Ls, adopted in column 9; these are: (1) Tripp et al. (1993); (2) Savage et al. (2001); (3) Hiltner et al. (1965); (4) Morgan et al. (1955); (5) Smartt et al. (1997); (6) Conti & Vacca (1990); (7) Crampton et al. (1976); (8) Walborn (1972); (9) Walborn (1972); (10) Walborn (1971); (11) Humphreys (1978); (12) Garmany & Stencel (1992); (13) Walborn (1973); (14) Turner (1976); (15) Reed (1993); (16) Garrison et al. (1977); (17) Mathys (1988); (18) Hoak & Cowley (1975); (19) Codina et al. (1984); (20) Stetson & Fitzgerald (1985); (21) Hiltner et al. (1969); (22) Schild et al. (1969); (23) García & Mermilliod (2001); (24) Garrison et al. (1983)

^aStar is identified as a spectroscopic binary (SB) either in the SB9 catalog (Pourbaix et al. 2004) or by García & Mermilliod (2001). Except for HD 114032 (where a *Hipparcos* distance is used) the distance is corrected by a factor determined by the prescription set out in Appendix B.1.2.

^bDistances to star taken from the literature for: HD187282 — Armal et al. (1999); HD190918 — van der Hucht (2001); HD191765 — van der Hucht (2001); HD005005A — Guetter & Turner (1997); LS277 — Reed (1993); HD093129A — Tapia et al. (2003); HD110432 — Rachford et al. (2001); HD151932 — van der Hucht (2001).

^c*Hipparcos* parallax distance used.

^d B and V magnitudes corrected; star is identified as a multiple system in the *Hipparcos Double and Multiples: Component solutions* catalog. Magnitude of the brightest given component used. Magnitude is actually H_p , which we take to be close to Johnson- V . (See Appendix B.1.1.)

^e B and V magnitudes corrected; star is not SB, but is listed as variable in the *Hipparcos Variability Annex*. Faintest magnitude listed is used. Magnitude is actually H_p , which we take to be close to Johnson- V . (See Appendix B.1.3.)

^f *B* and *V* magnitudes corrected; magnitudes taken from the literature. (See Appendix B.4.)

^g Star is cataloged as variable in the GCVS by Samus et al. (2004). Magnitude is not corrected, however. (See Appendix B.1.3.)

TABLE 2
SIGHT LINES OBSERVED WITH *FUSE* SORTED BY NAME, AND OBSERVATION LOG

Star Name	<i>FUSE</i> Prog ID	Unique ID ^a	<i>l</i> (deg)	<i>b</i> (deg)	Start Date	T_{exp} (ksec) ^b
BD+532820	P12232	34	101.24	-1.69	2000 08 06	11.3
CPD-417712	B02506	134	343.41	1.17	2001 08 09	9.6
CPD-592600	P12214	90	287.60	-0.74	2000 03 21	15.6
					2000 03 23	
					2000 03 25	
CPD-592603	P12215	88	287.59	-0.69	2000 03 21	6.0
HD000108	Z90101	43	117.93	1.25	2002 08 31	7.9
	D06401				2003 08 05	
HD005005A	P10201	44	123.13	-6.24	2000 08 14	6.4
HD012323	P10202	46	132.91	-5.87	1999 11 25	3.9
HD013268	P10203	47	133.96	-4.99	1999 11 24	4.4
HD013745	P10204	48	134.58	-4.96	1999 11 24	4.4
HD014434	P10205	49	135.08	-3.82	1999 11 24	4.4
HD015137	P10206	51	137.46	-7.58	1999 11 25	2.3
HD017520	B09702	50	137.22	0.88	2001 09 11	6.6
HD030677	P10208	56	190.18	-22.22	2001 01 01	4.2
HD034656	P10113	53	170.04	0.27	2000 03 01	4.2
HD039680	P10209	57	194.08	-5.88	2001 03 05	3.9
HD041161	P10210	52	164.97	12.89	2003 09 25	6.0
HD042087	P21603	54	187.75	1.77	2001 10 15	2.9
HD042088	P10211	55	190.04	0.48	2000 11 05	4.2
HD042401	P10212	59	197.64	-3.33	2000 11 05	1.4
HD045314	P10213	58	196.96	1.52	2000 03 16	5.5
HD046150	P10214	62	206.31	-2.07	2001 03 05	8.6
	C16802				2004 02 25	
HD046202	P11610	63	206.31	-2.00	2001 10 16	4.9
HD047088	P15104	61	205.92	-0.40	2001 02 20	4.6
HD047360	P10215	64	207.33	-0.79	2001 03 04	5.0
HD047417	P10216	60	205.35	0.35	2000 03 15	5.2
HD052463	P10218	70	238.90	-10.52	2000 01 24	3.1
HD058510	P10219	68	235.52	-2.47	2001 04 06	5.7
HD060196	P12209	73	242.95	-4.65	2000 04 16	5.7
HD060369	P10502	72	242.68	-4.30	2000 04 17	6.0
HD061347	P10220	67	230.60	3.79	2000 04 15	6.8
HD062866	P12210	69	237.48	1.80	2000 04 02	8.1
					2000 04 11	
HD063005	P10221	71	242.47	-0.93	2000 04 05	5.3
HD064568	P12211	74	243.14	0.71	2000 04 03	16.0
					2000 04 05	
					2000 04 11	
HD065079	P10222	65	217.87	15.93	2000 03 07	4.4
HD066788	P10118	75	245.43	2.05	2000 04 06	4.2
HD069106	P10223	76	254.52	-1.33	2002 12 31	0.4
HD074711	P10225	78	265.74	-2.61	2000 01 26	4.7

TABLE 2

Star Name	FUSE Prog ID	Unique ID ^a	l (deg)	b (deg)	Start Date	T_{exp} (ksec) ^b
HD074920	P10226	77	265.29	-1.95	2000 01 26	4.7
HD075309	P10227	79	265.86	-1.90	2000 01 26	4.7
HD088115	P10123	82	285.32	-5.53	2000 04 04	4.5
HD089137	P10228	80	279.70	4.45	2000 01 26	4.6
HD090087	P10229	81	285.16	-2.13	2000 04 03	3.1
HD091597	P10230	84	286.86	-2.37	2000 02 04	14.3
					2000 02 06	
					2000 02 08	
HD091651	P10231	83	286.55	-1.72	2000 05 25	18.1
					2000 05 27	
HD092554	P10232	89	287.60	-2.02	2000 05 26	14.7
HD093129A	P11702	85	287.41	-0.57	2000 01 27	3.8
HD093146	P10233	92	287.67	-1.05	2000 02 01	4.1
HD093205	P10236	87	287.57	-0.71	2000 02 01	4.7
HD093206	P10234	93	287.67	-0.94	2000 02 01	4.1
HD093222	P10237	94	287.74	-1.02	2000 02 03	2.9
HD093250	P10238	86	287.51	-0.54	2000 02 04	4.1
HD093827	P10239	96	288.56	-1.54	2000 02 02	4.2
HD093843	P10240	95	288.24	-0.90	2000 02 04	4.1
HD094493	P10241	97	289.02	-1.18	2000 03 26	4.4
HD096670	P10242	99	290.20	0.40	2000 02 01	4.3
HD096715	P10243	100	290.27	0.33	2000 02 01	4.6
HD096917	P10244	98	289.29	3.06	2000 05 26	8.0
HD097913	P12217	101	290.84	1.41	2000 05 26	16.0
HD099857	P10245	105	294.78	-4.94	2000 02 05	4.3
HD099890	P10246	102	291.75	4.43	2000 03 25	4.6
HD100199	P12218	104	293.95	-1.48	2000 03 24	4.6
HD100213	P10247	109	294.81	-4.14	2000 03 24	4.6
HD100276	P10248	103	293.31	0.77	2000 02 01	4.1
HD101131	P10249	106	294.78	-1.62	2000 03 23	4.3
HD101190	P10250	107	294.78	-1.49	2000 02 08	3.4
HD101205	P10251	110	294.85	-1.65	2000 05 27	0.1
HD101298	P10252	111	294.94	-1.69	2000 03 23	4.6
HD101413	P10253	112	295.03	-1.71	2000 03 24	4.2
HD101436	P10254	113	295.04	-1.71	2000 02 05	4.2
HD102552	P10255	114	295.21	1.35	2000 03 19	4.1
HD103779	P10256	115	296.85	-1.02	2000 04 09	47.5
	D07301				2004 04 09	
HD104705	P10257	116	297.46	-0.34	2000 02 05	4.5
HD108639	A12013	117	300.22	1.95	2000 03 20	5.0
HD110432	P11614	118	301.96	-0.20	2000 04 04	3.6
HD112784	Z90150	119	304.00	2.26	2002 04 21	1.4
HD114441	P10258	121	305.80	7.40	2000 03 23	4.4
HD115071	P10259	120	305.77	0.15	2000 05 14	5.9

TABLE 2

Star Name	FUSE Prog ID	Unique ID ^a	l (deg)	b (deg)	Start Date	T_{exp} (ksec) ^b
HD115455	A12007	122	306.06	0.22	2000 05 14	5.7
HD116538	P10260	124	308.23	10.68	2000 05 24	5.9
HD116781	P10261	123	307.05	-0.06	2000 04 06	3.0
HD118571	P12220	126	308.70	1.35	2000 03 25	4.4
HD118969	P12221	125	308.52	-1.39	2000 03 25	11.2
HD122879	B07105	127	312.26	1.79	2002 03 03	1.5
HD124314	P10262	128	312.67	-0.42	2000 03 22	4.4
HD124979	P10263	129	316.41	9.08	2000 07 01	5.1
HD134411	P10265	131	330.07	15.53	2000 07 10	3.9
HD148422	P10150	130	329.92	-5.60	2000 04 08	8.3
					2000 04 10	
					2000 04 12	
HD151805	P10266	132	343.20	1.59	2000 07 14	2.9
HD151932	P11708	133	343.23	1.43	2000 07 12	2.3
HD152200	B02501	135	343.42	1.22	2001 08 09	5.4
HD152218	P10154	140	343.53	1.28	2000 09 08	9.5
HD152233	P10267	138	343.48	1.22	2000 09 08	4.1
HD152245	Z90160	141	344.45	2.02	2002 08 14	1.6
HD152248	P10268	136	343.47	1.18	2000 07 12	4.4
HD152314	P10269	139	343.52	1.14	2000 07 12	4.0
HD152623	P10270	142	344.62	1.61	2000 07 11	6.1
HD152723	P10271	143	344.81	1.61	2000 09 09	5.0
HD153426	P10272	145	347.14	2.38	2000 03 31	5.7
					2000 07 14	
HD156292	P10274	144	345.35	-3.08	2000 04 03	10.8
					2000 04 05	
HD157857	P10275	11	12.97	13.31	2000 09 02	4.0
HD158661	P12222	7	8.29	9.05	2000 09 08	6.6
HD161807	P12223	146	351.78	-5.85	2000 08 17	2.0
					2000 09 08	
HD163758	P10159	147	355.36	-6.10	2000 08 16	5.4
HD163892	P10276	6	7.15	0.62	2001 04 27	12.0
					2001 04 29	
HD164906	P10277	3	6.05	-1.33	2000 08 31	5.3
HD165052	P10278	4	6.12	-1.48	2000 08 31	4.9
HD165955	P10279	148	357.41	-7.43	2000 08 17	4.1
HD167287	P12226	8	11.99	-0.93	2000 08 31	5.8
HD167402	P10162	1	2.27	-6.39	2000 08 31	3.9
HD167659	P10280	9	12.20	-1.27	2000 05 18	5.8
HD167771	P10281	10	12.70	-1.13	2000 08 31	3.8
HD168080	P12227	12	13.11	-1.27	2000 08 31	5.7
HD168941	P10165	2	5.82	-6.31	2000 08 30	8.1
					2000 09 01	
HD175754	P10168	13	16.39	-9.91	2001 04 29	1.9

TABLE 2

Star Name	FUSE Prog ID	Unique ID ^a	l (deg)	b (deg)	Start Date	T_{exp} (ksec) ^b
HD178487	P10172	14	25.79	-8.56	2000 08 27	8.9
HD185418	P11623	15	53.60	-2.17	2000 08 10	4.5
HD186994	P21608	27	78.62	10.06	2001 07 02	0.5
					2001 09 07	
HD187282	P11712	16	55.62	-3.79	2000 08 11	5.2
HD187459	P10282	19	68.81	3.85	2000 08 10	9.9
HD190429	P10284	21	72.59	2.61	2000 07 18	5.4
HD190918	P10285	22	72.65	2.06	2000 07 18	5.5
HD191495	P12229	23	72.74	1.41	2000 08 10	12.2
HD191765	P11713	24	73.45	1.55	2000 07 19	4.5
HD191877	P10287	17	61.57	-6.45	2000 06 05	6.1
HD192035	P10286	28	83.33	7.76	2000 06 17	17.6
					2000 06 19	
					2000 06 21	
HD192639	P11624	25	74.90	1.48	2000 06 12	19.4
	C17101				2002 09 04	
HD195965	P10288	30	85.71	5.00	2000 06 20	36.5
					2000 11 08	
HD199579	P11625	29	85.70	-0.30	2000 07 19	4.3
HD201345	P12230	26	78.44	-9.54	2000 06 13	5.1
HD202347	P10289	31	88.22	-2.08	2000 06 20	4.1
					2000 09 13	
HD207198	P11628	37	103.14	6.99	2000 07 23	10.2
HD210809	P12231	32	99.85	-3.13	2000 08 05	12.1
					2000 08 07	
HD210839	P11631	38	103.83	2.61	2000 07 22	6.1
HD212044	P12234	33	100.64	-4.35	2000 07 23	4.5
HD216044	P12238	39	105.94	-3.64	2000 07 23	5.6
HD218915	P10188	40	108.06	-6.89	2000 07 23	5.4
HD224151	P12241	41	115.44	-4.64	2000 08 11	18.2
					2000 08 13	
HD224868	P12202	42	116.87	-1.44	1999 11 28	5.1
HD326329	B02505	137	343.47	1.17	2001 08 09	5.5
HDE225757	P10177	20	69.64	4.85	2000 08 06	12.1
					2000 08 09	
HDE232522	P12201	45	130.70	-6.71	1999 11 28	2.1
HDE235783	P12233	35	101.69	-1.87	2000 08 05	11.3
HDE235874	P12237	36	101.97	-5.93	2000 07 23	5.4
HDE303308	P12216	91	287.60	-0.61	2000 05 25	13.0
					2000 05 27	
HDE308813	P12219	108	294.80	-1.61	2000 03 23	14.3
HDE315021	P12224	5	6.12	-1.33	2000 08 30	5.4
HDE332407	P12228	18	64.28	3.11	2000 06 10	8.5
					2000 06 12	

TABLE 2

Star Name	<i>FUSE</i> Prog ID	Unique ID ^a	<i>l</i> (deg)	<i>b</i> (deg)	Start Date	T_{exp} (ksec) ^b
LS277	P12208	66	223.34	1.57	2000 03 31	3.3

^aID number corresponding to panel numbers shown in Fig. 24 as well as entries in Tables 1, 4, 5, and 8.

^bTotal exposure time from coadded spectra actually used, summed over all dates and *FUSE* programs

NOTE.—All observations were made with the LWRS aperture except for HD175754, HD041161, and HD069106, which were observed using the MDRS aperture.

TABLE 3
 UV LINES USED IN THE ANALYSIS OF *FUSE* DATA

Line	λ_0 (Å)	<i>f</i> -value
HD 7–0 R(0)	1021.453	0.024
H ₂ 7–0 R(6)	1030.080	not used
H ₂ 6–0 P(3)	1031.192	0.011
Cl I λ 1031.5	1031.507	0.151
H ₂ 8–0 R(8)	1031.557	0.019
HD 6–0 R(0)	1031.909	0.023
O VI λ 1031	1031.927	0.133
H ₂ 6–0 R(4)	1032.354	0.017
O VI λ 1037	1037.617	0.066
H ₂ 7–0 R(8)	1042.745	0.018
H ₂ 5–0 R(4)	1044.542	0.015
HD 4–0 R(0)	1054.286	0.016
H ₂ 6–0 R(8)	1054.520	0.017
H ₂ 4–0 P(3)	1056.472	0.009
H ₂ 4–0 R(4)	1057.376	0.013
H ₂ 4–0 R(8)	1079.932	0.012
Cl I λ 1347 ^b	1347.240	not used

^bMeasured in STIS data, used for calibration of zero point in *FUSE* data.

TABLE 4
VOIGT PROFILE FITS TO DETECTED O VI LINES TOWARD TARGET STARS

ID (1)	Star (2)	ν (3)	b_l (4)	b (5)	b_u (km s ⁻¹) (6)	$\sigma(b)$ (7)	$\sigma(b)_r$ (8)	N_l (9)	N (10)	N_u (11)	$\sigma(N)$ (10 ¹⁴ cm ⁻²) (12)	N_{TOTAL} (13)	ZPF (14)	Cont (15)
1	HD167402	38	60.7	64.9	69.0	2.3	+4.7, -4.8	4.76	5.63	6.41	0.35		F	0
		138	59.6	62.2	65.3	2.7	+4.1, -3.7	3.88	4.43	4.90	0.36	10.05(+1.26, -1.42)		
2	HD168941	20	68.2	70.3	72.3	0.6	+2.1, -2.2	8.51	8.94	9.35	0.07		S	0
3	HD164906	153	51.6	52.5	53.6	2.3	+2.6, -2.5	1.30	1.39	1.47	0.06	10.33(+0.50, -0.52)		
4	HD165052	-20	33.4	35.9	38.6	0.6	+2.8, -2.6	1.07	1.18	1.29	0.02	1.18(+0.12, -0.11)	F	0
5	HDE315021	-23	27.8	30.2	32.7	0.7	+2.6, -2.5	0.75	0.83	0.91	0.01	0.83(+0.08, -0.08)	F	0
6	HD163892	-19	30.3	33.2	36.3	1.0	+3.2, -3.1	0.88	0.99	1.11	0.02	0.99(+0.12, -0.11)	F	0
7	HD158661	-9	23.1	29.8	36.7	2.0	+7.2, -7.0	0.18	0.30	0.44	0.01	0.30(+0.14, -0.12)	F	1
8	HD167287	-2	46.0	51.9	59.8	2.3	+8.2, -6.3	2.84	3.20	3.62	0.09	3.20(+0.43, -0.37)	F	0
9	HD167659	1	48.2	50.5	53.0	0.6	+2.6, -2.4	2.14	2.45	2.74	0.02	2.45(+0.30, -0.31)	F	2
10	HD167771	12	57.2	62.9	69.2	2.4	+6.7, -6.2	1.12	1.37	1.63	0.05	1.37(+0.27, -0.25)	F	0
11	HD157857	-25	53.7	60.7	64.2	1.1	+3.6, -7.1	1.49	1.85	2.17	0.03	1.85(+0.32, -0.36)	F	1
12	HD168080	3	33.4	37.1	41.1	1.4	+4.2, -3.9	1.45	1.64	1.83	0.04	1.64(+0.20, -0.19)	S	0
13	HD175754	2	36.8	40.9	45.5	1.4	+4.8, -4.3	0.98	1.20	1.44	0.04	1.20(+0.24, -0.22)	F	2
14	HD178487	-2	29.1	32.5	36.0	1.1	+3.7, -3.6	0.89	1.07	1.27	0.02	1.07(+0.20, -0.19)	X	0
16	HD187282	-1	21.3	24.2	28.6	1.3	+4.6, -3.2	1.41	1.83	1.98	0.13		F	0
17	HD191877	56	44.6	45.6	55.6	1.3	+10.1, -1.7	3.26	4.10	5.37	0.13	5.94(+1.41, -1.27)		
18	HDE332407	42	38.3	44.0	49.3	1.2	+5.4, -5.8	1.87	2.25	2.64	0.05	2.25(+0.39, -0.39)	X	0
19	HD187459	3	23.9	32.1	44.7	1.0	+12.6, -8.3	0.39	0.53	0.74	0.01	0.53(+0.20, -0.15)	F	2
20	HDE225757	2	32.4	41.0	50.5	1.6	+9.6, -8.7	1.74	2.13	2.58	0.06	2.13(+0.46, -0.39)	F	0
21	HD190429	27	27.2	33.6	41.4	3.1	+8.4, -7.1	0.13	0.21	0.30	0.02	0.21(+0.09, -0.08)	X	0
22	HD190918	0	35.2	38.4	42.1	1.1	+3.9, -3.4	4.11	4.45	4.82	0.08	4.45(+0.38, -0.35)	F	0
23	HD191495	-8	45.6	49.7	53.8	1.8	+4.5, -4.5	1.21	1.39	1.58	0.04	1.39(+0.19, -0.19)	F	0
24	HD191765	-26	38.2	40.3	42.3	0.8	+2.2, -2.2	1.17	1.27	1.38	0.02	1.27(+0.11, -0.11)	S	0
25	HD192639	13	29.9	35.8	41.2	1.1	+5.5, -6.0	0.85	1.01	1.18	0.02	1.01(+0.17, -0.16)	X	0
26	HD201345	0	37.8	43.4	49.3	3.4	+6.8, -6.6	1.01	1.23	1.46	0.06	1.23(+0.25, -0.23)	F	0
27	HD186994	11	21.4	24.8	29.4	3.5	+5.8, -4.9	0.39	0.51	0.66	0.05	0.51(+0.16, -0.13)	S	0
28	HD192035	3	32.3	46.6	58.4	0.9	+11.8, -14.3	0.40	0.75	1.14	0.01	0.75(+0.40, -0.34)	S	2
29	HD195965	0	28.7	31.4	34.3	1.7	+3.4, -3.2	0.66	0.76	0.88	0.03	0.76(+0.11, -0.11)	F	2
30	HD195965	1	33.5	36.0	38.7	1.7	+3.1, -3.0	0.92	1.01	1.11	0.04	1.01(+0.11, -0.10)	S	0
31	HD210809	-15	29.7	33.0	36.0	1.1	+3.2, -3.5	0.15	0.19	0.23	0.00	0.19(+0.04, -0.04)	F	0
32	HD210809	-25	33.3	37.5	41.4	0.8	+4.0, -4.3	0.97	1.25	1.53	0.02	1.25(+0.28, -0.28)	S	2

TABLE 4

ID	Star	v	b_l	b	b_u	$\sigma(b)$	$\sigma(b)_r$	N_l	N	N_u	$\sigma(N)$	N_{TOTAL}	ZPF	Cont
(1)	(2)	(3)	(4)	(5)	(6)	(7)	(8)	(9)	(10)	(11)	(12)	(13)	(14)	(15)
					(km s^{-1})						(10^{14} cm^{-2})			
33	HD212044	24	36.5	52.1	63.5	1.2	+11.4, -15.7	0.36	0.76	1.21	0.02	0.76(+0.45, -0.40)	F	0
34	BD+532820	-14	54.9	63.8	76.9	4.1	+13.7, -9.8	1.20	1.50	1.88	0.08	1.50(+0.38, -0.32)	S	0
35	HDE235783	0	50.0	57.4	72.0	3.8	+15.1, -8.3	0.57	1.85	3.05	0.10	1.85(+1.21, -1.27)	F	2
36	HDE235874	-23	27.5	39.8	54.2	3.5	+14.8, -12.8	0.85	1.29	1.82	0.07	1.29(+0.54, -0.45)	F	2
39	HD216044	-11	54.9	74.2	92.9	2.1	+18.8, -19.4	1.60	2.35	3.18	0.05	2.35(+0.83, -0.74)	F	0
40	HD218915	28	38.4	46.9	52.5	0.8	+5.7, -8.5	0.94	1.74	2.48	0.02	1.74(+0.73, -0.80)	S	0
41	HD224151	-26	28.3	30.5	32.7	1.3	+2.6, -2.6	0.38	0.46	0.54	0.01	0.46(+0.08, -0.08)	S	2
42	HD224868	5	42.4	57.5	71.3	4.7	+14.6, -15.8	0.56	1.06	1.63	0.07	1.06(+0.57, -0.51)	F	0
45	HDE232522	-58	23.4	28.4	33.6	3.3	+6.2, -6.0	0.87	1.06	1.27	0.07	1.06(+0.22, -0.20)	S	2
50	HD017520	-19	35.3	41.8	48.1	2.9	+6.9, -7.1	1.07	1.38	1.70	0.08	1.38(+0.33, -0.32)	F	0
53	HD034656	13	32.1	35.1	38.3	0.5	+3.2, -3.0	0.83	0.95	1.08	0.01	0.95(+0.13, -0.12)	F	0
54	HD042087	27	3.2	20.2	29.0	3.9	+9.6, -17.4	0.37	0.52	0.83	0.06	0.52(+0.31, -0.16)	F	2
55	HD042088	9	17.0	22.9	29.7	2.4	+7.2, -6.4	0.20	0.37	0.56	0.03	0.37(+0.20, -0.17)	F	0
56	HD030677	13	17.4	23.3	29.3	0.9	+6.1, -6.0	0.17	0.31	0.47	0.02	0.31(+0.16, -0.14)	F	2
57	HD039680	23	24.5	30.2	39.2	1.5	+9.1, -5.9	0.38	0.54	0.74	0.02	0.54(+0.21, -0.16)	F	0
58	HD045314	45	62.7	66.6	70.9	0.6	+4.3, -3.9	2.70	2.95	3.21	0.02	2.95(+0.26, -0.24)	F	0
60	HD047417	22	32.6	36.1	39.3	0.7	+3.3, -3.6	0.99	1.26	1.52	0.02	1.26(+0.26, -0.27)	F	2
61	HD047088	32	47.7	52.3	57.2	0.4	+4.9, -4.6	2.03	2.29	2.56	0.02	2.29(+0.27, -0.26)	F	0
62	HD046150	18	28.8	31.9	35.5	1.2	+3.8, -3.3	0.57	0.66	0.75	0.02	0.66(+0.09, -0.09)	F	0
63	HD046202	23	13.6	16.4	19.9	2.4	+4.3, -3.7	0.54	0.65	0.78	0.06	0.65(+0.13, -0.12)	F	2
64	HD047360	17	23.5	27.7	32.7	2.3	+5.5, -4.8	0.65	0.81	0.99	0.05	0.81(+0.19, -0.17)	F	0
65	HD065079	9	26.8	30.5	34.6	1.1	+4.3, -3.9	0.37	0.44	0.52	0.01	0.44(+0.08, -0.07)	F	0
66	LS277	16	26.8	30.1	34.2	2.4	+4.7, -4.1	0.99	1.16	1.35	0.06	1.16(+0.20, -0.18)	F	2
67	HD061347	48	34.3	41.3	50.8	2.0	+9.7, -7.3	1.67	2.16	2.70	0.09	2.16(+0.54, -0.49)	F	1
68	HD058510	41	32.6	36.3	40.1	0.7	+3.9, -3.8	1.23	1.54	1.85	0.02	1.54(+0.31, -0.31)	F	2
69	HD062866	71	42.7	48.1	54.2	3.7	+7.1, -6.6	1.04	1.22	1.44	0.08	1.22(+0.22, -0.20)	F	0
71	HD063005	43	35.9	39.1	42.5	0.9	+3.5, -3.3	1.73	1.92	2.11	0.03	1.92(+0.20, -0.19)	S	2
72	HD060369	47	20.8	25.6	31.1	1.4	+5.7, -5.0	0.47	0.71	0.96	0.03	0.71(+0.26, -0.24)	F	2
73	HD060196	42	30.9	30.9	38.4	1.4	+7.7, -1.4	1.34	1.44	1.70	0.05	1.44(+0.26, -0.12)	X	1
74	HD064568	60	31.6	38.3	45.8	1.2	+7.6, -6.8	1.22	1.54	1.89	0.04	1.54(+0.35, -0.32)	F	0
75	HD066788	48	39.7	43.2	47.0	0.6	+3.9, -3.6	2.17	2.40	2.64	0.03	2.40(+0.24, -0.23)	S	0
76	HD069106	18	41.9	44.5	47.2	0.9	+2.9, -2.8	1.89	2.12	2.35	0.04	2.12(+0.23, -0.23)	S	0

TABLE 4

ID	Star	v	b_l	b	b_u	$\sigma(b)$	$\sigma(b)r$	N_l	N	N_u	$\sigma(N)$	N_{TOTAL}	ZPF	Cont
(1)	(2)	(3)	(4)	(5)	(6)	(7)	(8)	(9)	(10)	(11)	(12)	(13)	(14)	(15)
					(km s^{-1})						(10^{14} cm^{-2})			
77	HD074920	-32	26.9	34.1	40.7	4.8	+8.2, -8.6	0.49	0.72	0.86	0.15		F	1
		22	31.0	30.9	33.1	1.9	+2.9, -1.9	1.24	1.24	1.31	0.15	1.96(+0.21, -0.23)		
78	HD074711	8	25.8	28.9	32.2	1.8	+3.8, -3.6	0.59	0.70	0.82	0.04	0.70(+0.12, -0.12)	F	0
79	HD075309	-73	32.4	35.6	38.2	0.4	+2.6, -3.2	2.51	2.93	3.31	0.02		S	1
		33	10.2	20.4	26.3	1.7	+6.1, -10.3	0.24	0.44	0.67	0.03	3.37(+0.62, -0.62)		
80	HD089137	17	18.1	32.1	38.7	0.8	+6.6, -14.0	0.38	0.95	1.47	0.02	0.95(+0.53, -0.57)	F	0
81	HD090087	16	30.1	31.9	33.8	0.7	+2.0, -1.9	1.16	1.25	1.35	0.02	1.25(+0.10, -0.10)	F	0
82	HD088115	18	27.2	39.2	45.5	5.0	+8.1, -13.0	0.66	1.45	2.16	0.09	1.45(+0.71, -0.79)	S	2
83	HD091651	-83	36.3	36.6	37.3	1.3	+1.4, -1.3	0.77	0.86	0.91	0.03		S	0
		-3	33.6	38.9	44.7	0.5	+5.8, -5.3	1.89	2.30	2.75	0.03	3.16(+0.51, -0.51)		
84	HD091597	3	33.1	34.4	35.8	0.5	+1.5, -1.4	3.05	3.17	3.29	0.03	3.17(+0.13, -0.13)	S	0
85	HD093129A	-37	52.9	59.8	67.5	0.7	+7.7, -6.9	3.91	4.72	5.55	0.04	4.72(+0.83, -0.81)	X	0
86	HD093250	-107	15.4	16.7	18.1	0.9	+1.6, -1.6	0.77	0.83	0.88	0.03		F	0
		-14	50.2	52.0	53.9	0.8	+2.1, -2.0	3.32	3.51	3.70	0.05	4.33(+0.25, -0.25)		
87	HD093205	-110	11.3	13.2	14.9	2.5	+3.0, -3.2	0.15	0.17	0.19	0.02		S	0
		-8	20.0	20.0	20.0	1.7	+1.7, -1.7	0.32	0.55	0.55	0.06			
		-8	49.2	74.3	80.6	2.7	+6.9, -25.2	1.32	1.94	2.61	0.05	2.66(+0.68, -0.87)		
88	CPD-592603	-12	30.5	34.8	39.0	1.7	+4.5, -4.6	1.27	1.57	1.87	0.05	1.57(+0.31, -0.30)	S	0
89	HD092554	-48	31.0	33.0	36.9	2.8	+4.8, -3.4	0.98	1.01	1.11	0.16		S	0
		5	32.7	34.5	36.2	0.9	+1.9, -2.0	3.19	3.36	3.54	0.16	4.38(+0.28, -0.20)		
90	CPD-592600	-32	23.3	38.1	27.8	3.3	+10.8, -15.2	0.69	0.69	0.90	0.02		F	1
		3	33.7	26.0	43.0	1.5	+17.1, -7.9	0.65	0.80	0.74	0.02	1.48(+0.16, -0.15)		
91	HDE303308	-106	16.5	10.3	4.9	1.9	+5.7, -6.5	0.68	0.34	0.28	0.03		S	0
		-45	49.1	71.2	82.6	1.2	+11.5, -22.1	3.81	4.37	5.41	0.10			
		-12	17.5	28.8	28.4	1.4	+1.4, -11.4	0.64	1.42	1.46	0.10	6.13(+1.02, -1.00)		
92	HD093146	-49	83.6	83.6	83.6	1.7	+1.7, -1.7	3.72	3.89	4.07	0.04		F	0
		-8	32.6	32.6	32.6	1.3	+1.3, -1.3	1.70	1.68	1.66	0.06			
		66	33.2	33.2	33.2	2.6	+2.6, -2.6	0.55	0.58	0.62	0.05	6.15(+0.19, -0.20)		
93	HD093206	-232	70.3	75.2	79.8	1.1	+4.7, -5.0	1.66	1.67	2.09	0.02		F	0
		-78	44.7	44.7	44.7	1.4	+1.4, -1.4	1.39	1.44	1.48	0.06			
		0	41.8	42.7	43.6	0.6	+1.1, -1.1	3.18	3.29	3.40	0.05	6.60(+0.36, -0.37)		
94	HD093222	-77	39.0	42.0	47.6	2.4	+6.1, -3.9	1.42	1.59	1.78	0.12		S	0

TABLE 4

ID	Star	v	b_l	b	b_u	$\sigma(b)$	$\sigma(b)_r$	N_l	N	N_u	$\sigma(N)$	N_{TOTAL}	ZPF	Cont
(1)	(2)	(3)	(4)	(5)	(6)	(7)	(8)	(9)	(10)	(11)	(12)	(13)	(14)	(15)
					(km s^{-1})						(10^{14} cm^{-2})			
95	HD093843	-2	38.5	42.0	46.5	1.1	+4.6,-3.7	3.23	3.60	3.97	0.12	5.20(+0.55,-0.54)	S	0
96	HD093827	-11	41.0	44.9	48.6	0.4	+3.7,-3.9	2.18	2.46	2.74	0.02	2.46(+0.28,-0.28)	F	0
		-45	33.0	44.2	59.0	9.9	+17.8,-14.9	0.69	1.22	1.87	0.32		F	0
97	HD094493	18	28.0	32.1	38.3	6.6	+9.1,-7.8	0.80	0.99	1.10	0.28	2.21(+0.76,-0.73)	S	2
98	HD096917	-1	22.1	24.3	26.4	0.5	+2.2,-2.3	0.96	1.10	1.24	0.02	1.10(+0.14,-0.14)	F	0
		-49	20.7	20.7	20.7	2.4	+2.4,-2.4	0.80	1.12	1.42	0.14		F	0
		26	59.3	59.3	59.3	3.6	+3.6,-3.6	1.70	3.33	4.53	0.19	4.45(+1.50,-1.96)		
99	HD096670	2	14.6	18.9	24.3	2.8	+6.1,-5.2	0.81	1.06	1.34	0.09	1.06(+0.29,-0.27)	F	0
100	HD096715	-97	34.6	38.8	46.4	4.1	+8.6,-5.9	0.79	1.04	1.49	0.10		F	0
		0	38.5	44.0	48.7	3.4	+5.8,-6.5	1.36	1.62	2.08	0.08	2.66(+0.91,-0.52)		
101	HD097913	0	27.8	30.7	33.8	0.8	+3.2,-3.0	1.50	1.72	1.94	0.03	1.72(+0.22,-0.22)	F	1
102	HD099890	-48	22.7	25.2	27.8	4.7	+5.4,-5.3	0.28	0.34	0.40	0.10		S	0
		0	27.3	29.4	31.4	1.8	+2.7,-2.8	1.06	1.21	1.35	0.11	1.54(+0.20,-0.21)		
103	HD100276	0	19.7	24.5	29.2	2.0	+5.1,-5.2	0.21	0.32	0.44	0.02	0.32(+0.12,-0.11)	F	2
104	HD100199	7	28.1	29.3	30.6	1.2	+1.8,-1.7	0.79	0.84	0.88	0.02	0.84(+0.05,-0.05)	F	0
105	HD099857	3	20.6	23.7	26.5	1.7	+3.3,-3.5	0.50	0.62	0.75	0.03	0.62(+0.13,-0.12)	S	2
106	HD101131	-8	28.8	30.9	33.2	0.5	+2.4,-2.2	1.34	1.45	1.57	0.02	1.45(+0.12,-0.12)	F	0
107	HD101190	-8	41.4	43.2	45.3	0.7	+2.2,-1.9	1.96	2.06	2.15	0.03	2.06(+0.10,-0.10)	F	0
108	HDE308813	-15	31.9	33.3	34.7	1.1	+1.8,-1.8	1.54	1.63	1.71	0.02	1.63(+0.09,-0.08)	S	0
109	HD100213	-7	25.2	29.6	35.1	3.5	+6.5,-5.6	0.54	0.65	0.78	0.19		F	0
		45	38.6	43.2	49.3	5.3	+8.1,-7.0	1.04	1.26	1.48	0.20	1.91(+0.35,-0.33)		
110	HD101205	-10	36.4	43.2	53.2	2.9	+10.4,-7.4	2.44	2.80	3.27	0.15	2.80(+0.49,-0.38)	F	0
111	HD101298	-10	39.0	40.6	42.3	1.2	+2.1,-2.0	1.79	1.86	1.94	0.05	1.86(+0.08,-0.08)	F	0
112	HD101413	-7	35.8	37.7	39.8	1.2	+2.4,-2.2	1.76	1.88	2.00	0.05	1.88(+0.13,-0.12)	F	0
113	HD101436	-23	33.1	37.1	41.7	0.8	+4.7,-4.1	1.63	1.84	2.06	0.03	1.84(+0.22,-0.21)	F	0
115	HD103779	2	23.6	27.9	31.2	0.6	+3.3,-4.3	0.20	0.32	0.43	0.00	0.32(+0.11,-0.11)	S	2
116	HD104705	-16	44.9	54.7	76.9	1.0	+22.2,-9.8	0.91	1.21	1.71	0.02	1.21(+0.50,-0.30)	S	0
117	HD108639	28	56.0	60.9	66.1	1.7	+5.5,-5.2	1.14	1.29	1.46	0.03	1.29(+0.17,-0.16)	F	0
118	HD110432	37	13.7	16.2	19.0	3.8	+4.7,-4.6	0.08	0.10	0.12	0.01	0.10(+0.03,-0.02)	F	0
119	HD112784	11	49.6	54.3	58.6	1.4	+4.5,-4.9	1.86	2.24	2.63	0.05	2.24(+0.39,-0.39)	F	0
120	HD115071	-8	32.6	35.8	39.2	2.0	+3.9,-3.8	1.23	1.39	1.55	0.05	1.39(+0.17,-0.16)	F	0
122	HD115455	-10	38.3	43.5	49.5	1.3	+6.1,-5.4	1.80	2.09	2.40	0.05	2.09(+0.31,-0.29)	F	0

TABLE 4

ID (1)	Star (2)	v (3)	b_l (4)	b (5)	b_u (km s ⁻¹) (6)	$\sigma(b)$ (7)	$\sigma(b)_r$ (8)	N_l (9)	N (10)	N_u (11)	$\sigma(N)$ (10 ¹⁴ cm ⁻²) (12)	N_{TOTAL} (13)	ZPF (14)	Cont (15)
123	HD116781	16	54.6	65.1	80.4	2.0	+15.4, -10.7	0.78	1.19	1.68	0.03	1.19(+0.50, -0.40)	S	0
124	HD116538	5	27.1	29.6	32.7	1.6	+3.5, -3.0	0.24	0.28	0.33	0.01	0.28(+0.05, -0.04)	F	0
125	HD118969	-14	45.2	51.1	55.9	1.0	+4.9, -6.0	1.66	2.06	2.46	0.04	2.06(+0.40, -0.40)	F	0
126	HD118571	-19	37.2	40.1	43.0	0.8	+3.0, -3.0	1.35	1.49	1.64	0.02	1.49(+0.15, -0.14)	F	0
127	HD122879	-18	18.6	20.7	23.2	1.5	+2.9, -2.6	0.40	0.45	0.51	0.02	0.45(+0.06, -0.06)	S	0
128	HD124314	-9	20.0	22.8	26.0	1.4	+3.5, -3.1	0.56	0.63	0.71	0.03	0.63(+0.08, -0.07)	S	0
129	HD124979	-4	36.1	39.0	42.4	2.5	+4.2, -3.8	1.17	1.29	1.43	0.07	1.29(+0.15, -0.14)	F	0
130	HD148422	-5	27.1	34.7	42.6	2.1	+8.2, -7.9	1.02	1.32	1.64	0.07	1.32(+0.33, -0.30)	F	0
131	HD134411	-17	16.2	20.0	24.9	1.4	+5.1, -4.1	0.29	0.36	0.45	0.02	0.36(+0.09, -0.08)	S	0
132	HD151805	-5	36.6	40.7	45.0	3.0	+5.3, -5.1	1.05	1.23	1.42	0.07	1.23(+0.20, -0.19)	S	0
133	HD151932	7	38.4	42.4	47.7	1.9	+5.6, -4.4	1.46	1.65	1.86	0.06	1.65(+0.21, -0.19)	F	0
134	CPD-417712	8	31.2	43.9	56.2	1.7	+12.4, -12.8	1.03	1.82	2.66	0.06	1.82(+0.84, -0.79)	F	0
135	HD152200	0	40.9	44.3	47.8	1.1	+3.7, -3.6	2.15	2.43	2.71	0.05	2.43(+0.28, -0.28)	F	0
136	HD152248	12	40.3	43.0	45.9	0.8	+3.0, -2.8	1.89	2.06	2.24	0.03	2.06(+0.18, -0.17)	F	0
137	HD326329	14	43.2	54.3	70.6	1.5	+16.4, -11.2	1.85	2.83	3.97	0.06	2.83(+1.14, -0.99)	F	0
138	HD152233	9	44.1	45.6	47.2	0.8	+1.8, -1.7	2.06	2.14	2.23	0.03	2.14(+0.09, -0.09)	F	0
139	HD152314	1	27.5	32.8	38.1	3.8	+6.5, -6.5	0.66	1.02	1.39	0.09	1.02(+0.38, -0.37)	F	0
140	HD152218	4	45.9	53.6	59.9	1.7	+6.5, -7.9	1.79	2.63	3.41	0.07	2.63(+0.78, -0.85)	F	0
141	HD152245	-10	47.2	52.6	57.8	1.9	+5.5, -5.7	1.74	2.15	2.56	0.06	2.15(+0.41, -0.41)	F	0
142	HD152623	-4	37.6	40.9	44.1	0.4	+3.2, -3.3	2.29	2.57	2.86	0.02	2.57(+0.28, -0.29)	F	1
143	HD152723	-17	44.2	49.2	54.1	0.7	+5.0, -5.0	2.29	2.68	3.08	0.03	2.68(+0.40, -0.39)	F	0
144	HD156292	-15	35.2	40.4	46.0	1.0	+5.7, -5.3	1.80	2.09	2.39	0.04	2.09(+0.31, -0.29)	F	2
145	HD153426	-10	38.4	39.5	40.6	0.7	+1.3, -1.3	1.84	1.91	1.98	0.02	1.91(+0.07, -0.07)	F	0
146	HD161807	-11	37.8	39.2	40.7	0.4	+1.6, -1.5	1.58	1.65	1.72	0.01	1.65(+0.07, -0.07)	F	0
147	HD163758	0	42.9	50.1	57.1	0.8	+7.0, -7.2	2.66	3.22	3.79	0.04	3.22(+0.57, -0.56)	F	0
148	HD165955	-22	26.3	28.2	30.4	1.5	+2.7, -2.4	0.55	0.61	0.68	0.02	0.61(+0.07, -0.06)	S	0

NOTE.—Explanation of columns: (1)—ID number corresponding to panel numbers shown in Fig. 24; (2)—star name; (3)—heliocentric velocity of Voigt-profile fit to the O VI absorption line; (4, 5, 6)—Doppler parameter of fit, for data normalized by lower, best, and upper continuum fits (see §2.6); (7)—Error in Doppler fit from Monte-Carlo simulations (§2.8.1); (8)—Final error in Doppler fit, combining $(b - b_l)$ or $(b_u - b)$ in quadrature with $\sigma(b)$

(§2.8.1); (9,10,11)—O VI column density of fit, for data normalized by lower, best, and upper continuum fits; (12)—Error in O VI column density from Monte-Carlo simulations; (13)—Total O VI column density summed over all components. (If only one component was fitted, this number is just a repeat of the value in column 10). The final error in the O VI column density is given in parentheses (see §2.8.1). (14)—Zero-point flag: indication of correction applied to wavelength zero-point: ‘S’—FUSE data shifted to match H₂ lines flanking O VI λ 1032 line with CI I λ 1347 line in STIS echelle data. For these data, the uncertainty in the velocity of the measured absorption lines is $\simeq 1.5 - 3.0 \text{ km s}^{-1}$; ‘X’—FPALXPOS > 200, MDRS aperture used, or not LiF1a channel data (and no STIS data available). Hence no correction made, and the error in the velocity of the absorption lines is unknown; ‘F’ — LiF1a data taken through LWRs aperture, and FPALXPOS < 200, so fixed offset of +10 km s⁻¹ applied. The uncertainties in v are $\simeq 5 \text{ km s}^{-1}$. See Appendix A for full details; (15)—Continuum selection flag: indicates potential ambiguity in the decisions made in selecting how a continuum should be applied to the stellar flux: ‘0’ — no ambiguity; ‘1’ — continuum could have been chosen to follow a significantly different path than the one adopted either side of the O VI line; ‘2’ — continuum could have been chosen to follow a significantly different path than the one adopted to the red side of the O VI. See §2.6 for a detailed schema of the selection of continua.

TABLE 5
AOD COLUMN DENSITY UPPER LIMITS TOWARDS STARS WITH NO DETECTED O VI

ID	Star	N_l	N	N_u	$\sigma(N)$	$\sigma(N)_T$	N_{limit}^a
(1)	(2)	(3)	(4)	(5)	(6)	(7)	(8)
15	HD185418	-3.11	0.58	3.95	0.45	3.56	8.52
29	HD199579	-0.17	0.55	1.37	0.28	0.82	2.29
31	HD202347	-0.94	0.22	1.29	0.16	1.13	2.72
37	HD207198	-2.01	0.17	2.28	0.94	2.34	5.45
38	HD210839	-1.50	-0.67	0.12	0.34	0.88	1.59
43	HD000108	-2.24	-0.33	1.43	0.69	1.96	4.25
44	HD005005A	-0.74	0.23	1.11	0.44	1.02	2.49
46	HD012323	-2.12	-0.49	1.10	0.44	1.67	3.47
47	HD013268	-1.18	0.25	1.62	1.10	1.78	4.22
48	HD013745	-4.00	1.27	5.94	1.10	5.09	12.52
49	HD014434	-9.44	-2.17	3.95	1.72	6.91	14.30
51	HD015137	-4.94	-1.06	2.26	0.99	3.74	7.81
52	HD041161	-1.78	-0.52	0.69	0.27	1.26	2.54
59	HD042401	-2.64	0.32	2.22	0.70	2.53	5.98
70	HD052463	-0.09	1.06	2.20	0.31	1.18	3.53
114	HD102552	-0.00	2.85	5.29	1.12	2.87	8.81
121	HD114441	-0.44	1.38	2.88	0.41	1.71	4.96

^a 2σ confidence upper limit. See §2.8.2 and Appendix D for details.

TABLE 6
REJECTED STARS FROM THE *FUSE* DISK SURVEY

Prog ID	Star Name	l (deg)	b (deg)	Sp/L ^a	Start Date	T_{exp} (ksec)
P10207	HD015642	137.09	-4.73	O9.5III:n	2000 09 15	5.1
P10224	HD074194	264.04	-1.95	O8.5Ibf	1999 12 27	3.4
P10235	HD093204	287.57	-0.71	O5Vf	2000 02 01	4.7
P12205	HD035215	176.46	-3.19	B1V	2000 02 29	10.1
P12212	HD066695	245.01	2.21	B0.5IV	2000 01 24	8.2
P12225	HD166546	10.36	-0.92	O9.5II-III	2000 09 03	3.4
P12235	BD+523210	102.44	-3.37	B1V	2000 08 06 2000 08 09	15.7
P12236	BD+532885	102.75	-2.93	B2III	2000 08 02 2000 08 05	11.8
P12239	HD216438	105.72	-5.12	B1II-III	2000 07 22	5.1

^aSpectral Type and Luminosity Class of star

TABLE 7
STARS OBSERVED AT MORE THAN ONE EPOCH

Unique ID	Star	Date	FUSE root	Aperture	Channel	T_{exp} (ksec)	$N(\text{O VI})^a$ (10^{14} cm^{-2})
84	HD091597	2001-02-04/06/08	P1023002/3/4	LWRS ^b	LiF1A	14.3	3.17 ± 0.12
		2003-06-13	D0640301	LWRS	LiF1A	13.5	3.14 ± 0.13
76	HD069106	2001-04-04	P1022301	LWRS	LiF1A	0.06	1.99 ± 0.28
		2002-12-31	P1022302	MDRS ^b	LiF1A	0.4	2.12 ± 0.23^c
62	HD046150	2001-03-05	P1021401	LWRS ^b	LiF1A	4.9	0.96 ± 0.16
		2004-02-25	C1680201	LWRS ^b	LiF1A	3.7	0.80 ± 0.13
		2004-02-24	P1021402/3	MDRS	LiF1A	16.3	0.90 ± 0.22^c
25	HD192639	2000-06-12	P1162401	LWRS ^b	LiF1A	4.8	0.90 ± 0.39
		2002-09-04	C1710101	LWRS ^b	LiF1A	14.6	0.25 ± 0.42
43	HD000108	2002-08-31	Z9010101	LWRS ^b	LiF1A	4.8	< 0.63
		2003-08-05	D0640101	LWRS ^b	LiF1A	3.1	< 0.62
115	HD103779	2000-04-09	P1025601	LWRS ^b	LiF1A	4.3	0.54 ± 0.11
		2004-04-09	D0730101/2	LWRS ^b	LiF1A	43.2	0.46 ± 0.13

^aColumn densities derived from profile fitting, with HD 6-0 R(0) line removed, as described in §2.8.1.

^bThese datasets were eventually coadded for each star to produce a final spectrum.

^cAssuming a MDRS instrumental resolution of 3 km s^{-1} FWHM (Feldman et al. 2001).

TABLE 8
FUSE SIGHT LINES PROJECTED THROUGH SNRS^a

Unique ID	Target star	Star's distance (kpc)	SNR Ident.	SNR's distance (kpc)	Ref. ^b
12	HD168080	2.7	G13.3 -1.3	2.0-4.7	1
15	HD185418	0.8	G53.6 +5.7 ^c	6.7	2
29	HD199579	1.1	G85.9 -0.6	5.	3
60	HD047417	1.2	G205.5 +0.5 ^d	0.8	4,5
77	HD074920 ^e	1.5	G266.2 -1.2	0.3 ^f	6
79	HD075309	1.5	G266.2 -1.2	0.3 ^f	6
128	HD124314	1.1	G312.4 -0.4	?	...
131	HD134411	2.1	G330.0 +15.0 ^g	0.5:	7

^aExcluding sight lines intercepting Vela

^bReferences for distance estimates: [1] Seward et al. 1995, [2] Rosado 1983, [3] Kothes et al. 2001, [4] Kirshner, Gull, & Parker 1978, [5] Lozinskaya 1981, [6] Redman et al. 2002, [7] Milne 1979

^c3C400.2

^dMonoceros Nebula (not to be confused with the much larger Monogem Ring)

^eThe star is located on the edge of the SNR, so the sight-line interception, even if the SNR is in the foreground, is uncertain.

^fThis SNR is presumed to be within the Vela SNR; see text for details.

^gThe Lupus Loop

TABLE 9
LINE OF SIGHT VOLUME DENSITIES OF O VI IN THE GALACTIC PLANE

(1)	No. (2)	$\langle \log[N(\text{O VI})/d] \rangle$ [log (cm ⁻³)] (3)	$\log \Sigma N(\text{O VI})/\Sigma d$ [log (cm ⁻³)] (4)
<i>stellar distances > 2000 pc</i>			
+LB, All <i>R</i>	102	-7.87 ± 0.32	-7.79
+LB, <i>R</i> = 0	56	-7.92 ± 0.31	-7.79
+LB, <i>R</i> > 0	46	-7.82 ± 0.32	-7.79
-LB, All <i>R</i>	96	-7.92 ± 0.36	-7.81
-LB, <i>R</i> = 0	55	-7.97 ± 0.36	-7.81
-LB, <i>R</i> > 0	41	-7.87 ± 0.36	-7.62
<i>200 pc < stellar distances < 2000 pc</i>			
+LB, All <i>R</i>	88	-7.75 ± 0.31	-7.69
+LB, <i>R</i> = 0	42	-7.78 ± 0.33	-7.75
+LB, <i>R</i> > 0	46	-7.73 ± 0.29	-7.64
-LB, All <i>R</i>	81	-7.91 ± 0.45	-7.72
-LB, <i>R</i> = 0	37	-7.96 ± 0.48	-7.81
-LB, <i>R</i> > 0	44	-7.86 ± 0.42	-7.66

NOTE.—Description of columns: (1)— “-LB” indicates that a contribution from the Local Bubble, [$N_{\text{LB}}(\text{O VI}) = 1.11 \times 10^{13} \text{ cm}^{-2}$] has been removed from all column densities, while “+LB” indicates that no such correction has been made; *R* indicates the *ROSAT* class assigned in §3.4 and §3.5; for the -LB samples, distances have also been reduced by the radius of the LB, which we take to be 100 pc; (2) — number of points used in statistical test. (Note that the numbers in the +LB sample for a given *ROSAT* class in each distance category are not quite the same as the number for the equivalent -LB class; this is because subtracting 100 pc for the -LB stars moves a few objects either from the far to near sample, or out of the near sample altogether.); (3) — mean of $\log N(\text{O VI})/d$ and the standard deviation of the distribution of column densities (see §3.7.1); (4) — distance weighted average of O VI column densities. Note: None of the statistics above include sightlines to Carina or Vela.

A. THE ZERO-POINT OF THE *FUSE* WAVELENGTH SCALE

As discussed in §2.4, measuring precise velocities for O VI absorption lines potentially requires a correction for any errors which might exist in the *FUSE* wavelength-scale zero-point associated with CalFUSE v2.0.5. Fortunately, many of the stars in our sample have also been observed with the *Space Telescope Imaging Spectrograph* (STIS) aboard *HST*, which has a well determined wavelength scale. In particular, a substantial number of E140M and E140H echelle data have been recorded which cover the Cl I $\lambda 1347$ line. According to the STIS Handbook, the relative accuracy of the STIS echelle modes is 0.25–0.5 pixels across the full format of the MAMA detectors, and the absolute accuracy is 0.5–1.0 pixels (Kim Quijano 2004). Somewhat larger wavelength-scale errors have been found in some STIS echelle spectra (Jenkins & Tripp 2001; Tripp et al. 2005) indicating relative wavelength scale accuracies ≈ 1 pixel. To be conservative, we assume that the uncertainty in the STIS wavelength calibration is ≈ 1 pixel. This corresponds to 1.5 and 3.0 km s⁻¹ for the E140H and E140M STIS gratings, respectively.

To derive corrections to the *FUSE* wavelength scale, we compared absorption lines of neutral chlorine with the molecular hydrogen lines flanking the O VI features, along individual stellar sight lines; H₂ clouds are efficient producers of Cl I (Jura 1974; Jenkins 1995), so a direct comparison between the H₂ lines which flank the O VI $\lambda 1032$ absorption in the *FUSE* data, and a strong (but unsaturated) Cl I line whose velocity is known precisely, should provide a suitable anchor to the *FUSE* wavelength scale. While in principle we could have used the Cl I $\lambda 1031.5$ Å line (see Table 3 and Figure 1), it was often too weak, or absent altogether, for its wavelength to be measured.

The STIS data are recorded at higher resolution than the *FUSE* spectra, so in order to compare the H₂ and Cl I lines directly, we smoothed the STIS data, scaled the Cl I to match the strength of the H₂ 6–0 R(4) and P(3) lines, and shifted the *FUSE* spectrum in wavelength space until the lines overlapped. The shape of the smoothed Cl I line well matched the *FUSE* H₂ line profiles in all cases, and we were able to record shifts to within ± 0.2 pixels, or just over 1 km s⁻¹ at the wavelength of the O VI $\lambda 1032$ line.

Apart from 46 sight lines in our Galactic disk sample which had also been observed with STIS, we were able to examine *FUSE* and STIS spectra of a few other non-survey stars. A total of 55 *FUSE* and STIS spectra enabled us to investigate whether the errors in the *FUSE* wavelength scale were dependent on the state of the spectrograph. We found a crude correlation between the more extreme shifts in the wavelength zero-point and the X-position of the Focal Plane Assembly, as recorded in the FPALXPOS keyword of the LiF1A headers. The data used in the study are listed in Table 10, while the measured shifts and their values of FPALXPOS are shown in Figure 20. We found no correlation between measured shifts and the Z-position of the FPA, as recorded in the data header keyword FPALZPOS.

We note the following in Figure 20. The error bars in the ordinate direction are *not* statistical errors. As explained in §2.3, we used the sub-spectrum with the highest S/N ratio to act as a template against which the other sub-exposures were compared before sub-exposures were coadded. The bars in Figure 20 represent the minimum and maximum excursions in the values of the shifts measured for a set of sub-exposures.

The majority of the *FUSE* spectra were taken with FPALXPOS in the range 117.0–175.0. For these data, a consistent shift of $\sim +10$ km s⁻¹ is required to correct the *FUSE* wavelength scale. (Again, this shift was not necessarily the shift of the first sub-exposure taken of a star, but was derived from the sub-exposure with the highest S/N.) The histogram on the right-hand side of Figure 20 shows the distribution of the shifts, along with a Gaussian fit to the distribution, which peaks at 9.2 km s⁻¹ and has a width of $\sigma = 5.1$ km s⁻¹. This implies that a +10 km s⁻¹ shift to *FUSE* data which have no companion STIS data will provide an accurate re-calibration of the wavelength scale to within ± 5 km s⁻¹.

With this information, we applied the following re-calibration to the survey stars. For the 46 stars also observed by STIS, the *FUSE* data were shifted by the numbers given in Table 10. Nine stars were observed either with the MDRS aperture, with a channel other than the LiF1A, or when the X-position of the FPA was > 200 ; no shifts were applied to these data. The remaining 93 spectra were shifted in wavelength by 0.0344 Å, or 10 km s⁻¹ at 1032 Å.

Finally, we note that later versions of CalFUSE (v3.0) automatically applied a correction of 10 km s⁻¹ to the zero-point of the wavelength calibration to correct for the offset described above. Versions of CalFUSE later than v3.2 used an improved scheme for the wavelength calibration of the raw data as a whole, reductions which are described in detail by Dixon et al. (2007).

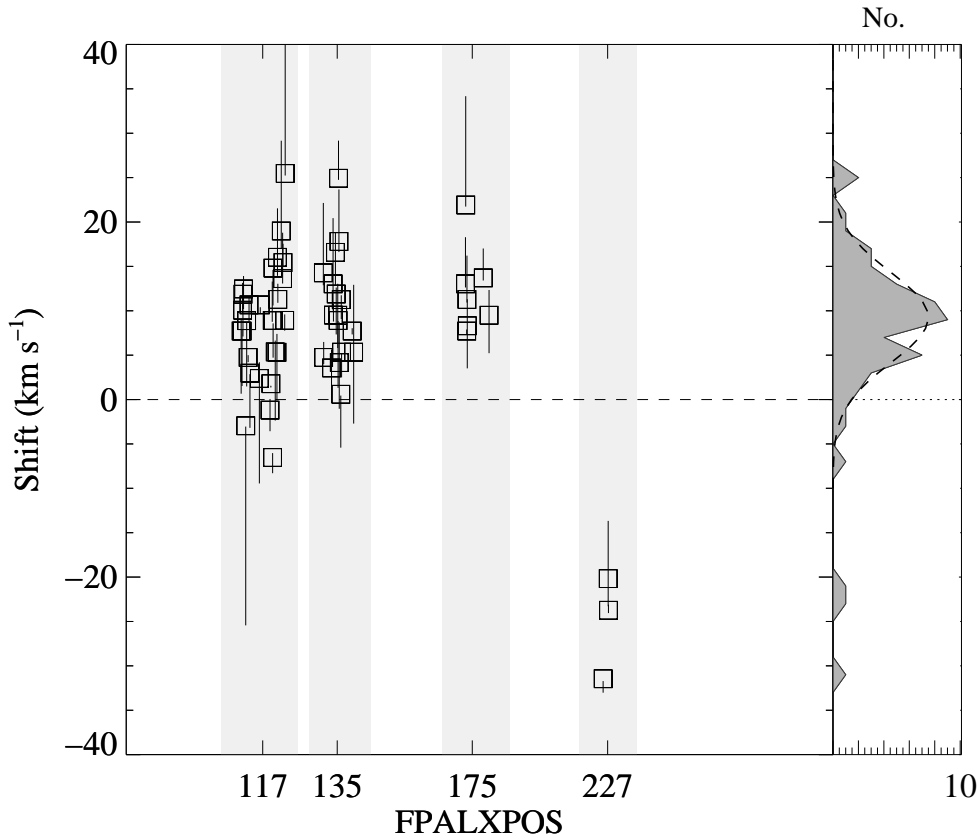


Figure 20: Plot of the shifts required to accurately calibrate the zero-point of the *FUSE* wavelength scale around the O VI $\lambda 1032$ line, as a function of X-position of the Focal Plane Assembly (as determined from the FPALXPOS keyword in the LiF1A headers). Values of FPALXPOS for our data fall close to one of four values: 117, 135, 175 and 227. To better show the error bars in the Y direction (see text for a full explanation of the error bars), we have randomized the FPALXPOS values by small amounts to make the points slightly offset from each other. It should be understood that points within a particular gray box actually have FPALXPOS values almost identical to the value shown on the X-axis at the bottom of each gray box. The distribution of the shifts is shown as a histogram to the right. For spectra with FPALXPOS in the nominal range ≤ 175 , the shift is centered at 9.2 km s^{-1} , with an rms deviation of $\simeq \pm 5.1 \text{ km s}^{-1}$.

TABLE 10
DERIVED SHIFTS FOR *FUSE* DATA

FUSE Root	Star	STIS dataset	STIS ID ^b	STIS grating	FPALXPOS	Shifts ^a		
						(pixs)	(Å)	(km s ⁻¹)
B07101	HD001383	O5C07C010	8241	E140H	117.0	1.7	0.035	10.1
B07104	HD091983	O5C08N010	8241	E140H	117.0	2.1	0.043	12.5
P10165	HD168941	O6LZ81010	9434	E140M	117.0	0.8	0.016	4.7
P10179	BD+354258	O6LZ89010	9434	E140M	117.0	1.8	0.037	10.7
P10188	HD218915	O57R05010	7270	E140H	117.0	0.5	0.010	3.0
P10285	HD190918	O6359J010	8662	E140M	117.0	1.5	0.031	8.9
P10286	HD192035	O6359K010	8662	E140M	117.0	1.5	0.031	8.9
P11631	HD210839	O54304010	8043	E140H	117.0	2.7	0.055	16.0
P12231	HD210809	O5C01V010	8241	E140H	117.0	2.3	0.047	13.6
Z90101	HD000108	O5LH01010-40	8484	E140H	117.0	4.3	0.088	25.5
B03001	HD203374A	O5LH08010-30	8484	E140H	117.2	1.3	0.027	7.7
B03004	HD208440	O5C06M010	8241	E140H	117.2	1.3	0.027	7.7
B03005	HD209339	O5LH0B020	8484	E140H	117.2	2.0	0.041	11.9
B07105	HD122879	O5LH07020	8484	E140H	117.2	-0.5	-0.010	-3.0
B07109	HD206773	O5C04T010	8241	E140H	117.2	1.5	0.031	8.9
P10231	HD091651	O6LZ34010	9434	E140M	117.2	0.4	0.008	2.4
P10232	HD092554	O6LZ36010	9434	E140M	117.2	1.8	0.037	10.7
P10265	HD134411	O6LZ60010	9434	E140M	117.2	-0.2	-0.004	-1.2
P10266	HD151805	O6LZ63010	9434	E140M	117.2	0.3	0.006	1.8
P10279	HD165955	O63599010	8662	E140M	117.2	-1.1	-0.022	-6.5
P10289	HD202347	O5G301010	8402	E140H	117.2	0.9	0.018	5.4
P11624	HD192639	O5C08T010	8241	E140H	117.2	0.9	0.018	5.3
P11627	HD206267	O5LH09010-20	8484	E140H	117.2	1.9	0.039	11.3
P12216	HDE303308	O4QX04020	7301	E140H	117.2	3.2	0.065	19.0
P12230	HD201345	O5C050010	8241	E140H	117.2	2.6	0.053	15.4
P12232	BD+532820	O6359Q010	8662	E140M	117.2	1.5	0.031	8.9
P10275	HD157857	O5C04D010	8241	E140H	117.5	2.5	0.051	14.8
P10123	HD088115	O54305010-30	8043	E140H	134.9	2.4	0.049	14.3
P10257	HD104705	O57R01010	7270	E140H	134.9	3.0	0.061	17.8
P10262	HD124314	O54307010	8043	E140H	134.9	1.9	0.039	11.3
P10118	HD066788	O6LZ26010	9434	E140M	135.1	0.8	0.016	4.7
P10221	HD063005	O63531010	8662	E140M	135.1	0.6	0.012	3.6
P10230	HD091597	O6LZ33010	9434	E140M	135.1	2.2	0.045	13.0
P10236	HD093205	O4QX01020	7301	E140H	135.1	2.8	0.057	16.6
P10237	HD093222	O4QX02020	7301	E140H	135.1	2.0	0.041	11.9
P10241	HD094493	O54306010	8043	E140H	135.1	1.6	0.033	9.5
P10245	HD099857	O54301010-30	8043	E140H	135.1	4.2	0.086	24.9
P10246	HD099890	O6LZ45010	9434	E140M	135.1	0.7	0.014	4.2
P10258	HD114441	O6LZ53010	9434	E140M	135.1	0.1	0.002	0.6
P10261	HD116781	O5LH05010-20	8484	E140H	135.1	0.9	0.018	5.3
P12215	CPD-592603	O40P01D6Q	7137	E140H	135.1	1.3	0.027	7.7
P12219	HDE308813	O63559010	8662	E140M	135.1	0.9	0.018	5.3
P10227	HD075309	O5C05B010	8241	E140H	135.4	1.6	0.033	9.5
P10240	HD093843	O5LH04010-20	8484	E140H	135.4	1.5	0.031	8.9

TABLE 10

FUSE Root	Star	STIS dataset	STIS ID ^b	STIS grating	FPALXPOS	Shifts ^a		
						(pixs)	(Å)	(km s ⁻¹)
P10203	HD013268	O63506010	8662	E140M	175.1	2.2	0.045	13.0
P10205	HD014434	O63508010	8662	E140M	175.1	1.3	0.027	7.7
P10206	HD015137	O5LH02010-40	8484	E140H	175.1	1.4	0.029	8.3
P12201	HDE232522	O5C08J010	8241	E140H	175.1	2.3	0.047	13.7
S3040201	HD224151	O54308010	8043	E140H	175.1	1.6	0.033	9.5
P10202	HD012323	O63505010	8662	E140M	175.4	3.7	0.075	21.9
P10204	HD013745	O6LZ05010	9434	E140M	175.4	1.9	0.039	11.3
S3040202	HD224151	O54308010	8043	E140H	227.0	-4.0	-0.082	-23.7
P11623	HD185418	O5C01Q010	8241	E140H	227.2	-5.3	-0.108	-31.5
P12241	HD224151	O54308010	8043	E140H	227.2	-3.4	-0.069	-20.2

^aThis is the shift which must be added to the *FUSE* data to align the P(3) and R(4) 6–0 H₂ lines with the Cl I λ 1347 line in the STIS data

^bData from GO programs: 8241—“A SNAPSHOT survey of Interstellar Absorption Lines”, Lauroesch PI; 8662, 9434—“A SNAPSHOT survey of the Hot Interstellar Medium”, Lauroesch PI; 8043, 8484—“Physical Properties of H I and H II Regions”, Jenkins PI.

B. STELLAR DISTANCES, THEIR ERRORS, AND CORRECTIONS TO AVAILABLE DATASETS

A key set of parameters for our *FUSE* sample is the distance to each star, d , and its uncertainty. These quantities are important because one of our objectives was to measure as accurately as possible the mean and dispersion of the average density of O VI using all the available sight lines. To derive d in pc we need to calculate the spectroscopic distance (often referred to as the “spectroscopic parallax”) given by

$$5 \log d = (m_V - A_V - M_V + 5) \quad (\text{B1})$$

where m_V is the observed apparent magnitude in the V band, A_V is the interstellar extinction in the V -band, and M_V is the absolute V -band magnitude of the star of a particular spectral type and luminosity class (hereafter, ‘Sp/L’). In the following subsections, we discuss how we derived each of these quantities. We show that it is possible to derive observed magnitudes and interstellar extinctions quite accurately using *Hipparcos* satellite data and infrared magnitudes obtained from the ground. We also show that the absolute magnitude of a star of known Sp/L is probably known to ~ 0.2 – 0.3 mags. What remains poorly known, however, is how well an Sp/L can be measured for a star, particularly for stars later in type than B0.

B.1. Observed Magnitudes; Multiple Systems & Intrinsic Variability

In order to use a set of magnitudes obtained in a uniform way and at a single epoch, we took stellar magnitudes from the *Tycho* Starmapper (ESA 1997a) catalogs. This instrument, part of the ESA *Hipparcos* mission, provides two-color photometry, B_T and V_T , in a magnitude system close to that of Johnson B and V bands (van Leeuwen et al. 1997). The two magnitude bands are related via the transformation

$$\begin{aligned} V &= V_T - 0.090(B - V)_T & (\text{B2}) \\ (B - V) &= 0.850(B - V)_T & (\text{B3}) \end{aligned}$$

provided $-0.2 < (B - V)_T < 1.8$ (Eqn. 1.3.20 of ESA 1997b)²⁰. The errors in the V magnitudes and in the $B - V$ colors are given by equations 1.3.21 and 1.3.22 of ESA (1997b) and are reproduced here for convenience:

$$\sigma(V) = (1.09\sigma_{V_T}^2 + 0.09\sigma_{B_T}^2)^{1/2} \quad (\text{B4})$$

$$\sigma(B - V) = G \times \sigma(B - V)_T \simeq G \times (\sigma_{V_T}^2 + \sigma_{B_T}^2)^{1/2} \quad (\text{B5})$$

The factor G in the above equation provides the slope of the local $(B - V)$ against $(B - V)_T$ relation and ranges from 0.85 to 0.97. We calculate a precise value of G for each value of $(B - V)_T$ by extrapolating the values given in Table 1.3.4 of (ESA 1997b). Using this scheme, the majority of the stars in our sample has B and V magnitude errors of < 0.04 mags.

We note the following exceptions where we did not use these relationships: HD 326329 only has an entry for V_T ($=8.90$) in the *Tycho* catalog, with no B_T . For this star we used V and B from Baume et al. (1999). HD 152314 is also not in the *Tycho* catalog, but does exist in the *Tycho-2* catalog²¹ (Høg et al. 2000), which lists both B_T , V_T and associated errors. Several stars have unusually large errors in the *Tycho* catalog, and their values are replaced by values from the literature. These stars are: CPD–417712 (Baume et al. 1999), and CPD–592600 & CPD–592603 (Massey & Johnson 1993). All the adopted magnitudes are listed in Table 1.

B.1.1. Photometric Binaries

It is well known that stars are often members of multiple stellar systems. This presents the simple problem that a star’s measured magnitude may not be a true measure of its distance if the measured flux really comes from two

²⁰The “Guide to the Data” can be found at http://www.rssd.esa.int/Hipparcos/CATALOGUE_VOL1/catalog_vol1.html

²¹VizieR catalog I/259

(or more) unresolved stars. The *Hipparcos* data can again be used — at least for a subset of stars — to help identify multiple systems.

Of the 148 stars in our sample, 106 are listed in the *Hipparcos* catalog and could therefore be analyzed in more detail than was possible from their *Tycho* data alone. Of these, 19 are listed in the *Hipparcos Double and Multiples System Annex: Component solutions* (DMSA/C) catalog (ESA 1997d), which means that these system can be modeled as individual stars. (The *Hipparcos* catalogs labels these as “Component Solutions”.) For a particular system, we adopt the magnitudes of the brightest component listed in the DMSA/C catalog; we thereby assume that the bulk of the flux which defines the Sp/L of the star comes from the brightest component. Six stars (HDs 099857, 101190, 101413, 101436, 190918, 152248) are cataloged in the DMSA/C catalog, but the magnitude of only one component is given. We take this to mean that the secondary is too faint to be modeled; its presence is therefore not expected to alter the magnitude of the primary star. (We use the DMSA/C catalog magnitude nonetheless.)

In the DMSA/C catalog, only *Hipparcos* magnitudes H_p are available, and not the V_T used to convert to Johnson V magnitudes for the other stars. A comparison between H_p and Johnson V for stars not labelled as multiple show that in all cases, differences in V (calculated from V_T) and H_p are small (≤ 0.05 mags). The transformations suggested by Harmanec (1998) also show that for $B-V = \pm 0.2$ — the minimum and maximum values for our stars — the difference in H_p and V should only be ∓ 0.06 mags.

Two of the 106 stars (HD 185418 and HDE 232522) are listed in the *Hipparcos* catalog as being multiple due to their non-linear motion (“Acceleration Solutions” — similar to astrometric binaries) although they have no entry in the DMSA/C catalog. Both are actually spectroscopic binaries, and their V magnitudes are corrected for in same way as the rest of the spectroscopic binaries in our sample, discussed below.

For the 42 stars not in the *Hipparcos* catalog, the *Tycho* catalog provides a flag to indicate which stars may be multiple systems²². None of the 42 stars not in the *Hipparcos* catalog were flagged as multiples in the *Tycho* catalog.

B.1.2. Spectroscopic Binaries

An important class of multiple systems are the spectroscopic binaries (SBs). These stars are too close together to be resolved by *Hipparcos* (except for those which might also be eclipsing binaries — see below). Given the luminosity of the primary and secondary stars to be L_1 and L_2 , the correct distance to the system d' is

$$d' = \left(1 + \frac{L_2}{L_1}\right)^{1/2} d \quad (\text{B6})$$

where d is the distance to the system estimated from the integrated $(L_1 + L_2)$ luminosity. In the worst case, L_1 and L_2 are equal and d is incorrect by a factor $\sqrt{2}$. If the magnitudes of the primary and secondary, m_1 and m_2 respectively, are known, the ratio of the luminosities can be calculated in the usual way $L_2/L_1 = 10^{0.4(m_1 - m_2)}$. In many cases, however, the value of Δm is unavailable. How then can we estimate what correction to make for these systems?

For double-lined SBs, the ratio of the radial velocities for each component gives the mass ratio of the system M_2/M_1 . The mass-luminosity relation for main sequence (MS) stars with mass $> 0.2M_\odot$ is given by Schmidt-Kaler (1982):

$$\log \frac{L}{L_\odot} = 3.8 \log \frac{M}{M_\odot} - 0.8. \quad (\text{B7})$$

To convert between the bolometric luminosity L , and V -band luminosity L_V , we must apply a bolometric correction (BC) to equation B7. The BC is a function of luminosity, but can be derived for a given Sp/L; for MS stars, the BC can be shown to be $-0.9 \log(L/L_\odot) + 1.2$ (Schmidt-Kaler 1982) which gives

$$\log \frac{L_1}{L_2} = 2.4 \log \frac{M_1}{M_2} \quad (\text{B8})$$

²²Field T36 of the *Tycho* catalog, *Source of photometric data*; see ESA (1997c)

where the luminosities are those measured in the V -band. This can then be applied to equation B6 to correct the distance to the system.

To identify spectroscopic binaries in our sample of stars, we used *The Ninth Catalogue of Spectroscopic Binary Orbits* (SB9) by Pourbaix et al. (2004), and the list of binaries in NGC 6231 by García & Mermilliod (2001), who note that HD 152314 (S161), HD 152200 (S266), HD 152233 (S306) and HD 152248 (S291) are probably spectroscopic binaries. We identify 21 of our stars to be SBs. For 11 of these stars, values of ΔL or ΔM are available, and their distances can be corrected directly from equation B6 or indirectly from equation B8. For the remaining ten stars, we note that Pinsonneault & Stanek (2006) find that 50% of binaries have mass ratios > 0.87 , and use this as a generic correction. This mass ratio corresponds to $\Delta L = 0.72$, and hence the distance to the system is increased by a factor of 1.3. A superscript next to the distance to a star in Table 1 indicates that the star was treated as a SB.

As noted above, equation B7 is probably only applicable for MS stars, and evolved stars may well not obey the same $M-L$ relationship. Unfortunately, only seven of our SBs are MS stars. It may be that equation B7 does not represent a precise conversion between mass and luminosity, and, therefore, that the correction we make to the stellar distance is similarly imprecise. The distances to these systems should be treated with caution.

B.1.3. Variable Stars

Stars which are not multiple systems may still exhibit variability. These may be rotating, pulsating, eruptive or cataclysmic types of variability. B-type emission line stars may also show variations in luminosity. 14 stars in our sample which are not in SB9 or in the *Hipparcos Double and Multiples* catalog are listed in the *Hipparcos Variability Annex* (ESA 1997e). For these stars, we take the maximum H_p magnitude (minimum luminosity) from the fitted light curve derived from the *Hipparcos* photometry. The assumption here is that the minimum luminosity of the star represents its ‘true’ luminosity for its given spectral type and luminosity class. This assumption is based on the idea that Be stars are brighter than B stars for a given spectral type (Briot et al. 1997); obviously, for stars whose luminosities are not increased by mechanisms such as the emission from circumstellar disks which are thought to surround Be stars, this assumption may be invalid. However, of the 14 stars corrected, all but one have a difference between the faintest magnitude and the mean magnitude of less than 0.06 mags. (HD 042401 shows a difference of 0.17 mags). Although these corrections are therefore largely irrelevant, they have been applied to our data. Distances adjusted this way are noted with a superscript in Table 1.

Variable stars may, of course, be (partially) eclipsing binaries, more akin to the SBs discussed above. However, most of the stars in the *Variability Annex* which are labelled as likely (or already known) eclipsing binaries (field ‘P5’ in the *Annex*) are already identified in SB9, and their distances are corrected in the way described above. (Only HD 042401 is identified as a β Lyrae type of eclipsing binary and is not in SB9.) Hence the luminosities for these stars are not corrected in the same way that the spectroscopic binaries were corrected above.

Unfortunately, for the 42 stars of our sample not in the *Hipparcos* catalog, the *Tycho* analysis provides no clear information on which stars are intrinsically variable. Although a variability flag does exist, the flag appears unreliable (failing to note variability when detected by *Hipparcos*, and flagging variability when *Hipparcos* detects none) and we have not included the information in Table 1. Instead, we searched for our stars in the *Combined General Catalogue of Variable Stars* (GCVS) and the *GCVS Suspected Variable stars and Supplement* catalogs (Samus et al. 2004)²³. This catalog contains a very inhomogeneous set of data, but can indicate that a star was recorded to have a fainter magnitude than was seen during the $\simeq 3$ year *Hipparcos* mission.

For stars which have no entries in the *Hipparcos* catalogs, are not SBs, or which have distances that are not taken from the literature, we find that: a) only one has a minimum-maximum variation listed in the GCVS catalogs greater than 0.06 mags [Lipunova & Putilina (1985) noted that HDE 332407 fell from $V = 8.51$ (close to the *Hipparcos* value of $V = 5.82$) by $\simeq 0.1$ mags. *Hipparcos* found no variation, but we have made this correction in Table 1]; and b) six stars have variations less than 0.06 mags²⁴, which we consider small enough to ignore.

²³vizieR catalog II/250

²⁴Using a value of 0.06 mags to separate ‘weak’ from ‘strong’ variability is purely arbitrary, but the value is used in the *Hipparcos* catalog to provide a coarse variability flag (Field H6 of the main catalog), which is why we use that same value here. Stars in our sample which show a variability

Given the short lifetime of the *Hipparcos* mission, it is also interesting to consider whether the maximum magnitudes of the variable stars that are indeed in the *Variability Annex* are significantly different from the maxima given by the GCVS catalogs. In fact, for the six stars for which there is a difference > 0.06 mags (excluding SBs), the distances we use are taken from the literature, measured by *Hipparcos* parallax, or the GCVS magnitude is not from V -band measurements. There is therefore no evidence that our distances are affected by not considering a long enough timeline for the variable stars²⁵.

B.2. Interstellar Extinction

The relationship between interstellar extinction A_V and the color excess of stars $E(B-V)$ is usually taken to be $A_V = R_V E(B-V)$, where R_V is the ratio of total to selective visual extinction. In the Milky Way, a typical value of R_V through the diffuse ISM is $\simeq 3.1$. In a compilation of R_V values for 417 O3- to B5-type stars, Valencic et al. (2004) found a Gaussian distribution of R_V centered at 3.0 (largely as expected), but with a 1σ dispersion of 0.35. Assuming that a large fraction of this dispersion arises from real line-of-sight differences in R_V , and not just from measurement errors, then using a value of 3.1 for R_V to calculate A_V might lead to errors of at least $0.35 E(B-V)$ mags in calculating the distance to a star in equation B1, even if the errors in $E(B-V)$ were zero. For values of R_V very different from $\simeq 3$ the errors are even larger.

We would therefore like to have a way to measure A_V along a sight line directly. Whittet (1992) describes a method which uses infrared (IR) magnitudes: $R_V \simeq 1.1 E(V-K)/E(B-V)$. Since $A_V = R_V E(B-V)$, we can directly measure the extinction from

$$A_V = 1.1 E(V-K) \quad (\text{B9})$$

To obtain K -band magnitudes, we used the *Two Micron All Sky Survey* (2MASS) (Skrutskie et al. 2006)²⁶. The 2MASS magnitude was converted to Johnson K using the relation²⁷ $K = K_{2\text{MASS}} + 0.027 + 0.00787(J_{2\text{MASS}} - K_{2\text{MASS}})$ unless the $J_{2\text{MASS}}$ was flagged as unreliable, in which case the color term was neglected. Values of $K_{2\text{MASS}}$ were only used if an ‘A’ photometric quality flag (Qflg) was given (see the 2MASS catalog for a full explanation of this flag). Intrinsic IR colors for early type stars were taken from Wegner (1994).

We calculated the error in the IR color excess as $\sigma(E_{V-K})^2 = \sigma(V)^2 + \sigma(K)^2 + 0.03^2$, where the last term is adopted as a typical error in the intrinsic $V-K$ colors given by Wegner (1994); $(V-K)_0$ appears to vary slowly with luminosity class, but strongly with stellar type. With this error, we were able to reject poorly determined IR color excesses when $E(V-K) < 2\sigma(E_{V-K})$, and did not use equation B9. $E(V-K)$ was also not used if more than one stellar type or luminosity class was given for a particular star, or if the star was in the *Hipparcos Variability Annex* or DMSA/C catalogs, since we have no information on how a star might vary in the IR from 2MASS. We allowed $E(V-K)$ to be used for the SBs; here we assume that ΔL in the optical is similar to ΔL in the IR.

If we were unable to use $E(V-K)$ to estimate A_V , we fell back to the more usual practice of calculating $A_V = 3.1 E(B-V)$. $E(B-V)$ is given for most of our stars in Table 1, except when distances were taken from the literature. The error in the Johnson $B-V$ color is given by equation B5 above; we again used Wegner (1994) for the intrinsic $(B-V)$ colors of the stars, and assumed a value of ~ 0.01 mags as a likely error, since the intrinsic color varies very slowly with spectral type and luminosity class for early type stars.

B.3. Absolute Magnitudes of O-type and Early B-type Stars

Beyond the problems in measuring the observed magnitudes of, and the extinction towards, a particular star, the largest uncertainty in measuring its distance comes from a poor knowledge of its absolute magnitude M_V in equation B1. There are two problems: knowing the absolute magnitude of a star given its MK-system spectral type and

< 0.06 mags usually do not show up in the *Variability Annex*. Hence we cannot correct the magnitudes of these stars anyway.

²⁵Such variations may exist of course, but they have not been recorded in the literature.

²⁶vizieR catalog II/246

²⁷From the *Explanatory Supplement to the 2MASS All Sky Data Release* at http://www.ipac.caltech.edu/2mass/releases/allsky/doc/sec6_4b.html by R. M. Cutri et al..

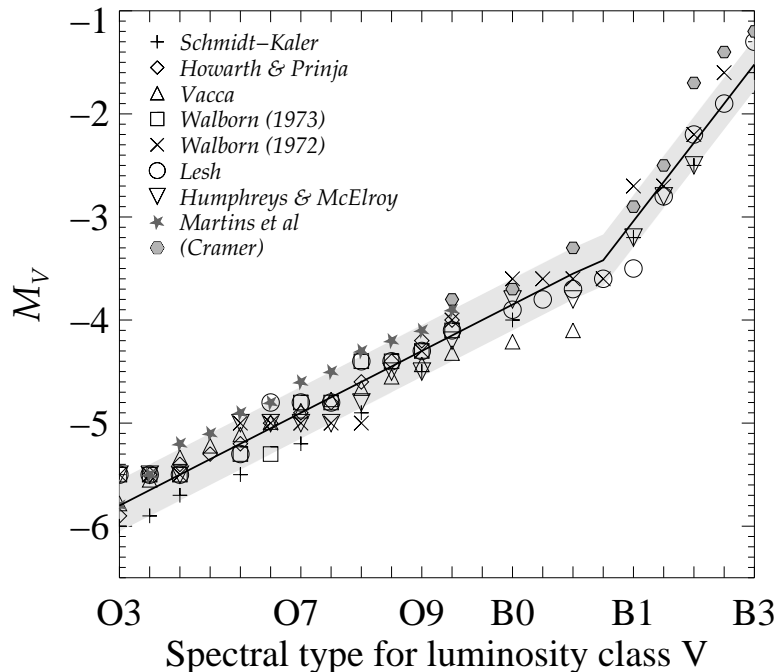


Figure 21: Plot of absolute V -band magnitude M_V against spectral type (O3–B3) from the authors listed at the top left of the figure. Our adopted relationship between M_V and spectral type is shown as a solid black line; the gray region either side marks a difference of ± 0.25 mags which we take as the error in knowing M_V for any given stellar type.

luminosity class [at least, the extension developed by Walborn (1971), since the original MK classification by Morgan et al. (1943) did not cover stars earlier than O9]; and, more importantly, knowing precisely the spectral type and luminosity class of any given star.

The first of these problems is largely tractable, thanks to surveys which use stars with well-defined Sp/Ls, carefully measured observed magnitudes, and distances measured using methods other than the spectroscopic parallax. Although the measurements of all these quantities are fraught with their own uncertainties, there appears to be consensus on how M_V varies with Sp/L for early type stars. To produce our own M_V -Sp/L scale, we collated data from Walborn (1972), Walborn (1973), Lesh (1979), Schmidt-Kaler (1982), Humphreys & McElroy (1984), and Howarth & Prinja (1989). We also added, when an Sp/L was available, magnitudes from models by Vacca et al. (1996) and Martins et al. (2005) for comparison. Not every available published scale was included: for example, absolute magnitudes for OB stars have been given by Wegner (2000) based on *Hipparcos* parallaxes, but these values differ so significantly from the other authors just cited that we did not include them. The final M_V magnitudes for a given Sp/L are tabulated in Table 11.

An example of one M_V -Sp/L scale is shown in Figure 21, which plots M_V against spectral type for luminosity Class V stars. (These, along with Class III stars, are the most well studied of the luminosity classes.) In general, authors tend to agree on the relation between M_V and spectral type to within several tenths of a magnitude for this luminosity class. In Figure 21 we show our adopted scale as a straight line, along with an error of ± 0.25 mags (shown by gray boundaries). Theoretical values are also in good agreement with the data: the models by Martins et al. (2005) appear to be too faint by only ≈ 0.25 mags, while those from Vacca et al. (1996) agree well with observations for the early stellar types until B0.

Figure 21 also shows the values of M_V derived by Cramer (1997) for B-type stars whose parallaxes were measured

by *Hipparcos*. We did not use these data in setting our M_V -Sp/L scale as no O-type stars were included, and a complete analysis remains unpublished. The variation of M_V with Sp is not entirely smooth, presumably due to the small number of B-type stars close enough to the Sun for an accurate parallax to be determined. Nevertheless, although the stars as a group seem to be slightly fainter than our adopted scale, the values of M_V are largely consistent with our adopted scale, to within an error of ≈ 0.25 mags. (We return to the question of how well our spectroscopic distances compare to *Hipparcos* parallaxes in Appendix C.1.3.)

Plots of M_V and spectral type for other luminosity classes show similar results, although the Class I stars have no ‘break’ around B0 but have roughly constant absolute magnitudes for all spectral types, as expected.

One other problem which remains is that of the Be stars, those which presently, or in the past, have shown emission lines. There are nine Be stars in our sample; the adopted Sp/L for these should probably be used with caution, since the classification of Be stars is known to be problematic, due to emission lines filling-in the diagnostic absorption lines, and due to the large rotation speeds which are usually associated with these systems. Unpublished studies of the difference in M_V between B and Be stars using *Hipparcos* parallax distances by Briot et al. (1997) and Briot & Robichon (2000) suggests that although Be stars of a given Sp/L are indeed brighter than B stars of the same Sp/L, the differences for the stars of interest in this paper, B0-B3, are negligible. Hence we make no additional corrections to M_V for Be stars.

Given the relative small dispersions in M_V and the general agreement with theoretical values (when available), we assume that M_V can be known for a star of a particular Sp/L to within ± 0.25 mags.

The second problem in determining M_V for a given star — that of knowing its Sp/L precisely — is not so straightforward. Stellar classification depends not only on the quality, resolution, and wavelength extent of the spectra used to make the classification, but on the experience of the observer making the classification. (Many stars were assigned their Sp/Ls several decades before the development of automatic classification of digital spectra, for example.) Moreover, although a particular set of stars can be used to define a class and type (e.g. Garrison 1994), Sp/L categories are discrete, and any given star may in reality fall between the designated category. For example, the absolute magnitudes in Figure 21 decreases rapidly for stars between types B1 and B2, though only very small changes are seen in line ratios used to define the Sp/Ls. Hence a star may have a magnitude a few tenths different from the M_V assigned from the adopted Sp/L. More serious, however, is the fact that the use of a poor quality spectrum of a star can lead to a complete mis-classification of a star, an occurrence which appears more frequently for the B-type stars.

In most cases, we have no access to the original data used to determine the Sp/L of the stars in our survey. We have therefore searched through the available literature to find suitable Sp/Ls for our stars. The references for the Sp/Ls we adopt are given in the final column (16) of Table 1.

Given the difficulties which exist in assigning an Sp/L to a star, we have developed a simple procedure for measuring the likely range of plausible distances to an individual star. Our primary goal is to quantify a generic error in M_V for each star. Assigning only a single number for this error is inappropriate, since uncertainties in M_V are larger for, e.g. B-type stars than for O-type stars of the same luminosity class. Instead, we calculate an error in three parts: we first take the difference in magnitude between the adopted value and the magnitude of the next spectral type in the series; we then calculate the difference in magnitude between the adopted spectral type and that of the same spectral type in the next luminosity class. Finally, we add these two values in quadrature with the error we adopt for assigning M_V to a given Sp/L, which we take to be $\sigma(M_V)_C = 0.25$ mags, as discussed above. In notation form, we calculate an error in M_V for possible positive deviations from the adopted M_V thus:

$$\sigma[M_V, (\text{Sp/L})_i]^2 = \Delta M_V(\text{Sp}_{i+1} - \text{Sp}_i)^2 + \Delta M_V(L_{i+1} - L_i)^2 + \sigma(M_V)_C^2 \quad (\text{B10})$$

So, for example, the positive error in a B3 III star is formed from taking $M_V(\text{B4 III}) - M_V(\text{B3 III})$ in Table 11, $M_V(\text{B3 IV}) - M_V(\text{B3 III})$, and adding these in quadrature, along with 0.25 mags for $\sigma(M_V)_C$. The negative deviation is calculated in the same way, only taking differences between Sp_i and Sp_{i-1} , and L_i and L_{i-1} . Using these values of M_V leads to an upper and lower bounds for the distance, d_u and d_l , respectively.

Even this method is imprecise however, since it is easier to classify, e.g. an O4 star than a B1 star. In this sense, the ranges in M_V determined for O type stars may be somewhat over-estimated, while for B type stars the errors may

be too small. However, the magnitude of the errors are likely to be roughly correct, since in the scheme outlined in equation B10, O stars have smaller errors than B stars.

From estimating distance ‘errors’ in this way, we conclude that *the errors we derive in M_V dominate all other errors discussed in this Appendix*. For example, for the Class V dwarfs and Class IV subgiants, errors range from $\simeq 0.3$ –1.0 mags for O3–B3 type stars, or a 14–46% error in the distance²⁸. The largest errors in this scheme occur for the B3 Class II giants, since their magnitudes are furthest from both the Ia supergiants as well as the Class III giants; errors range from 0.4–1.5 mags for O3–B3 type stars, 20–70 % in distance. Clearly, the errors associated with the extinction A_V ($\simeq 0.1$ –0.2 mags) and those with the *Tycho* and *Hipparcos* catalog magnitudes ($\ll 0.1$ mags), are insignificant compared to the errors in M_V .

Further, in some cases, the stars in our sample have no published luminosity class, or only a range of luminosity classes are given. In these cases we calculate the distances for the brightest and faintest of the specified classes (or ‘V’ and ‘Ia’ if no Class is given), and use the average value for the distance. The minimum and maximum error are simply the minimum and maximum values calculated for each class in the way described above. The value of $E(B-V)$ in Table 1 is also an average value (although the average was not used in the calculation of the distance.)

B.4. Distances from the Literature

There are some exceptions to this scheme for calculating the distance to our survey stars. Our sample contains four Wolf-Rayet stars; distances and values of $E(B-V)$ for three of these, HD 151932 (WR 78), HD 191765 (WR 134) and HD 190918 (WR 133) are taken from the catalog of van der Hucht (2001), while data for HD 187282 (WR 128) come from Conti & Vacca (1990). HD 93129A is an O2 If star (Walborn et al. 2002b) in Trumpler 14, one of the ionizing clusters in Carina, and since O2 stars have no defined values of M_V , we adopt the distance given by Tapia et al. (2003). The *Hipparcos* DMSA/C catalog lists four components to the multiple system of which HD 005005A is a member, but their membership of the IC 1590 cluster seems unequivocal — unlike the Sp/L of HD 005005A — and an accurate distance is given by Guetter & Turner (1997), which we use. LS 277 has no published Sp/L, and its distance is taken from Reed (1993). Finally, HD 110432 is close enough that the parallax distance from *Hipparcos* (300 ± 50 pc) should be more accurate than its distance determined from its Sp/L (see Appendix C.1).

Note that in Table 1, use of a distance from the literature is indicated with a superscript next to the distance. If no errors for a published distance are available, we adopt a value of ± 20 % of the distance.

²⁸ $\sigma(d)/d = 0.46\sigma(M_V)$

TABLE 11
ADOPTED M_V MAGS FOR GIVEN SPECTRAL TYPES AND CLASSES

Type	Luminosity Class						
	V	IV	III	II	Ib	Iab	Ia
O3	-5.80	-6.00	-6.30	-5.95	-6.30	-6.65	-6.90
O4	-5.65	-5.88	-6.20	-5.94	-6.29	-6.64	-6.91
O5	-5.50	-5.76	-6.10	-5.93	-6.28	-6.63	-6.92
O5.5	-5.35	-5.64	-6.00	-5.92	-6.27	-6.62	-6.93
O6	-5.20	-5.52	-5.90	-5.91	-6.26	-6.61	-6.94
O6.5	-5.05	-5.40	-5.80	-5.90	-6.25	-6.60	-6.95
O7	-4.90	-5.28	-5.70	-5.89	-6.24	-6.59	-6.96
O7.5	-4.75	-5.16	-5.60	-5.88	-6.23	-6.58	-6.97
O8	-4.60	-5.04	-5.50	-5.87	-6.22	-6.57	-6.98
O8.5	-4.45	-4.92	-5.40	-5.86	-6.21	-6.56	-6.99
O9	-4.30	-4.80	-5.30	-5.85	-6.20	-6.55	-7.00
O9.5	-4.15	-4.68	-5.20	-5.84	-6.19	-6.54	-7.01
O9.7	-4.00	-4.56	-5.10	-5.83	-6.18	-6.53	-7.02
B0	-3.85	-4.44	-5.00	-5.82	-6.17	-6.52	-7.03
B0.2	-3.70	-4.32	-4.90	-5.70	-6.10	-6.51	-7.04
B0.5	-3.55	-4.20	-4.80	-5.50	-6.05	-6.50	-7.05
B0.7	-3.42	-4.08	-4.60	-5.30	-6.00	-6.49	-7.06
B1	-3.04	-3.96	-4.25	-5.10	-5.95	-6.48	-7.07
B1.5	-2.66	-3.50	-3.90	-4.90	-5.90	-6.47	-7.08
B2	-2.28	-3.10	-3.55	-4.70	-5.85	-6.46	-7.09
B2.5	-1.90	-2.70	-3.20	-4.50	-5.80	-6.45	-7.10
B3	-1.52	-2.30	-2.85	-4.30	-5.75	-6.44	-7.11
Refs: ^a	1-7	1,3-5	1-7	1,2,4,5	1,2,4,5	1,2,4,5	1,2,4,5,7

^aCollation of data from: (1)—Walborn (1972); (2)—Walborn (1973); (3)—Lesh (1979); (4)—Schmidt-Kaler (1982); (5)—Humphreys & McElroy (1984); (6)—Howarth & Prinja (1989); (7)—Vacca et al. (1996)

C. REVISITING EARLIER SURVEYS

C.1. Corrections Made to *Copernicus* Data

C.1.1. Notes on Stellar Parameters

In §3.1.2 we introduced the stars studied by J78. Since they are both bright and comparatively nearby, there is a considerable amount of data available in the literature for these stars. In deriving distances to the *Copernicus* stars, we have tried to treat them in exactly the same way as our *FUSE* sample. All the *Copernicus* stars are listed in the *Hipparcos* main catalog, which means that they can be treated even more uniformly than the *FUSE* sample of stars. The stellar data for the *Copernicus* stars are given in Table 12; below, we outline some of the changes we have made to the stellar data since the stars were studied by J78.

Sp/Ls: these are taken directly from Table 1 of J78. Many of these stars have been studied since the advent of stellar spectroscopy, and their Sp/Ls are well understood (and often actually define a particular Sp/L). Small changes have been made to the Sp/Ls of γ Cas, ϵ Per, ζ Ori, ζ Pup, β Cen, β Lup, δ Sco, and σ Sgr since improved classifications are available in Garrison & Beattie (1996).

Magnitudes: V and B magnitudes are converted from B_T and V_T given in the *Tycho* catalog in the same way as described above. We have again tried to use $E(V-K)$ to calculate A_V , but we find that many of the stars are saturated in the 2MASS data.

Emission line stars: more information is now available for whether emission lines have been detected in the stellar spectra of the *Copernicus* stars, and we have appended 'e' suffixes to the Sp/Ls in Table 12 for the following stars: α Eri (Hanuschik et al. 1996), η Tau (Tycner et al. 2005), α Cam (Morel et al. 2004), λ Eri (Hanuschik et al. 1996), 25 Ori (Banerjee et al. 2000), ϵ Ori (Morel et al. 2004), HD 051283 (Irvine 1990), HD 052918 (Cote & van Kerkwijk 1993), δ Sco (Galazutdinov & Kretowski 2006), λ Pav (Mennickent 1991), 2 Vul (Barker 1983), κ Aql (Cote & van Kerkwijk 1993), 60 Cyg (Koubský et al. 2000), and 8 Lac (Chauville et al. 2001).

Spectroscopic binaries: we have again used the SB9 to flag which stars are SBs, and have adopted values of ΔL or ΔM when available (Appendix B.1.2). For HD 057060 (29 CMa), ΔL and its Sp/L are taken directly from Bagnuolo et al. (1994). HD 037303 is cited by Morrell & Levato (1991) as being an SB in the Orion OB1 association, though the star is not listed in SB9. We assume this designation is correct. For HD 047839 (15 Mon) *Hipparcos* gives the magnitude of the primary component ($V = H_p = 4.61$), and we take $\Delta m = 1$ mag between primary and secondary from Gies et al. (1993). HD 158926 (λ Sco) is composed of two early-type B stars and a low-mass pre-main-sequence star, according to Uytterhoeven et al. (2004), but *Hipparcos* finds no multiplicity in the DMSA/C catalog, and the system is not listed in SB9. We use these authors' estimate for the mass ratio of the two stars, $\Delta M \simeq 0.84$.

Variables: in general, stars flagged by the GCVS as variable are also found in the *Hipparcos* catalog. There is little published evidence that any of the *Copernicus* stars have been substantially fainter over the last century than the faintest magnitudes found by *Hipparcos*. We know of two clear exceptions: the long period V -band light curve for HD 005394 (γ Cas) has a minimum luminosity of $V = 2.75$ (Doazan et al. 1983), while HD 200120 is known to show a minimum of at least $V = 5.05$ (Harmanec et al. 2002). We adopt these magnitudes as the 'true' values for these two stars.

Multiple systems: HD 36486 (δ Ori) is a triple system. *Hipparcos* resolves the eclipsing binary, but the primary is an SB. Harvin et al. (2002) show that the flux from the SB is dominated by the O9.5II primary, and that ΔL is small, only 0.09. We use the magnitude of component Aa, and correct that using $\Delta L = 0.09$. For HD 57061 (τ CMa), *Hipparcos* finds two components; using the magnitude of the primary, and assuming this is composed of two stars, we obtain a distance of 1224 pc. However, the system appears to be quite complicated [see the discussions by van Leeuwen & van Genderen (1997) and Stickland et al. (1998)]. Although we could use the distance to NGC 2362, [e.g. 1480 pc by Moitinho et al. (2001)], van Leeuwen & van Genderen (1997) note that HD 57061 may no longer be near the center of the cluster. Given the lack of information, we simply retain the derived distance of 1224 pc.

C.1.2. Errors on Copernicus O VI Column Densities

The *Copernicus* stars tend to probe distances in the Galactic disk in the range between the WDs and the stars studied in the present survey. As such, their inclusion in an analysis of how, e.g., $N(\text{O VI})$ varies with distance, is valuable. Unfortunately, no *errors* on the column density $\sigma(N)$ were given by either J78 or Jenkins & Meloy (1974). Yet $\sigma(N)$ for these stars is an important quantity, since we need to know how much statistical weight to give $N(\text{O VI})$ when deriving quantities such as the average volume density in the Milky Way disk (as discussed in §3.8).

We can estimate these errors by using the coadded scan data of the stars from the *Copernicus* MAST archive. These data include a 2σ noise error array, which can be used to measure $\sigma(N)$.

Deriving $N(\text{O VI})$ from *Copernicus* MAST archive data is complicated; estimating the continuum of the star around the O VI line is often difficult, and the precise subtraction of the HD absorption (when other HD lines are available to produce a satisfactory model of the absorption) is challenging. We believe we are unlikely to improve upon the actual values of $N(\text{O VI})$ given by J78, and so concentrate on how best to obtain $\sigma(N)$. The *Copernicus* data are of variable quality, so a fixed percentage (for example) of the measured $N(\text{O VI})$ would be an inappropriate measure of the error in the column density. Since we only require approximate estimates of $\sigma(N)$, our approach is to produce a very crude re-measurement of $N(\text{O VI})$ and extract a value of $\sigma(N)$ associated with that column density. To first order, this value of $\sigma(N)$ should be close to the real value. The values are likely to be less precise than those derived for the *FUSE* sample, but they can be used to correctly weight the *Copernicus* values when data from all samples are combined.

We fitted the available *Copernicus* coadded scans made around the O VI $\lambda 1032$ line in the same way as described for the *FUSE* sample in §2.6, and measured $N(\text{O VI})$ with the AOD method (§2.8.2). The velocity range used by J78 to measure $N(\text{O VI})$ was variable, anywhere between $[-50, +50]$ km s⁻¹ to twice that range. For simplicity, we measured $\sigma(N)$ between -70 and $+70$ km s⁻¹. We calculated a final value of $\sigma(N)$ by adding in quadrature the errors from the continuum uncertainties and the noise errors given by the coadded scan error arrays.

Despite the simplicity of this approach, our measurements of $N(\text{O VI})$ and those published by J78 are in reasonable agreement. More importantly, J78 plotted profiles of the optical depth at each pixel, τ_i , along with 2σ error envelopes, $2\sigma(\tau_i)$, for about half of the *Copernicus* sample. This means we can directly compare the values of $\sigma(\tau_i)$ measured from the Archive data with those shown in Figure 2 of J78 for many of the stars. In general, the agreement was very good. Only three stars showed apparent problems: HD 064740, HD 106490 and HD 121263 had unusually large values of $\sigma(\tau_i)$ compared to the envelopes shown in J78, all because of inexplicably large noise errors σ_i in the Archive data error arrays. We estimated that the errors were too large by approximately a factor of 4–5, and subsequently reduced all values of σ_i by a factor of 5 before calculating $\sigma(\tau_i)$.

Compared with the dataset as a whole, $\sigma(\tau_i)$ for another three stars, HD 52918, HD 157246 and HD 158926, also seemed unreasonably large given the apparently good S/N of the data. These stars were originally discussed by Jenkins & Meloy (1974) but neither they or J78 showed plots of $\tau(v)$ against which we could compare the new values. (The original analysis of these stars is no longer available.) We therefore again reduced the values of σ_i by a factor of five, to give errors in $\sigma(\tau_i)$ apparently commensurate with the S/N of the data.

Values of $\sigma(N)$ are given in Table 12 [along with the original values of $N(\text{O VI})$ given by J78]. Again, we emphasize that *these values of $\sigma(N)$ are only approximations* and may only be useful for the statistical weights they provide for the *Copernicus* column densities.

C.1.3. Comparison Between Sp/L and Hipparcos Parallax Distances for Copernicus Stars

While we derived the distances to the *Copernicus* stars in exactly the same way as we did for *FUSE* stars, it is also true that reliable *Hipparcos* parallax distances are also available for many of the *Copernicus* stars. The parallax distance d_π can be derived from the parallax π given in the *Hipparcos* catalog from the relation $d_\pi = 1000/\pi$ pc, where π is the parallax measured in mas, which has an error of $\sigma(\pi)$.

Apart from providing a direct measure of the distance to a star, these data also enable us to compare distances with those derived from given Sp/Ls, and examine how good the M_V and color calibrations discussed above actually are. In Figure 22 we plot the *Hipparcos* distance against the distance derived from spectral typing. In the figure, we distinguish between those stars with $\pi/\sigma(\pi) \geq 5$ (black circles) and the rest of the sample (gray circles). Within 100–200 pc,

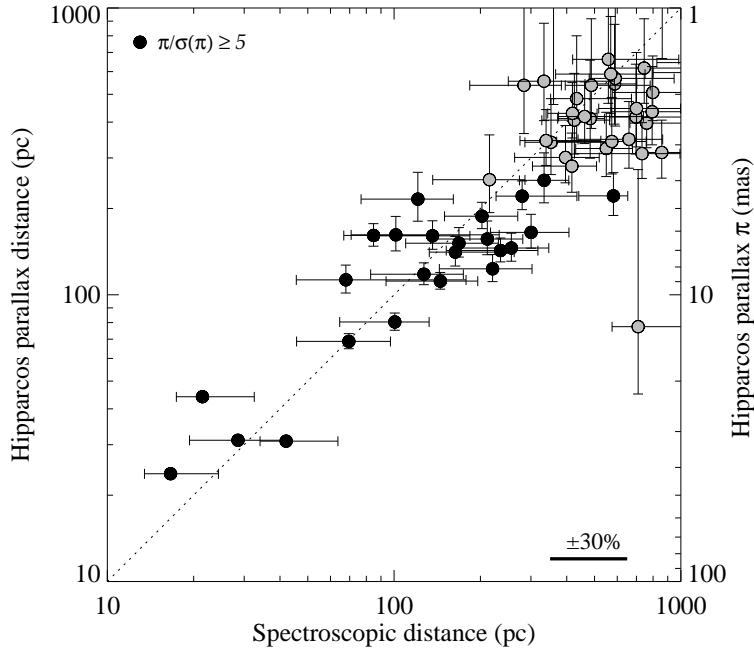


Figure 22: Comparison between parallax distances estimated from *Hipparcos* data and those derived from adopted spectral type and luminosity classes, for stars observed with Copernicus. One star in the sample (HD 149881) has a negative parallax, and is not plotted.

the correlation between the distances derived in the two different ways is quite good, and the spectroscopic distances are generally equal to the *Hipparcos* distances to within at least twice our estimates of the error range determined by equation B10. This substantiates our use of the errors from equation B10 as a useful ‘ 1σ ’ estimate. Beyond 200–300 pc, parallaxes become too small to be measured accurately by *Hipparcos*. We note that the Be stars do not have errors in spectroscopic distances much different from B stars.

Given that the *Hipparcos* distances for the nearest stars have much smaller errors than the spectroscopic distances, we adopt the *Hipparcos* distance for any star with $\pi/\sigma(\pi) > 5$. (We note our adoption of the *Hipparcos* parallax distance with a superscript ‘*c*’ against the value of d in column 11 of Table 12.) For these stars, the errors in their distances should be $< 5\%$ (Brown et al. 1997). In keeping with the range in errors adopted for the *FUSE* targets, we take the range in possible distances, d_l and d_u , to be $1000/[\pi + \sigma(\pi)]$ and $1000/[\pi - \sigma(\pi)]$, respectively.

C.2. Notes on Corrections Made to Data from Z03

All the stars observed by Zsargó et al. (2003) can be found in the *Hipparcos* catalog, so we have again used the cataloged values for the stellar magnitudes. In many cases, however, Sp/Ls are either not known, are only poorly determined, or are irrelevant—as in the case of the small number of post-asymptotic giant branch (PAGB) stars. For these stars, we have taken distances directly from the literature. Details are given in Table 13.

TABLE 12
Copernicus DATA OBTAINED BY J78

Star Name (1)	Alt Name (2)	l (deg) (3)	b (deg) (4)	B (5)	V (6)	K (7)	Sp/L (8)	$E(B-V)$ (9)	$E(K-V)$ (10)	d (kpc) (11)	d_r (kpc) (12)	v_c (km s ⁻¹) (13)	$ R $ (14)	v_{\odot} (km s ⁻¹) (15)	b (km s ⁻¹) (16)	N (10 ¹³ cm ⁻²) (17)	$\sigma(N)$ (10 ¹³ cm ⁻²) (18)
HD175191	σ Sgr	9.36	-12.44	1.93	2.06	...	B3IV	0.05 \pm 0.01	...	0.07 ^c	0.06, 0.07	9.1	1	< 0.79	...
HD149881	HD 149881	31.37	36.23	6.84	7.01	7.57	B0.5III	0.05 \pm 0.01	-0.11 \pm 0.04	2.85 ^a	2.10, 4.06	15.3	0	-3.1	19.7	3.47	2.7
HD184915	κ Aql	31.77	-13.29	4.92	4.96 ^b	...	B0.5IIIine	0.17 \pm 0.01	...	0.70	0.52, 1.00	12.0	0	6.6	6.6	3.72	1.3
HD214080	HD 214080	44.80	-56.92	6.68	6.82 ^b	7.24	B0.5Ib	0.05 \pm 0.01	-0.09 \pm 0.04	3.42	2.27, 4.48	2.2	0	20.1	13.6	2.88	3.9
HD180968	2 Vul	56.36	4.85	5.49	5.50 ^d	...	B1Vne	0.22 \pm 0.01	...	0.57	0.37, 0.75	15.5	0	7.6	44.9	12.59	3.5
HD219188	HD 219188	83.03	-50.17	6.91	7.04 ^b	7.48	B0.5IIIin	0.09 \pm 0.01	-0.23 \pm 0.04	0.46	1.53, 2.96	2.9	0	-9.1	40.2	12.59	3.6
HD200310	60 Cyg	87.15	-0.10	5.17	5.37	...	B1Vne	0.03 \pm 0.01	...	0.46	0.37, 0.74	12.4	1	1.7	20.3	1.45	0.7
HD200120	59 Cyg	88.03	0.97	4.85	5.05	...	B1.5Ve	0.02 \pm 0.01	...	0.34	0.27, 0.53	12.4	1	-9.9	14.1	1.32	0.6
HD214168	8 Lac	96.37	-16.15	6.35	6.49 ^d	...	B1Ve	0.09 \pm 0.01	...	0.71	0.58, 1.14	8.5	1	-17.6	28.3	3.55	1.0
HD120315	η UMa	100.70	65.32	1.75	1.85 ^b	...	B3V	0.08 \pm 0.01	...	0.03 ^c	0.03, 0.03	10.5	1	< 0.25	...
HD005394	γ Cas	123.58	-2.15	2.70	2.75	...	B0IVe	0.21 \pm 0.01	...	0.19 ^c	0.17, 0.21	4.7	2	< 0.10	...
HD014633	HD 014633	140.78	-18.20	7.22	7.44	8.15	O8V	0.07 \pm 0.01	-0.13 \pm 0.04	3.13 ^a	2.74, 3.99	-1.6	1	-9.6	33.6	5.25	2.2
HD030614	α Cam	144.07	14.04	4.29	4.30	...	O9.5Iae	0.23 \pm 0.01	...	1.73 ^a	1.35, 1.94	1.4	0	< 2.51	...
HD022928	δ Per	150.28	-5.77	2.93	3.03 ^d	...	B5III	0.05 \pm 0.01	...	0.16 ^c	0.14, 0.19	-2.6	0	< 5.01	...
HD024760	ϵ Per	157.35	-10.09	2.73	2.90	...	B0.5IV	0.07 \pm 0.01	...	0.17 ^c	0.15, 0.19	-4.9	2	62.5	22.8	0.87	0.8
HD024912	ξ Per	160.37	-13.11	4.02	4.04 ^b	...	O7.5IIInf	0.26 \pm 0.01	...	0.59	0.46, 0.70	-5.9	2	7.1	24.5	2.19	2.1
HD024398	ζ Per	162.29	-16.69	2.97	2.88 ^b	...	B1Ib	0.27 \pm 0.01	...	0.40	0.26, 0.52	-6.7	2	20.2	24.5	1.51	2.4
HD023630	η Tau	166.67	-23.46	2.81	2.87 ^b	...	B7IIIe	0.05 \pm 0.01	...	0.11 ^c	0.10, 0.13	-8.3	1	< 2.00	...
HD093521	HD 093521	183.14	62.15	6.78	7.01	7.72	O9Vp	0.05 \pm 0.01	-0.08 \pm 0.04	1.76	1.54, 2.29	1.7	0	-15.8	32.5	7.24	2.7
HD040111	139 Tau	183.97	0.84	4.74	4.82	5.06	B1Ib	0.10 \pm 0.01	-0.28 \pm 0.04	1.24	0.82, 1.63	-9.7	0	15.5	27.4	6.76	1.9
HD036861	λ Ori	195.05	-12.00	3.32	3.50 ^d	...	O8III	0.10 \pm 0.01	...	0.55	0.43, 0.68	-13.0	2	5.1	37.4	1.62	0.7
HD045995	HD 045995	200.62	0.68	6.02	6.13 ^d	...	B2.5Ve	0.08 \pm 0.01	...	0.36	0.29, 0.55	-12.5	0	28.7	26.2	1.95	1.6
HD035439	25 Ori	201.96	-18.29	4.70	4.87 ^b	...	B1Vne	0.06 \pm 0.01	...	0.35	0.29, 0.57	-14.4	1	17.7	16.2	0.95	0.7
HD047839	15 Mon	202.94	2.20	4.38	4.61 ^d	...	O7Vf	0.07 \pm 0.01	...	0.86 ^a	0.75, 1.07	-12.7	3	34.8	36.6	3.16	0.9
HD036486	δ Ori A	203.86	-17.74	2.25	2.41 ^d	...	O9.5II	0.08 \pm 0.01	...	0.42 ^a	0.30, 0.51	-14.6	2	-5.9	56.0	5.50	1.3
HD036695	VV Ori	204.84	-17.81	5.18	5.35	5.89	B1V	0.06 \pm 0.01	-0.12 \pm 0.04	0.59 ^a	0.48, 0.95	-14.7	0	4.6	31.2	8.32	2.2
HD037128	ϵ Ori	205.21	-17.24	1.59	1.70 ^b	...	B0Iae	0.10 \pm 0.01	...	0.48	0.37, 0.54	-14.7	0	8.7	16.2	1.48	1.6
HD037742	ζ Ori	206.45	-16.59	1.71	1.82 ^d	...	O9.5Ib	0.13 \pm 0.01	...	0.25	0.21, 0.31	-14.8	1	13.2	23.6	1.78	0.8
HD028497	HD 028497	208.78	-37.40	5.39	5.59 ^b	...	B1.5Ve	0.02 \pm 0.01	...	0.43	0.35, 0.67	-15.1	1	7.2	35.7	7.24	1.1
HD033328	λ Eri	209.14	-26.69	4.07	4.25 ^b	...	B2Vne	0.03 \pm 0.01	...	0.28	0.18, 0.38	-15.3	0	4.3	36.2	4.47	0.5
HD037043	ι Ori	209.52	-19.58	2.56	2.76	...	O9III	0.06 \pm 0.01	...	0.43 ^a	0.33, 0.56	-15.3	2	-3.6	26.5	2.00	1.0
HD037303	HD 037303	209.79	-19.15	5.81	6.01	...	B1.5V	0.01 \pm 0.01	...	0.70 ^a	0.57, 1.08	-15.3	0	-8.4	25.4	3.55	0.9
HD038771	κ Ori	214.51	-18.50	1.94	2.05 ^b	...	B0.5Ia	0.09 \pm 0.01	...	0.22	0.19, 0.27	-15.7	2	9.9	29.4	2.51	0.9
HD052918	HD 052918	218.01	0.61	4.78	4.96 ^b	...	B1Vne	0.04 \pm 0.01	...	0.57	0.37, 0.76	-14.4	0	61.0	20.1	1.23	1.2
HD087901	α Leo	226.43	48.93	1.37	1.40	...	B7V	0.10 \pm 0.01	...	0.02 ^c	0.02, 0.02	-4.5	1	< 2.51	...
HD051283	HD 051283	234.01	-9.33	5.14	5.29	...	B2IIIe	0.03 \pm 0.01	...	0.56	0.42, 0.98	-15.9	0	28.8	33.0	6.03	1.8
HD091316	ρ Leo	234.89	52.77	3.69	3.84 ^b	...	B1Iab	0.04 \pm 0.01	...	1.09	0.83, 1.47	-3.5	0	-12.1	28.7	1.58	0.8
HD038666	μ Col	237.29	-27.10	4.89	5.15	6.01	O9.5V	0.01 \pm 0.01	0.10 \pm 0.04	0.76	0.66, 1.00	-16.5	0	17.6	46.1	6.61	2.1
HD058978	HD 058978	237.41	-3.00	5.51	5.64 ^b	...	B0.5IVnpe	0.11 \pm 0.01	...	0.79	0.57, 1.08	-15.3	1	45.3	31.6	9.33	1.3
HD057060	29 CMa	237.82	-5.37	4.74	4.90	...	O7Iabfp	0.15 \pm 0.02	...	1.87 ^a	1.53, 2.30	32.1	33.8	32.1	33.8	2.88	0.9
HD057061	τ CMa	238.18	-5.54	4.73	4.89 ^d	...	O9II	0.11 \pm 0.01	...	1.57 ^a	1.19, 1.92	-15.5	2	30.9	31.9	3.31	0.8
HD044506	HD 044506	241.63	-20.78	5.35	5.52 ^b	...	B1.5IIIin	0.02 \pm 0.01	...	0.75	0.57, 1.23	-16.3	1	17.2	39.7	6.92	2.5
HD066811	ζ Pup	255.98	-4.71	2.01	2.21 ^b	...	O5Ibnf	0.12 \pm 0.01	...	0.42	0.34, 0.51	-14.3	2	15.0	33.0	3.24	0.7

TABLE 12

Star Name (1)	Alt Name (2)	l (deg) (3)	b (deg) (4)	B (5)	V (6)	K (7)	Spl/L (8)	$E(B-V)$ (9)	$E(K-V)$ (10)	d (kpc) (11)	d_r (kpc) (12)	v_c (km s $^{-1}$) (13)	[R] (14)	v_{\odot} (km s $^{-1}$) (15)	b (km s $^{-1}$) (16)	N (10 13 cm $^{-2}$) (17)	$\sigma(N)$ (10 13 cm $^{-2}$) (18)
HD064760	HD 064760	262.06	-10.42	4.09	4.23 ^s	...	B0.5Ib	0.05 ± 0.01	...	1.06	0.80, 1.34	-14.1	0	28.7	14.1	12.02	0.7
HD068273	γ^2 Vel	262.80	-2.69	1.67	1.81	...	WC8+O9I	0.00 ± 0.01	...	0.26 ^{ca}	0.23, 0.30	-13.3	2	1.7	25.6	4.47	1.1
HD042933	δ Pic	263.30	-27.68	4.49	4.71	...	B0.5IV	0.02 ± 0.01	...	0.80 ^a	0.58, 1.08	-14.7	2	-3.7	33.3	3.89	0.5
HD064740	HD 064740	263.38	-11.19	4.40	4.61 ^s	...	B1.5Vp	0.01 ± 0.01	...	0.22 ^c	0.20, 0.25	-14.0	0	22.2	33.0	1.78	0.6
HD104337	HD 104337	286.92	41.63	5.08	5.26	5.85	B1V	0.04 ± 0.01	-0.07 ± 0.04	0.49 ^a	0.40, 0.78	-2.0	0	-13.6	21.2	1.51	1.6
HD010144	α Eri	290.84	-58.79	0.47	0.53	...	B3Vpe	0.13 ± 0.02	...	0.04 ^c	0.04, 0.05	-10.1	0	17.0	30.1	1.15	0.7
HD106490	δ Cru	298.23	3.79	2.59	2.77 ^s	...	B2IV	0.02 ± 0.01	...	0.11 ^c	0.10, 0.12	-5.8	0	55.7	19.9	0.52	0.4
HD112244	HD 112244	303.55	6.03	5.38	5.40 ^f	...	O8.5Iabf	0.25 ± 0.01	...	1.71	1.41, 2.15	-4.2	0	-15.1	28.0	7.24	3.6
HD122451	β Cen	311.77	1.25	0.44	0.58 ^f	...	B1III	0.06 ± 0.02	...	0.16 ^c	0.15, 0.18	-2.8	0	16.6	22.8	0.91	0.4
HD121263	ζ Cen	314.07	14.19	2.34	2.52	...	B2.5IV	0.02 ± 0.01	...	0.12 ^{ca}	0.11, 0.13	-0.6	0	-2.5	22.7	1.26	0.4
HD120307	ν Cen	314.41	19.89	3.19	3.39	...	B2IV	0.01 ± 0.01	...	0.15 ^{ca}	0.13, 0.16	0.3	1	18.2	31.8	1.48	0.4
HD121743	ϕ Cen	315.98	19.07	3.61	3.81 ^s	...	B2IV	0.02 ± 0.01	...	0.14 ^c	0.13, 0.16	0.5	1	-9.1	10.8	0.51	0.3
HD116658	α Vir	316.11	50.84	0.91	1.04	...	B1IV	0.10 ± 0.02	...	0.08 ^{ca}	0.08, 0.09	4.3	0	1.1	19.0	2.69	0.4
HD135591	HD 135591	320.13	-2.64	5.33	5.43	...	O7.5IIIf	0.18 ± 0.01	...	1.25	0.99, 1.50	-1.1	2	6.2	30.6	4.17	1.3
HD132058	β Lup	326.25	13.91	2.49	2.66	...	B2IV	0.03 ± 0.01	...	0.16 ^c	0.14, 0.18	2.5	1	4.0	37.2	1.91	0.3
HD150898	HD 150898	329.98	-8.47	5.48	5.57 ^s	5.77	B0.5Ia	0.11 ± 0.01	-0.35 ± 0.04	2.80	2.12, 3.14	0.8	0	-5.6	28.8	6.92	3.2
HD136298	δ Lup	331.32	13.82	3.01	3.20 ^f	...	B1.5IV	0.02 ± 0.01	...	0.16 ^c	0.14, 0.18	3.8	0	-7.0	22.9	2.19	0.5
HD173948	λ Pav	333.61	-23.87	4.06	4.21 ^s	...	B2IIIf	0.05 ± 0.01	...	0.33	0.25, 0.59	-0.3	0	17.3	37.1	6.03	1.0
HD157246	γ Ara	334.64	-11.48	3.18	3.31	...	B1Ib	0.05 ± 0.01	...	0.66	0.44, 0.86	1.6	2	-6.7	26.5	1.45	0.8
HD143118	η Lup	338.77	11.01	3.21	3.41 ^s	...	B2.5IV	0.00 ± 0.01	...	0.15 ^c	0.14, 0.17	5.3	0	-15.2	23.7	1.62	0.6
HD165024	θ Ara	343.33	-13.82	3.56	3.66	...	B2Ib	0.06 ± 0.01	...	0.73	0.43, 0.99	3.4	2	-21.2	23.9	4.27	0.7
HD151890	μ^1 Sco	346.12	3.91	2.82	2.98	...	B1.5IV	0.05 ± 0.01	...	0.22 ^a	0.14, 0.29	6.3	0	-19.3	26.2	2.75	0.9
HD143018	π Sco	347.21	20.23	2.73	2.88	...	B1V	0.08 ± 0.01	...	0.14 ^{ca}	0.13, 0.16	8.2	1	-12.5	24.5	0.25	0.5
HD209952	α Gru	350.00	-52.47	1.69	1.76 ^f	...	B7IV	0.06 ± 0.01	...	0.03 ^c	0.03, 0.03	-1.4	0	< 0.79	...
HD143275	δ Sco	350.10	22.49	2.31	2.39 ^f	...	B0.3IVe	0.00 ± 0.01	...	0.12 ^{ca}	0.11, 0.14	8.9	1	-11.5	15.0	1.82	0.5
HD158926	λ Sco	351.74	-2.21	1.48	1.62 ^f	...	B1.5IV	0.08 ± 0.01	...	0.22 ^a	0.18, 0.27	6.9	2	-19.9	22.8	1.82	0.2
HD155806	HD 155806	352.59	2.87	5.59	5.64 ^f	...	O7.5Ve	0.23 ± 0.01	...	0.86	0.75, 1.09	7.7	1	-12.8	33.7	16.60	1.5

NOTE.—Explanation of columns: (1)—HD number; (2)—Alternative star name; (3,4)—Galactic l and b ; (5,6)—Johnson B - and V -band magnitudes, converted from *Tychio* B_T and V_T values; (7)—Johnson K -band magnitude, converted from 2Mass K -band magnitude. Value is not given if $E(K-V)$ was not derived for the sight line (see Appendix B.2); (8)—spectral type and luminosity class; (9)—optical $B-V$ color excess; (10)—IR $K-V$ color excess; (11) distance to star based on spectral type and luminosity class, except for stars with *Hipparcos* parallaxes such that $d_p/\sigma(d_p) > 5$; (12)—range in possible distances, based on the uncertainties discussed in Appendix B.3, except for distances derived from *Hipparcos* parallax values; (13)—correction required to move heliocentric velocities observed along a sight line to LSR velocities ($v_{LSR} = v_c + v_{\odot}$); (14)—our *ROSAT* classification discussed in §3.4 and §3.5. (15)—Heliocentric velocity of O VI absorption, converted from Table 1 of Jenkins (1978a) via $v_{\odot} = v_{LSR} - v_c$; (16)—Doppler parameter of O VI absorption, converted from Table 1 of Jenkins (1978a) with $b = \sqrt{2\Delta}$; (17)—O VI column density from Table 1 of Jenkins (1978a); (18)—Approximate errors in the O VI column density, derived from Archive coadded data scans. Note that the superscript marks for columns 6 and 11 refer to the same footnotes given in Table 1: that is, 'a' means that the star is identified as a spectroscopic binary (SB) either in the SB9 catalog (Pourbaix et al. 2004) or by García & Mermilliod (2001), and 'c' means that a *Hipparcos* parallax distance was used.

TABLE 13
FUSE DATA OBTAINED BY ZSARGÓ ET AL

Star Name (1)	l (deg) (2)	b (deg) (3)	B (4)	V (5)	K (6)	Sp/L (7)	$E(B-V)$ (8)	$E(K-V)$ (9)	d (kpc) (10)	d_r (kpc) (11)	v_c (km s $^{-1}$) (12)	[R] (13)	v_{\odot} (km s $^{-1}$) (14)	b (km s $^{-1}$) (15)	$\log N$ [log(cm $^{-2}$)] (16)	dist ref ^a (17)
NGC6723-III60	0.02	-17.30	PAGB	8.0	6.8, 9.2	6.5	1	17.5	44.3	14.37 \pm 0.12	1
NGC-5904-ZNG-1	3.87	46.80	PAGB	7.7	7.0, 8.5	11.8	1	-17.6	36.5	14.41 \pm 0.08	2
HD175876	15.28	-10.58	6.80	6.92	7.28	O6.5III	0.16 \pm 0.01	-0.49 \pm 0.04	2.7	2.2, 3.1	10.3	0	-26.6	59.2	14.14 \pm 0.13	3
HD177989	17.81	-11.88	9.22	9.34	9.61	B0III	0.11 \pm 0.01	-0.42 \pm 0.05	6.0	4.5, 8.9	10.5	0	0.7	49.5	14.31 \pm 0.06	3
vZ-1128	42.50	78.69	PAGB	10.0	9.1, 10.9	9.7	1	-41.0	52.8	14.49 \pm 0.03	4
HD121800	113.01	49.76	8.98	9.07 ^b	...	B1.5V	0.13 \pm 0.02	...	1.8	1.5, 2.9	10.2	1	1.9	52.0	14.40 \pm 0.03	3
HD003827	120.79	-23.23	7.76	7.95	8.74	B0.7V	0.05 \pm 0.02	0.12 \pm 0.04	2.0	1.8, 2.9	2.4	0	-17.3	39.0	13.80 \pm 0.04	3
HDE233622	168.17	44.23	9.82	9.97 ^b	...	B2V	4.7	4.0, 5.4	0.3	1	-21.7	47.2	13.87 \pm 0.19	5
BD+382182	182.16	62.21	10.95	11.18	...	B3V	4.5	3.8, 5.2	1.8	0	-5.2	35.2	14.10 \pm 0.07	6
HD018100	217.93	-62.73	8.23	8.44	...	B5II/III	3.1	2.6, 3.6	-12.8	1	4.5	45.0	13.77 \pm 0.13	7
HD100340	258.85	61.23	9.84	10.07	...	B1V	3.0	2.8, 3.2	-0.4	0	10.3	78.3	14.28 \pm 0.16	8
HD097991	262.34	51.73	7.18	7.39	...	B1V	1.2	1.0, 1.9	-2.6	0	<13.69	3
IL212	303.63	-61.03	10.28	10.35 ^b	...	B2V	2.2	1.9, 2.6	-8.5	0	22.7	37.0	14.21 \pm 0.07	9
HD116852	304.88	-16.13	8.37	8.49	8.80	O9III	0.14 \pm 0.01	-0.46 \pm 0.04	4.5	3.5, 6.0	-6.4	0	-6.7	38.7	14.30 \pm 0.02	3
NGC-5139-WOR-197	308.94	15.07	PAGB	5.5	5.2, 5.8	-1.7	0	-15.8	43.2	14.54 \pm 0.12	10
HD121968	333.97	55.84	10.04	10.16	...	B1V	3.8	3.4, 4.2	7.4	0	-6.8	38.2	13.97 \pm 0.06	11
NGC-6397-162	338.19	-11.94	PAGB	2.5	2.2, 2.9	2.4	0	6.8	48.2	14.25 \pm 0.06	12

NOTE.—See Table 1 for a full explanation of the table entries.

^aDistances to the stars taken from the following references: 1—Martins & Fraqielli (1987); 2—Testa et al. (2004); 3—this paper; 4—Rood et al. (1999); 5—Ryans et al. (1997); 6—Keenan et al. (1986); 8—Ryans et al. (1999); 9—Magee et al. (2001); 10—Bellazzini et al. (2004); 11—Little et al. (1995); 12—Gratton et al. (2003).

^bDetected by *Hipparcos* as variable—faintest H_p used.

D. Upper Limits

Astronomical observations sometimes exhibit measurement outcomes that are not significantly above the noise. Ideally, in such circumstances one should report the formal measurement and the associated error, as we have done in columns 3–7 of Table 5. This procedure conveys the most information. Nevertheless, it is a common practice to define a minimum measurement level above which one can claim a “detection” (with an associated uncertainty), and this comfort-level threshold is usually expressed as some factor N times the standard deviation of the noise σ . On the occasion that a measurement is found to fall below this threshold, it is customary to state that only an upper limit at the $N\sigma$ level of confidence for the true signal is warranted. In defining this upper limit, many investigators arbitrarily discard the actual measurement outcome and claim that the upper limit is simply equal to $N\sigma$. When this is done, there is a complete loss of potentially useful information about whether the measurement came out at just barely below the threshold, or alternatively, below zero by some one or two standard deviations of the noise (which can happen with reasonable frequency for null signal levels in the absence of any noise). The former represents a weaker case for an upper limit than the latter, since we know that it is much more difficult for a noise deviation to drive any moderately positive signal to a negative outcome than to cancel it just enough to go somewhat below the defined threshold level. This difference is not reflected in the claimed degree of confidence for the upper limit. Moreover, there is an untidy discontinuity in the upper limits inferred from the “upper limit only” cases for outcomes just below the threshold, compared with “detections plus $N\sigma$ ” for outcomes just above the threshold. For these reasons, we adopted a more refined procedure.

In §2.8.2 we made use of a scheme described by Marshall (1992) for creating upper limits at a given level of confidence α (we chose to use the “ 2σ ” level of significance, making $\alpha = 0.97725$) for marginal or negative measurement outcomes, under the condition that we have *a priori* information that the quantity being measured must be positive. Here, we derive the formula for evaluating these upper limits and show a plot that allows one to find quickly what the upper limits would be at a few levels of significance that differ from the “ 2σ ” value.

Our derivation differs somewhat from that given by Marshall (1992), and makes use of an extension of Bayes’ Theorem for determining the probability of condition A , given conditions B and C ,

$$\text{Prob}(A|B,C) = \text{Prob}(A|B)\text{Prob}(C|A,B)/\text{Prob}(C|B) . \quad (\text{D1})$$

If we designate the true value of the quantity as t , our stated upper limit as u , and have a measurement outcome datum d with an associated noise amplitude n , we can make the assignments for the conditions $A \equiv t > u$, $B \equiv t > 0$ and $C \equiv d, n$. Restating Eq. D1 in terms of our explicit conditions yields

$$\text{Prob}(t > u|t > 0, d, n) = \text{Prob}(t > u|t > 0)\text{Prob}(d, n|t > u, t > 0)/\text{Prob}(d, n|t > 0) , \quad (\text{D2})$$

We set the first term on the right-hand side of this equation equal to 1 (this clearly must be true if $u < 0$ given that $t > 0$; for $u > 0$ there is no constraint on the probability). The second term represents the small probability $(1 - \alpha')$ that we could have obtained an outcome d with noise n when the true value t violates our declared upper limit u . This term is given by the area under the one-sided tail of a Gaussian distribution with unit variance and zero mean integrated from $(u - d)/n$ to infinity, i.e.,

$$\text{Prob}(d, n|t > u, t > 0) = \frac{1}{2}\text{erfc}\left(\frac{u-d}{\sqrt{2}n}\right) \quad (\text{D3})$$

where erfc is the complementary error function, defined as

$$\text{erfc}(x) \equiv 1 - \text{erf}(x) = \frac{2}{\sqrt{\pi}} \int_x^\infty \exp(-t^2) dt \quad (\text{D4})$$

Similarly,

$$\text{Prob}(d, n|t > 0) = \frac{1}{2}\text{erfc}\left(\frac{-d}{\sqrt{2}n}\right) = 1 - \frac{1}{2}\text{erfc}\left(\frac{d}{\sqrt{2}n}\right) \quad (\text{D5})$$

so that our final result for the probability that there will be a violation of the upper limit is given by

$$1 - \alpha = \text{erfc}\left(\frac{u-d}{\sqrt{2}n}\right) \bigg/ \left[2 - \text{erfc}\left(\frac{d}{\sqrt{2}n}\right) \right] , \quad (\text{D6})$$

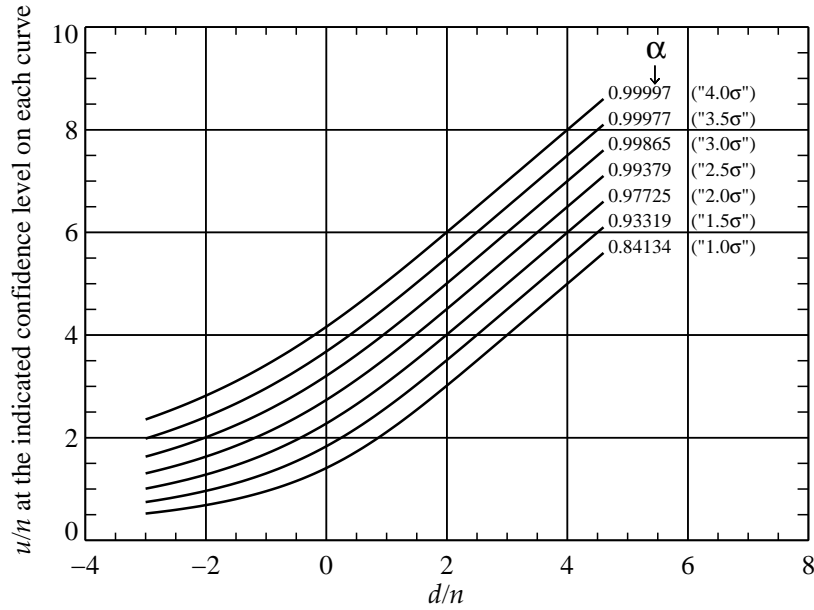


Figure 23: The family of curves for different levels of confidence α , plotted in terms of the declared upper limits divided by the measurement uncertainties (ordinates), u/n , vs. the measurement outcomes divided by their uncertainties d/n (abscissae).

for which α represents our level of confidence that u is a valid upper limit for t .

Figure 23 shows the solutions to equation D6 for various confidence levels α . This figure should help one to convert our raw measurements of barely or undetected O VI into upper limits of one's choice. The values that we had listed in Table 5 corresponded to $\alpha = 0.97725$, i.e., a "2 σ " upper limit.

E. Final Spectra

The spectra obtained from our *FUSE* survey are shown in Figure 24. These include all the data we deemed usable from the PI Team programs P102 and P122 as well as sight lines taken from the *FUSE* Archive prior to April 2003 (see §2.1). Several stars from programs P102 and P122 were not used, and are not shown here (see §2.10, and Fig. 5 instead). For each spectrum in Figure 24, there are three panels which depict the data analyzed in the ways discussed throughout §2. Below, we describe the information presented in each panel.

Top panel: This panel shows the coadded spectra for each sight line. All data come from the LiF1A *FUSE* channel, unless indicated at the bottom right of the panel, where the channel used is indicated. Spectra are plotted in specific flux units, along with the continuum used to normalize the data (solid line). The $\pm 1\sigma$ error 'envelopes' to the fitted continuum are shown as dotted lines about the adopted best-fit continuum. The star's name, Galactic co-ordinates $[l, b]$, spectral type, and *ROSAT* designation R (see §3.4 and 3.5) are shown at the top left of the panel. The distance to the star d , along with the difference between the distance and the upper and lower bounds to the distance (Appendix B.3), are also given at the top left of the panel. The *FUSE* program identification number is given at the top right. A unique identification number is shown above the top left corner of the top panel. This number corresponds to the ID numbers given in Tables 1, 2, 4, and 5.

If the wavelength scale has been corrected using data from *HST*, then an "S" is marked beneath the program number. Similarly, an "X" indicates that no shift has been made (for the reasons given in Appendix A), and the velocities of the

absorption should be considered uncertain. Otherwise, a $+10 \text{ km s}^{-1}$ shift ($+0.0344 \text{ \AA}$) has been applied to the data, which is indicated by an “F”. (This is the same nomenclature used in column 14 of Table 4.) Stars that lie against the X-ray emission of the inner regions of the Carina Nebula or the Vela SNR are noted as such with a label at the top of the panel. Note that these are included only to indicate the region of interest, and do *not* imply that the star is at the same distance as Carina or Vela. Sight lines which likely pass through the SNRs listed in Table 8 have a label ‘SNR’ (except for Vela). The flux is shown with the HD 6–0 R(0) line already removed; the region shaded in gray near the bottom of the O VI profiles represents the difference in the spectrum before and after the removal of the HD line.

Middle panel: The data normalized by the best-fit continuum are plotted in wavelength (bottom x -axis) and observed heliocentric velocity for the O VI $\lambda 1032$ transition (top x -axis). The wavelengths of five lines are marked as follows. “1”: the *predicted* position of the H₂ 7–0 R(6) line at 1030.08 \AA , based on the measured velocity of the H₂ 6–0 R(4) line; “2”: the measured position of the H₂ 6–0 P(3) line; “3”: the *predicted* wavelength of the Cl I $\lambda 1031$ line, based on the velocity of the H₂ 6–0 R(4) line. “4”: the measured position of the HD 6–0 R(0) line which is removed from the data as discussed in § 2.7; “5”: the measured position of the H₂ 6–0 R(4) line.

Line profiles corresponding to the best-fit solutions discussed in §2.8.1 over-plot the data (histogram) with curved lines. If more than one component is fitted to the O VI line, individual profiles are shown with dotted lines. The best-fit values of b , v and N for the O VI feature are listed at the bottom left of the panel, in units of km s^{-1} , km s^{-1} , and cm^{-2} , respectively. The total column density is given at the bottom right of the panel, along with two ‘errors’: the first two values in parentheses represent the range in $N(\text{O VI})$ from the upper and lower continuum fits, $N_u - N$ and $N - N_l$, where N is the O VI column density measured from the best-fit continuum; the second value in parentheses is the error from Poisson statistics alone. The central velocities/wavelengths of O VI absorption components are marked with filled triangles. The b and N values which are used to model the H₂ lines shown, are fixed by fits to other H₂ lines in different regions of the *FUSE* data. Two components are sometimes fitted to the H₂ lines in these other regions; these are indicated with two tick marks for an individual H₂ line.

Bottom panel: The variation of $N(v)$ as a function of heliocentric velocity for the O VI $\lambda 1032$ line derived from the AOD method is shown in the bottom panel. All $N(v)$ profiles are plotted at the same scale except for HDs 167402 (star #1), 168941 (#2), 178487 (#14), and HDE 225757 (#20); the O VI absorption towards these stars is so strong that the y -axis is compressed to accommodate the larger profile.

To enable calculation of an AOD column density even when the O VI line is contaminated by one or both of the H₂ lines, the P(3) and R(4) lines have been removed from the profile (see §2.8.2 for more details). The dotted lines show the positions and strengths of the removed H₂ lines, scaled as if they had the same f -value as O VI $\lambda 1032$. They are included to illustrate how the O VI AOD profile was affected by the H₂ lines before they were removed.

$N(v)$ profiles derived using the continuum-fitting error envelopes (yielding values of N_u and N_l) are shown above and below the best-fit $N(v)$ (which forms the middle, shaded histogram). The 1σ Poisson noise errors in $N(v)$ are shown as normal vertical error bars for each pixel, although they are only plotted for the middle (adopted) $N(v)$ profile.

The total column density measured over all velocities using the AOD method is quoted at the top right of the bottom panel. The velocity range used was $-120 \text{ km s}^{-1} < v_{\odot} < +120 \text{ km s}^{-1}$, although this was modified for profiles that clearly extended beyond this interval. The velocity range used can be inferred from the total range covered by gray pixels; these are the $N(v)$ values that contribute to the calculation of the total column density. As with the total column densities that we listed for the profile fits (middle panel), the differences in the column density from the upper and the best continuum fit, and the best and the lower continuum fit, $[N_u - N, N - N_l]$, are shown in the first set of parentheses. The value in the second set of parentheses gives the total error from Poisson noise.

Below the $N(v)$ profile, a gray bar indicates the range of velocities expected from differential Galactic rotation for absorbing gas along the line of sight. (These are the same bars that are shown in Fig. 17.) Darker colors mark velocities where the velocity of the gas is changing only very slowly with distance. This is discussed more fully in §3.11. A small ‘0’ above the bar marks the value of v_c given in Table 1 to indicate which end of the bar corresponds to distances of $d = 0$. As in the middle panel, small triangles along the baseline show the central velocities of the O VI components derived from profile fitting (for comparison with the AOD profile), along with the velocities of the H₂ 6–0 R(4) components, which are shown as crosses.

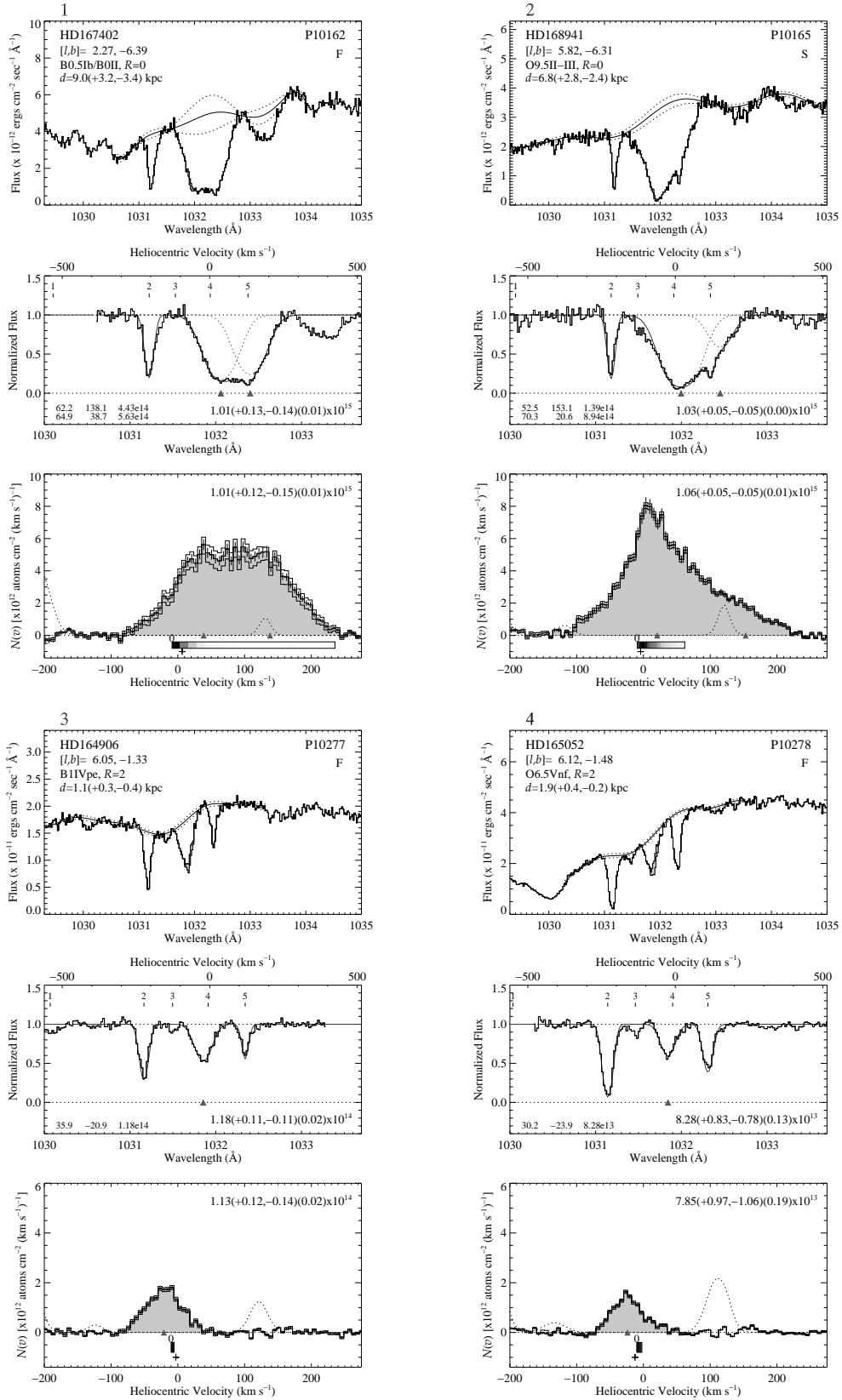
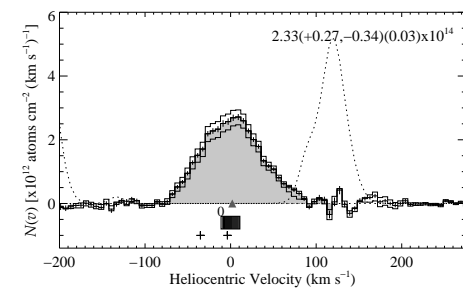
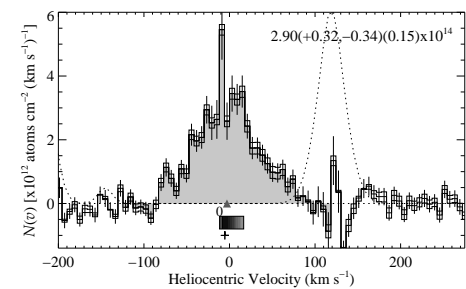
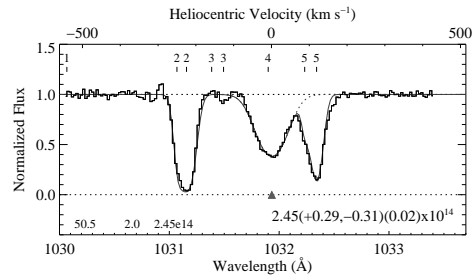
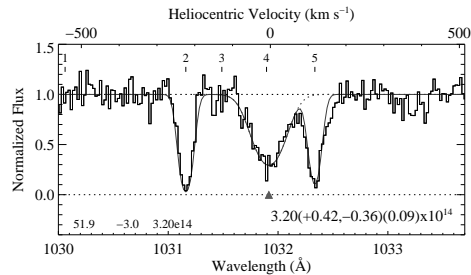
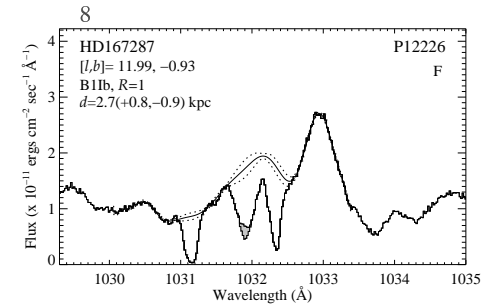
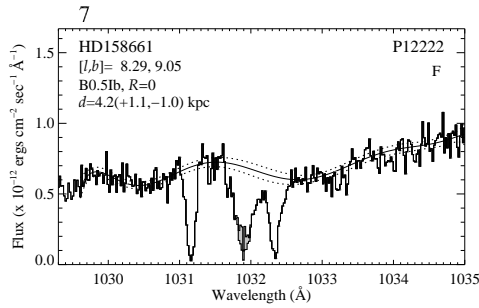
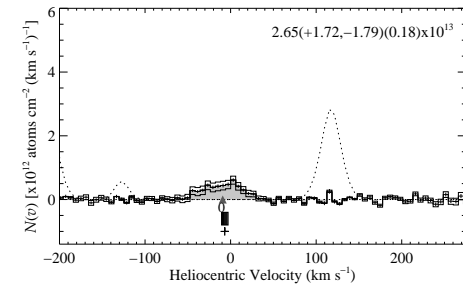
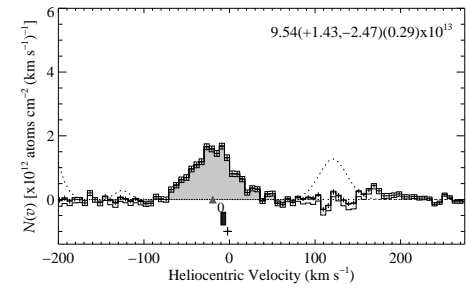
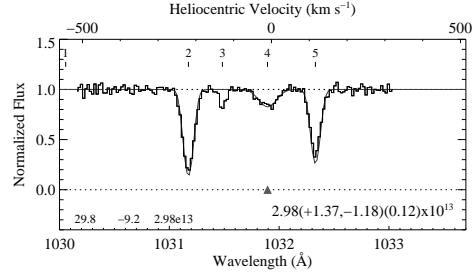
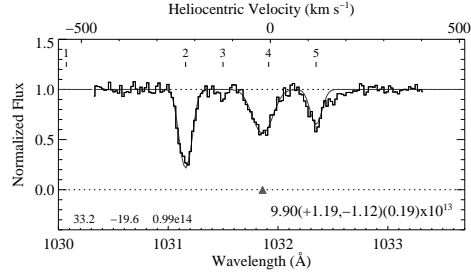
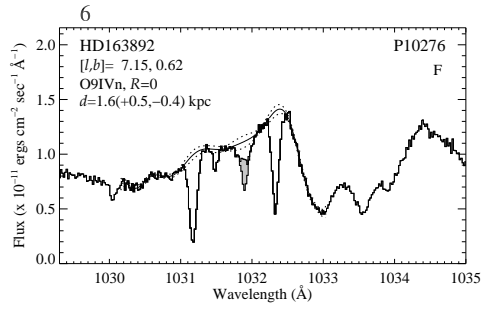
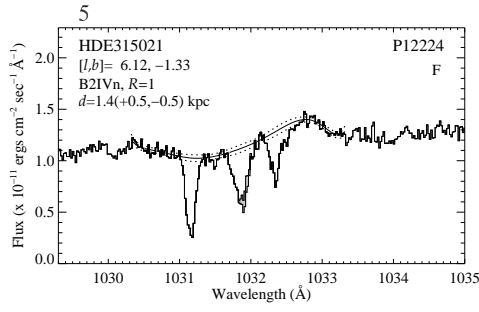
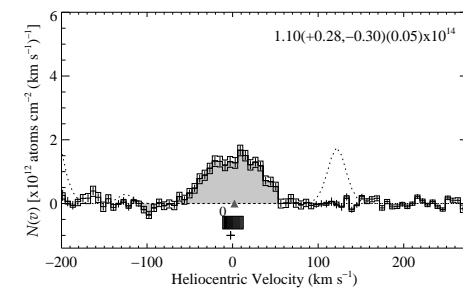
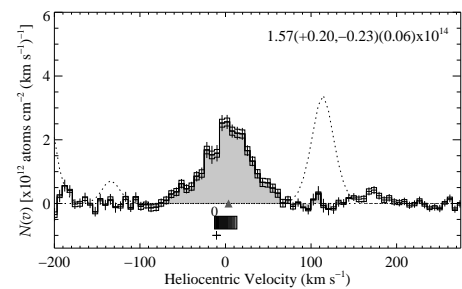
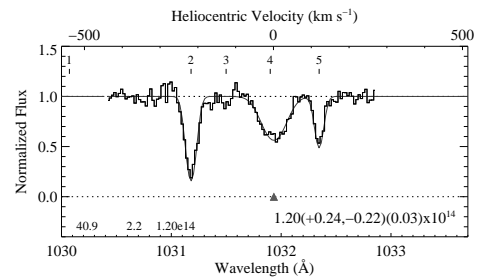
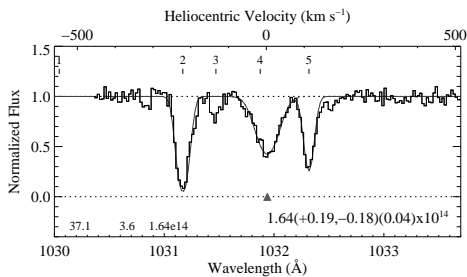
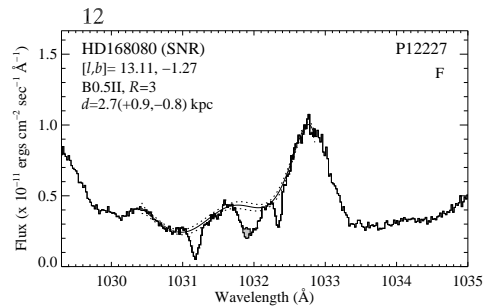
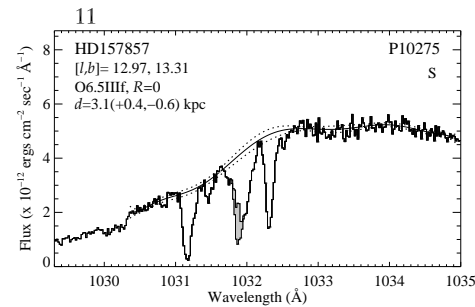
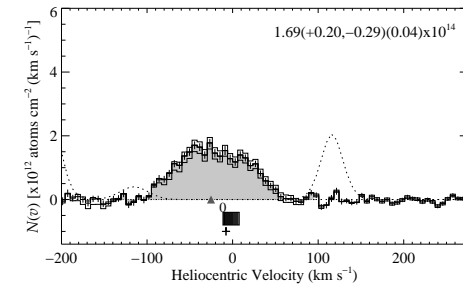
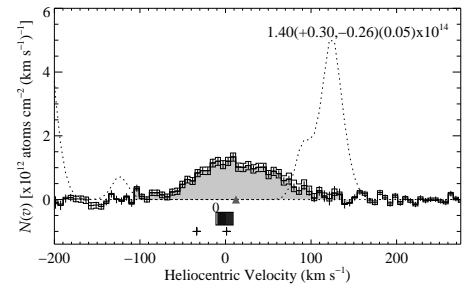
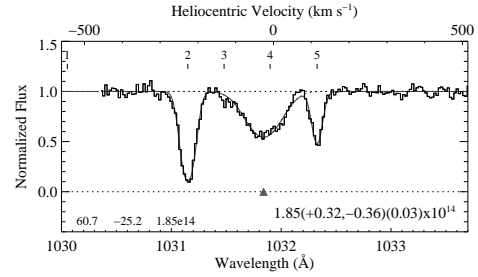
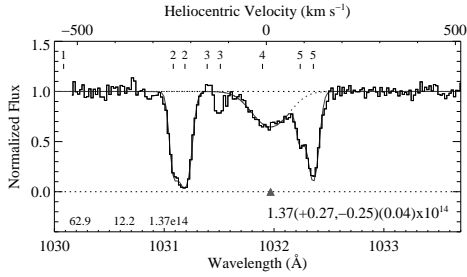
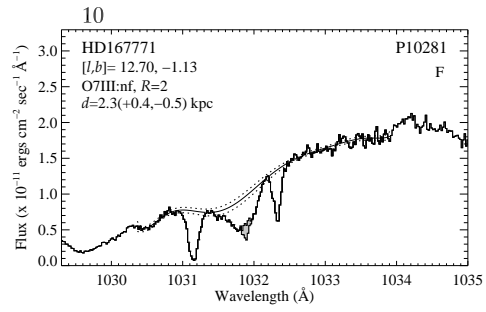
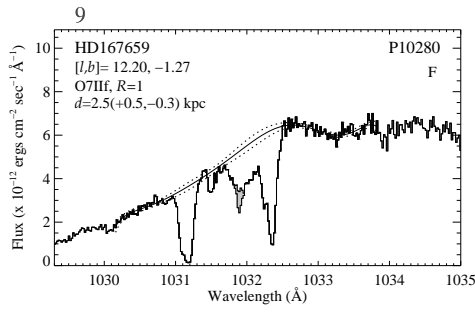


Figure 24: Spectra of Milky Way disk stars observed with *FUSE* around the wavelength region of O VI λ 1032. See text in Appendix E for full details.



105

Figure 24: cont



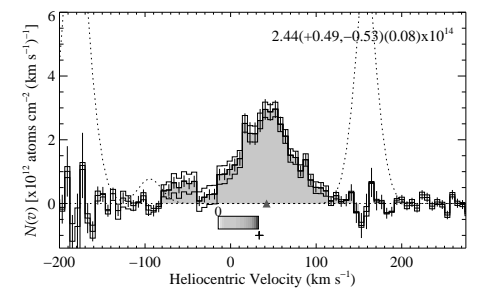
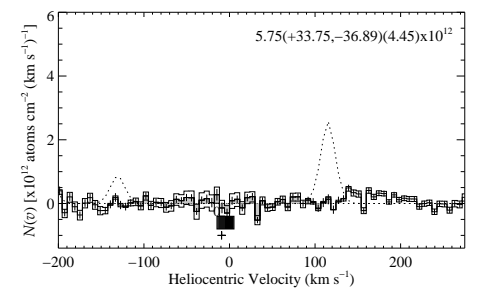
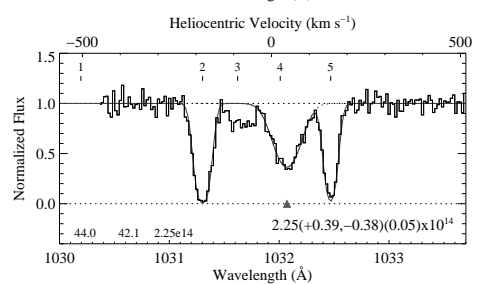
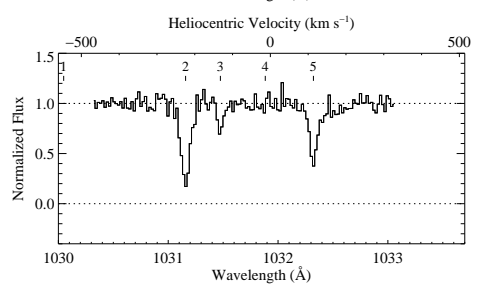
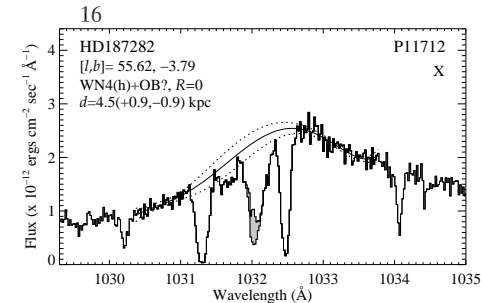
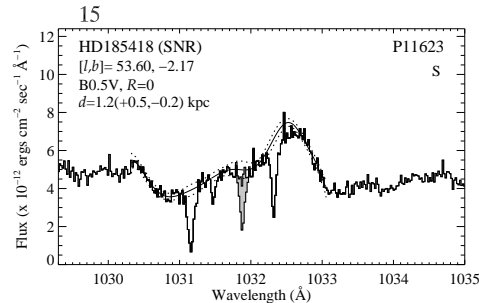
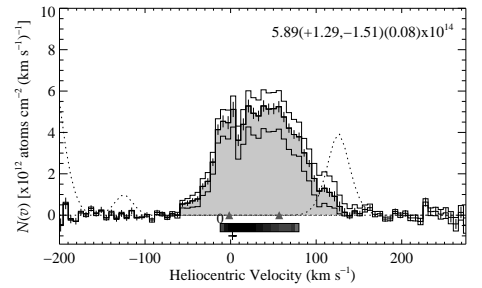
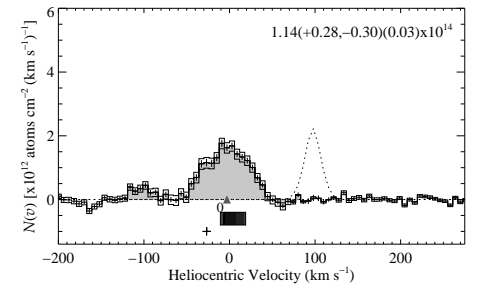
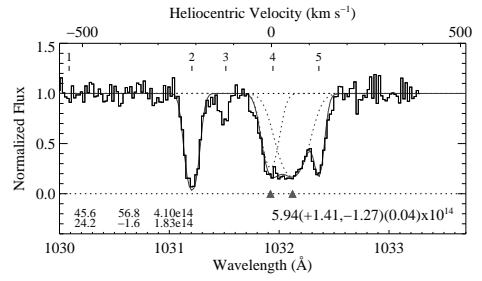
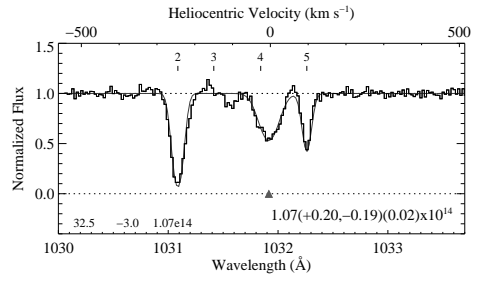
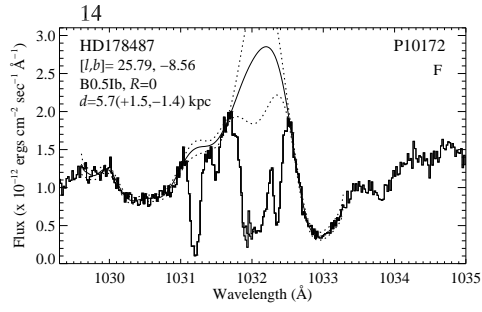
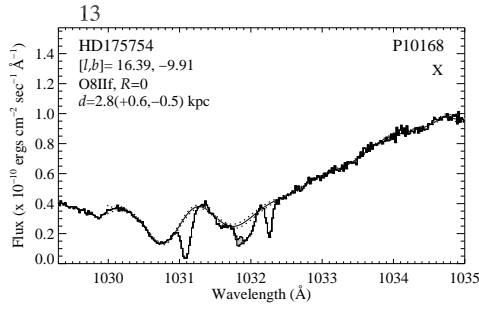


Figure 24: cont

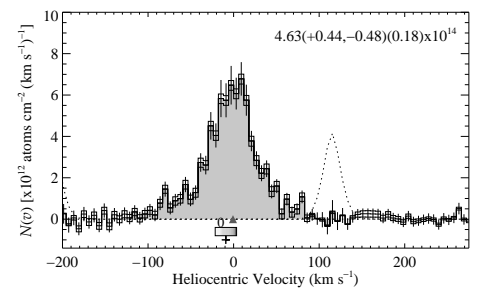
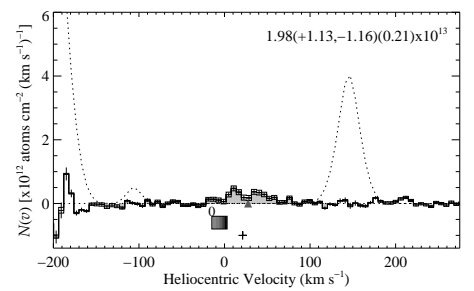
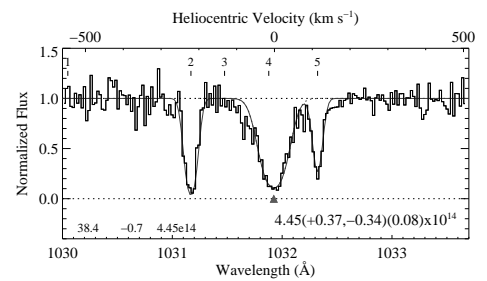
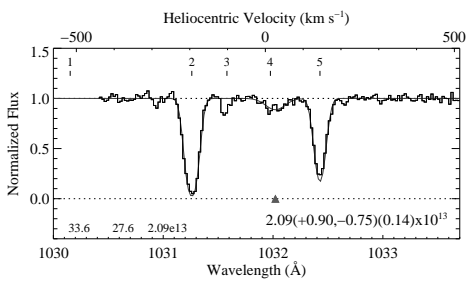
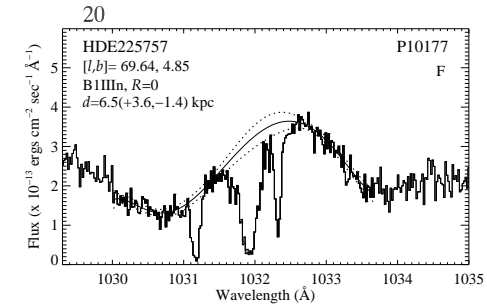
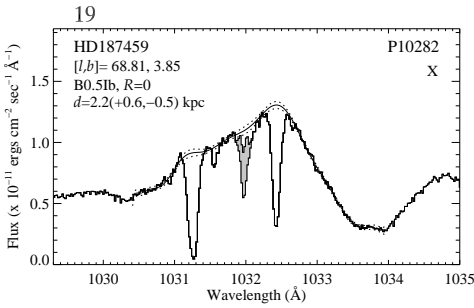
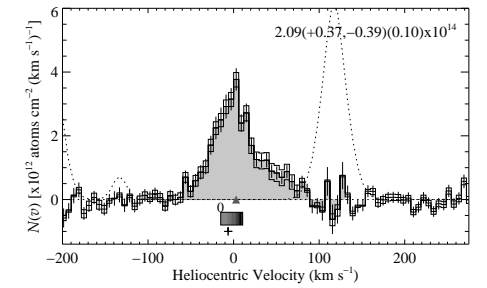
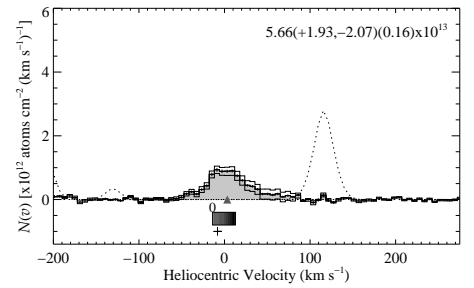
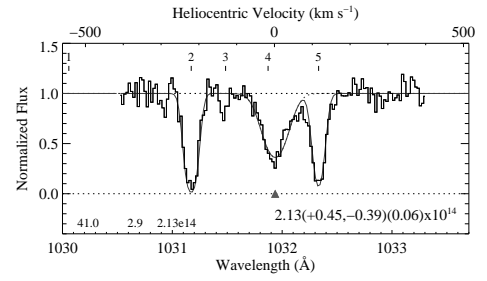
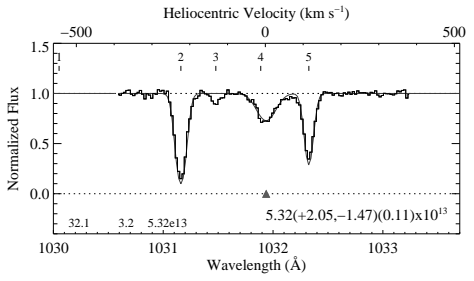
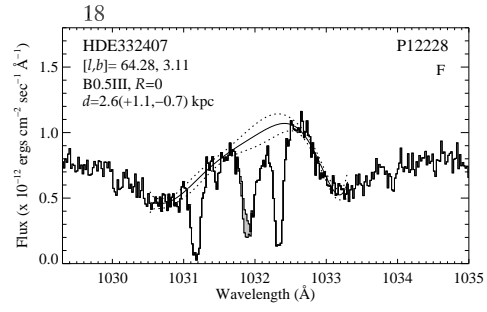
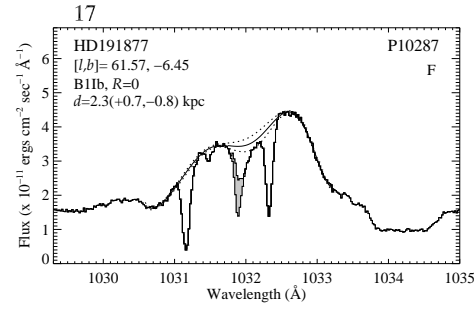


Figure 24: cont

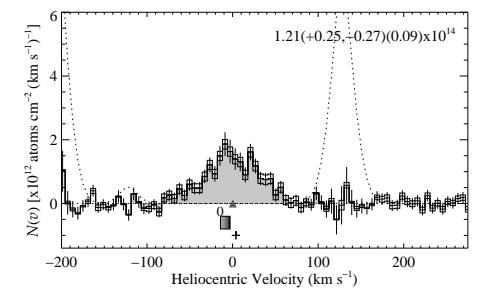
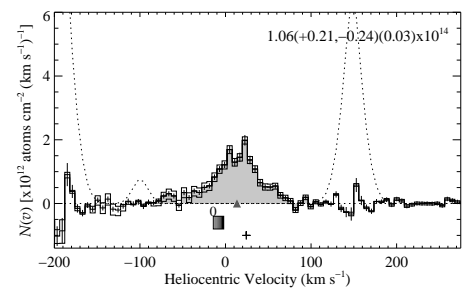
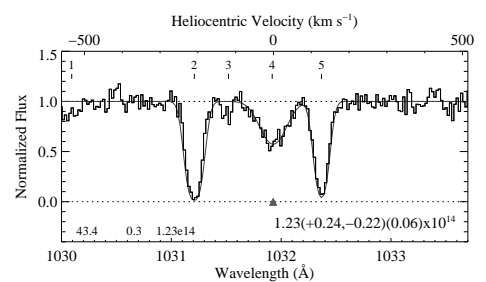
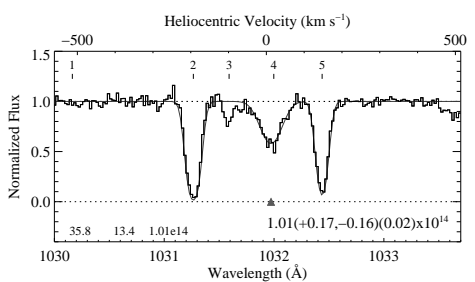
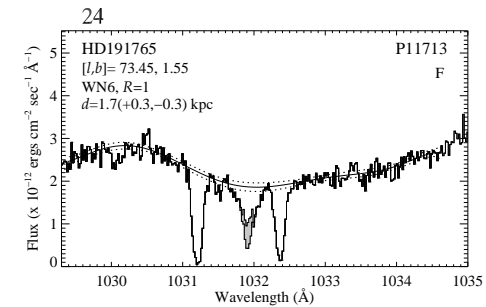
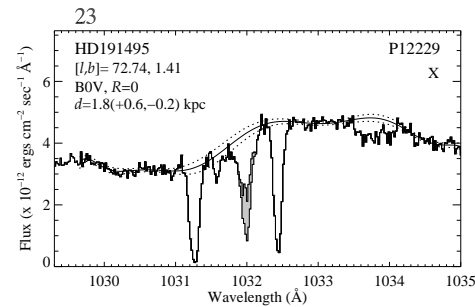
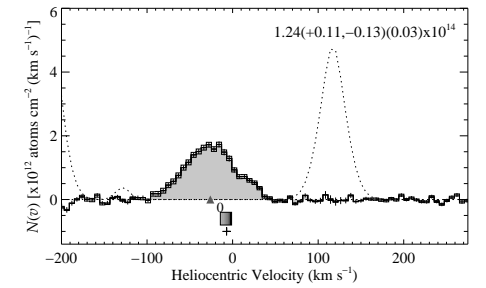
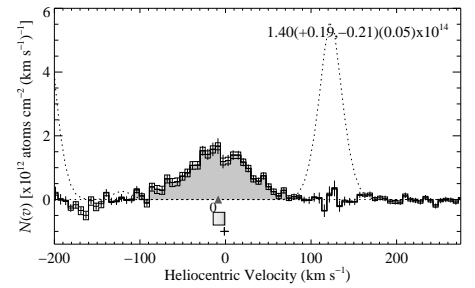
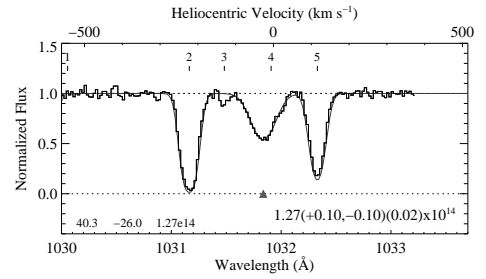
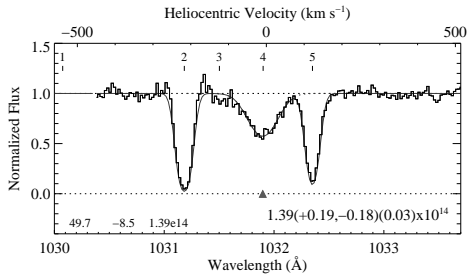
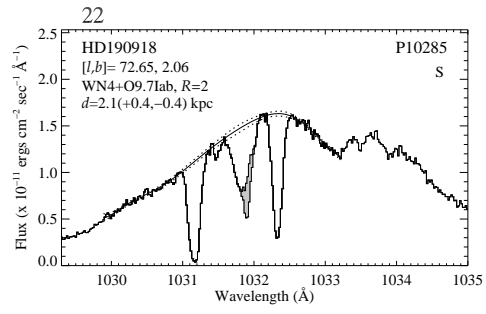
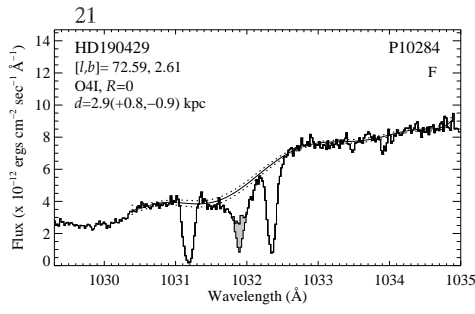


Figure 24: cont

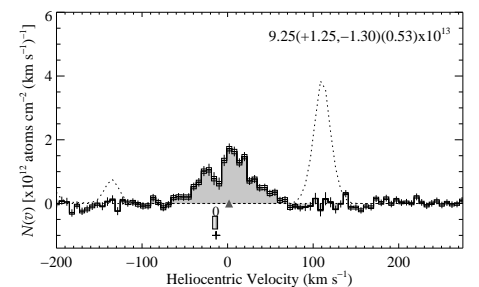
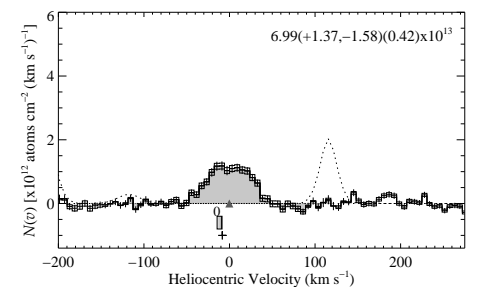
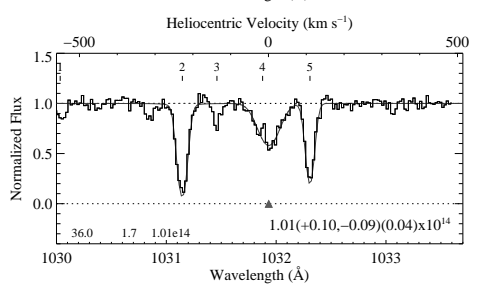
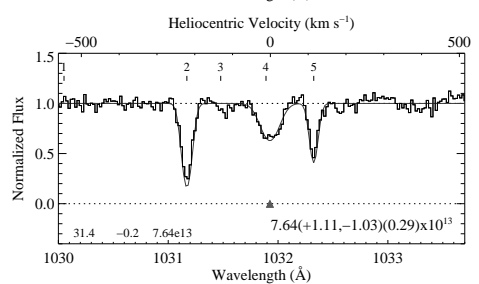
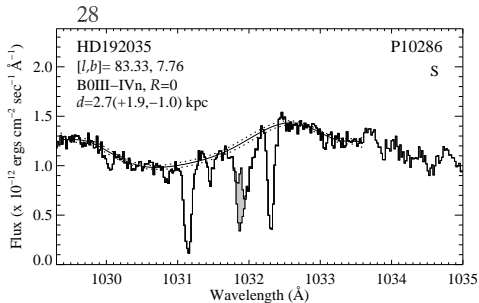
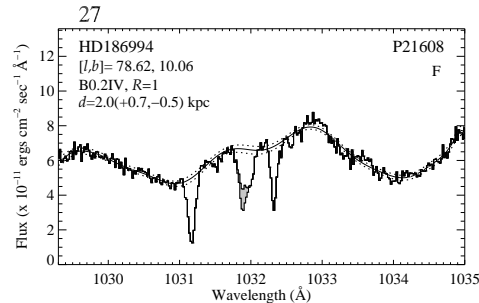
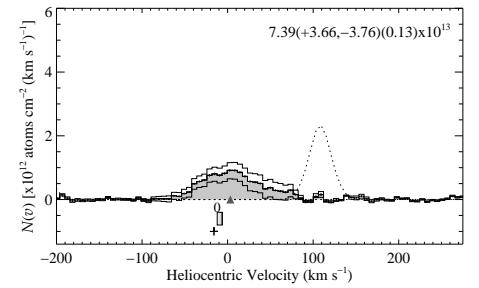
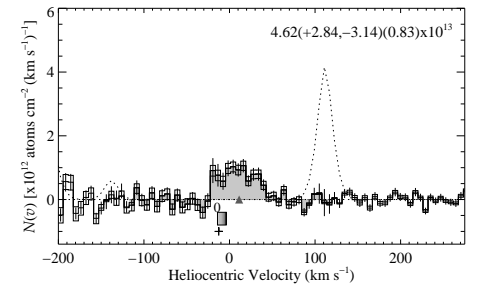
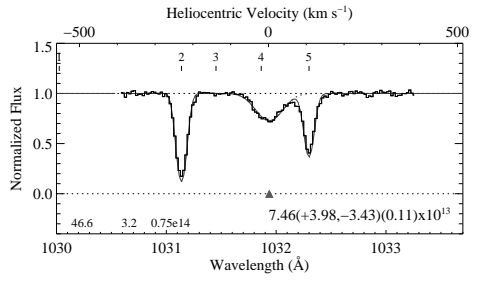
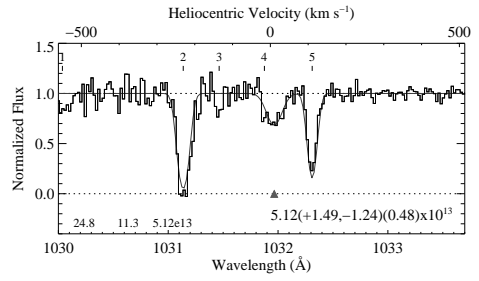
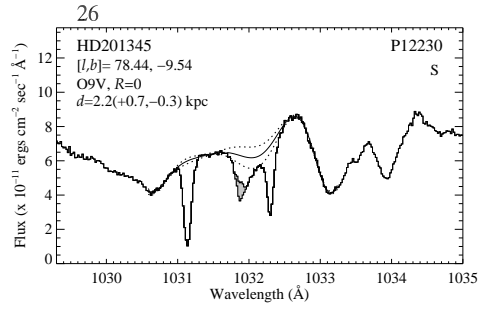
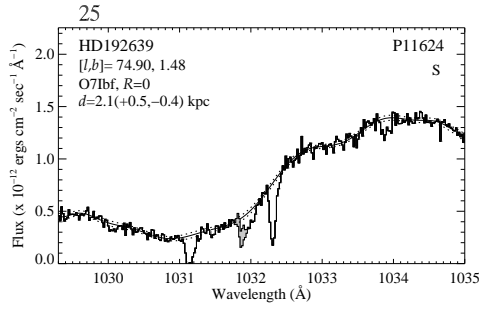


Figure 24: cont

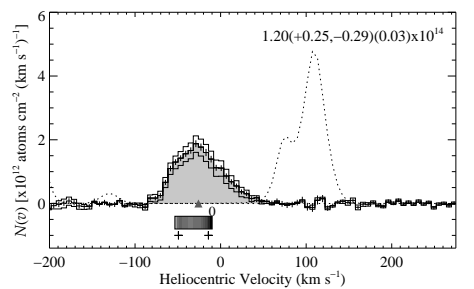
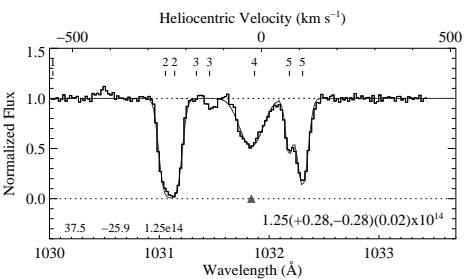
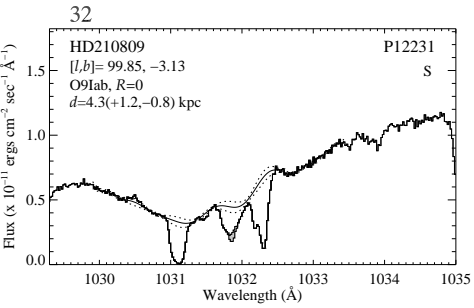
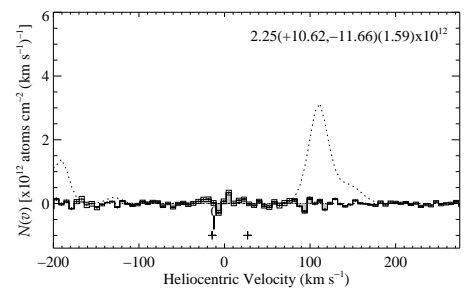
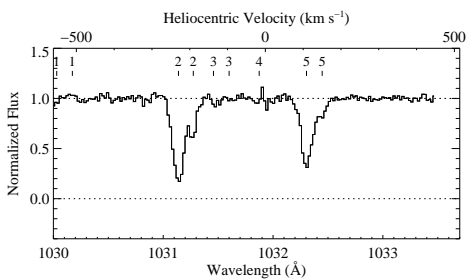
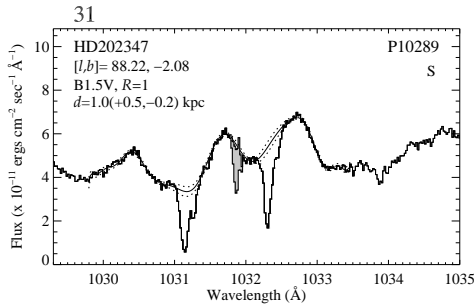
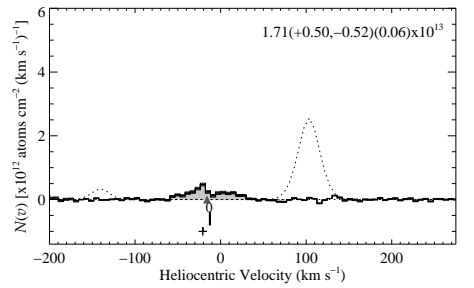
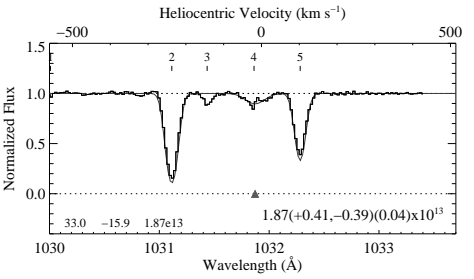
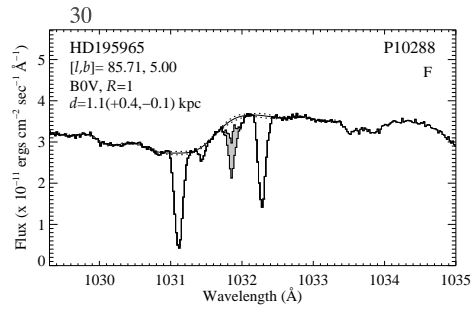
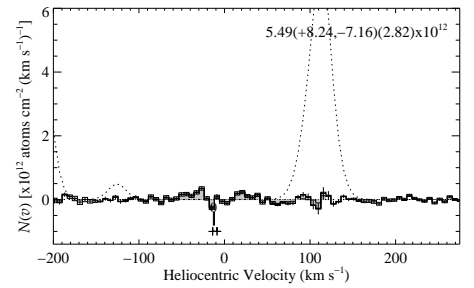
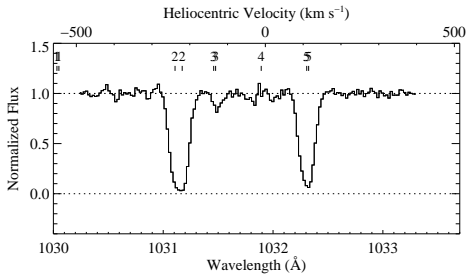
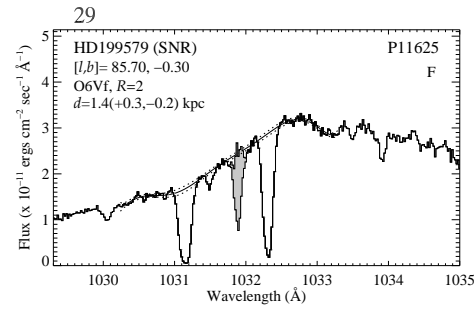


Figure 24: cont

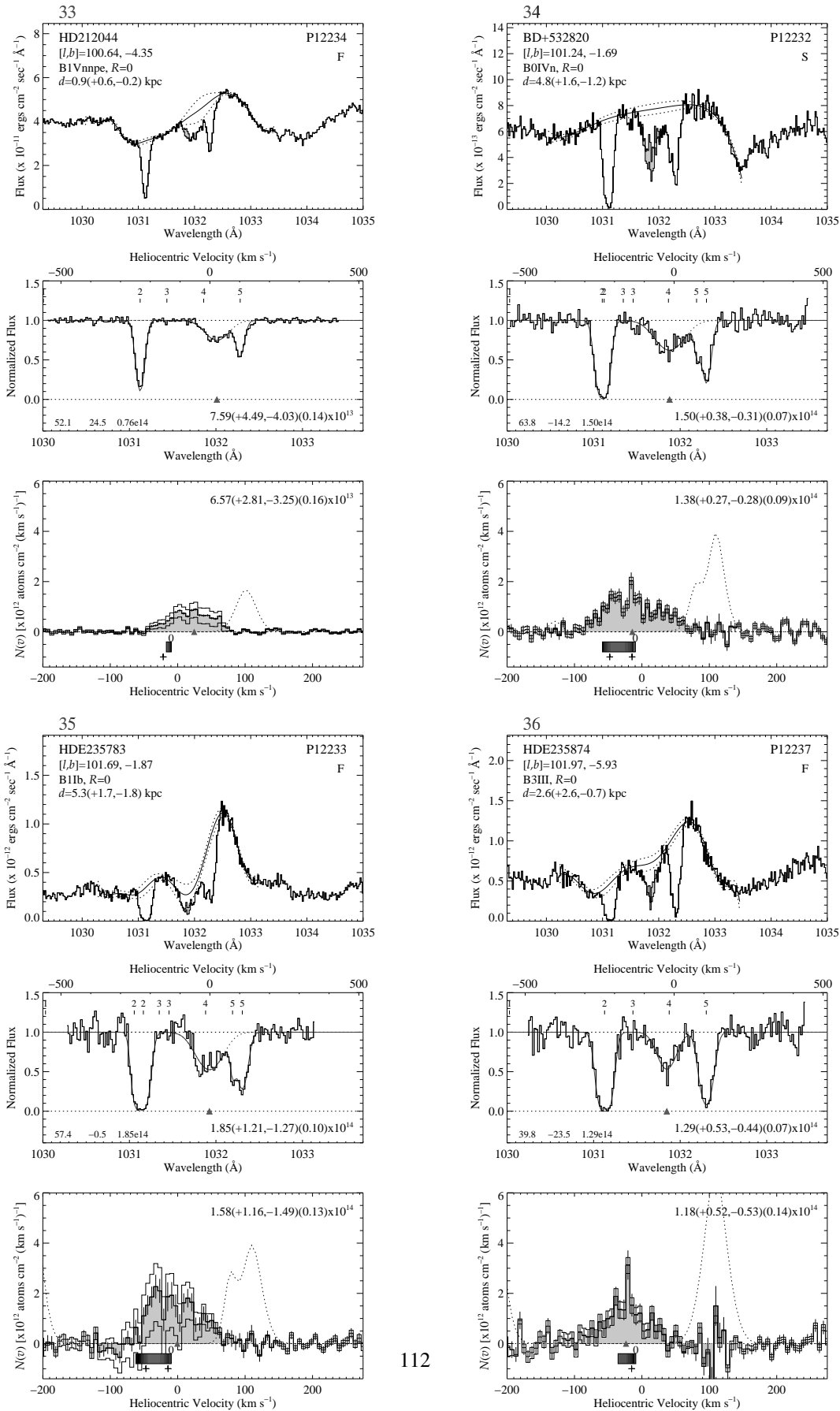


Figure 24: cont

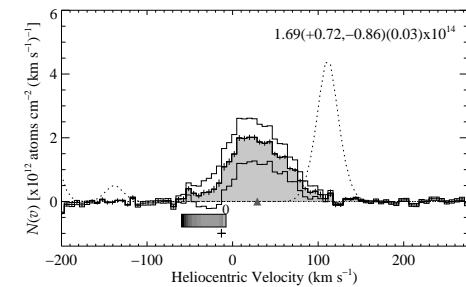
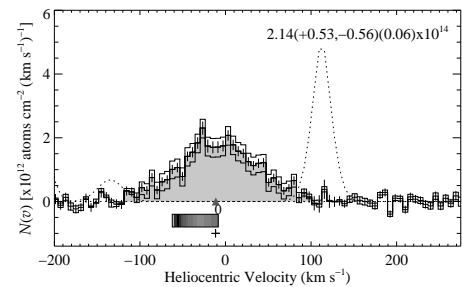
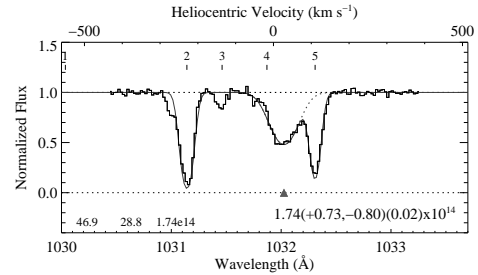
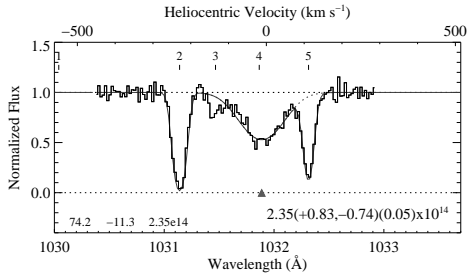
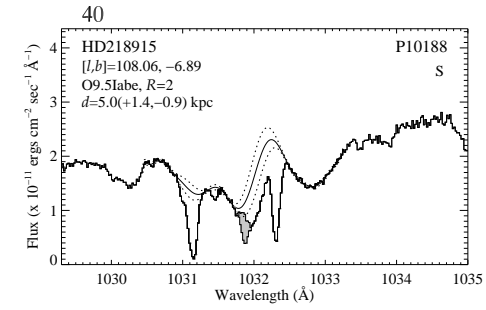
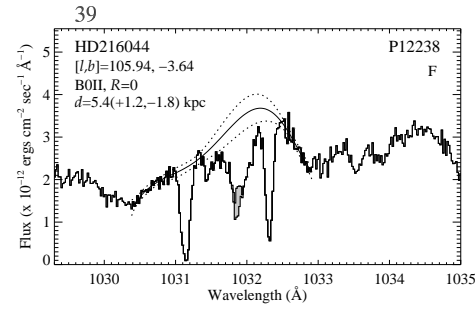
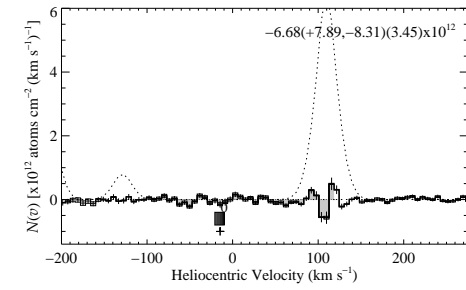
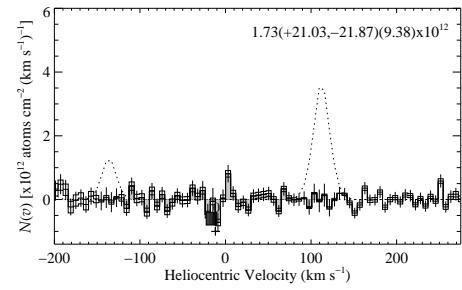
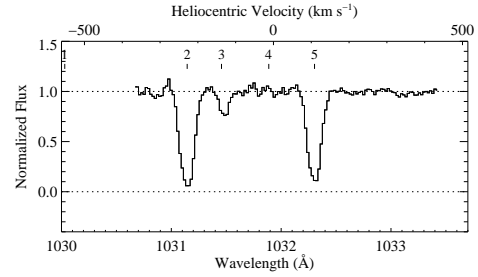
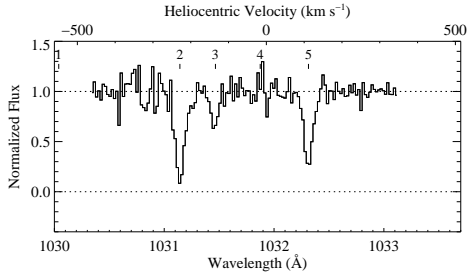
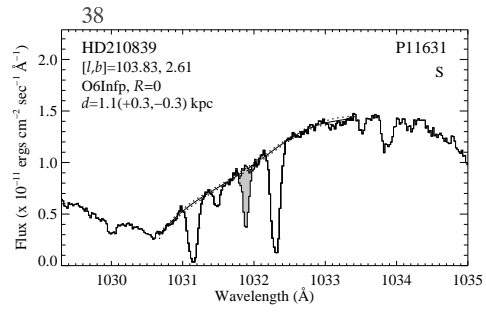
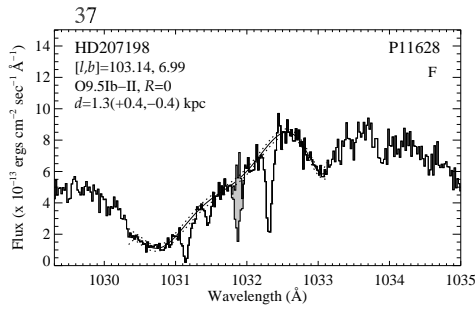


Figure 24: cont

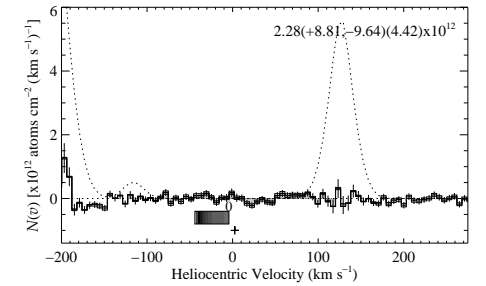
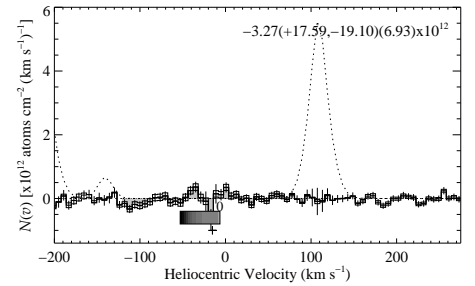
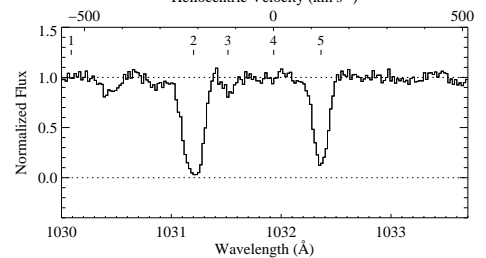
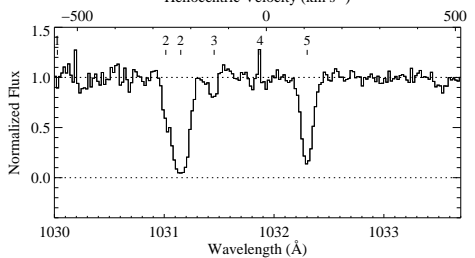
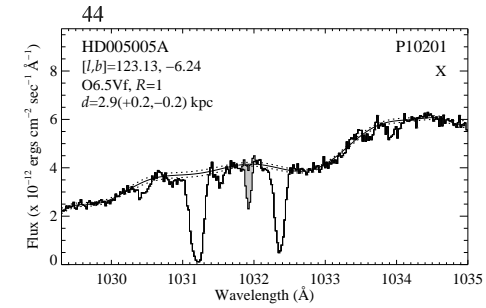
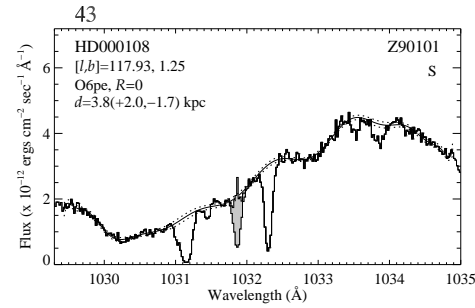
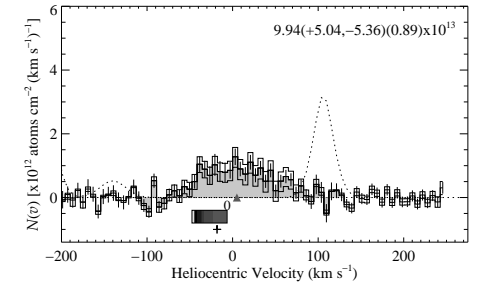
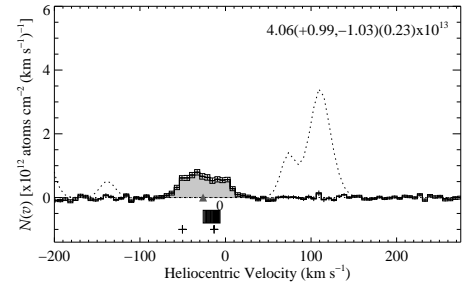
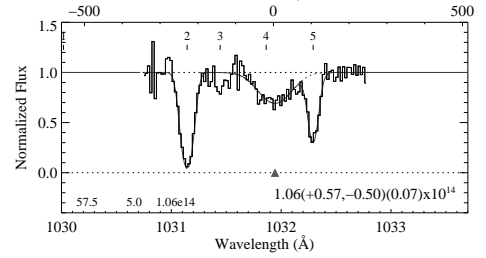
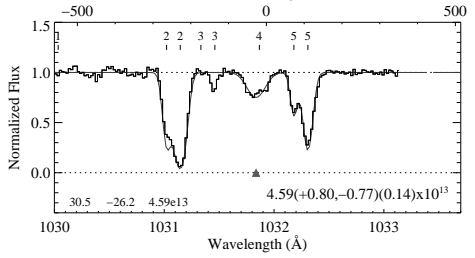
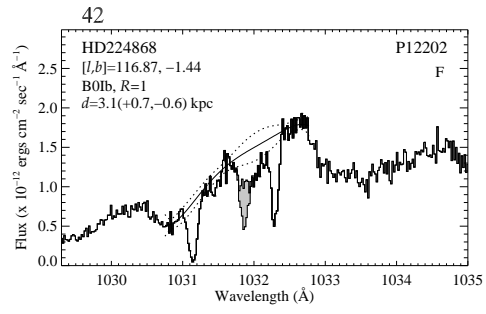
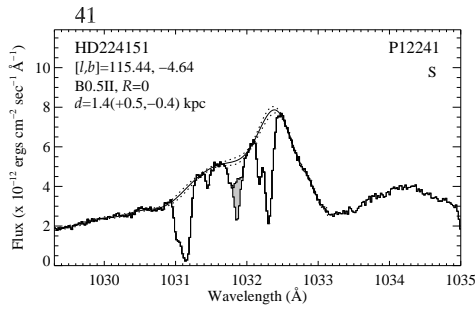
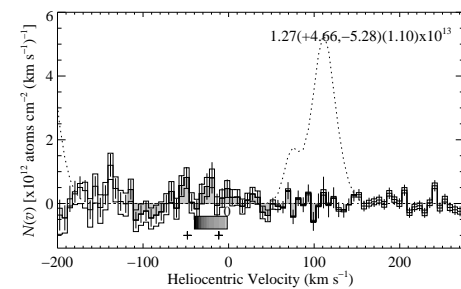
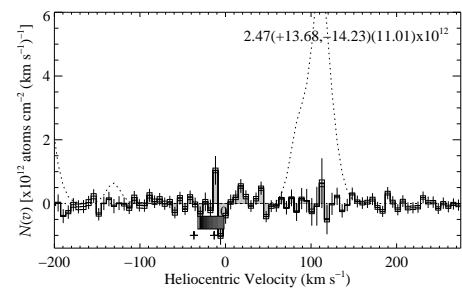
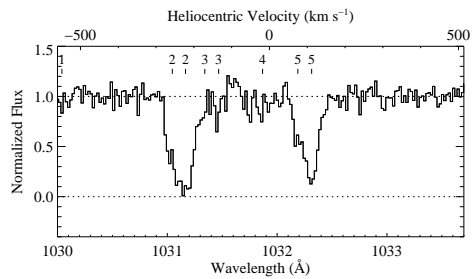
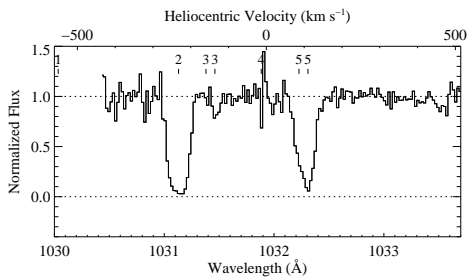
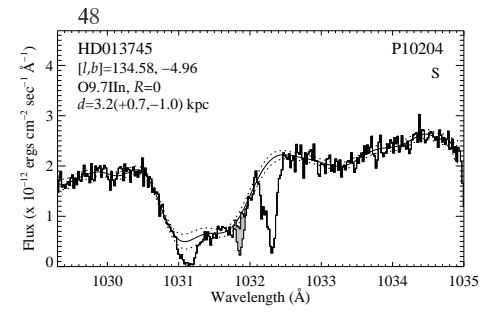
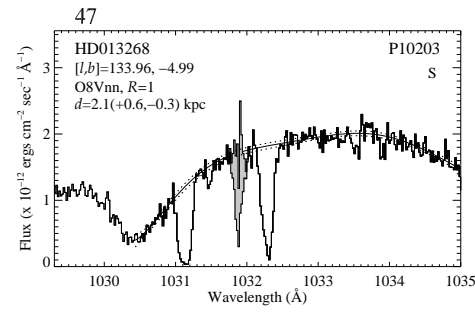
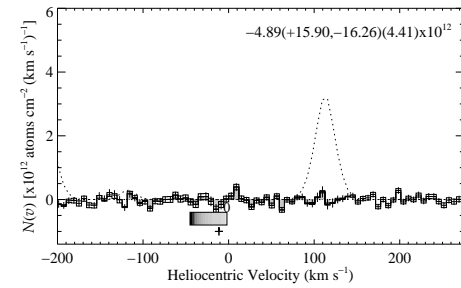
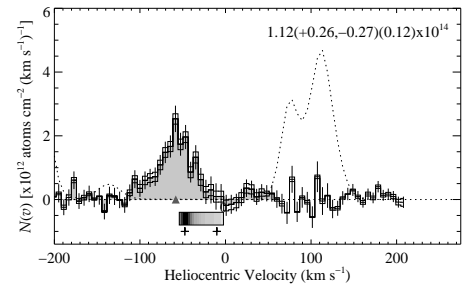
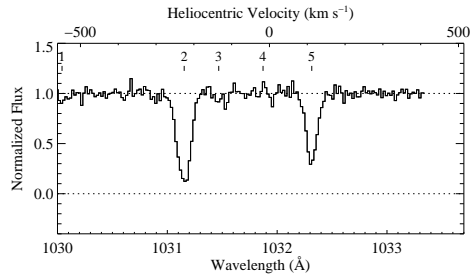
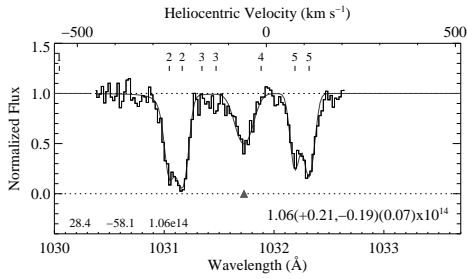
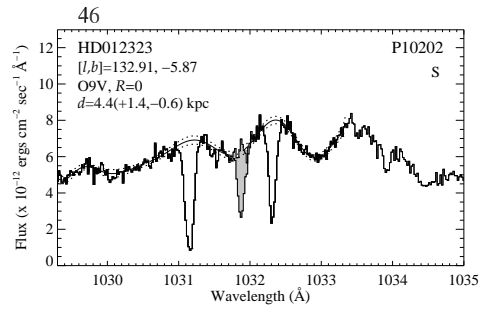
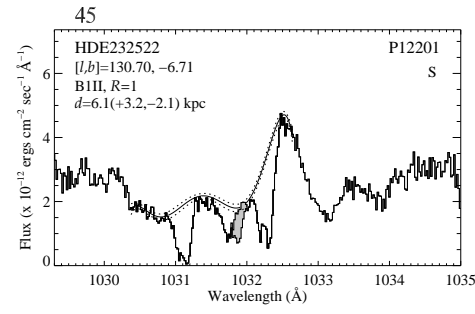
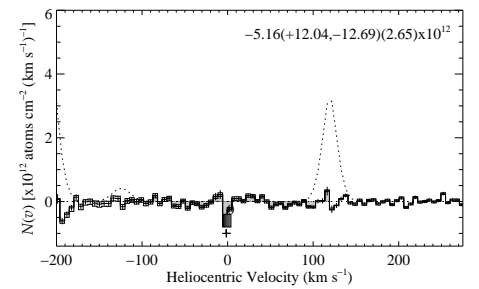
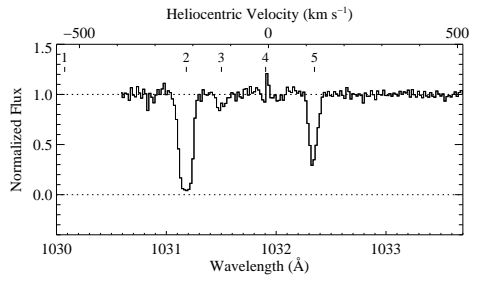
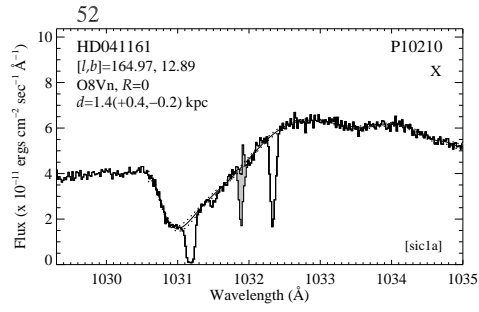
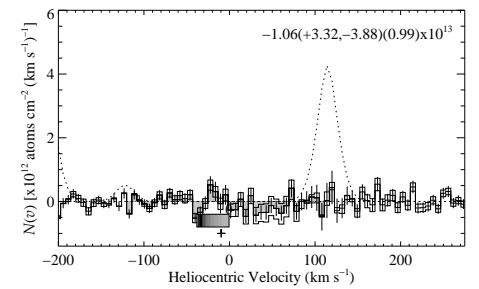
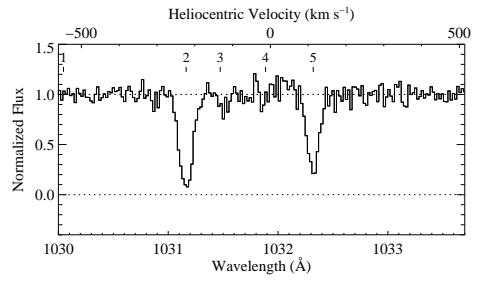
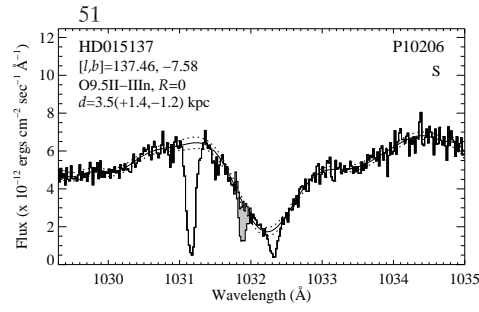
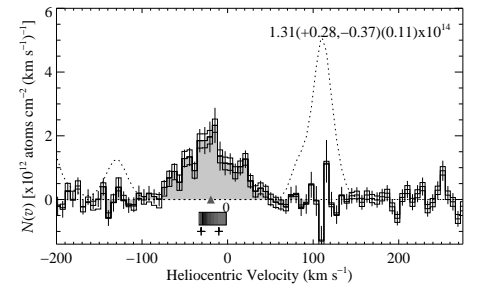
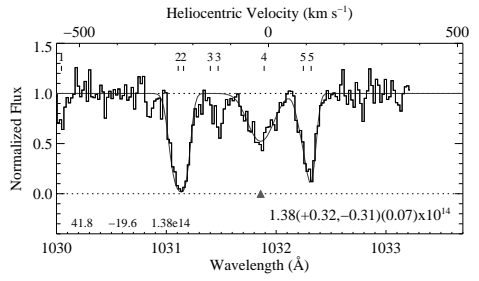
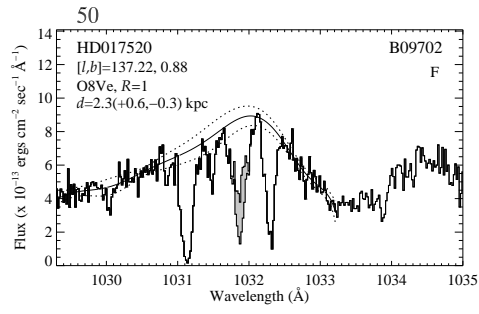
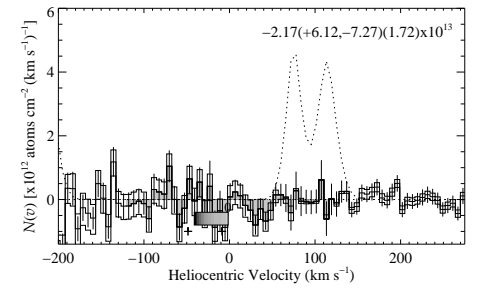
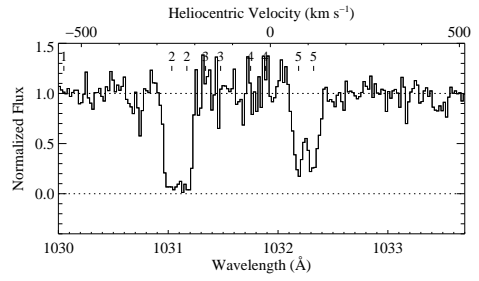
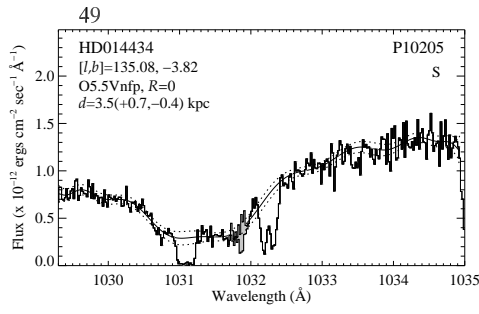
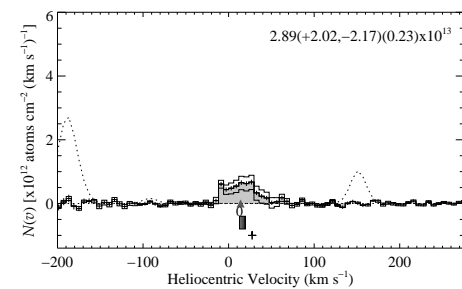
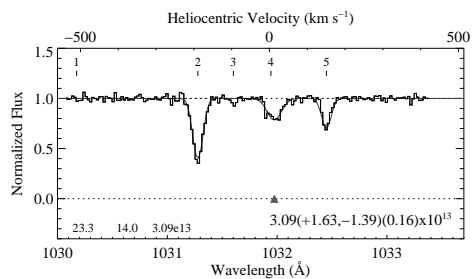
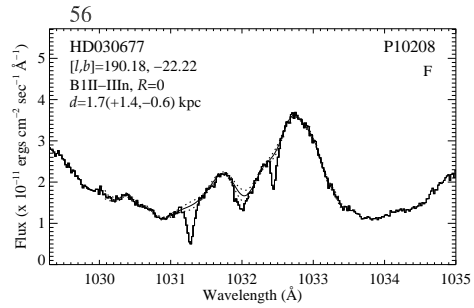
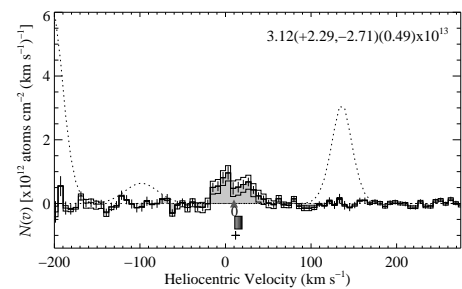
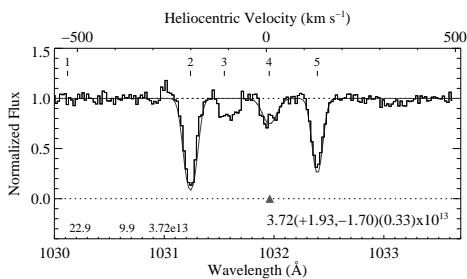
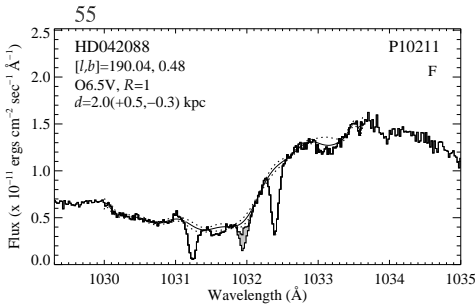
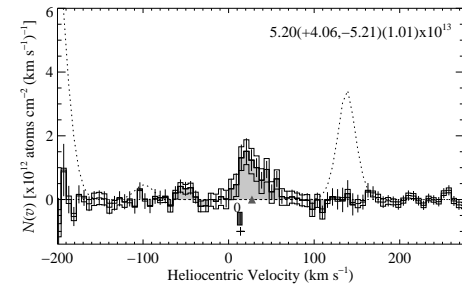
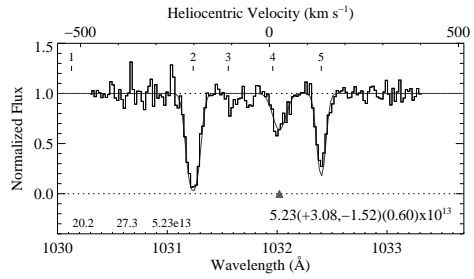
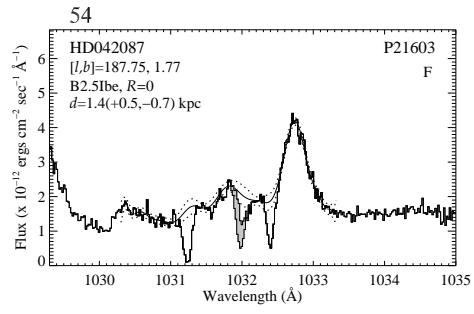
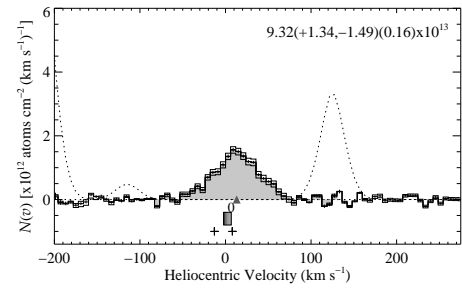
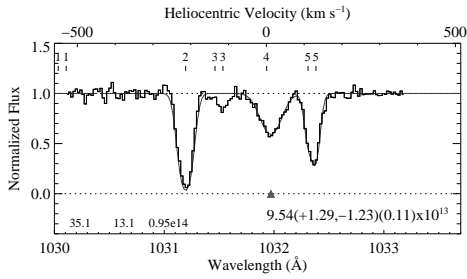
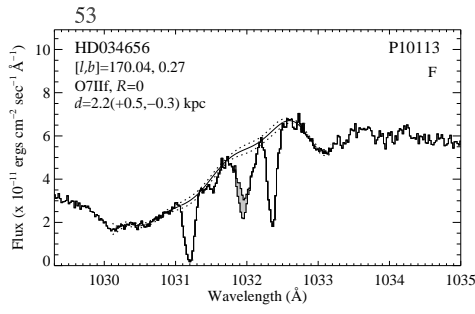


Figure 24: cont







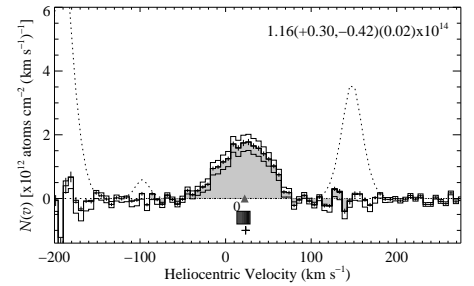
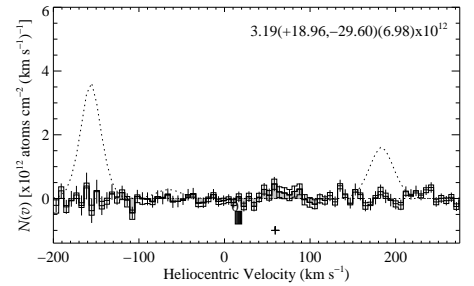
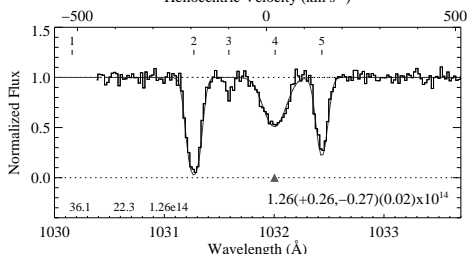
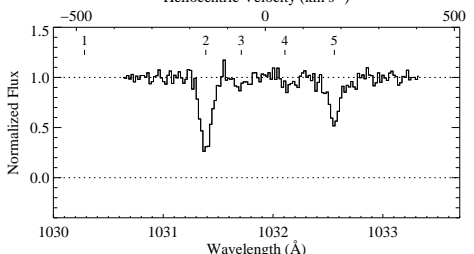
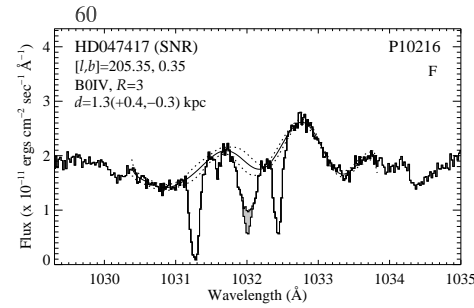
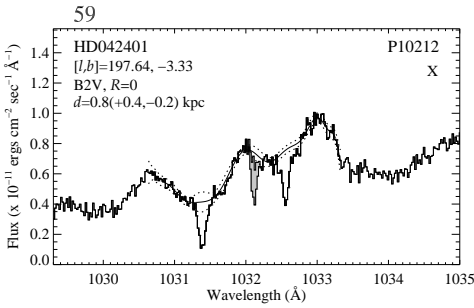
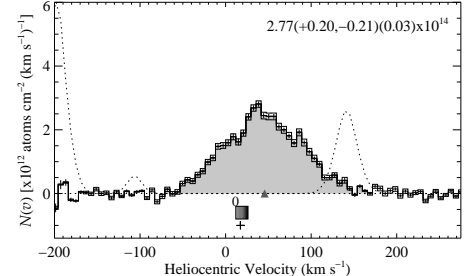
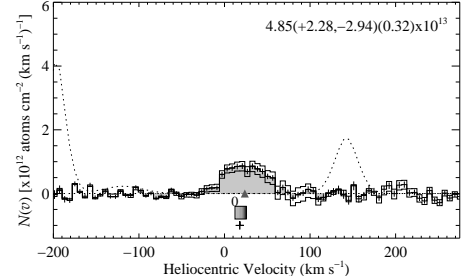
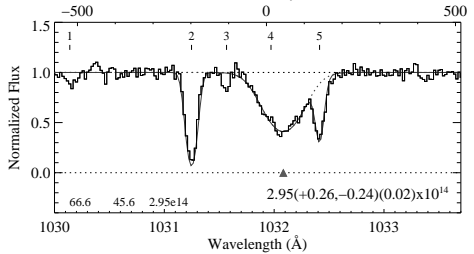
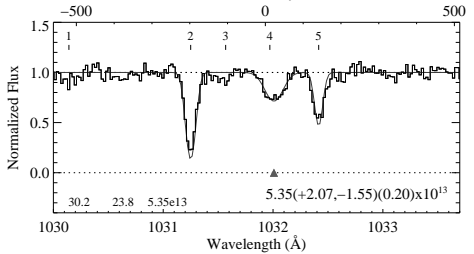
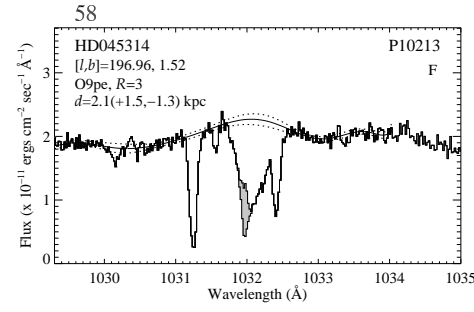
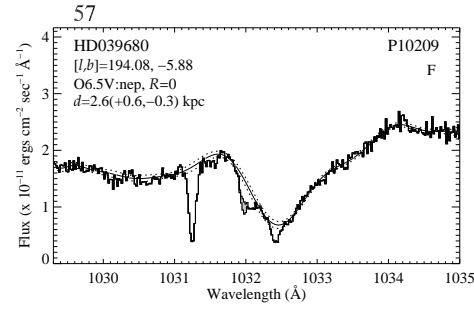
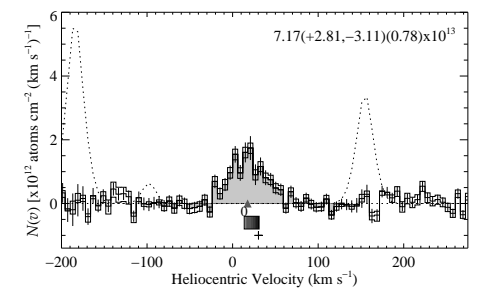
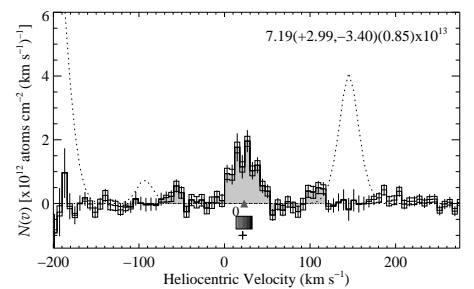
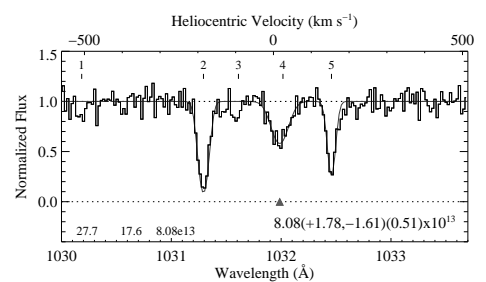
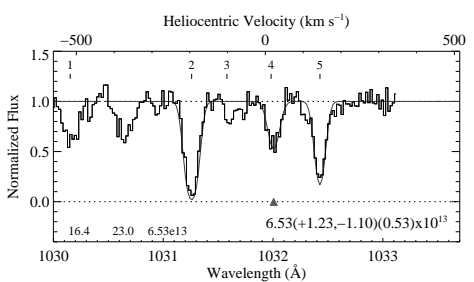
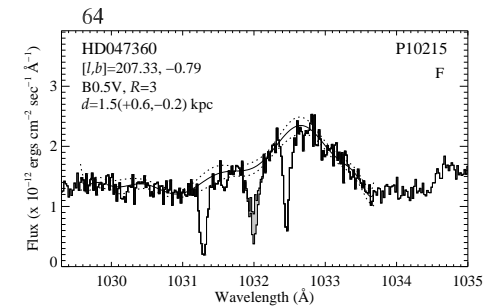
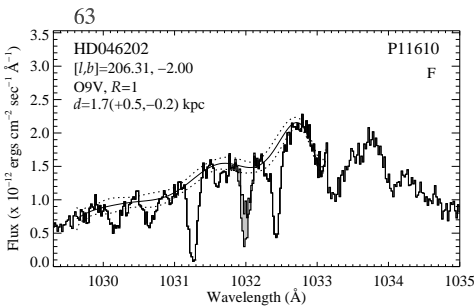
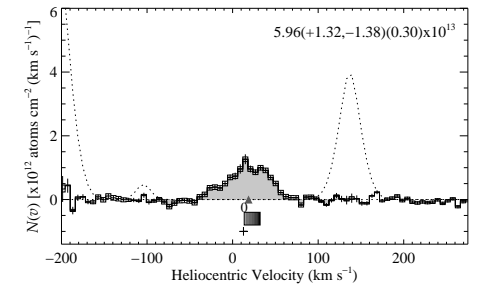
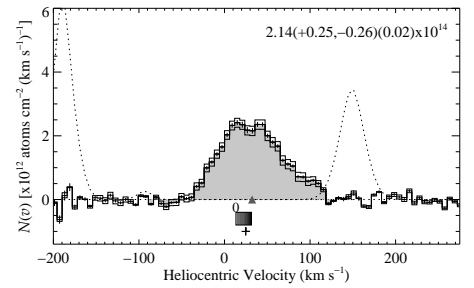
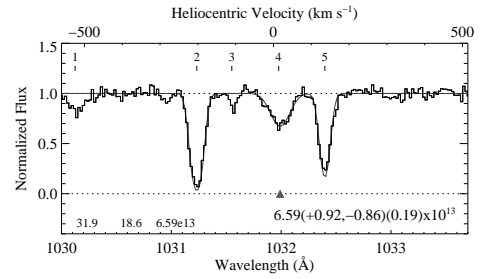
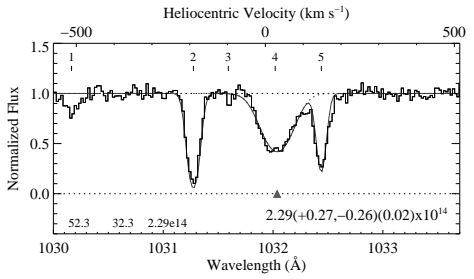
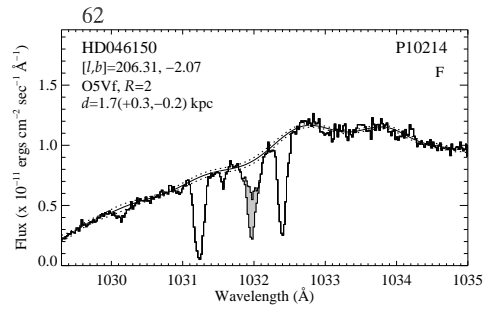
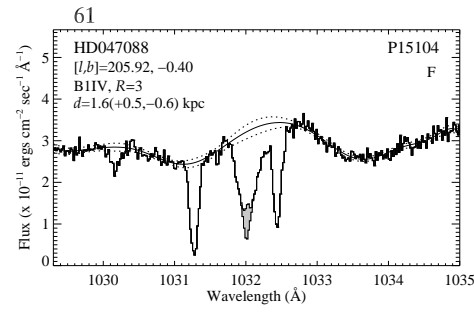


Figure 24: cont



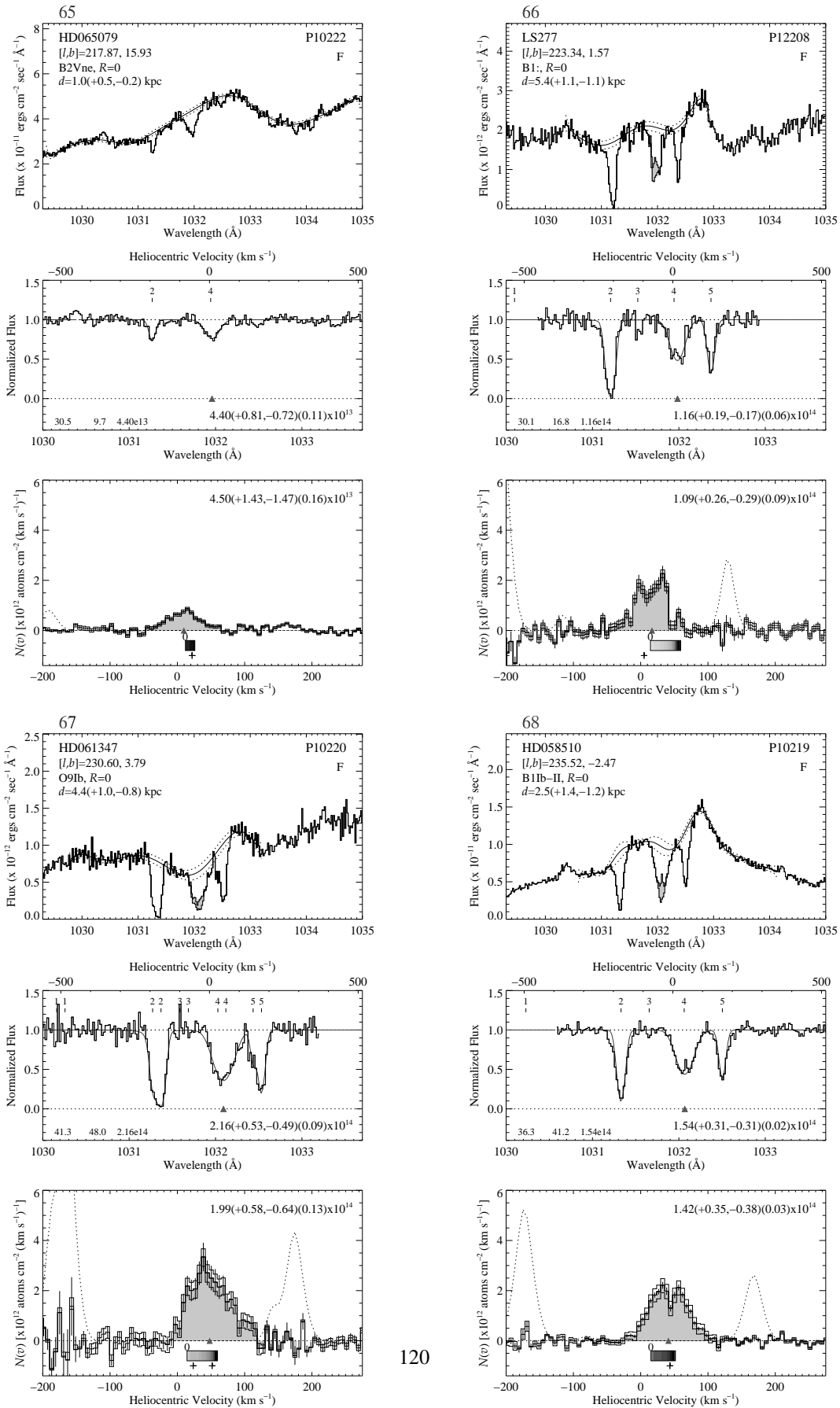
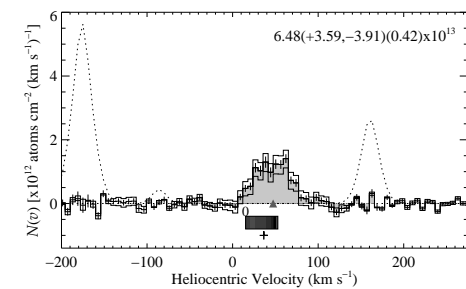
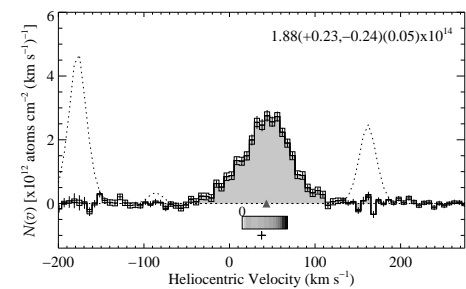
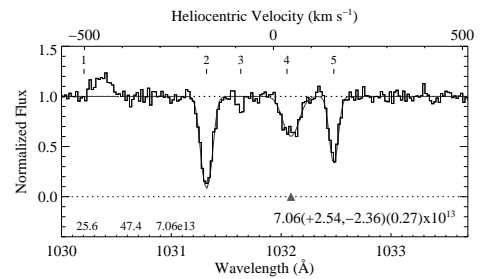
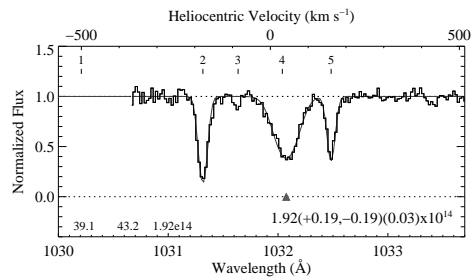
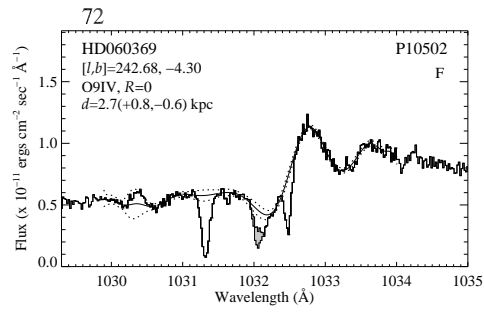
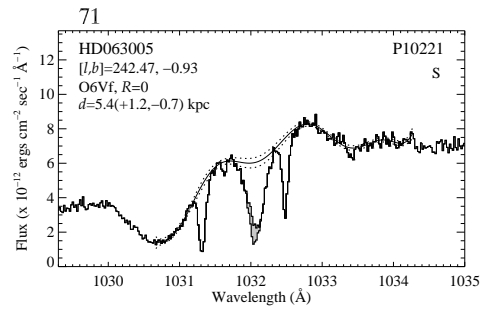
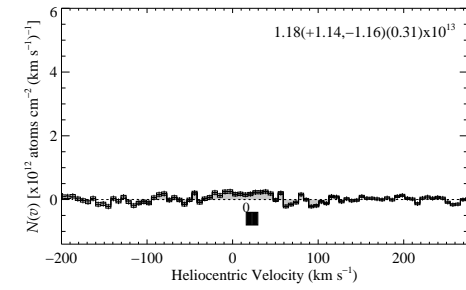
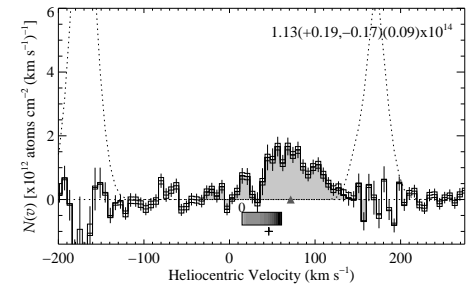
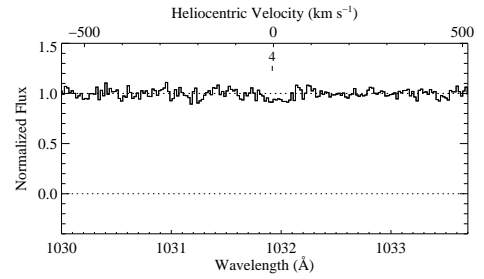
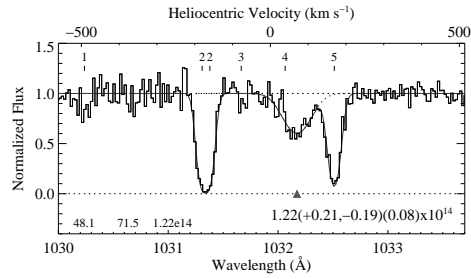
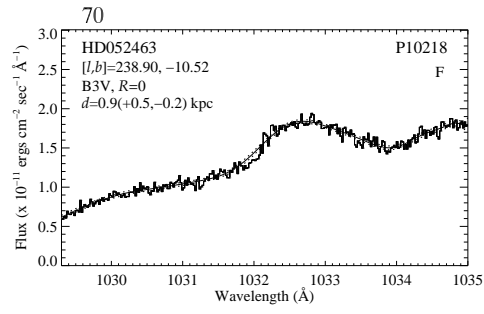
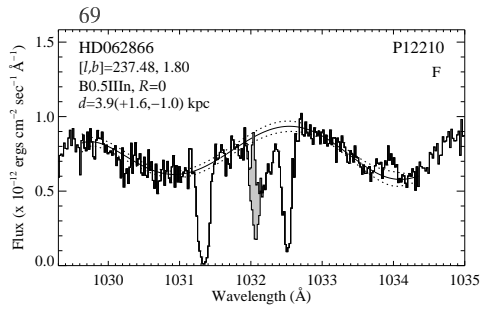


Figure 24: cont



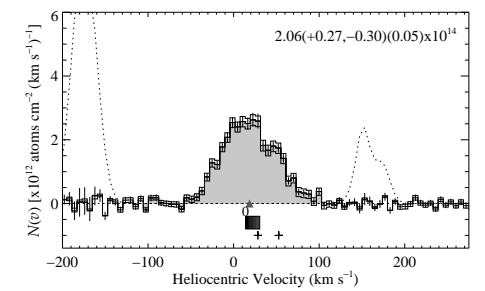
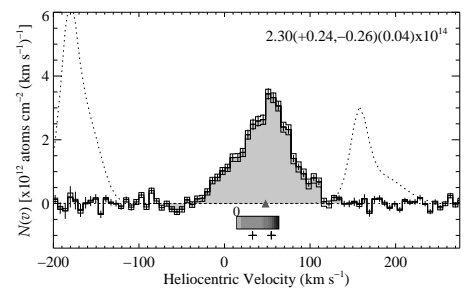
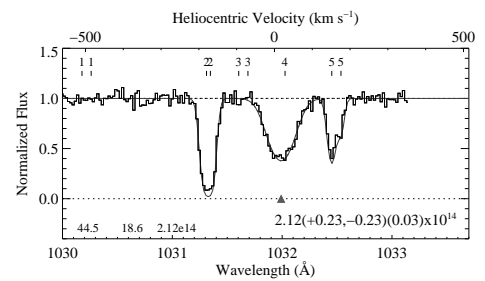
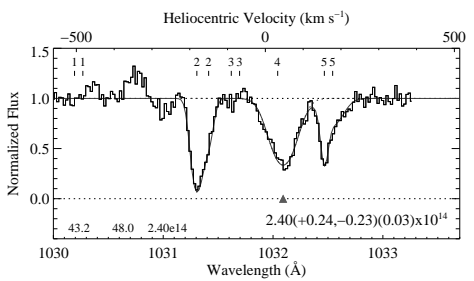
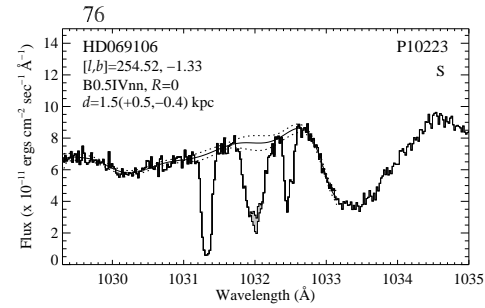
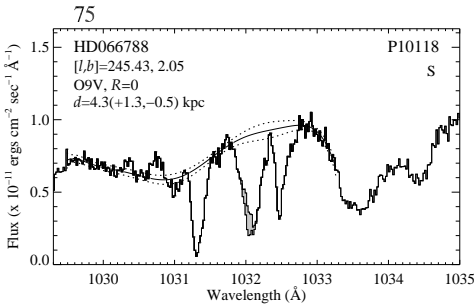
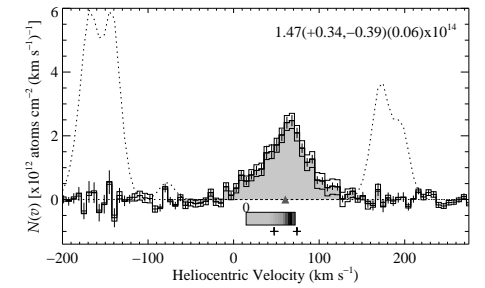
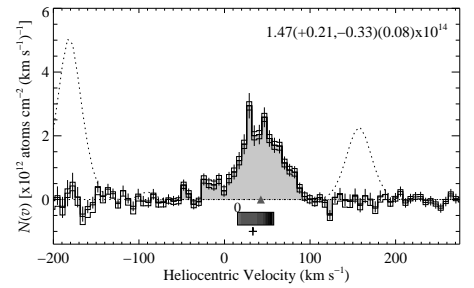
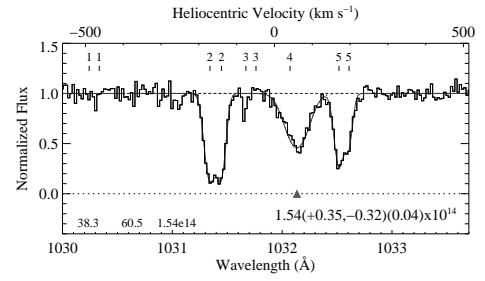
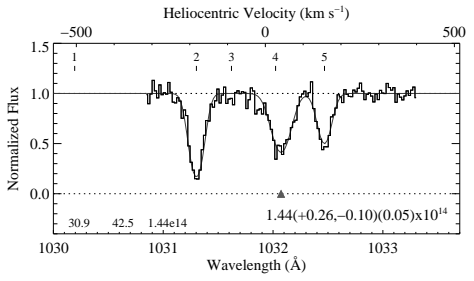
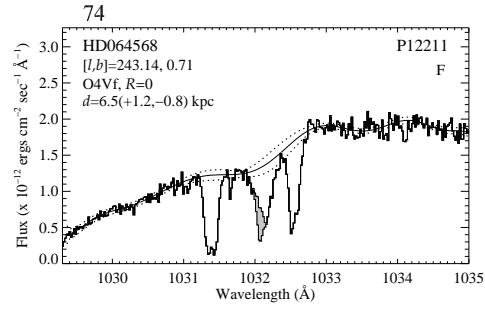
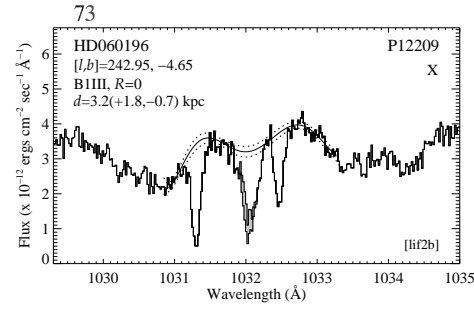
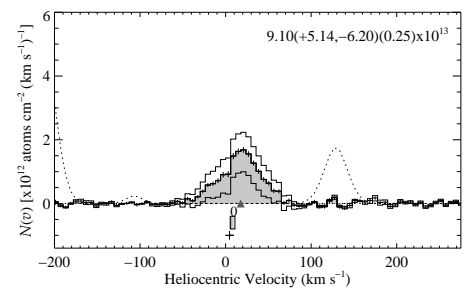
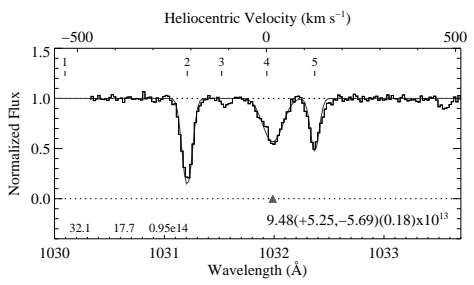
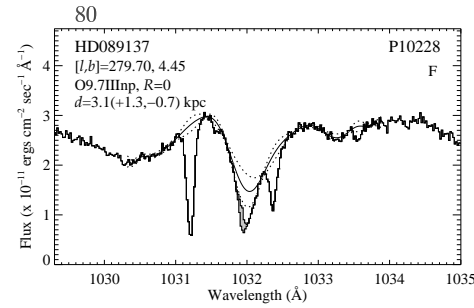
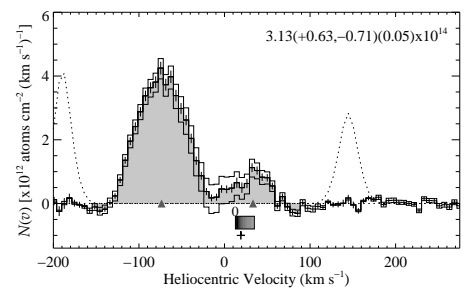
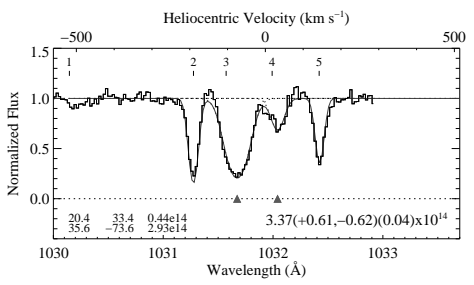
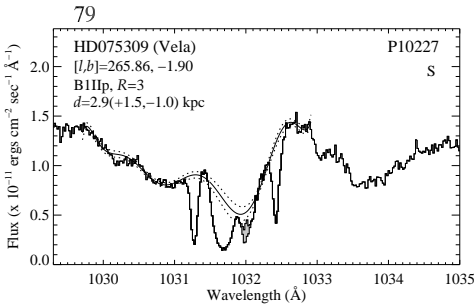
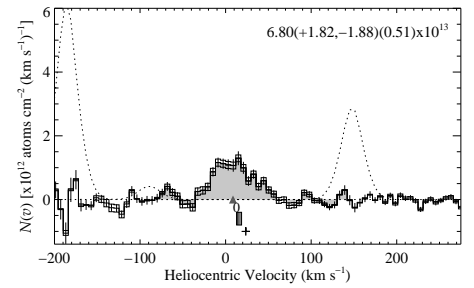
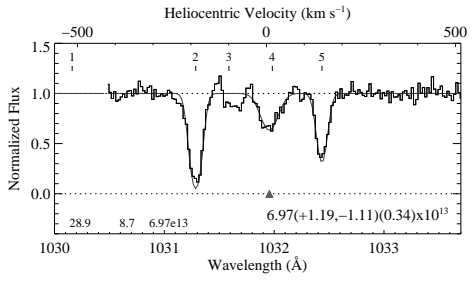
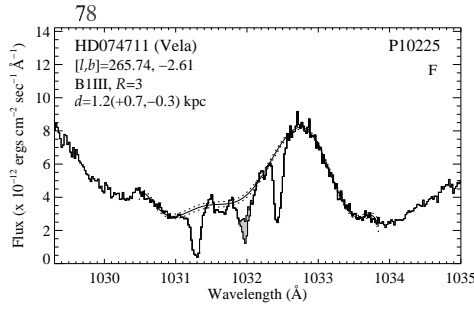
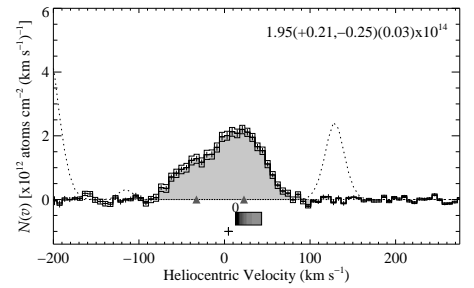
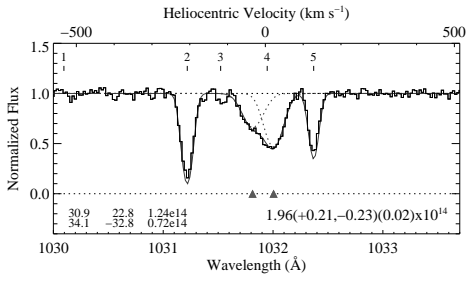
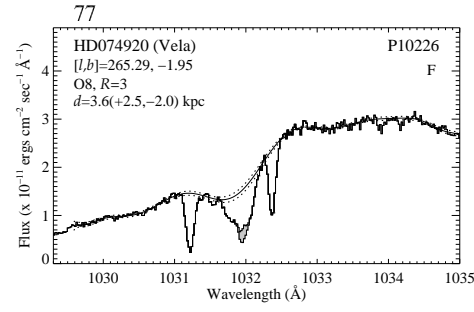
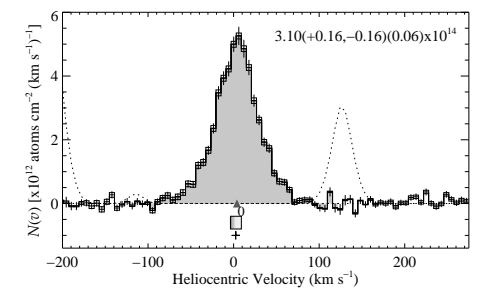
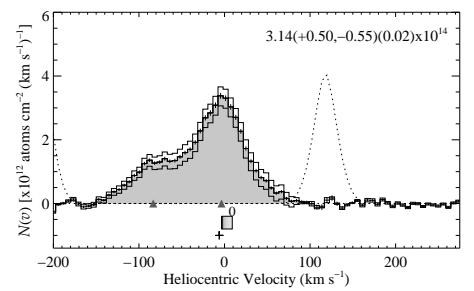
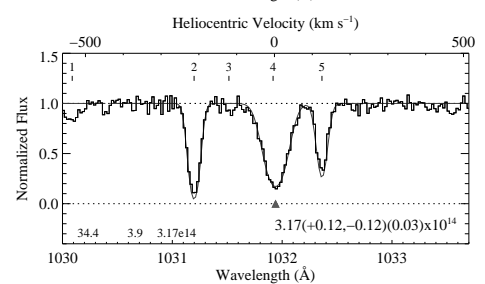
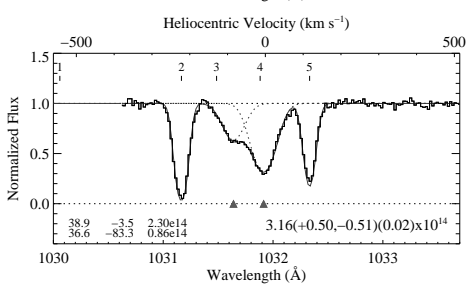
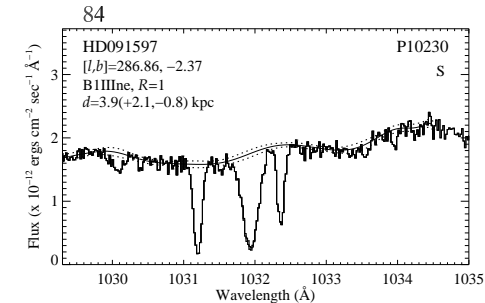
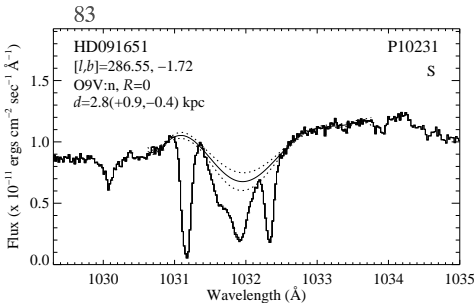
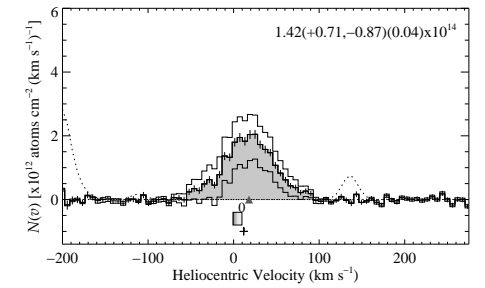
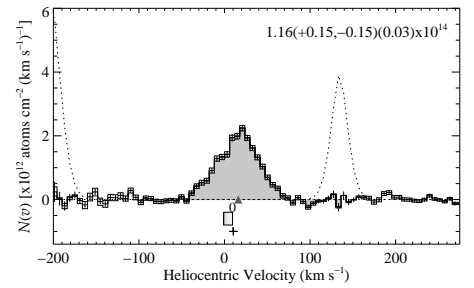
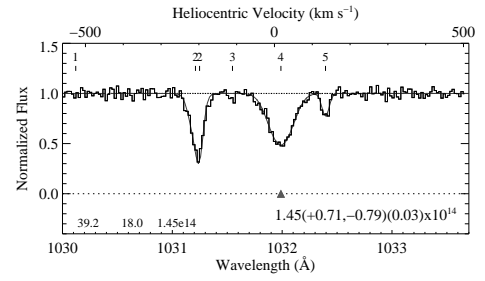
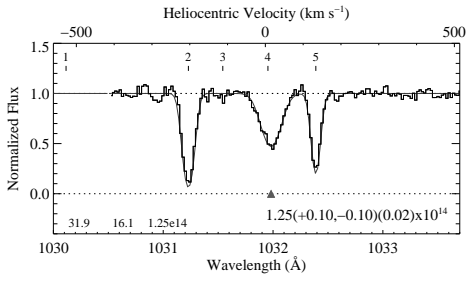
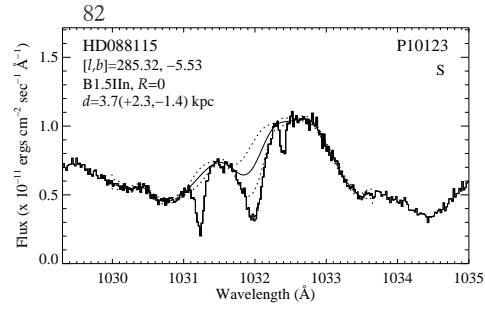
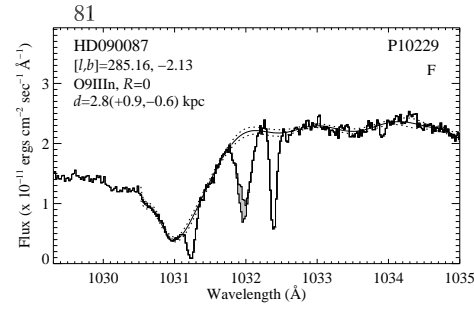
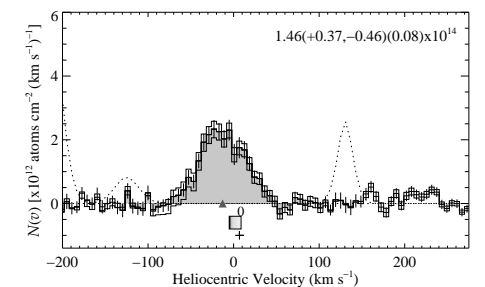
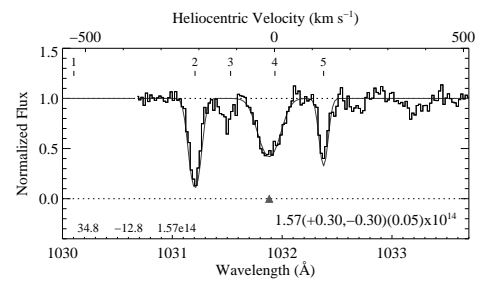
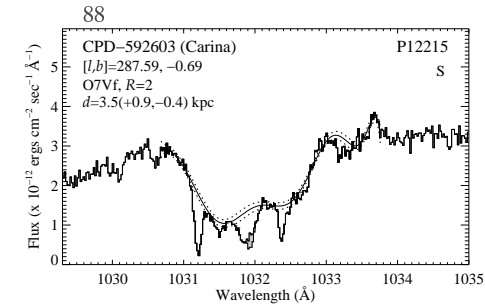
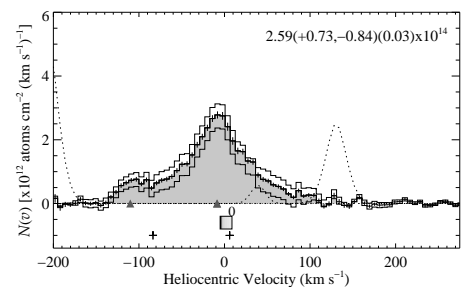
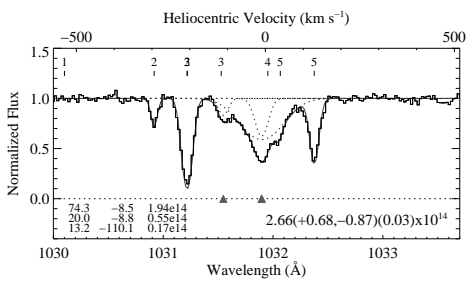
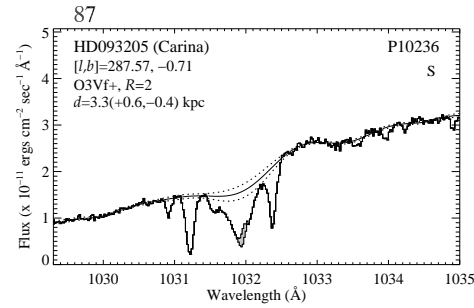
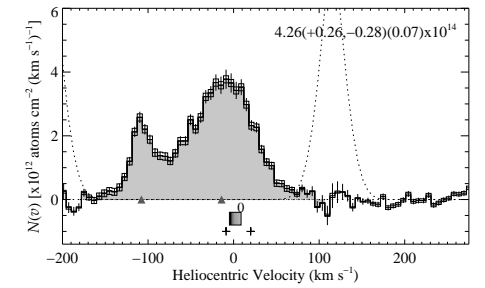
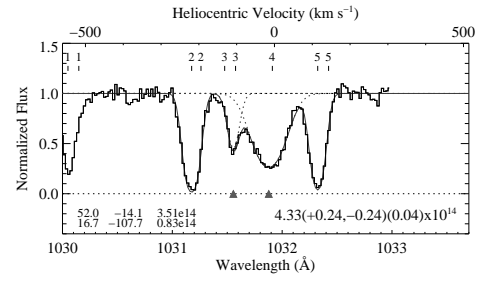
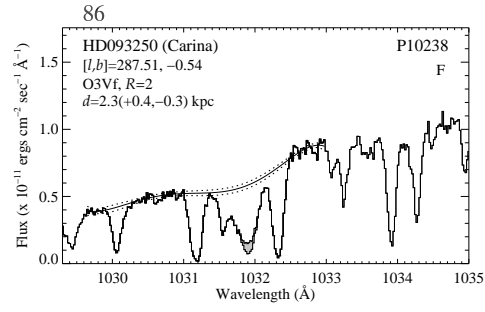
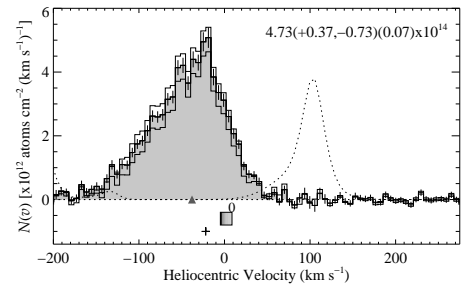
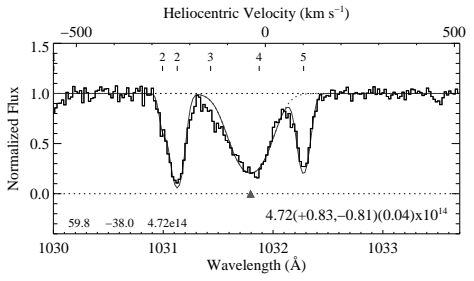
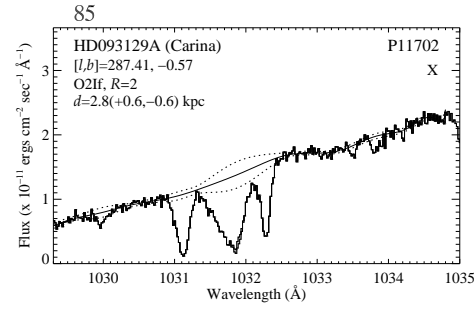
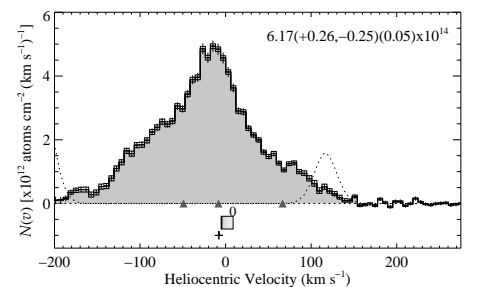
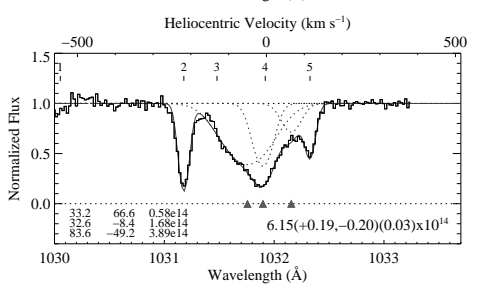
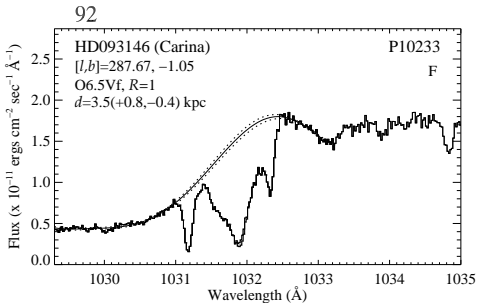
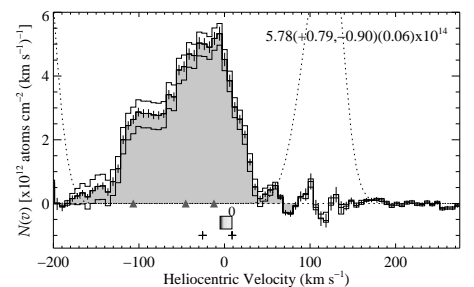
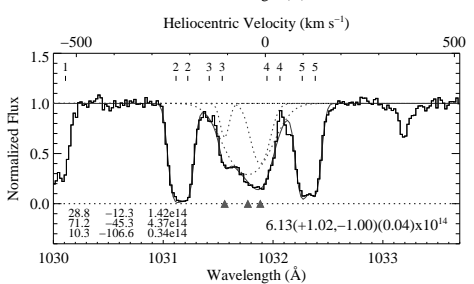
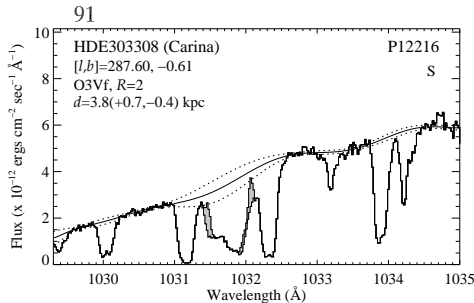
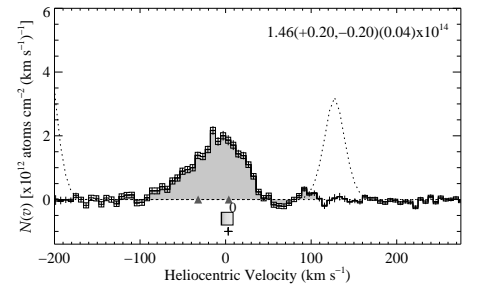
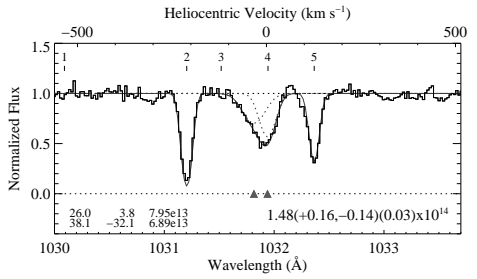
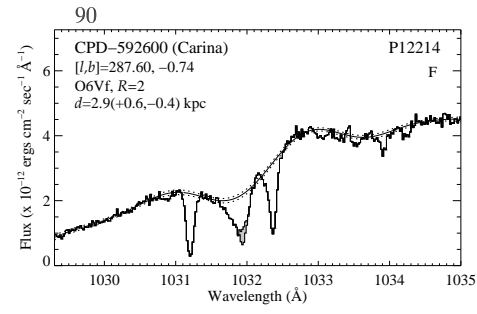
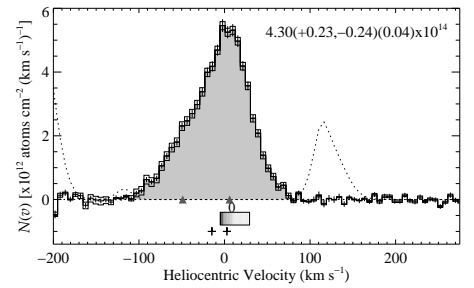
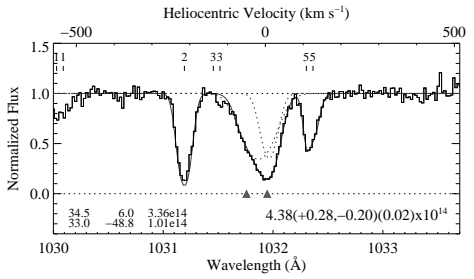
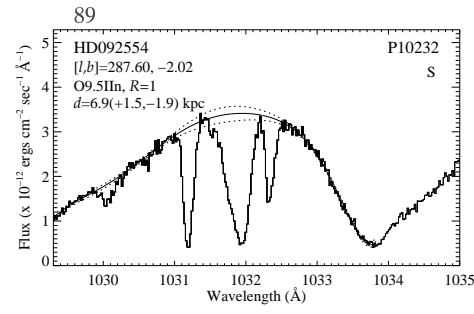


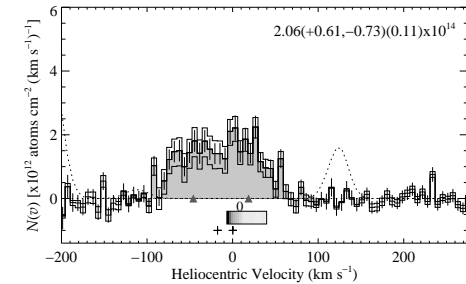
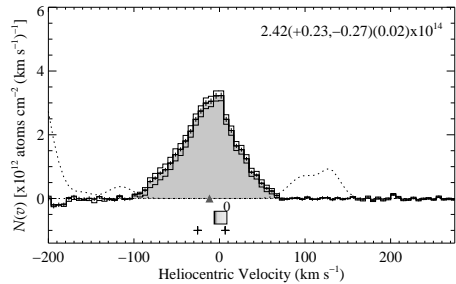
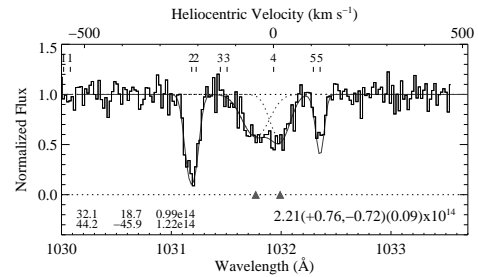
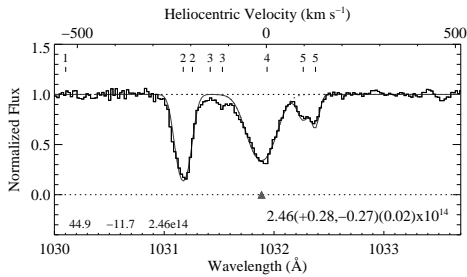
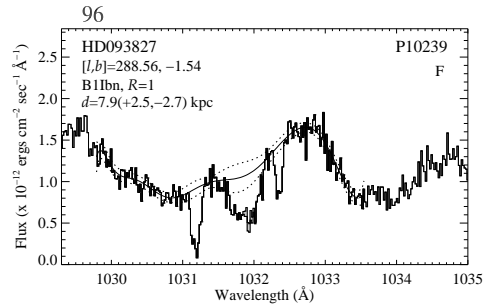
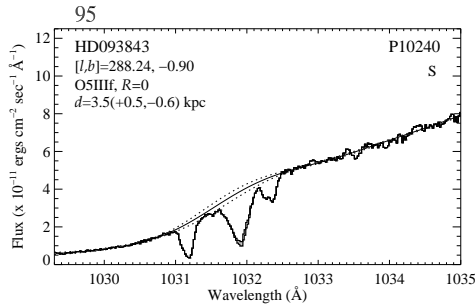
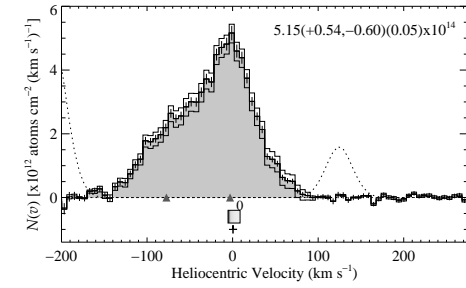
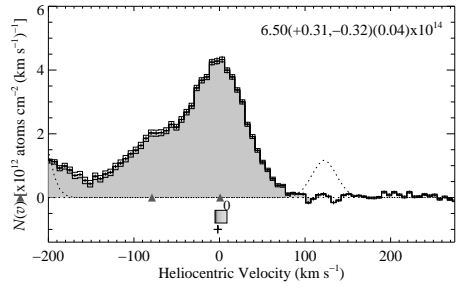
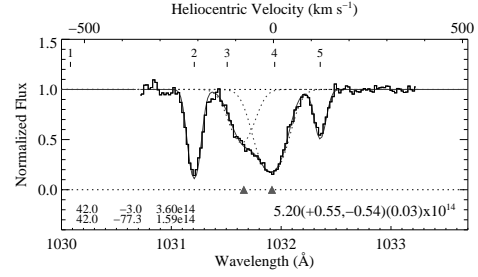
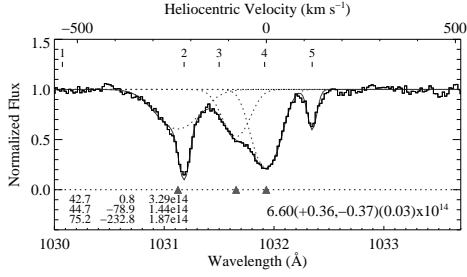
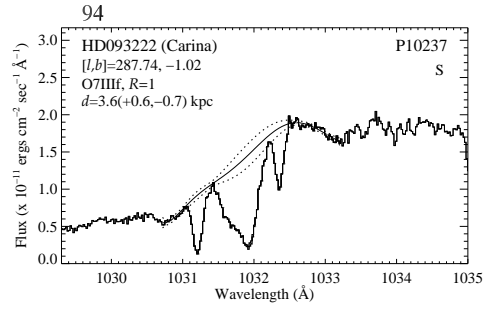
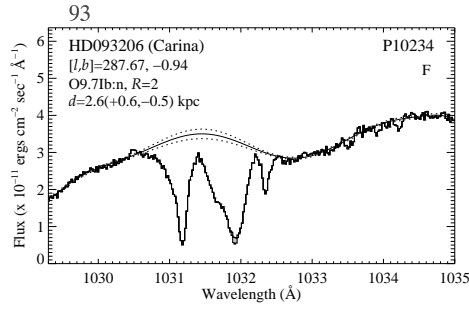
Figure 24: cont

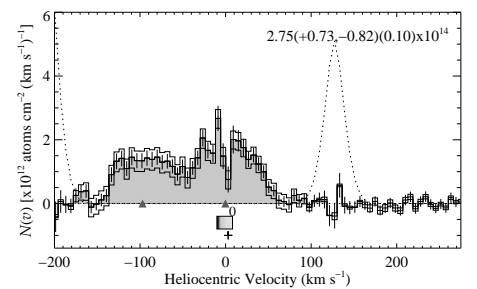
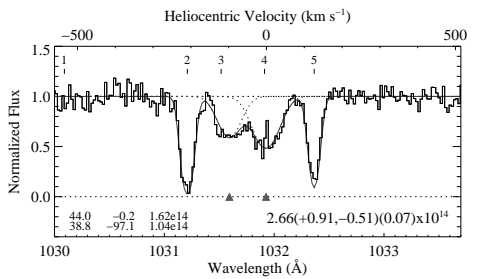
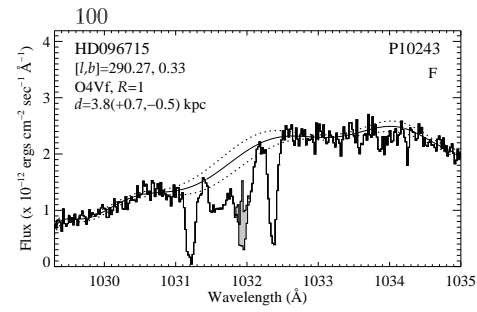
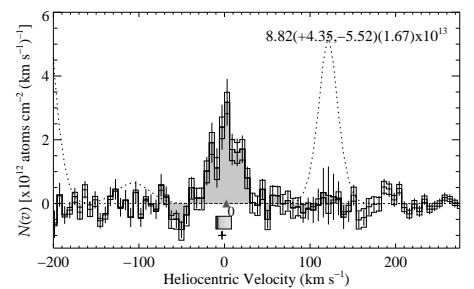
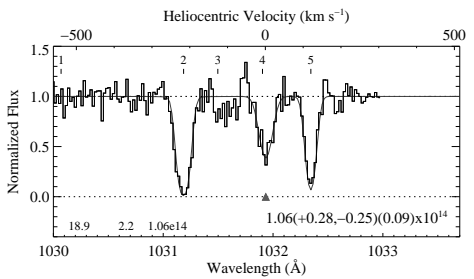
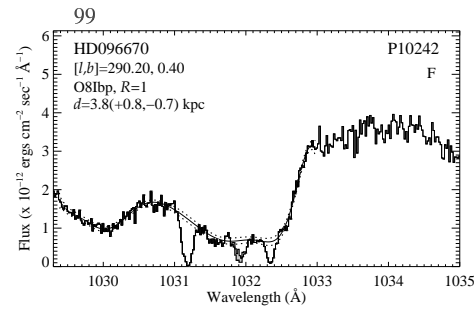
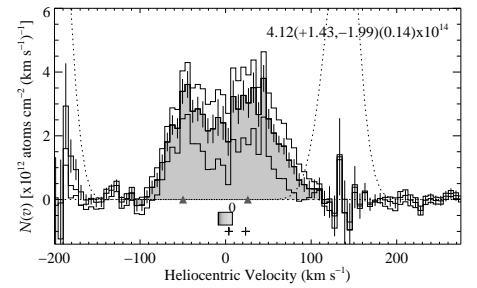
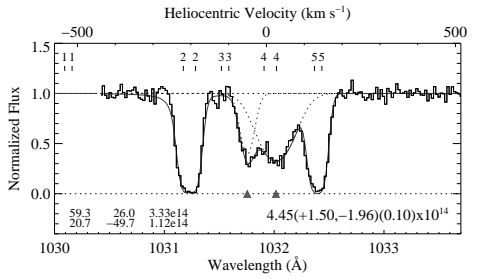
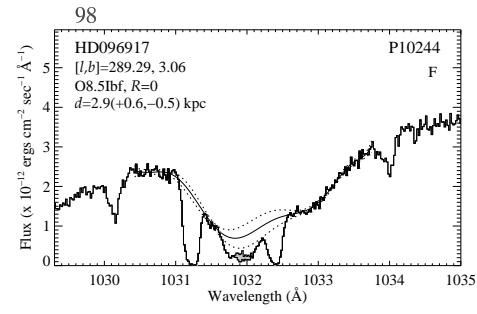
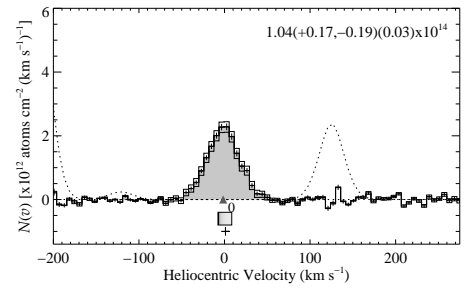
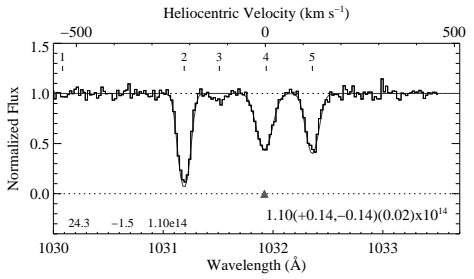
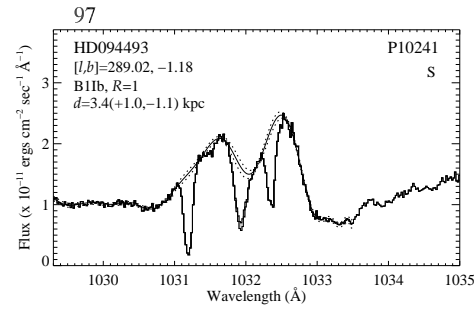


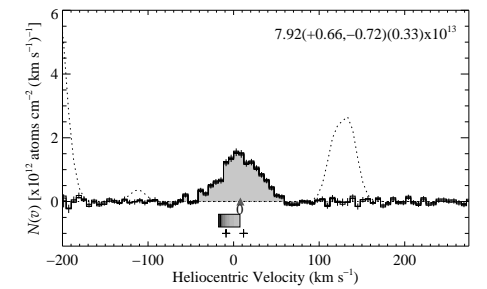
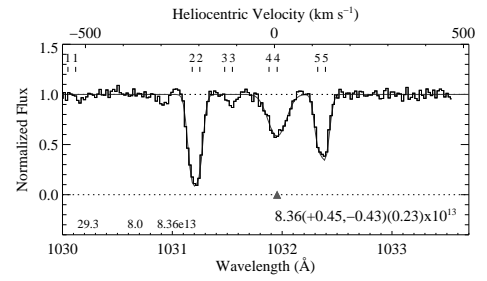
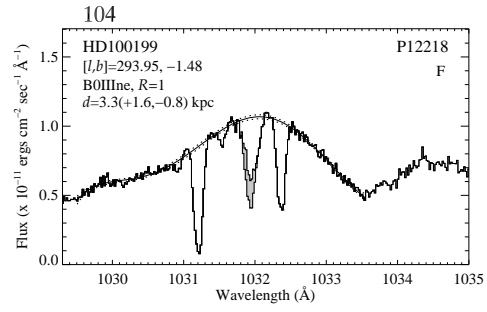
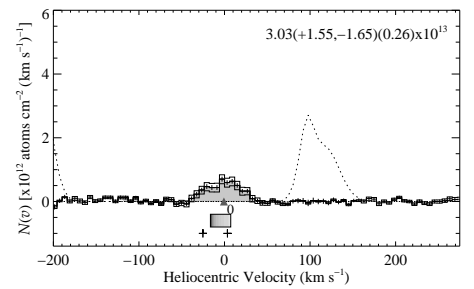
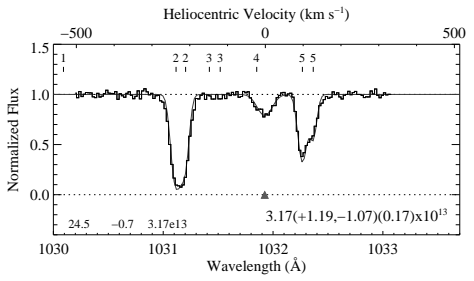
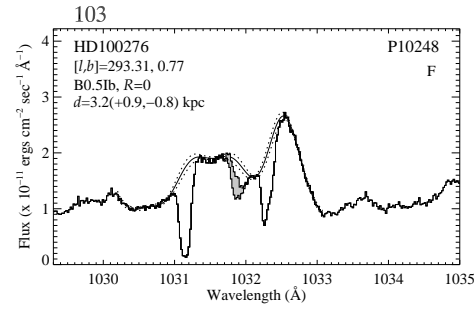
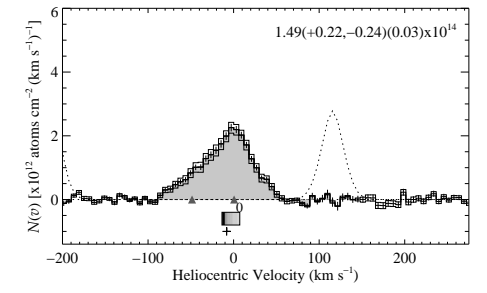
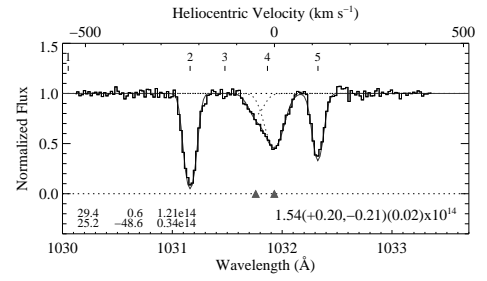
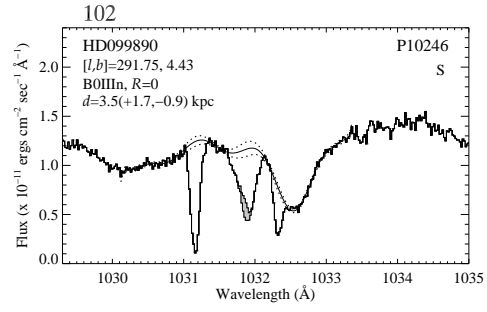
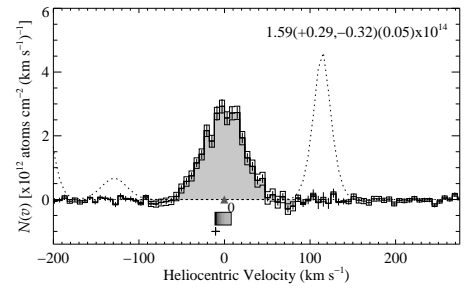
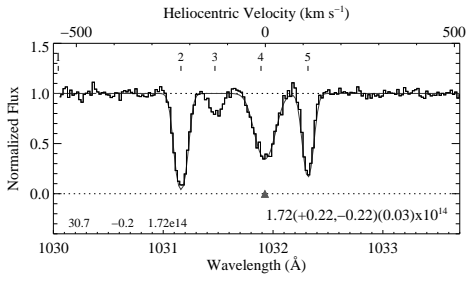
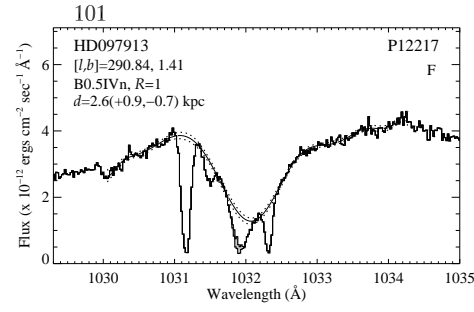


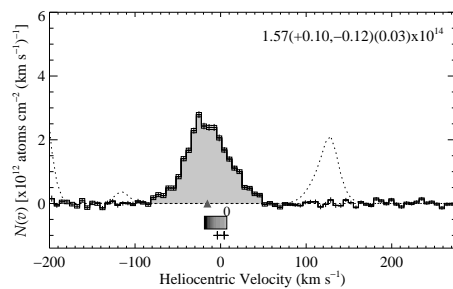
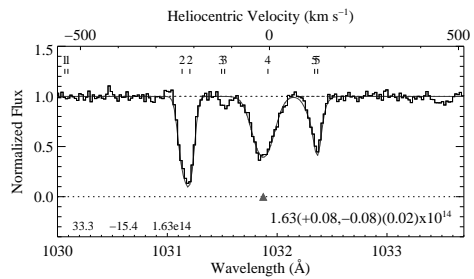
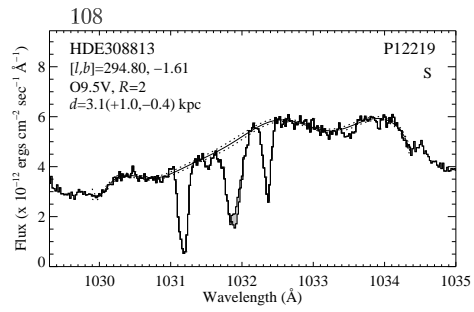
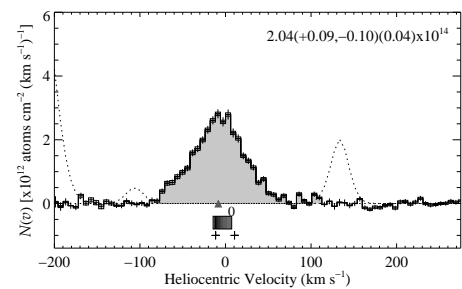
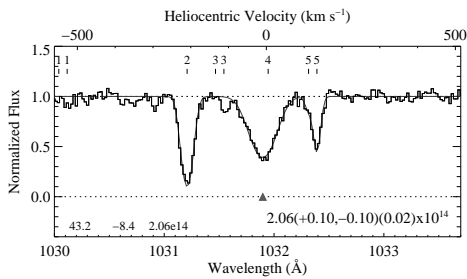
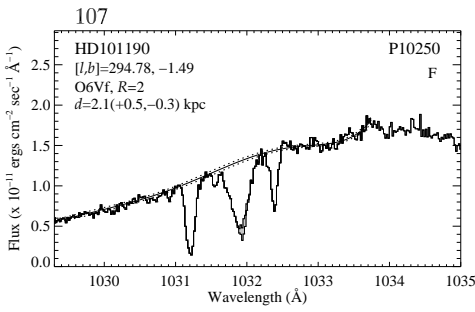
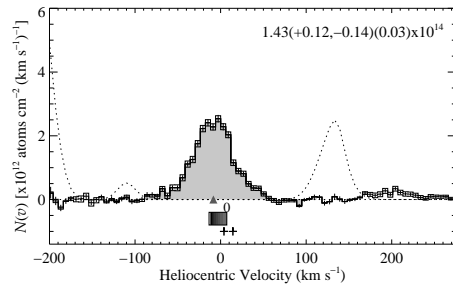
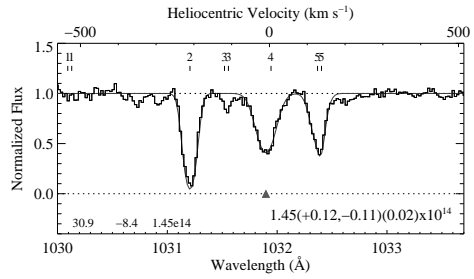
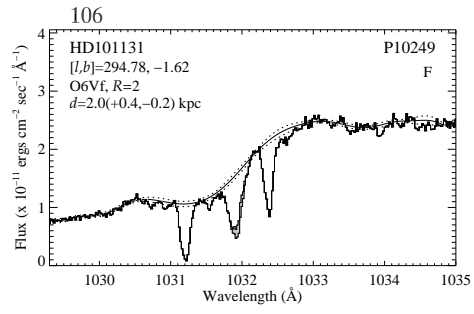
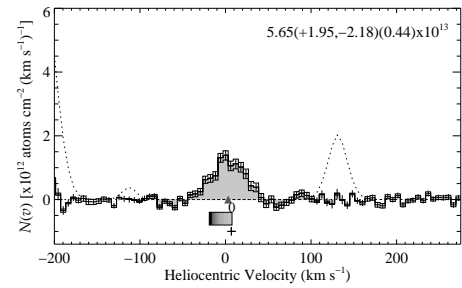
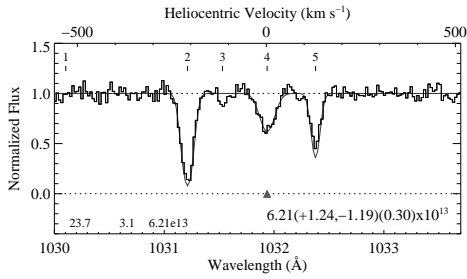
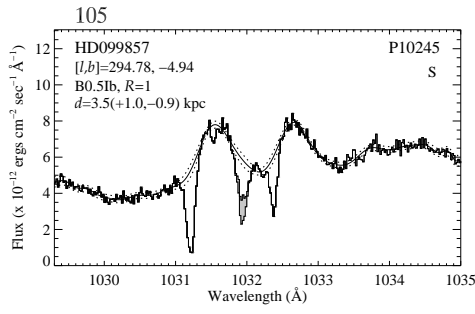






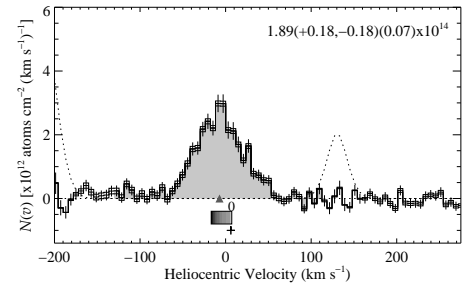
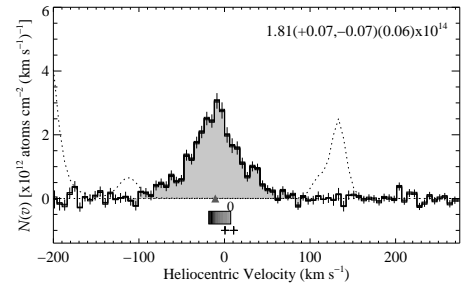
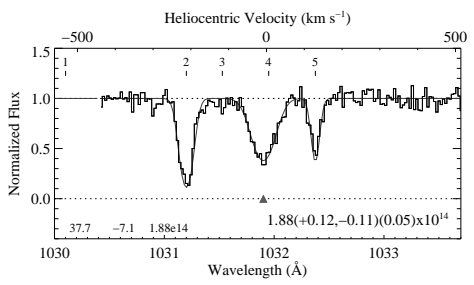
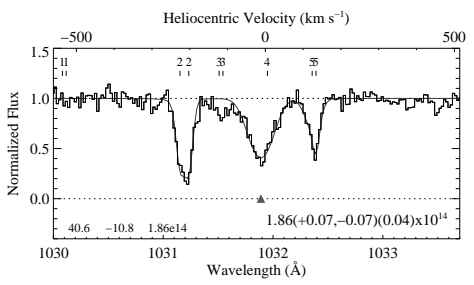
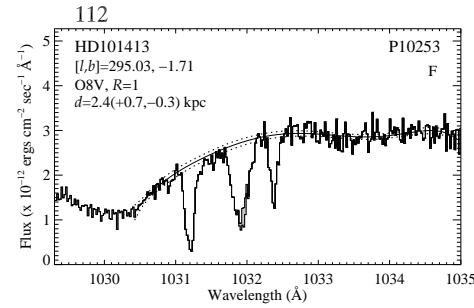
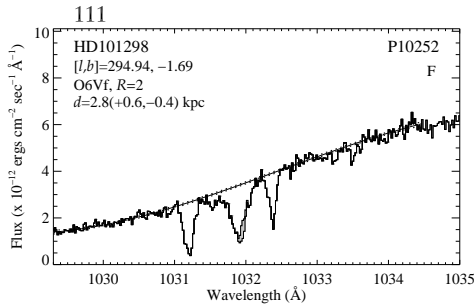
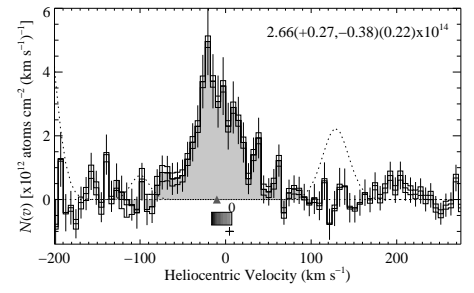
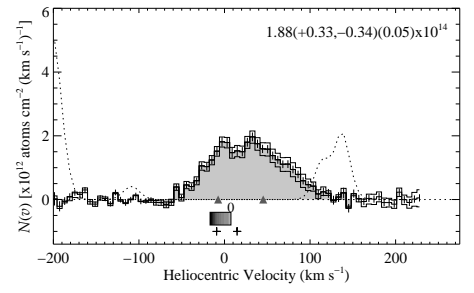
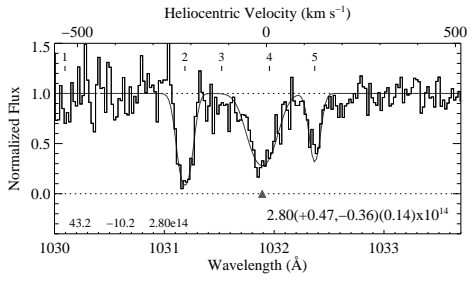
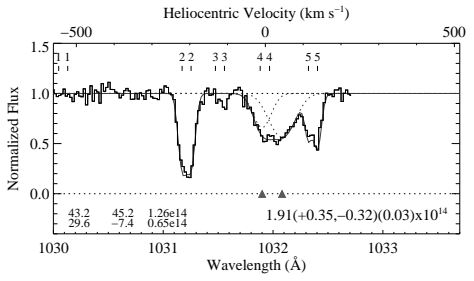
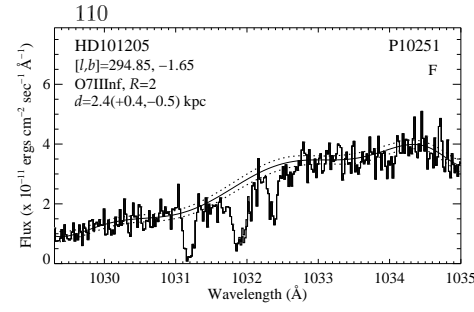
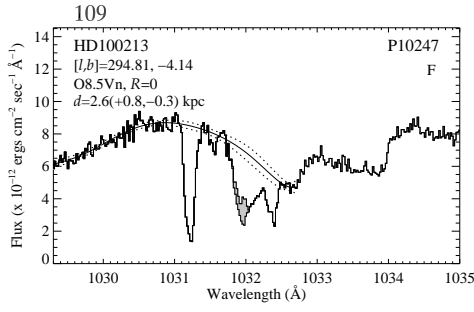






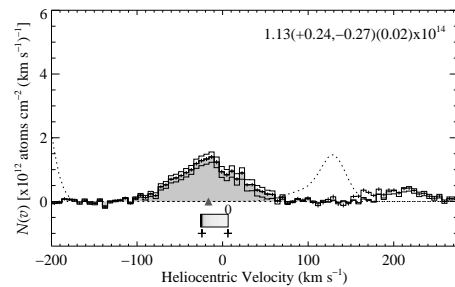
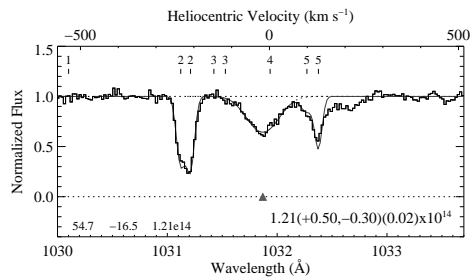
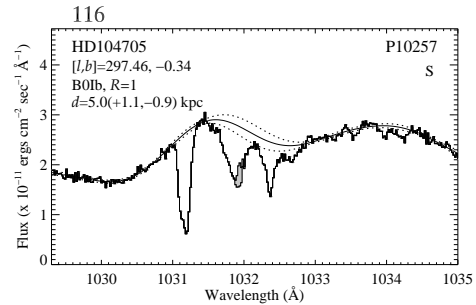
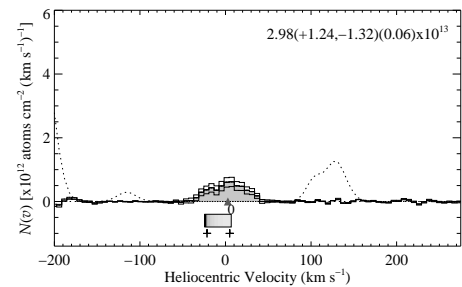
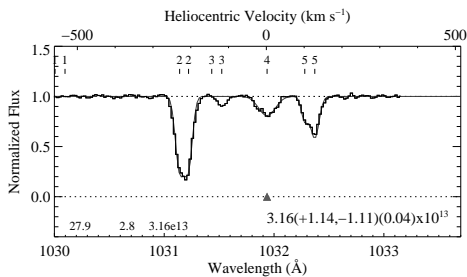
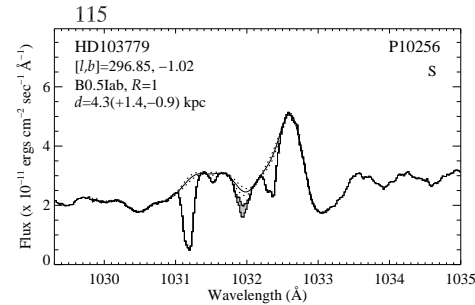
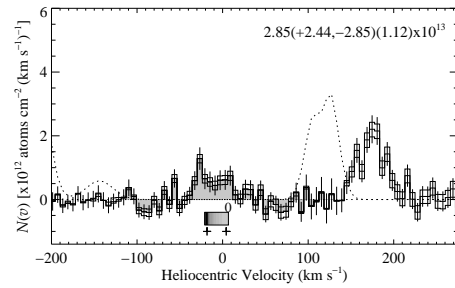
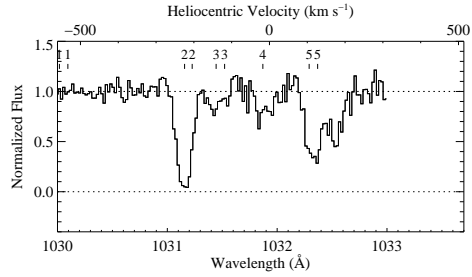
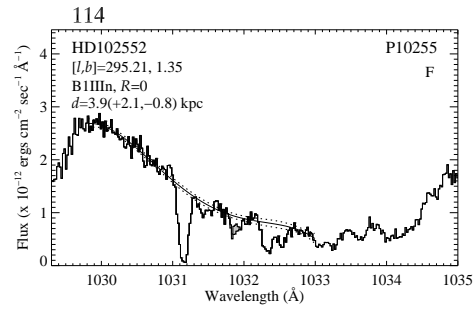
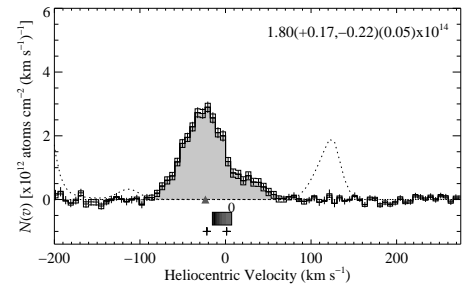
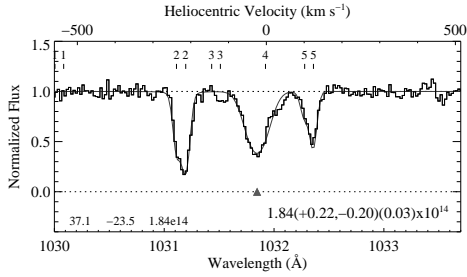
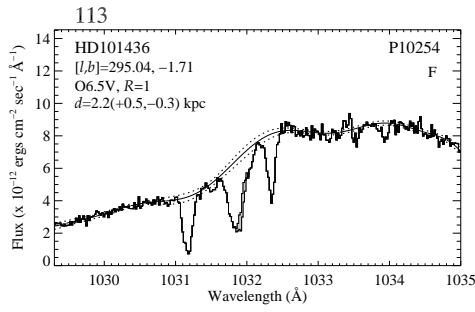
130

Figure 17: cont



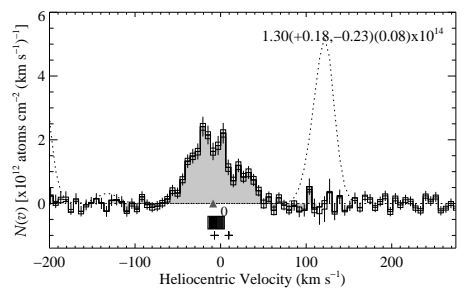
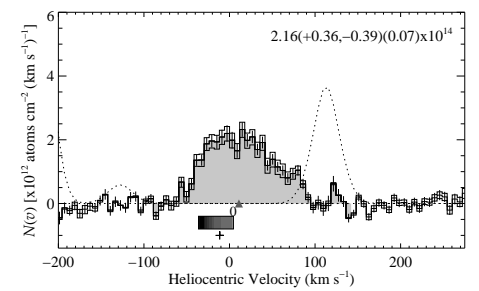
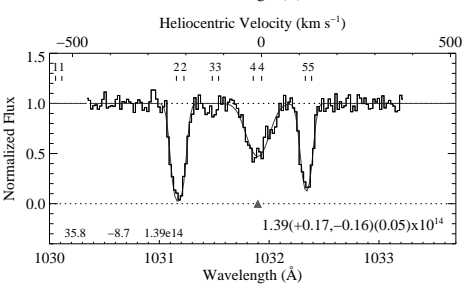
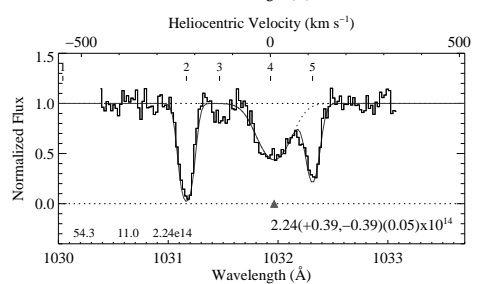
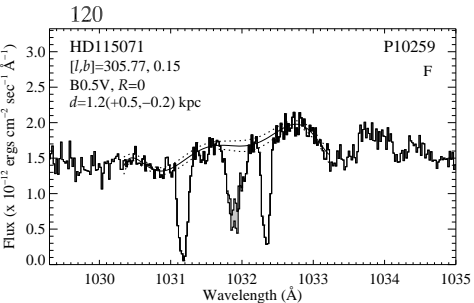
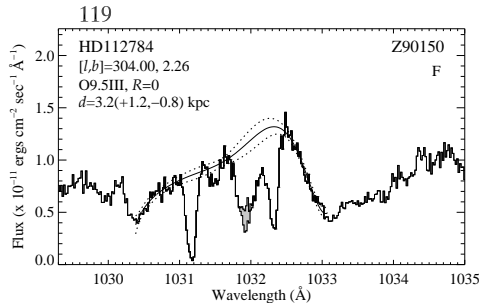
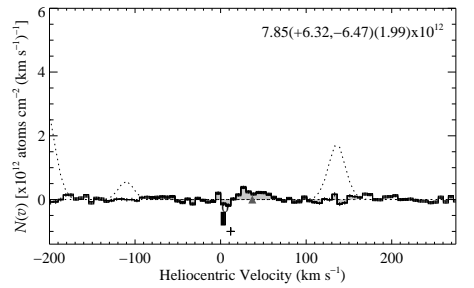
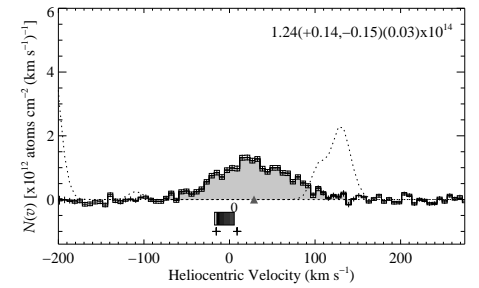
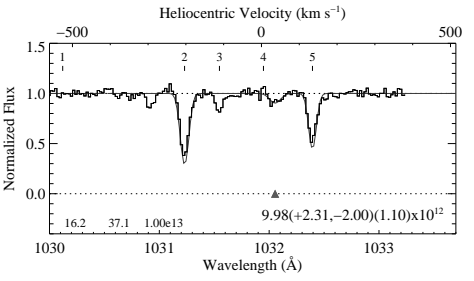
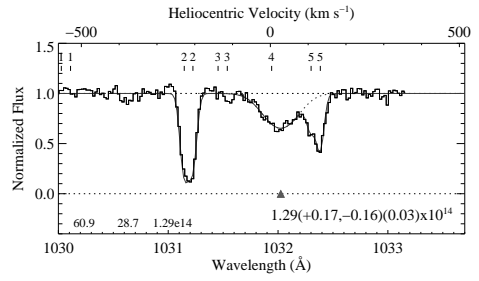
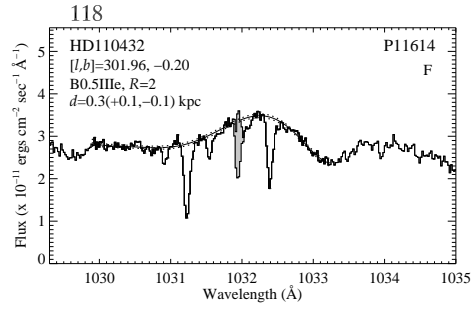
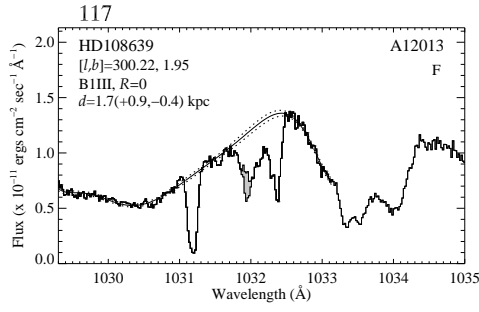
131

Figure 17: cont



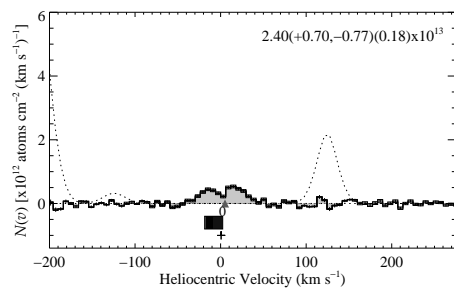
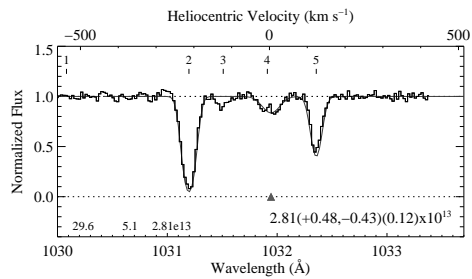
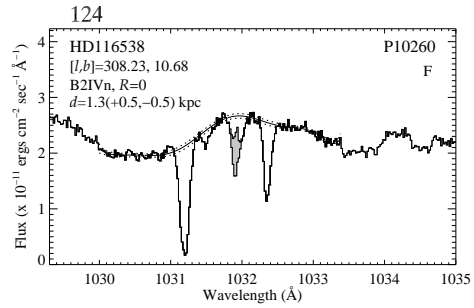
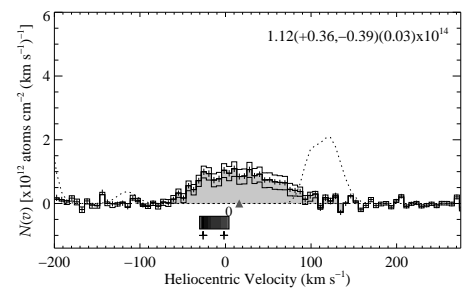
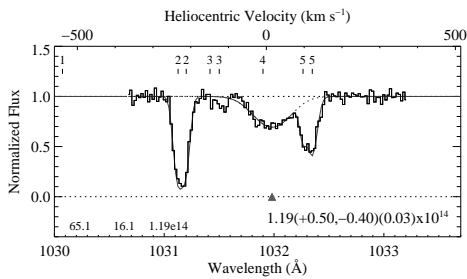
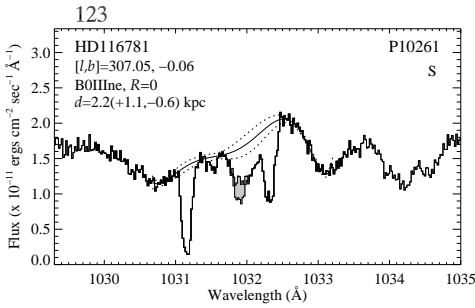
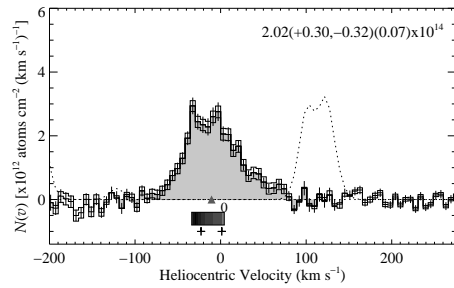
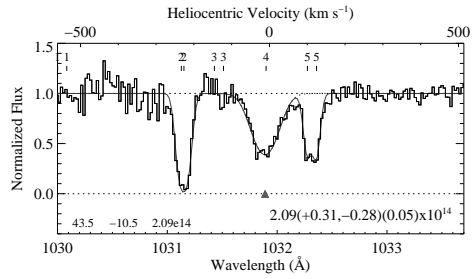
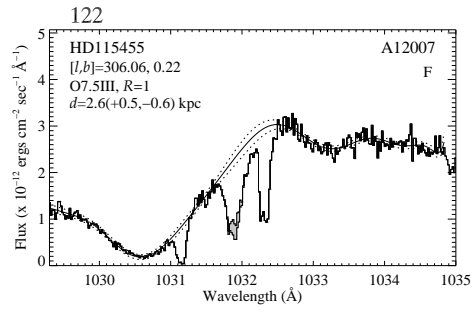
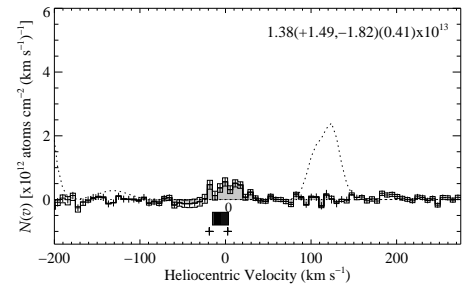
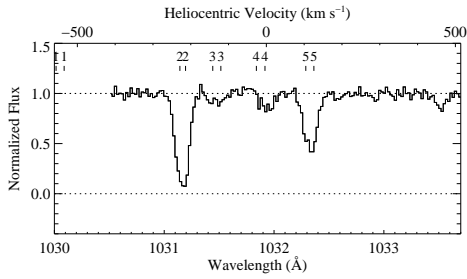
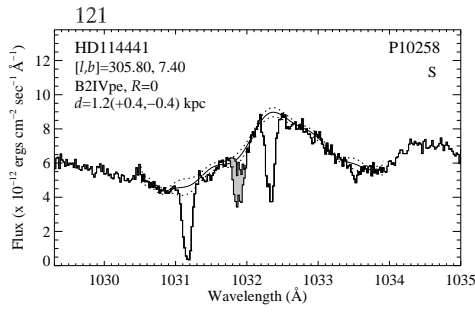
132

Figure 17: cont



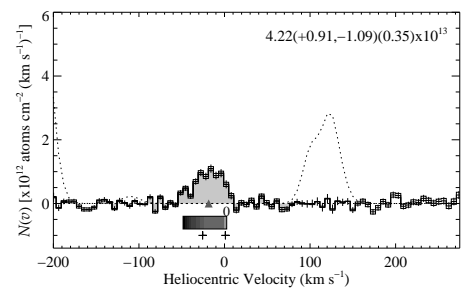
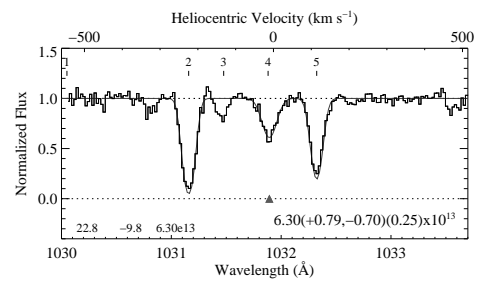
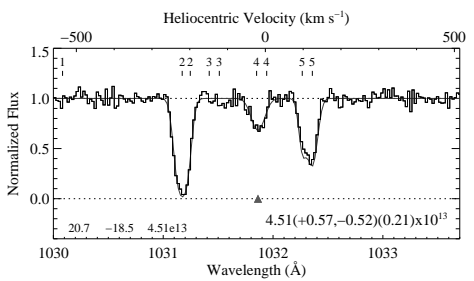
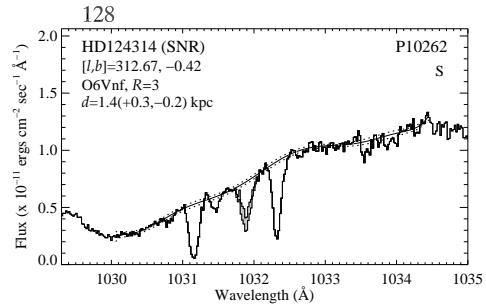
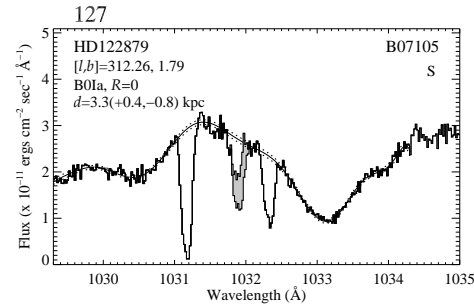
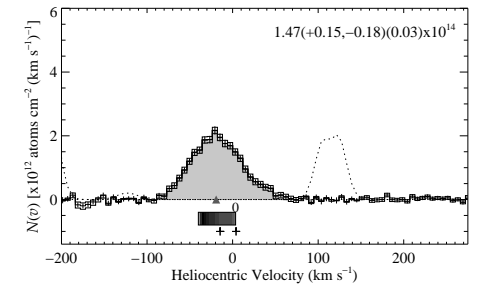
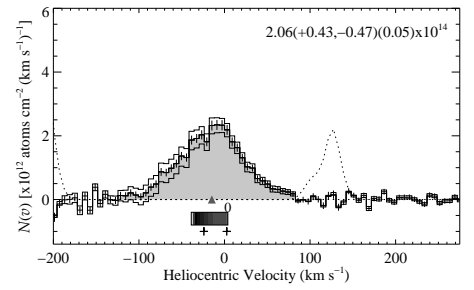
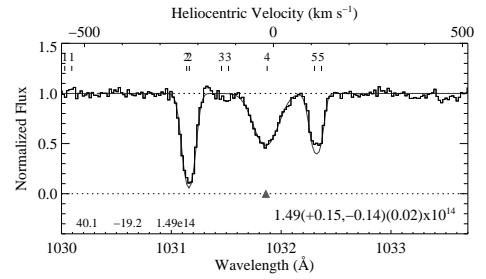
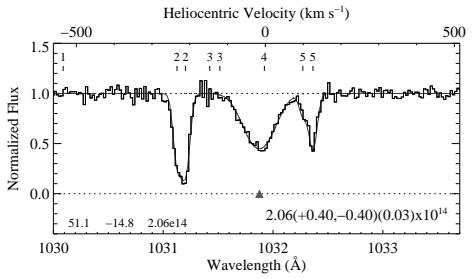
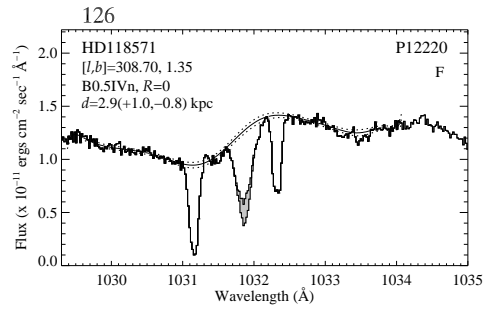
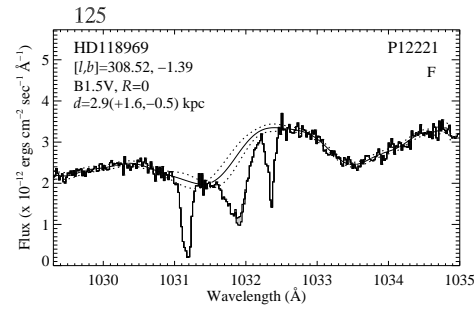
133

Figure 17: cont



134

Figure 17: cont



135

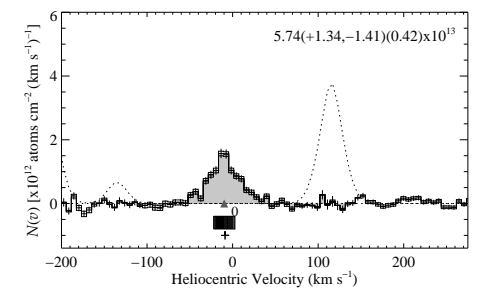
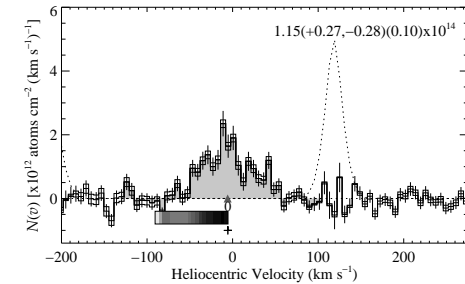
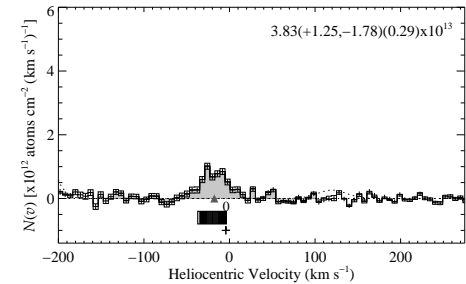
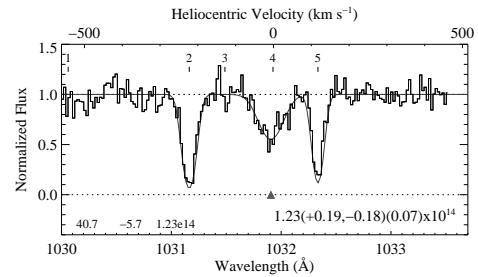
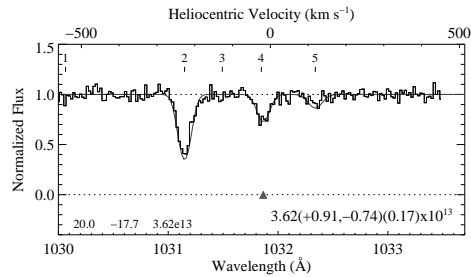
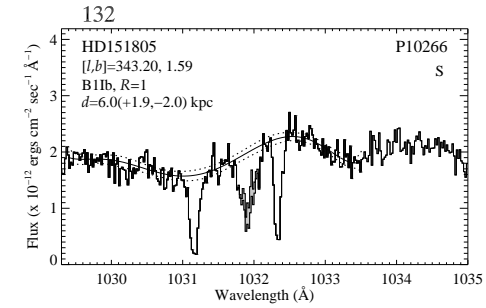
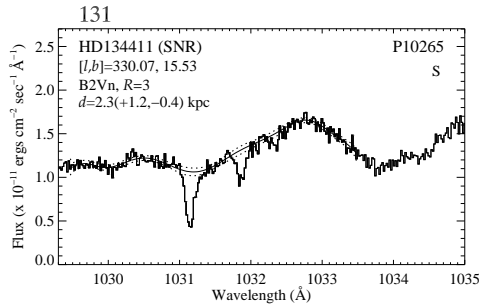
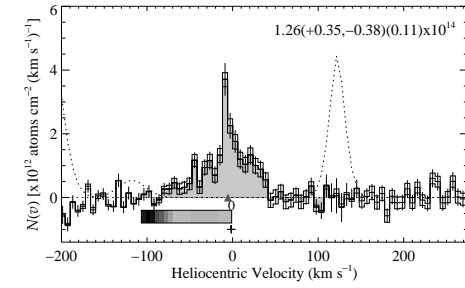
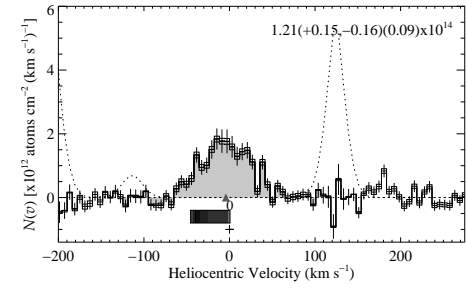
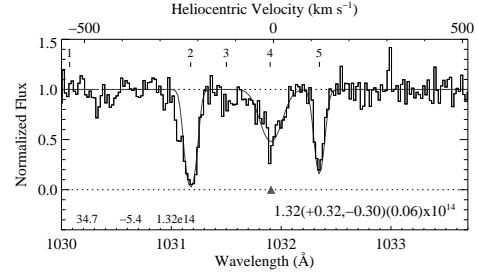
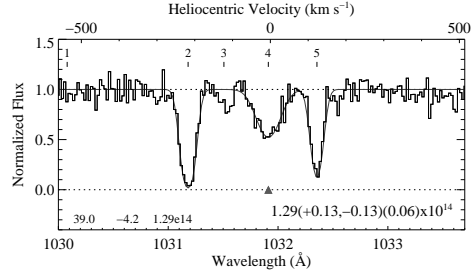
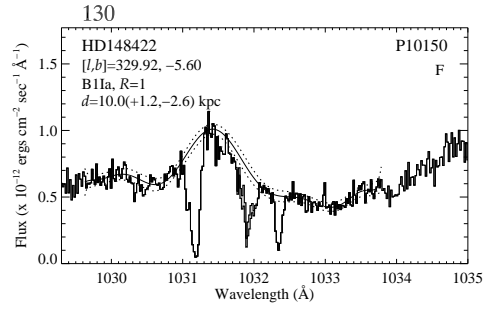
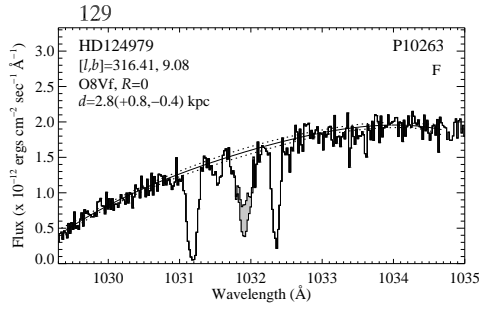
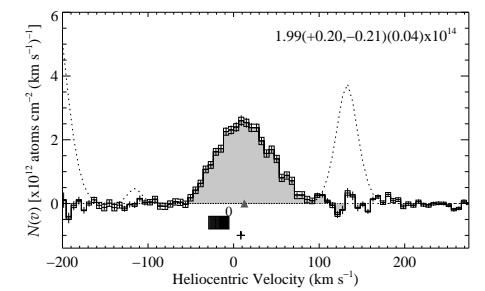
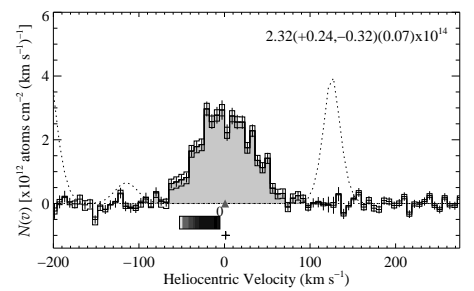
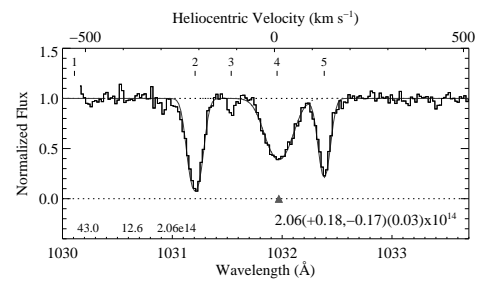
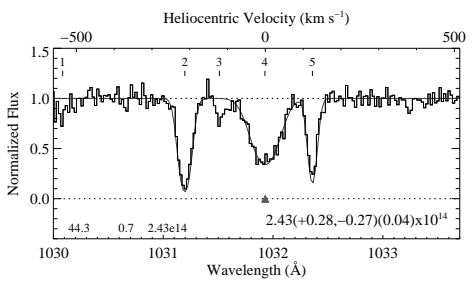
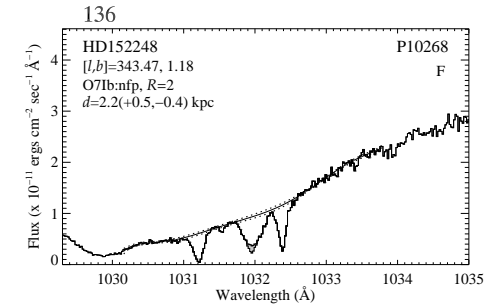
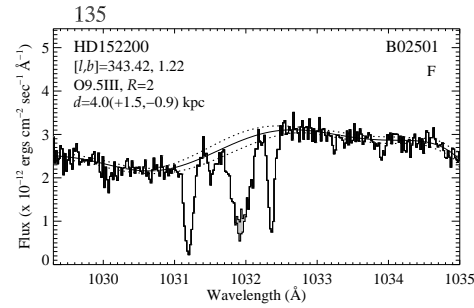
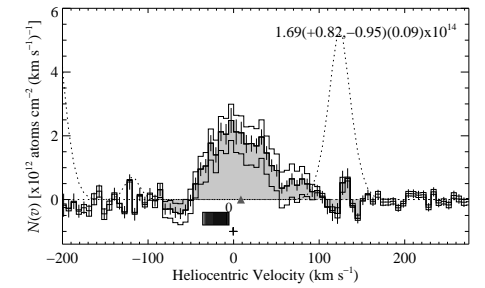
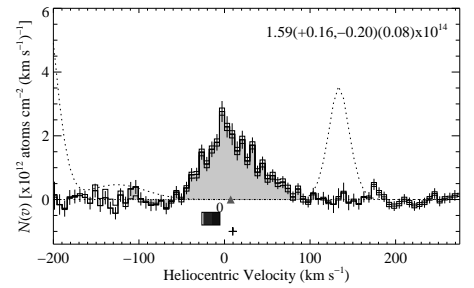
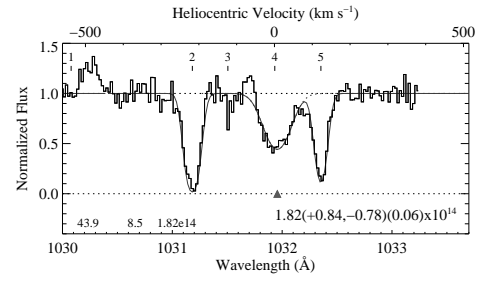
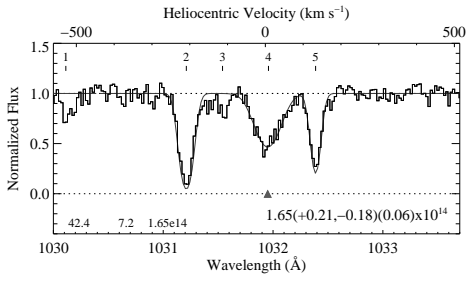
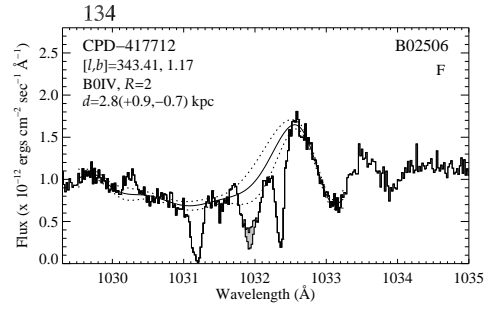
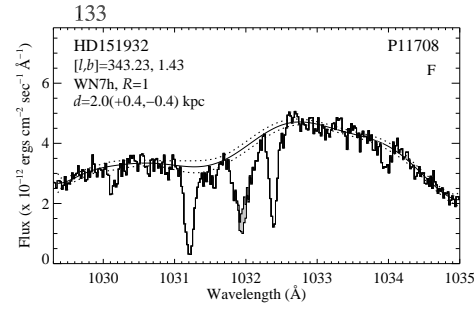


Figure 17: cont



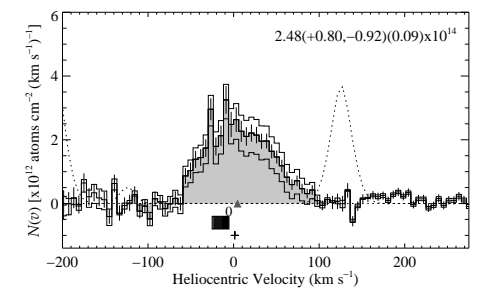
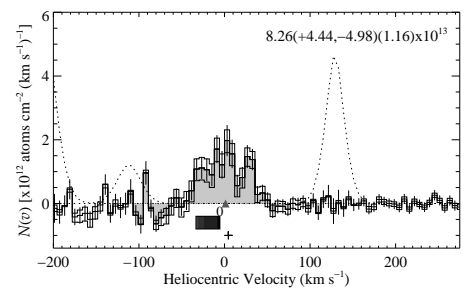
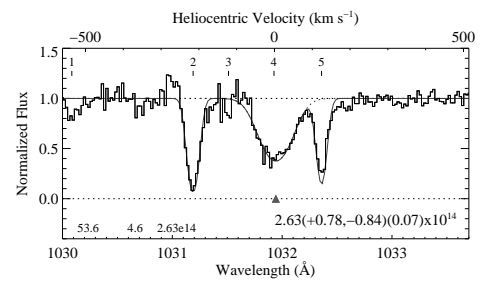
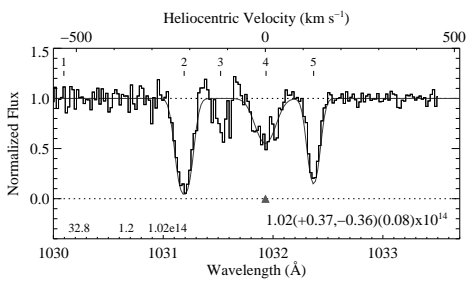
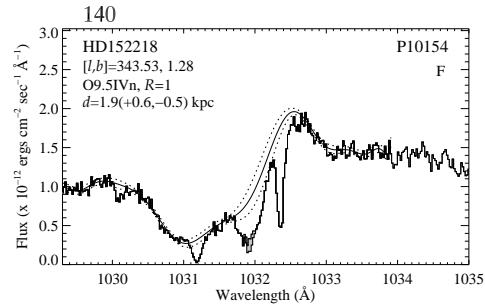
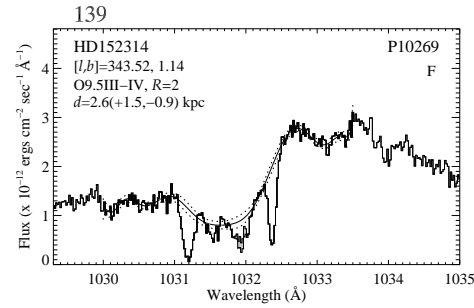
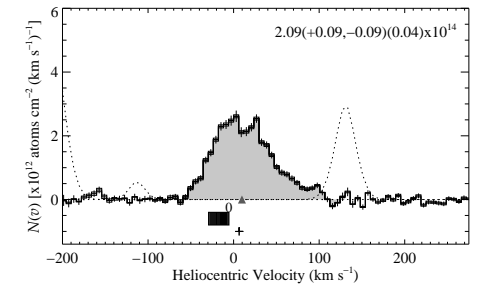
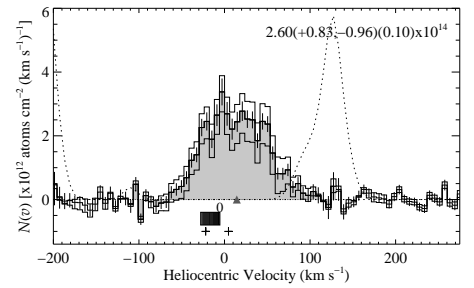
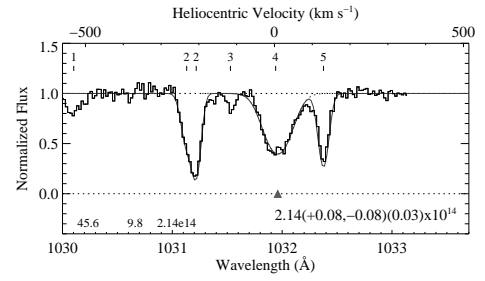
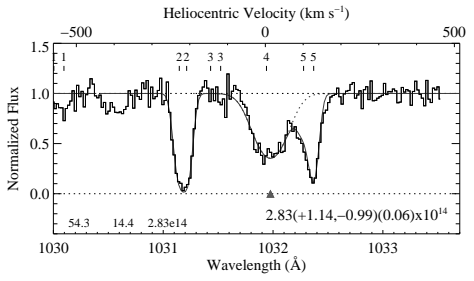
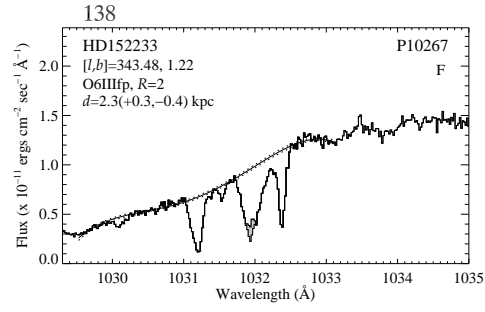
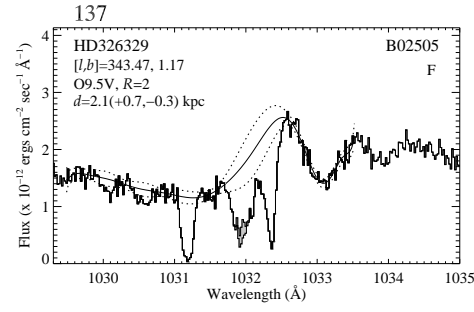
136

Figure 17: cont



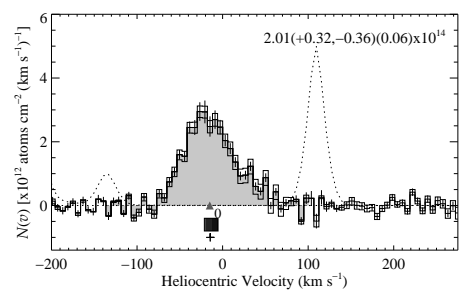
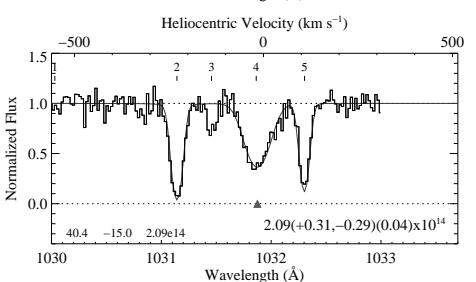
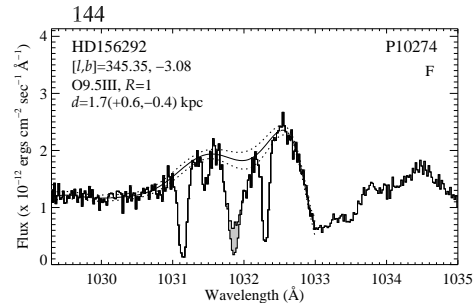
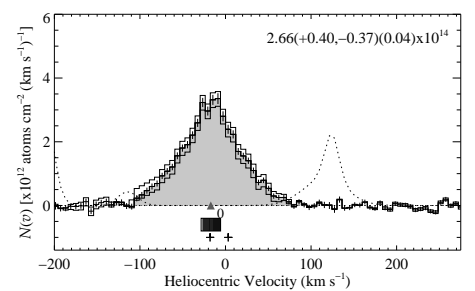
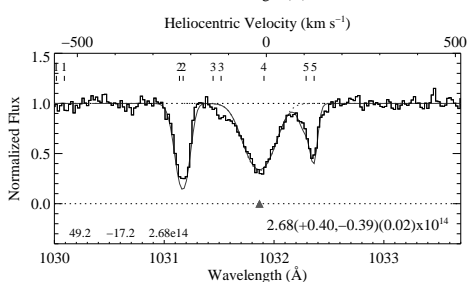
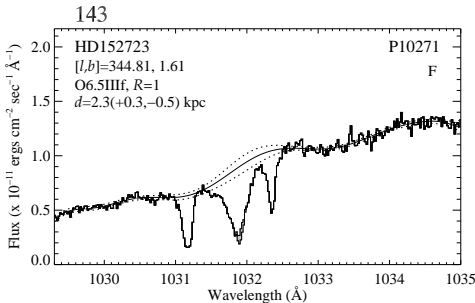
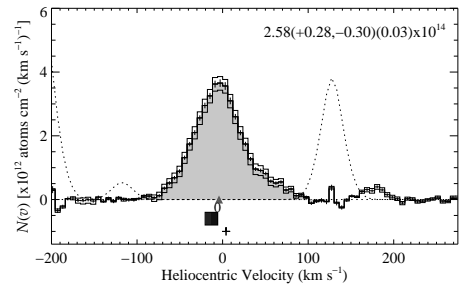
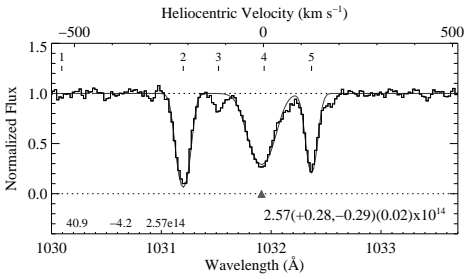
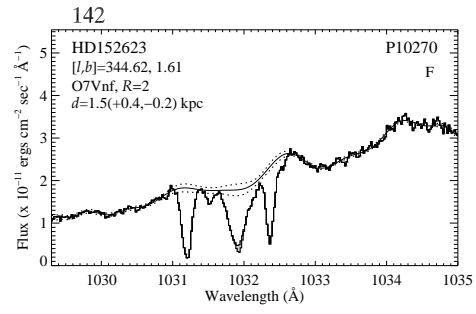
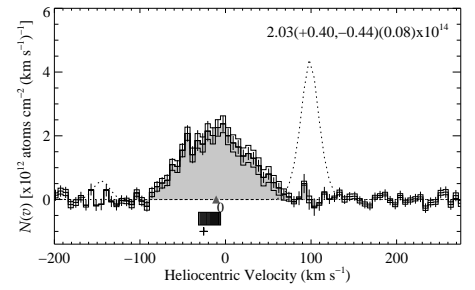
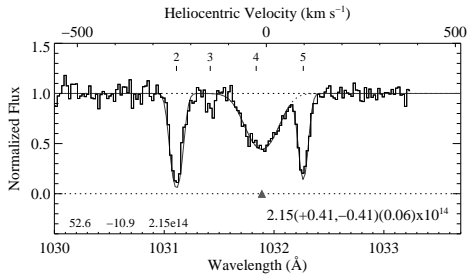
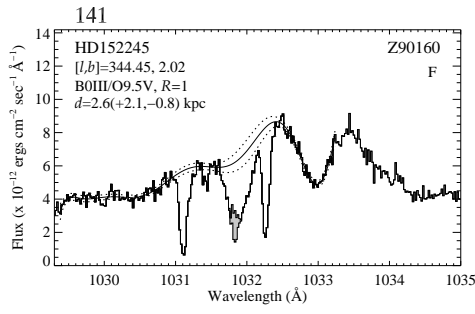
137

Figure 17: cont



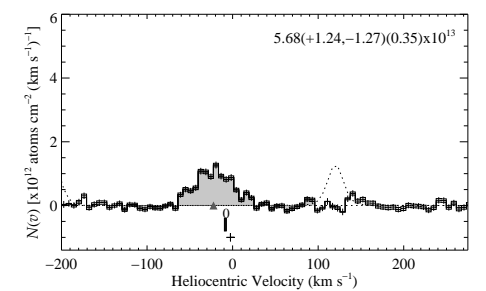
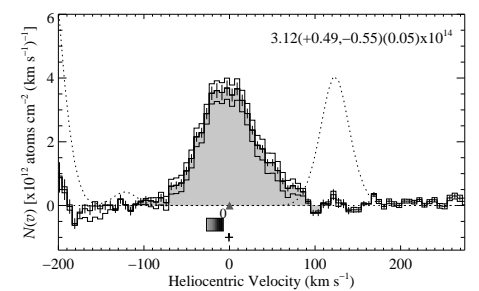
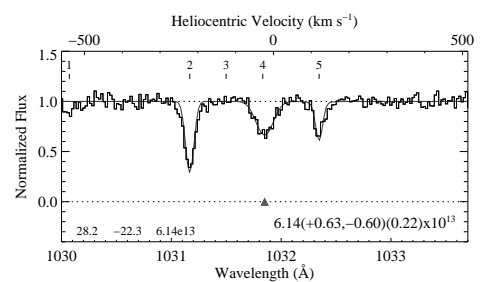
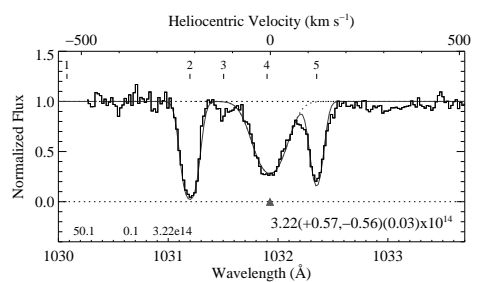
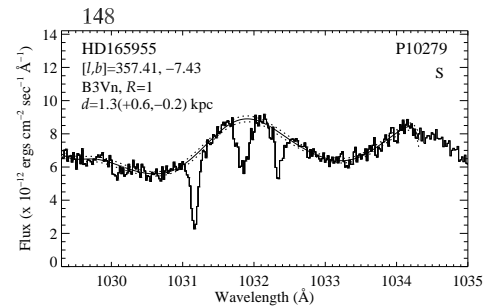
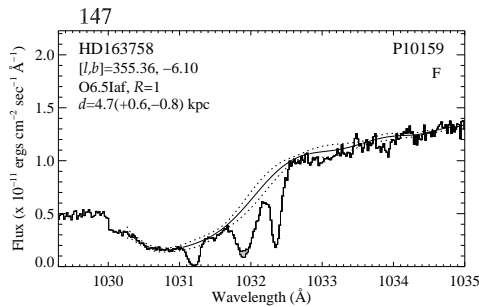
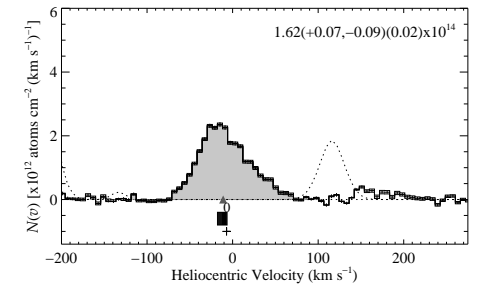
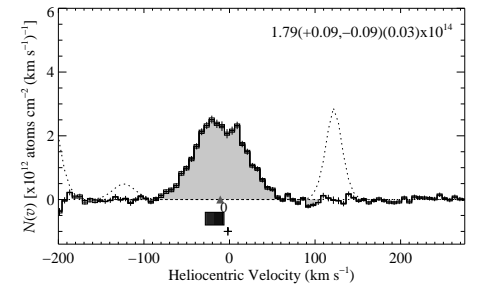
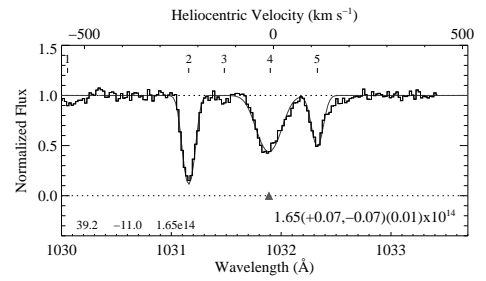
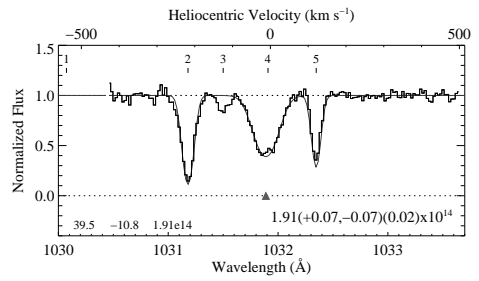
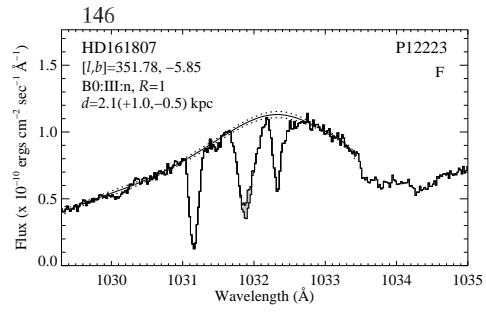
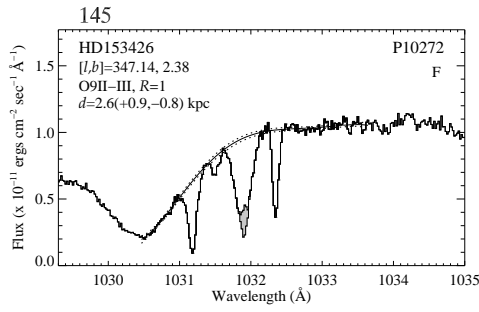
138

Figure 17: cont



139

Figure 17: cont



140

Figure 17: cont